

TABLE OF CONTENTS

		Page
SECTION 1.0	SUMMARY	1 1/A12
SECTION 2.0	INTRODUCTION	3 1/A14
	2.1 Background	3 1/A14
	2.2 Program Description	4 1/B1
	2.2.1 Test Matrices	5 1/B2
	2.2.2 Test Program Description	5 1/B2
	2.2.3 Aerodynamic and Acoustic Prediction Procedure	6 1/B3
SECTION 3.0	APPARATUS – MODEL TEST AND TEST FACILITIES	7 1/B4
	3.1 Jet Noise Test Facility (X-206 Stand)	7 1/B4
	3.1.1 Test Chamber	7 1/B4
	3.1.2 Acoustic Data Acquisition System	10 1/B7
	3.1.3 Pressure and Temperature Instrumentation	10 1/B7
	3.1.3.1 Nozzle Operating Condition Instrumentation	10 1/B7
	3.1.3.2 Nozzle Exhaust Plume Traverse Instrumentation	12 1/B10
	3.1.3.3 Exhaust Plume Traverse System Description	12 1/B10
	3.1.3.4 Data Acquisition Equipment	15 1/B13
	3.1.4 Acoustic Test Matrix	15 1/B13
	3.1.5 Test Procedure	19 1/C6
	3.2 UTRC Large Nozzle Thrust Facility	19 1/C6
	3.2.1 System Description	19 1/C6
	3.2.2 Instrumentation	20 1/C7
	3.2.3 Facility Thrust Balance Calibration	21 1/C8
	3.2.4 Aerodynamic Performance Test Matrix	23 1/C10
	3.3 Nozzle Models	24 1/C11
	3.3.1 Configuration Selection	24 1/C11
	3.3.2 Model Designs	26 1/C13
SECTION 4.0	TEST DATA	31 1/D4
	4.1 Acoustic Data	31 1/D4
	4.1.1 Acoustic Data Reduction	31 1/D4
	4.1.1.1 Theoretical Day SPL (Model)	32 1/D5
	4.1.1.2 Scaled Engine Data	35 1/D10
	4.1.1.3 Calculation of Acoustic Power Levels	36 1/D11
	4.1.2 Acoustics Results and Discussion	37 1/D12
	4.1.2.1 Comparison of Convergent Nozzle Data With SAE Predictions	38 1/D13
	4.1.2.2 Unsuppressed Coannular Nozzle Results	39 1/D14
	4.1.2.3 Definition of the Acoustic Characteristics of a Single Stream Plug Nozzle	54 1/F1

TABLE OF CONTENTS (Cont'd)

		Page
	4.1.2.4 Definition of the Acoustic Characteristics of a Coannular Nozzle with Primary Flow Leakage	57 1/F4
4.2	Aerodynamic Data	61 1/F8
	4.2.1 Aerodynamic Data Reduction	61 1/F8
	4.2.1.1 Thrust and Discharge Coefficient Data Reduction	61 1/F8
	4.2.1.2 Traverse Data Reduction	64 1/F11
4.2.2	Aerodynamic Results and Discussion	64 1/F11
	4.2.2.1 Thrust Coefficient	64 1/F11
	4.2.2.2 Discharge Coefficient	70 1/G4
	4.2.2.3 Nozzle Velocity and Temperature Profiles	76 1/G10
SECTION 5.0	ACOUSTIC ENGINEERING PREDICTION PROCEDURE	81 2/A5
	5.1 General Approach	81 2/A5
	5.1.1 Description of the Acoustic Data Base	81 2/A5
	5.1.2 Definition of Spectral Decomposition	84 2/A8
	5.1.3 Definition of Acoustic Models Used in Developing the Prediction Procedure	90 2/A14
	5.1.4 Definition of Characteristic Velocity, Temperature, and Area for Initial and Merged Regions	91 2/B1
5.2	Static Jet Exhaust Noise Prediction Procedure	93 2/B3
	5.2.1 Development of Mixing Noise Data Correlations	93 2/B3
	5.2.1.1 Merged Region Mixing Noise	98 2/B8
	5.2.1.2 Initial Region Mixing Noise	109 2/C5
	5.2.2 Development of Shock Noise Data Correlations	117 2/C13
	5.2.2.1 Development of Fan Stream Shock Noise Data Correlations	117 2/C13
	5.2.2.2 Development of Primary Stream Shock Noise Data Correlations	125 2/D7
5.3	Flight Jet Exhaust Noise Prediction Procedure	130 2/D12
	5.3.1 General Background	130 2/D12
	5.3.2 Definition of the Effect of Flight on Mixing Noise	132 2/D14
	5.3.2.1 Definition of the Effect of Flight on the Low Frequency Mixing Noise Component	134 2/E2
	5.3.2.2 Definition of the Effect of Flight on the High Frequency Mixing Noise Component	136 2/E4
	5.3.3 Definition of the Effect of Flight on the Shock Noise Component	138 2/E6

TABLE OF CONTENTS (Cont'd)

	Page	
5.4 Summary of Acoustic Prediction Procedure	139	2/E7
5.4.1 General Approach	139	2/E7
5.4.2 Summary of the Static Acoustic Prediction Procedure	140	2/E8
5.4.2.1 Low Frequency Mixing Noise Component	140	2/E8
5.4.2.2 High Frequency Mixing Noise Component	141	2/E9
5.4.2.3 Fan Stream Shock Noise	142	2/E10
5.4.2.4 Primary Stream Shock Noise	143	2/E11
5.4.3 Summary of the Flight Acoustic Prediction Procedure	144	2/E12
5.4.3.1 Low Frequency and High Frequency Mixing Noise Components	145	2/E13
5.4.3.2 Fan Stream and Primary Stream Shock Noise Components	145	2/E13
5.5 Sample Calculation	146	2/E14
5.5.1 Inputs Required for the Acoustic Prediction	147	2/F1
5.5.2 Prediction of the Static Jet Exhaust Noise	147	2/F1
5.5.2.1 Low Frequency Mixing Noise	147	2/F1
5.5.2.2 High Frequency Mixing Noise	148	2/F2
5.5.2.3 Fan Stream Shock Noise	149	2/F3
5.5.2.4 Primary Stream Shock Noise	149	2/F3
5.5.3 Prediction of the Flight Jet Exhaust Noise	151	2/F5
5.5.3.1 Low Frequency and High Frequency Mixing Noise Components	151	2/F5
5.5.3.2 Fan Stream and Primary Stream Shock Noise Components	151	2/F5
5.6 Comparison of Data with Predictions Using the Acoustic Prediction Procedure	152	2/F6
5.6.1 Comparison of IVP Coannular Nozzle Noise Predictions with Measured Data	153	2/F7
5.6.2 Analysis of the Accuracy of the Prediction Procedure	165	2/G5
SECTION 6.0	STATIC AERODYNAMIC PERFORMANCE PREDICTION PROCEDURE	
6.1 Approach	167	2/G7
6.1.1 Subsonic and Supersonic Nozzle Loss Mechanisms	167	2/G7
6.1.2 Prediction Procedure Concept	167	2/G7
6.2 Viscous Losses	168	2/G8
6.2.1 Internal Duct Loss	168	2/G8
6.2.2 External Scrubbing Loss	170	2/G10
6.2.3 Correlation of Subsonic Model Performance	171	2/G11

TABLE OF CONTENTS (Cont'd)

	Page
6.3 Shock Loss	172 2/G12
6.3.1 Plug Nozzle Operating Characteristics	172 2/G12
6.3.2 Off-Design Shock Loss	173 2/G13
6.4 Application of the Aerodynamic Performance Prediction Procedure	176 3/A6
6.4.1 Procedural Steps and Input Requirements	176 3/A6
6.4.2 Numerical Example of the Procedure Use	179 3/A9
6.5 Evaluation of the Static Aerodynamic Performance Prediction Procedure	182 3/A12
 SECTION 7.0	
SUMMARY OF RESULTS AND CONCLUSIONS	187 3/B3
7.1 Acoustic Results and Conclusions	187 3/B3
7.1.1 Acoustic Prediction Procedure	187 3/B3
7.1.2 Acoustic Test Results	188 3/B4
7.2 Aerodynamic Performance Results and Conclusions	188 3/B4
7.2.1 Static Aerodynamic Performance Prediction Procedure	188 3/B4
7.2.2 Aerodynamic Performance Test Results	189 3/B5
7.3 Prediction System Accuracy	190 3/B6
 APPENDIX A	191 3/B7
 APPENDIX B	205 3/D5
 LIST OF SYMBOLS	211 3/D11
 REFERENCES	214 3/D14

83044-16

NAS 1.26:3168

OCT 5 1979

NASA Contractor Report 3168

COMPLETED
ORIGINAL

**Aerodynamic and Acoustic Investigation
of Inverted Velocity Profile Coannular
Exhaust Nozzle Models and Development
of Aerodynamic and Acoustic
Prediction Procedures**

**Richard S. Larson, Douglas P. Nelson,
and Bradley S. Stevens**

**CONTRACT NAS3-20061
AUGUST 1979**

NASA

**REPRODUCED FROM
BEST AVAILABLE COPY**

224

**Aerodynamic and Acoustic Investigation
of Inverted Velocity Profile Coannular
Exhaust Nozzle Models and Development
of Aerodynamic and Acoustic
Prediction Procedures**

**Richard S. Larson, Douglas P. Nelson,
and Bradley S. Stevens**
*United Technologies Corporation
East Hartford, Connecticut*

**Prepared for
Lewis Research Center
under Contract NAS3-20061**



National Aeronautics
and Space Administration

**Scientific and Technical
Information Branch**

BLANK PAGE

TABLE OF CONTENTS

	Page	
SECTION 1.0	SUMMARY	1
SECTION 2.0	INTRODUCTION	3
2.1	Background	3
2.2	Program Description	4
2.2.1	Test Matrices	5
2.2.2	Test Program Description	5
2.2.3	Aerodynamic and Acoustic Prediction Procedure	6
SECTION 3.0	APPARATUS – MODEL TEST AND TEST FACILITIES	7
3.1	Jet Noise Test Facility (X-206 Stand)	7
3.1.1	Test Chamber	7
3.1.2	Acoustic Data Acquisition System	10
3.1.3	Pressure and Temperature Instrumentation	10
3.1.3.1	Nozzle Operating Condition Instrumentation	10
3.1.3.2	Nozzle Exhaust Plume Traverse Instrumentation	12
3.1.3.3	Exhaust Plume Traverse System Description	12
3.1.3.4	Data Acquisition Equipment	15
3.1.4	Acoustic Test Matrix	15
3.1.5	Test Procedure	19
3.2	UTRC Large Nozzle Thrust Facility	19
3.2.1	System Description	19
3.2.2	Instrumentation	20
3.2.3	Facility Thrust Balance Calibration	21
3.2.4	Aerodynamic Performance Test Matrix	23
3.3	Nozzle Models	24
3.3.1	Configuration Selection	24
3.3.2	Model Designs	26
SECTION 4.0	TEST DATA	31
4.1	Acoustic Data	31
4.1.1	Acoustic Data Reduction	31
4.1.1.1	Theoretical Day SPL (Model)	32
4.1.1.2	Scaled Engine Data	35
4.1.1.3	Calculation of Acoustic Power Levels	36
4.1.2	Acoustics Results and Discussion	37
4.1.2.1	Comparison of Convergent Nozzle Data With SAE Predictions	38
4.1.2.2	Unsuppressed Coannular Nozzle Results	39
4.1.2.3	Definition of the Acoustic Characteristics of a Single Stream Plug Nozzle	54

TABLE OF CONTENTS (Cont'd)

	Page
4.1.2.4 Definition of the Acoustic Characteristics of a Coannular Nozzle with Primary Flow Leakage	57
4.2 Aerodynamic Data	61
4.2.1 Aerodynamic Data Reduction	61
4.2.1.1 Thrust and Discharge Coefficient Data Reduction	61
4.2.1.2 Traverse Data Reduction	64
4.2.2 Aerodynamic Results and Discussion	64
4.2.2.1 Thrust Coefficient	64
4.2.2.2 Discharge Coefficient	70
4.2.2.3 Nozzle Velocity and Temperature Profiles	76
 SECTION 5.0 ACOUSTIC ENGINEERING PREDICTION PROCEDURE	81
5.1 General Approach	81
5.1.1 Description of the Acoustic Data Base	81
5.1.2 Definition of Spectral Decomposition	84
5.1.3 Definition of Acoustic Models Used in Developing the Prediction Procedure	90
5.1.4 Definition of Characteristic Velocity, Temperature, and Area for Initial and Merged Regions	91
5.2 Static Jet Exhaust Noise Prediction Procedure	93
5.2.1 Development of Mixing Noise Data Correlations	93
5.2.1.1 Merged Region Mixing Noise	98
5.2.1.2 Initial Region Mixing Noise	109
5.2.2 Development of Shock Noise Data Correlations	117
5.2.2.1 Development of Fan Stream Shock Noise Data Correlations	117
5.2.2.2 Development of Primary Stream Shock Noise Data Correlations	125
5.3 Flight Jet Exhaust Noise Prediction Procedure	130
5.3.1 General Background	130
5.3.2 Definition of the Effect of Flight on Mixing Noise	132
5.3.2.1 Definition of the Effect of Flight on the Low Frequency Mixing Noise Component	132
5.3.2.2 Definition of the Effect of Flight on the High Frequency Mixing Noise Component	134
5.3.3 Definition of the Effect of Flight on the Shock Noise Component	138

TABLE OF CONTENTS (Cont'd)

	Page
5.4 Summary of Acoustic Prediction Procedure	139
5.4.1 General Approach	139
5.4.2 Summary of the Static Acoustic Prediction Procedure	140
5.4.2.1 Low Frequency Mixing Noise Component	140
5.4.2.2 High Frequency Mixing Noise Component	141
5.4.2.3 Fan Stream Shock Noise	142
5.4.2.4 Primary Stream Shock Noise	143
5.4.3 Summary of the Flight Acoustic Prediction Procedure	144
5.4.3.1 Low Frequency and High Frequency Mixing Noise Components	145
5.4.3.2 Fan Stream and Primary Stream Shock Noise Components	145
5.5 Sample Calculation	146
5.5.1 Inputs Required for the Acoustic Prediction	147
5.5.2 Prediction of the Static Jet Exhaust Noise	147
5.5.2.1 Low Frequency Mixing Noise	147
5.5.2.2 High Frequency Mixing Noise	148
5.5.2.3 Fan Stream Shock Noise	149
5.5.2.4 Primary Stream Shock Noise	149
5.5.3 Prediction of the Flight Jet Exhaust Noise	151
5.5.3.1 Low Frequency and High Frequency Mixing Noise Components	151
5.5.3.2 Fan Stream and Primary Stream Shock Noise Components	151
5.6 Comparison of Data with Predictions Using the Acoustic Prediction Procedure	152
5.6.1 Comparison of IVP Coannular Nozzle Noise Predictions with Measured Data	153
5.6.2 Analysis of the Accuracy of the Prediction Procedure	165
SECTION 6.0	STATIC AERODYNAMIC PERFORMANCE PREDICTION PROCEDURE
6.1 Approach	167
6.1.1 Subsonic and Supersonic Nozzle Loss Mechanisms	167
6.1.2 Prediction Procedure Concept	167
6.2 Viscous Losses	168
6.2.1 Internal Duct Loss	168
6.2.2 External Scrubbing Loss	170
6.2.3 Correlation of Subsonic Model Performance	171

TABLE OF CONTENTS (Cont'd)

	Page
6.3 Shock Loss	172
6.3.1 Plug Nozzle Operating Characteristics	172
6.3.2 Off-Design Shock Loss	173
6.4 Application of the Aerodynamic Performance Prediction Procedure	176
6.4.1 Procedural Steps and Input Requirements	176
6.4.2 Numerical Example of the Procedure Use	179
6.5 Evaluation of the Static Aerodynamic Performance Prediction Procedure	182
 SECTION 7.0	
SUMMARY OF RESULTS AND CONCLUSIONS	187
7.1 Acoustic Results and Conclusions	187
7.1.1 Acoustic Prediction Procedure	187
7.1.2 Acoustic Test Results	188
7.2 Aerodynamic Performance Results and Conclusions	188
7.2.1 Static Aerodynamic Performance Prediction Procedure	188
7.2.2 Aerodynamic Performance Test Results	189
7.3 Prediction System Accuracy	190
 APPENDIX A	191
 APPENDIX B	205
 LIST OF SYMBOLS	211
 REFERENCES	214

SECTION 1.0

SUMMARY

This program is a continuation of experimental and design study programs conducted by Pratt & Whitney Aircraft to identify and investigate the aero/acoustic technology for advanced power plants in second-generation supersonic cruise aircraft. This program was directed toward the acquisition of static acoustic and aerodynamic performance data that when combined with existing data supported the development of an aero/acoustic prediction procedure for inverted velocity profile coannular jet nozzles.

Acoustic and aerodynamic performance tests were conducted using five 12.7 cm (5 in) coannular nozzle models designed and fabricated for this program. The acoustic tests were conducted in the Pratt & Whitney Aircraft Willgoos Laboratory Anechoic Test Noise Facility (X-206 stand) where the pressures and temperatures of both the fan and primary streams were varied to study both inverted velocity profiles (outer stream velocity greater than that of the inner stream) and noninverted velocity profiles. These same models were then tested for aerodynamic performance at the United Technologies Research Laboratory cold flow large nozzle test facility. In these tests, two levels of primary nozzle pressure ratio (PNPR), 1.53 and 2.0, were evaluated over a range of fan nozzle pressure ratios (FNPR) from 1.5 to 4.0.

The geometries of the five models were selected to provide a systematic variation in fan and primary nozzle radius ratio (for each stream, the radius ratio is defined as the ratio of inner to outer radius at the throat). This was accomplished by designing each configuration with the same fan and primary throat areas (fan to primary area ratio of 1.48) but positioning the annular throats at different mean radii. The fan nozzle radius ratios tested were 0.69, 0.75, and 0.83. The primary nozzle radius ratios were 0 (no plug), 0.6, and 0.81. The 0 radius ratio primary nozzle was tested with all three fan nozzle radius ratios. The 0.6 radius ratio primary nozzle was tested with the fan nozzle radius ratio of 0.75; the 0.81 radius ratio primary nozzle was tested with the fan nozzle radius ratio of 0.83. The primary plugs and fan nozzle afterbodies were all 15 degree conical sections. The annular throats were also oriented at 15 degrees to direct the flow along the afterbody/plug. The convergent (no plug) primary configuration directed the primary flow axially.

Acoustic testing defined the additional acoustic benefit that high radius ratio exhaust systems can contribute to the inherent acoustic benefit of the inverted velocity profile. This additional benefit was most pronounced at moderate fan stream velocities. The zero primary radius ratio models operating at a fan stream velocity of 610 m/sec (2000 ft/sec) and a primary stream velocity of 427 m/sec (1400 ft/sec) showed a PNL reduction of 3 dB when fan radius ratio increased from 0.69 to 0.83. Also, increasing primary radius ratio from 0 to 0.81 (fan radius ratio held constant at 0.83) reduced peak perceived noise level (PNL) an additional 1 dB. However, as fan stream velocity was increased to 854 m/sec (2800 ft/sec), a condition more typical of presently envisioned advanced supersonic technology (AST) propulsion systems at takeoff, there was no added acoustic benefit with increasing fan and primary stream radius ratio.

An acoustic engineering prediction procedure was developed using the acoustic and plume traverse data from this program in conjunction with existing data. The procedure is capable of predicting jet noise sound pressure level spectra at all angles, for coannular nozzles with inverted velocity profiles, as a function of nozzle geometry, operating condition and flight velocity. In the development of the acoustic procedure, the noise spectra at each angle and operating condition were decomposed into four noise components: a high frequency mixing noise component, a low frequency mixing noise component, a fan stream shock noise component, and a primary stream shock noise component. Data correlations were then developed for each noise component as a function of nozzle geometry, operating condition, and flight velocity. The data correlations collapsed the data with standard deviations varying from ± 0.8 dB to ± 2.7 dB.

Although increasing fan radius ratio was beneficial acoustically at some operating conditions, it adversely affected the nozzle aerodynamic performance. For the zero primary radius ratio models operating at a PNPR of 1.53, increasing fan radius ratio from 0.69 to 0.83 reduced the nozzle thrust coefficient from 0.9 to 1.4 percent over the FNPR range tested. At a PNPR of 2.0, the reduction was 0.9 to 1.9 percent.

Installing a plug in the primary nozzle to increase the primary radius ratio alleviated the nozzle performance penalty of the highest fan radius ratio model. This occurred because the fan cowl afterbody was cut back to keep the primary throat area fixed, which reduced the surface area scrubbed by the fan flow. For example, increasing primary radius ratio from 0 to 0.60 at a fan radius ratio of 0.75 increased nozzle thrust coefficient 0.1 to 1.3 percent at a PNPR of 1.53; at a PNPR of 2.0, performance increased from 0 to 1.1 percent.

In general, the configurations achieved reasonable levels of thrust coefficient; the lowest thrust coefficient was 0.965 and the highest was 0.988. A significant result of the performance testing was the pronounced primary stream flow restriction that occurred in the zero primary radius ratio configuration, particularly at a PNPR of 1.53. Reducing PNPR from 2.0 to 1.53 reduced the primary discharge coefficient (CD_p) from 0.908 to 0.671 (at a FNPR of 2.85). This flow restriction was also affected by the axial separation or cowl extension between the primary and the fan nozzles (L) that occurred as the fan radius ratio was varied. For example, as the ratio of cowl extension to passage height (L/H) increased from 1.0 to 7.7, the CD_p dropped from 0.774 to 0.605 (at PNPR of 1.53). The effect was less pronounced at a PNPR of 2.0 where CD_p decreased from 0.93 to 0.84 with this same geometry change.

A thrust coefficient prediction system was developed by combining analytical predictions and an experimental correlation. Data acquired from the static aerodynamic performance testing provided an empirical correlation for shock loss at nozzle pressure ratios in excess of 2.0, which when combined with analytically-determined internal duct loss and external scrubbing loss, established the basis for the prediction system. At a fan nozzle pressure ratio of a 3.2, the measured thrust coefficients were collapsed with a range from ± 0.001 to ± 0.006 at a primary nozzle pressure ratio of 1.53 and from ± 0.001 to ± 0.003 at a primary nozzle pressure ratio of 2.0. Application of the prediction system to coannular plug nozzles, configured somewhat differently than the present program models, resulted in a prediction accuracy of ± 1 percent in thrust coefficient. No attempt was made to formulate a prediction system for primary stream flow restriction.

All of the detailed acoustic and performance data taken are contained in the companion Comprehensive Data Report (Reference 19).

SECTION 2.0

INTRODUCTION

2.1 BACKGROUND

The increasing importance of environmental considerations is expected to require significant reductions in exhaust system noise levels for the next generation of supersonic transport aircraft. Adequate noise reduction must be obtained with a high level of exhaust system aerodynamic performance. Prior to this program, extensive analytical and experimental propulsion system studies, conducted as part of the NASA-sponsored Supersonic Cruise Airplane Research (SCAR) effort, identified the Variable Stream Control Engine (VSCE) as a promising cycle in terms of both system performance and low noise generation. The VSCE cycle can be matched to provide a high velocity duct (fan) stream surrounding a low velocity core (primary) stream resulting in an exit velocity profile which has inherent jet noise benefits without the use of mechanical noise suppressors.

The noise characteristics of conventional coannular exhaust systems (the fan stream is of lower velocity than the primary stream) have been extensively investigated during the past few years. The work of Williams (Reference 1) first pointed out that the noise of a coannular jet was related to fan to primary stream velocity ratio and showed that the noise of a coannular jet was less than the noise of the primary jet under isolated conditions for a large range of fan to primary velocity ratios less than one. The basic results of Williams were extended by Eldred (Reference 2) to include coannular jets having a heated stream and included the effects of fan to primary stream exhaust area ratio. Analytical models developed in References 1 and 2 showed that the gross results of the coannular jet could be related to the aerodynamic characteristics of the jet exhaust plume. For example, high frequencies were shown to be reduced due to the relative velocity effect of the fan exhaust surrounding the primary stream, and low frequency characteristics were ascribed to the presence of a merged jet resulting from the mixing of the fan and primary jets downstream of the nozzle. The experimental investigations of Olsen (Reference 3) and Bielak (Reference 4) confirmed the results of Williams and Eldred, and the SAE Subcommittee on Jet Noise has developed a coannular jet noise prediction procedure drawing upon some of the results from References 1 through 4 as well as additional coannular jet noise data produced during recent experimental testing. Predictions made using the SAE procedure have shown reasonable agreement with model and full-scale engine noise data but have been limited to subsonic flow conditions where the fan exit velocity is less than the primary velocity. The more recent prediction procedure of Stone (Reference 5) includes the effects of supersonic jets. The work of Dosanjh (Reference 6) focused on the noise from coaxial and tertiary unheated supersonic jets. Results from his investigation have shown that the jet noise could be minimized for certain combinations of pressure ratios for coaxial and tertiary jets, including cases where the inner stream velocity was less than the velocity of the outer stream. However, due to the use of unheated jets, Dosanjh's results relate to the shock noise component of jet noise and are not directly applicable to the noise of the hot jet exhausts existing in a duct burning turbofan engine.

More recently, studies sponsored by NASA Lewis Research Center have focused on the noise produced by coaxial nozzles with an inverted velocity profile and heated fan and primary streams. In the investigation conducted by Kozlowski and Packman (References 7 and 8), the noise produced by coaxial nozzles with inverted velocity profiles was studied for an extensive range of fan primary stream operating conditions. It was demonstrated that substantial noise benefits were obtainable from inverted velocity profile nozzles relative to the noise produced by two nozzles operated at the fan stream and primary stream conditions. The effects of flight on the noise produced by an inverted velocity profile coaxial nozzle were defined in a study by Kozlowski and Packman (References 9 and 10) by simulating the effect of forward flight in a free jet wind tunnel. It was determined that the noise benefits of an inverted velocity profile nozzle were maintained in flight. The study by Knott (References 11 and 12) confirmed the inverted velocity profile noise benefit for additional nozzle geometries to those tested in References 7 and 8. In addition to these NASA-sponsored experiments, several theoretical studies have been conducted to define the origin of the inverted velocity profile noise benefit. A theoretical prediction procedure based on the Lilley (Reference 13) model of jet noise generation was developed by Grieve (Reference 14) and applied to an inverted velocity profile coaxial nozzle. The noise benefit was determined to be related to the rapid mixing of the fan and primary stream flows when the velocity profile is inverted. Similar results were obtained by Larson (Reference 15) in a study of the acoustic power spectra generated by inverted velocity profiles. A prediction procedure was developed by Stone (Reference 16) for inverted velocity profile jets using some results of the present investigation.

2.2 PROGRAM DESCRIPTION

This program was conducted to develop an aero/acoustic prediction procedure using the expanded data base applicable to the evaluation of coannular inverted velocity profile nozzles.

In this program, five scale model coannular nozzles with a fan to primary area ratio of 1.48 were designed to simulate representative VSCE geometries. The five nozzles were constructed so that the effect of fan stream (outer) and primary stream (inner) radius ratios and exit separation on jet noise could be independently determined. Three nozzles had a primary radius ratio of zero (no plug in the primary flow) but different fan radius ratios of 0.69, 0.75, and 0.83. The other two nozzles contained plugs in the primary stream; one had a fan radius ratio of 0.75 and a primary radius ratio of 0.60 while the other had a fan radius ratio of 0.83 and a primary radius ratio of 0.81.

An extensive testing program was conducted to define the effect of fan and primary stream radius ratio and exit separation over a wide range of nozzle operating conditions.

2.2.1 Test Matrices

The acoustic test matrix consisted of 95 sets of operating conditions covering a range of fan stream temperatures between 700°K (1260°R) and 1089°K (1960°R) and velocities between 314 m/sec (1030 ft/sec) and 853 m/sec (2800 ft/sec) for the five nozzles. The primary temperature was held constant at 811°K (1460°R), and two primary velocities of 427 m/sec (1400 ft/sec) and 539 m/sec (1770 ft/sec) were tested. In addition to being operated as dual flow coannular nozzles, two of the five nozzles were tested with fan flow only over a limited range of operating conditions. A limited series of tests was also conducted with the primary flow alone.

In conjunction with the acoustic tests, sixteen aerodynamic plume surveys were conducted. For each plume survey, total pressure, total temperature, and static pressure measurements were obtained along a radial line in five axial planes. These measurements were used to calculate velocity profiles.

The aerodynamic performance test matrix comprised a total of 65 cold flow performance test points including:

- (1) 50 coannular flow points (ten for each of five configurations) at 1.53 and 2.0 primary nozzle pressure ratios over a range of five fan nozzle pressure ratios from 1.3 to 4.1.
- (2) Ten fan only flow points (five for each of two plug configurations) over a range of five fan nozzle pressure ratios from 1.3 to 4.1.
- (3) Five primary only flow points (for 1 plug configuration) over a range of five primary nozzle pressure ratios from 1.3 to 4.1.

2.2.2 Test Program Description

The acoustic measurements and aerodynamic plume surveys were conducted at the X-206 stand in the Pratt & Whitney Aircraft Willgoos Turbine Laboratory located in East Hartford, Connecticut. The X-206 stand is an indoor anechoic jet testing facility capable of producing two independently controlled flows for simulating VSCE operating conditions. Far-field noise was measured on a 4.57 m (15 ft) radius with microphones placed every 10 degrees between 60 and 160 degrees from the inlet axis. Plume surveys were obtained with a telescoping two dimensional traverse system. Flow, pressure, and temperature data were recorded on magnetic tape.

The nozzle aerodynamic performance testing was performed at the United Technologies Research Center Large Nozzle Thrust Facility in East Hartford. This facility operates on the blowdown principle and consists basically of a $2.758 \times 10^6 \text{ N/m}^2$ (400 psig) air supply connected to an apparatus which measures thrust and airflow. Dried air enters the test stand from the $2.758 \times 10^6 \text{ N/m}^2$ (400 psig) blowdown system through a large 1.06 m (40 inch) diameter plenum.

The aerodynamic performance and acoustic test operating conditions were set using total pressure instrumentation located in a strut case (charging station) located approximately 21 inches upstream from the model nozzle exit plane. Total and primary airflows were measured with individual critical flow venturis.

Each model was operated over a range of fan nozzle pressure ratios at each of two fixed primary nozzle pressure ratios. Nozzle thrust was measured with a calibrated strain gage ring type force balance in the aerodynamic performance test. The force balance output and flow measurement data were recorded on magnetic tape for each test point. Estimated duct pressure losses were used to compute total pressure at the nozzle exit.

All the basic data obtained in this program are reported separately in the companion Comprehensive Data Report (Reference 19).

2.2.3 Aerodynamic and Acoustic Prediction Procedure

The aero/acoustic data obtained in this program were analyzed to determine the effects of fan and primary stream radius ratio and exit separation on jet noise and aerodynamic performance. The data were then combined with the data of References 7, 8, 9, 10, 11, and 12 to develop an acoustic prediction procedure capable of predicting inverted velocity profile jet noise sound pressure level spectra at all angles as a function of nozzle geometry and flight velocity and an aerodynamic performance prediction system capable of predicting coannular nozzle performance over a range of nozzle geometries at static operating conditions.

APPARATUS – MODEL TEST AND TEST FACILITIES

The experimental apparatus used in this program is described in this section. Included are descriptions of the jet noise test facility (X-206 Stand), the United Technologies Research Laboratory Large Nozzle Thrust Facility, and the model nozzles fabricated in this program.

3.1 JET NOISE TEST FACILITY (X-206 STAND)

The Pratt & Whitney Aircraft Anechoic Jet Noise Facility, X-206 stand, was used to obtain both acoustic and exit velocity profile measurements required for the program. This facility, located at the Andrew Willgoos Turbine Laboratory, was specially designed to provide an accurate simulation of pure jet noise characteristics using scale model nozzles.

3.1.1 Test Chamber

The test chamber, illustrated in Figure 3.1-1, has a volume of approximately 340 m^3 ($12,000 \text{ ft}^3$) and is lined on all surfaces with specially constructed anechoic wedges to provide an anechoic environment for frequencies above 150 Hz. The walls are constructed with an air passage between the concrete block outer wall and a perforated sheet inner wall. Blowers are used to provide a slight inflow of air through the perforated wall in order to eliminate any secondary air currents induced by the flow from the test nozzle and to avoid flow recirculation at the exhaust duct. A honeycomb exhaust silencer further reduces the potential for secondary air currents as well as eliminates the transmission of outdoor noise sources into the stand. Chamber temperature, relative humidity and pressure are recorded for each test point at the locations shown in Figure 3.1-1.

It is necessary to have a floor in the anechoic chamber to provide personnel access to the microphones and test nozzles. The floor, designed to be acoustically transparent, is constructed of tensioned wire mesh of 0.254 cm (0.10 in) diameter and 5.08 cm (2 in) grid size located at two levels above the floor wedges. Compared to a metal floor grating, the tensioned wire floor system is preferred from an acoustical design viewpoint (Reference 17).

Test nozzles are situated to exhaust in a vertical position directly beneath the exhaust stack. Air required to provide the two streams for the coannular test nozzle is supplied from the laboratory compressed air system at a maximum flow rate of 14.06 kg/sec (31 lb/sec) at $4.14 \times 10^5 \text{ N/m}^2$ (60 psia). The flow for each air stream is independently controlled by pneumatically operated valves in each line. Flow rates are measured independently for each air stream by flow measuring venturis which have been calibrated, within ± 0.2 percent at the Colorado Engineering Experimentation Station, Inc. To prevent duct noise from reaching the test nozzle section, airflow silencers capable of 25 dB noise suppression are installed in each air stream.

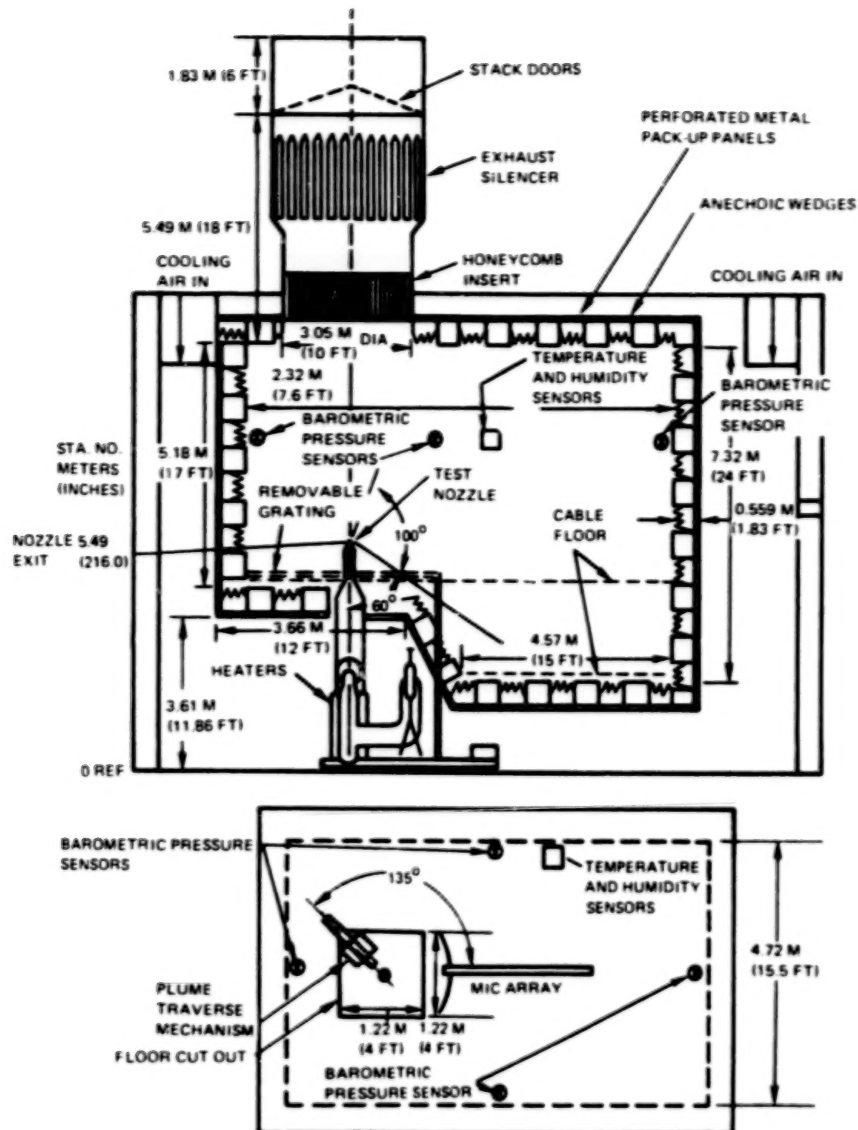


Figure 3.1-1 Anechoic Jet Noise Test Facility (X-206 Stand)

The flows are heated by direct natural gas fired heater burners with a maximum capability of 1089°K (1960°R) at nozzle pressure ratios up to 4.0. The fuel flow into the system is measured by calibrated fuel flow venturis. Both flows are then turned 90 degrees through separate plenum chambers and formed to provide coannular flows to the transition section. A schematic of the air supply system is shown in Figure 3.1-2. The transition section, positioned downstream of the direct burners, is lined with high temperature acoustic and thermal insulation material to provide attenuation of upstream noise sources, in addition to that obtained from the airflow silencers.

The instrumentation and support section, illustrated in Figure 3.1-3, is connected to the transition duct via a bellows assembly in the primary flow duct. The bellows, fabricated from 2 ply Inconel 718, takes no axial load but compensates for axial growth occurring upstream of the instrumentation section due to thermal contraction and expansion.

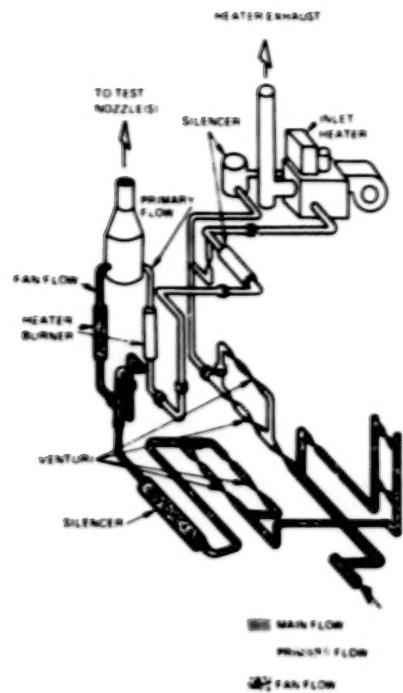


Figure 3.1-2 Schematic of Air Supply Heating and Silencing Mechanisms for X-206 Stand

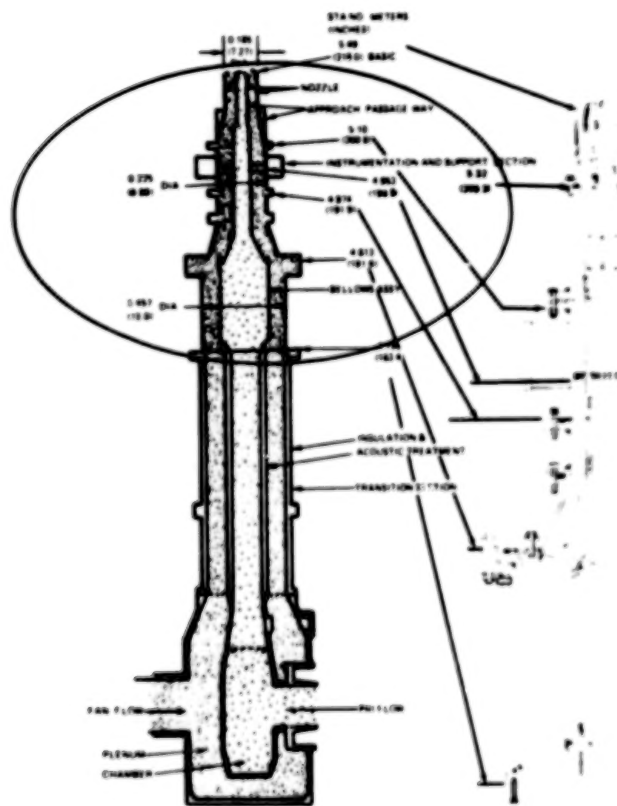


Figure 3.1-3 Exhaust System Test Installation

MICROFILMED FROM
BEST AVAILABLE COPY

3.1.2 Acoustic Data Acquisition System

Acoustic signals were detected by a polar array of 0.635 cm (0.25 in) diameter Brüel and Kjaer (B&K) microphones (Model No. 4135) positioned at normal incidence (0 degrees) to the centerline of the test nozzle exit plane at a distance of 4.57m (15 ft). Microphones were located every 10 degrees from 60 to 160 degrees relative to the upstream jet axis. The 60 and 70 degree microphones are located below the tensioned wire floor. The signals were transmitted to the control room and recorded on magnetic tape with a Honeywell System 96, 14 Channel Wide Band Group I tape recorder. During the test, selected acoustic data were monitored on-line by a B&K No. 2107 one-third octave band sound analyzer. All microphones were calibrated prior to the tests by a procedure traceable to the National Bureau of Standards. Daily calibrations were performed by a B&K No. 4220 Pistonphone. The frequency response of the entire data acquisition system is flat within ± 1.0 dB up to 80,000 Hz.

3.1.3 Pressure and Temperature Instrumentation

3.1.3.1 Nozzle Operating Condition Instrumentation

The instrumentation and support section is located 0.533 m (21 in) upstream from the fan nozzle exit plane and serves a dual purpose. It maintains the concentricity of the coannular nozzle assembly and contains all of the necessary instrumentation to define the properties of the flow entering the nozzles.

The major portions of the instrumentation duct are shown in Figure 3.1-4. A single strut, having an 18 percent NACA series 400 airfoil cross-section, passes through the primary duct and is welded in place at the primary duct walls. The same strut passes freely through the fan duct walls where clearance is provided to allow for relative growth due to temperature differentials in the two streams. Two short struts, welded to the outer diameter of the primary tube and positioned 90 degrees to the primary strut, also pass freely through the fan duct wall. When operating with a thermal gradient, the fan duct is allowed to change in diameter relative to the primary duct without distorting the duct shape and without any significant variation in concentricity. Outer seal housings are provided around the floating struts to prevent leakage from the fan stream.

The instrumentation in the primary passage consisted of six total pressure probes, six total temperature probes and four wall static pressure taps. The fan stream instrumentation consisted of two total pressure probes and two total temperature probes mounted in each of the two duct struts and four static taps in both the inner and outer wall. The total pressure and total temperature probes were installed protruding through the leading edge of the struts. The probes are made up of removable rakes which are held in place at the ends of the support struts. The rakes may be installed or removed after rig assembly without having direct access to the primary or secondary flow passages.

The fan and primary duct rakes were used to establish the total pressures and temperatures of each stream. The probes (P_t and T_t) were arranged radially in each duct at the centers of equal areas. An arithmetic average of the probe readings was then used to provide area-averaged value of total pressure and temperature. Pressure and temperature probes were both included in each rake so that the flow properties were sampled across the entire duct.

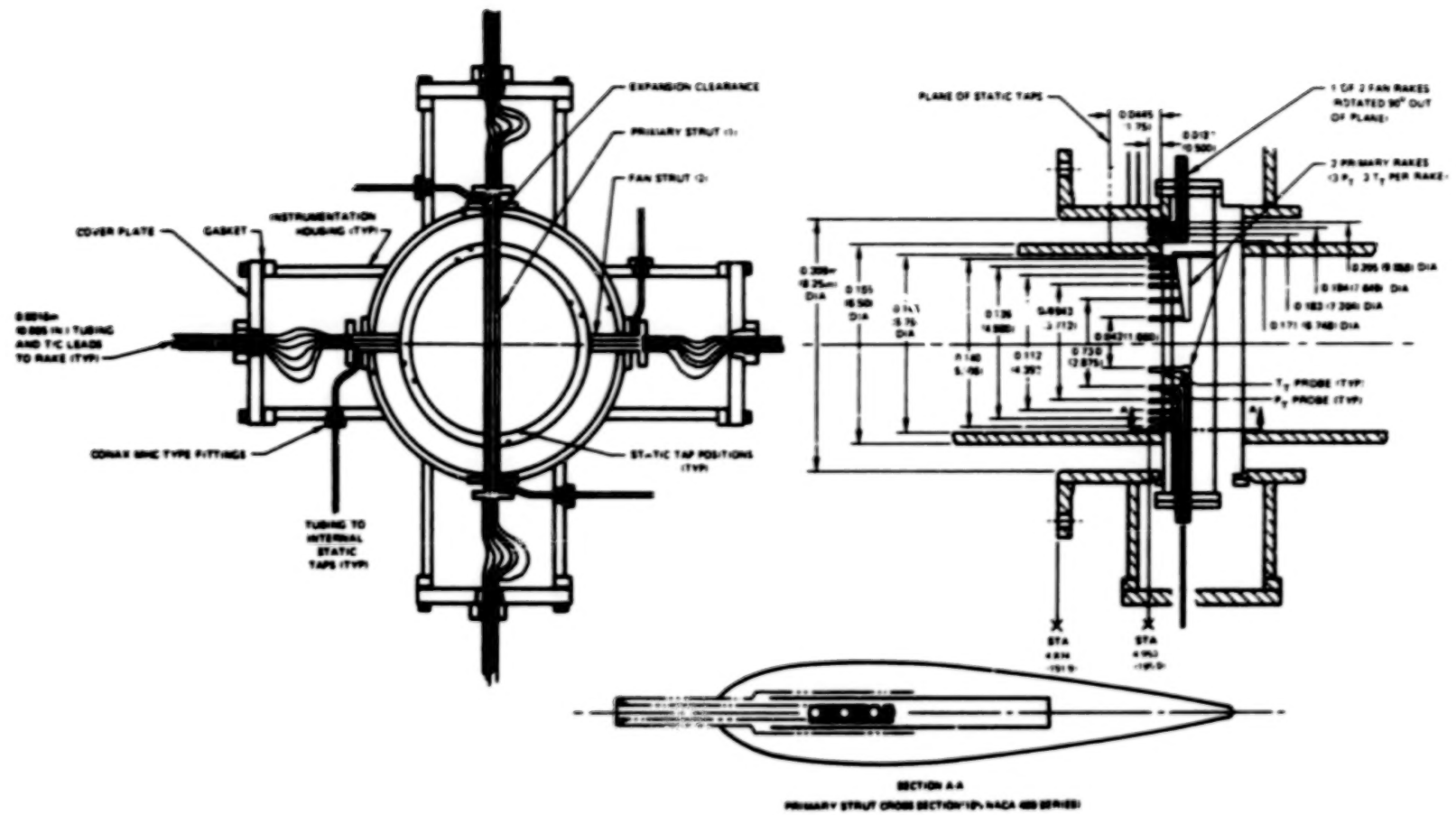


Figure 3.1-4 Details of Instrumentation and Support Section

3.1.3.2 Nozzle Exhaust Plume Traverse Instrumentation

Traverses of the jet exhaust plume were conducted at several elevations downstream of the model to determine the radial pressure and temperature profiles.

A combination wedge probe with total pressure, total temperature, and static pressure measurement capability was used for this program. This type of probe has been used extensively on other NASA and in-house sponsored programs during recent years. A sketch of the probe is shown in Figure 3.1-5. The static pressure is measured with two orifices (a and b), one on each side of the 20-degree wedge. The total temperature is determined by means of a thermocouple that is exposed to flow through ports at the rear of the wedge at points d and e. The flow exits at the base of the wedge through port f, which controls the flow past the thermocouple head. This port was sized to establish the best balance between conductive and convective heat transfer. The probe was extensively calibrated for pressure and temperature recovery up to Mach 1.6 and yaw angle of ± 5 degrees at high and low Reynolds numbers. Strain gages were placed at high stress areas on the wedge so that probe stress could be monitored while traversing the jet plume.

3.1.3.3 Exhaust Plume Traverse System Description

A photograph and a schematic of the traverse system are shown in Figures 3.1-6 and 3.1-7, respectively. The mechanism is located 135 degrees from the microphone array, as shown in Figure 3.1-1. The probe support traverse bed traveled in a vertical plane parallel to the nozzle centerline via two telescoping tubes which collapsed within themselves when in the stowed position. The tube assembly centerline was located 0.61 m (24 in) from the nozzle centerline to allow sufficient plume clearance at the fully extended position. The system had the capability to travel 1.40 m (55 in) above the nozzle exit and was stowed in a rotated position 0.152 m (6 in) below the nozzle exit in order to avoid reflection problems during acoustic testing. The tops and sides of the system were acoustically and thermally insulated.

The traverse mechanism provided two degrees of movement in a plane normal to the nozzle exhaust flow. This movement was a polar type motion, i.e., radial and angular movements, which permitted positioning of the probe in any desired location at any given plane normal to the exhaust of the nozzle. The apparatus consisted of two numerically controlled actuators: one, a chain driven radial traverse actuator to which the probe was attached, the other, a chain driven unit which was used to rotate the radial actuator providing angular positioning. Each unit has a potentiometer which provided positional information, i.e., a millivolt signal, to the traverse control console and the data acquisition system. Automatic positioning of the radial and angular actuators was achieved by means of a two channel Slo-Syn Numerical Tape Control console. A preprogrammed tape was read by this console allowing any desired probing pattern to be achieved.

Due to the relative thermal growth of the nozzle assembly with respect to the floor mounted traverse system it was necessary to determine the true position of the nozzle so that the axial measurement planes could be repeated at any operating condition. In order to accomplish this, an arm was attached to the traverse table which, when lowered, accurately sensed the location of the fan nozzle via a limit switch. All axial traverse positions were then adjusted with respect to this base position. Furthermore, through the use of micro switches and a television monitor, traverse system and probe were protected from interference damage with the test nozzle.

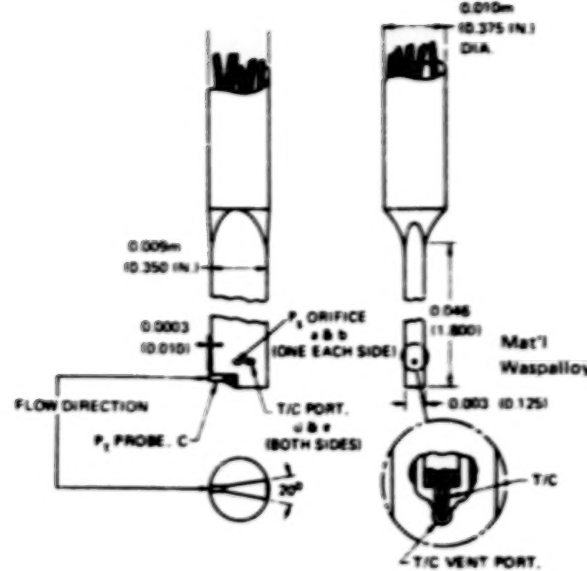
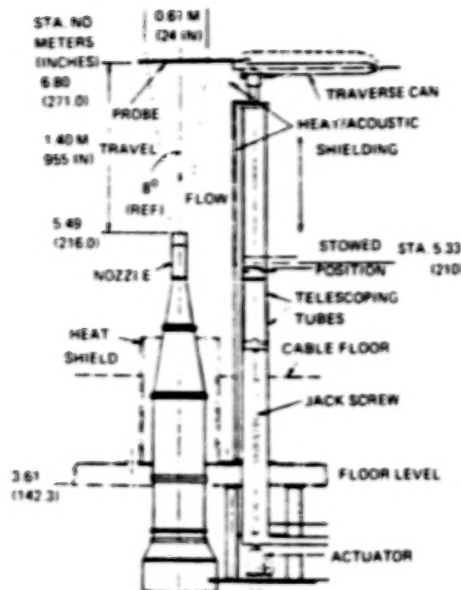


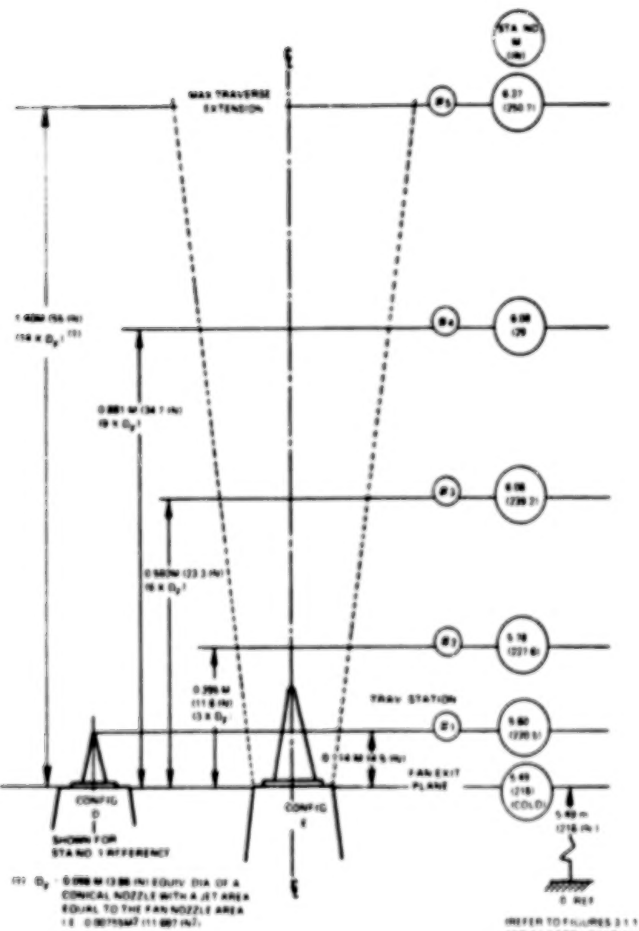
Figure 3.1-5 Details of Traverse Probe



Figure 3.1-6 Exit Profile Traverse Rig



(a)



(b)

Figure 3.1-7 Exit Profile Traverse Rig (a) and Traverse (b) Station Locations

3.1.3.4 Data Acquisition Equipment

A portable data unit was utilized to record on magnetic tape all pressure and temperature readings of the traverse probe and rig operating condition instrumentation as well as the probe location at each sampling point. The magnetic tapes were processed on a Xerox SIGMA 8 computer that converted raw millivolt data acquired from pressure transducers and thermocouples to engineering units and applied appropriate calibrations to the pressure data. The SIGMA 8 generated a hard copy printout of the data in raw millivolts and engineering units, data validity information and punch cards containing the calibrated data in engineering units.

3.1.4 Acoustic Test Matrix

A total of five coannular jet model nozzles was evaluated at the X-206 Anechoic Test Facility. Three of the models had a conical convergent primary nozzle and two had plug type primary nozzles. A summary of the pertinent model geometric parameters, including nominal fan to primary jet area ratio, fan and primary radius ratios, nozzle extension to annulus height ratios, cowl extension and plug angles, is tabulated in Table 3.1-I. The effects of thermal growth on fan to primary jet area ratio at the elevated temperature test conditions are tabulated in Table 3.1-II.

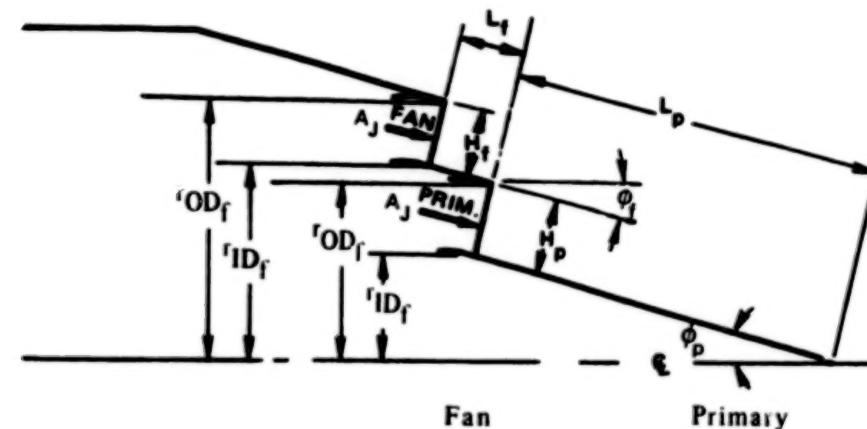
The test matrix used is shown in Table 3.1-III. A total of 95 acoustic and 16 aerodynamic traverse points was recorded over a range of flow conditions including a nozzle pressure ratio range from 1.3 to 4.1 and fan and primary temperature ranges of 700°K (1260°R) to 1089°K (1960°R). The range of test conditions was selected to provide a parametric variation of velocity and temperature ratio to systematically identify their effects on jet noise. The range of test conditions also covered the fan-to-primary velocity ratios typical of VSCE type nozzles. The actual nozzle operating conditions listed in Table 3.1-III were based on charging station instrumentation measurements. Data were acquired with primary flow alone and fan flow alone as well as for coannular flow conditions.

The 16 traverse data points were distributed among the five nozzle configurations to determine the jet plume aerodynamic characteristics over a variety of operating conditions. Each traverse point consisted of radial measurements taken at five axial planes, as shown in Figure 3.1-7b. The axial traverse stations are defined relative to the fan nozzle exit plane, Station 216 (defined in Figure 3.1-1 and 3.1-3). The first traverse plane was chosen at a distance 0.114 m (4.5 in.) from the fan nozzle exit plane of Configuration D, and the fifth plane was located at the maximum traverse extension. The remaining intermediate traverse stations were biased toward the nozzle exit because in this region the plume develops rapidly.

Traverse measurements were taken along one radial line from the nozzle centerline to the extremity of the jet plume as shown in Table 3.1-IV. In some cases aerodynamically-induced vibration (as indicated by traverse probe strain gage instrumentation) prevented taking data at every radius for every traverse test point. These few instances generally occurred at or near the center of the plume, at the two highest axial traverse stations. The number of such instances was small and did not significantly affect use of the traverse data for acoustic analysis.

TABLE 3.1-I
MODEL GEOMETRIC PARAMETERS*

Configuration	Fan						Primary		
	A_j Total (M^2)	(F^2)	A_{j_f}/A_{j_p}	R_f	L_f/H_f	ϕ_f Primary Cowl Exten- tion Angle (deg)	R_p	L_p/H_p	ϕ_p Plug Angle (deg)
A	.0126	.136	1.48	0.69	1.0	15	—	—	—
B	.0126	.136	1.48	0.75	2.9	15	—	—	—
C	.0126	.136	1.48	0.83	7.7	15	—	—	—
D	.0126	.136	1.48	0.75	1.0	15	0.60	5.37	15
E	.0126	.136	1.48	0.83	1.0	15	0.81	15.27	15



* Radius Ratio (R) r_{ID_f}/r_{OD_f} r_{ID_p}/r_{OD_p}

Centerbody Length
Annulus Height L_f/H_f L_p/H_p

Configuration	1089°K (1960°R) Fan		700°K (1260°R) Fan	
	811°K (1460°R) Primary	811°K (1460°R) Primary	811°K (1460°R) Primary	811°K (1460°R) Primary
A	1.45		1.45	
B	1.45		1.45	
C	1.44		1.44	
D	1.45		1.45	
E	1.43		1.44	

TABLE 3.1-III
ACOUSTIC TEST MATRIX

Point No.	FAN			PRIMARY			Data Taken On										
	T_f °K	T_f °R	Pressure Ratio	m/sec	Velocity (ft/sec)	T_p °K	T_p °R	Pressure Ratio	m/sec	Velocity (ft/sec)	A	B	C	D	E		
1	700	(1260)	1.3	314	(1030)	811	(1460)	1.53	427	(1400)	■	■	■	■	■		
2	700	(1260)	1.8	457	(1500)	811	(1460)	1.53	427	(1400)	■	■†	■	■†	■		
3	700	(1260)	2.5	564	(1850)	811	(1460)	1.53	427	(1400)	■	■	■	■	■		
4	700	(1260)	3.2	625	(2050)	811	(1460)	1.53	427	(1400)	■	■†	■	■†	■		
5	1089	(1960)	1.8	573	(1880)	811	(1460)	1.53	427	(1400)	■	■†	■	■†	■		
6	1089	(1960)	2.5	707	(2320)	811	(1460)	1.53	427	(1400)	■†	■†	■†	■†	■†		
7	1089	(1960)	4.1	853	(2800)	811	(1460)	1.53	427	(1400)	■	■	■	■	■		
8	700	(1260)	1.3	314	(1030)	811	(1460)	2.0	540	(1770)	■	■	■	■	■		
9	700	(1260)	1.8	457	(1500)	811	(1460)	2.0	540	(1770)	■	■	■	■	■		
10	700	(1260)	2.5	564	(1850)	811	(1460)	2.0	540	(1770)	■	■	■	■	■		
11	700	(1260)	3.2	625	(2050)	811	(1460)	2.0	540	(1770)	■	■†	■	■†	■		
12	1089	(1960)	1.8	573	(1880)	811	(1460)	2.0	540	(1770)	■	■	■	■	■		
13	1089	(1960)	2.5	707	(2320)	811	(1460)	2.0	540	(1770)	■	■	■	■	■		
14	1089	(1960)	4.1	853	(2800)	811	(1460)	2.0	540	(1770)	■	■	■	■	■		
15 ^{1,2}	No Fan Flow			700	(1260)	1.3	314	(1030)			■						
16	No Fan Flow			700	(1260)	1.8	457	(1500)			■						
17	No Fan Flow			700	(1260)	2.5	564	(1850)			■						
18	No Fan Flow			700	(1260)	3.2	625	(2050)			■						
19	700	(1260)	1.3	314	(1030)	No Primary Flow					■						
20	700	(1260)	1.8	457	(1500)	No Primary Flow					■						
21	700	(1260)	2.5	564	(1850)	No Primary Flow					■						
22	700	(1260)	3.2	625	(2050)	No Primary Flow					■†	■†					
23	1089	(1960)	1.8	573	(1880)	No Primary Flow					■						
24	1089	(1960)	2.5	707	(2320)	No Primary Flow					■						
25	1089	(1960)	4.1	853	(2800)	No Primary Flow					■						
26	No Fan Flow			700	(1260)	1.3	314	(1030)									
27	No Fan Flow			700	(1260)	1.8	457	(1500)									
28	No Fan Flow			700	(1260)	2.5	564	(1850)									
29	No Fan Flow			700	(1260)	3.2	625	(2050)			■†						
30	No Fan Flow			1089	(1960)	1.8	573	(1880)									
31	No Fan Flow			1089	(1960)	2.5	707	(2320)									
32	No Fan Flow			1089	(1960)	4.1	853	(2800)									
TOTALS																	
Acoustic (a) 14																	
Traverse (t) 1																	
Grand Total 1																	
95 Acoustic Pts																	
16 Traverse Pts																	

1. Convergent nozzle reference points

2. The fan cowl was removed when testing with primary flow alone

TABLE 3.1-IV
LOCATIONS FOR TRAVERSE MEASUREMENTS

Configurations A, B, & D		Radial Distance From Centerline													
Traverse Station Station #	Distance	1	2	3	4	5	6	7	8	9	10	11	12	13	14
meters 1 (inches)	5.601 (220.5)	0.032 (1.25)	0.038 (1.50)	0.042 (1.65)	0.046 (1.80)	0.050 (1.95)	0.053 (2.10)	0.057 (2.25)	0.061 (2.40)	0.065 (2.55)	0.069 (2.70)	0.072 (2.85)	0.076 (3.00)	0.083 (3.25)	0.089 (3.50)
meters 2 (inches)	5.781 (227.6)	0	0.019 (0.75)	0.027 (1.07)	0.035 (1.39)	0.043 (1.71)	0.052 (2.03)	0.060 (2.35)	0.067 (2.65)	0.072 (2.83)	0.080 (3.16)	0.089 (3.50)	0.095 (3.75)		
meters 3 (inches)	6.076 (239.2)	0	0.021 (0.81)	0.041 (1.63)	0.062 (2.44)	0.083 (3.25)	0.103 (4.06)	0.124 (4.88)	0.145 (5.69)	0.165 (6.50)					
meters 4 (inches)	6.368 (250.7)	0	0.029 (1.14)	0.058 (2.29)	0.087 (3.43)	0.115 (4.54)	0.145 (5.71)	0.174 (6.86)	0.203 (8.00)						
meters 5 (inches)	6.883 (271.0)	0	0.046 (1.83)	0.093 (3.67)	0.140 (5.50)	0.186 (7.33)	0.233 (9.16)	0.279 (11.00)							
Configurations C & E															
meters 1 (inches)	5.601 (220.5)	0.032 (1.25)	0.035 (1.37)	0.038 (1.50)	0.043 (1.68)	0.044 (1.75)	0.047 (1.87)	0.051 (2.00)	0.054 (2.13)	0.057 (2.25)	0.064 (2.50)	0.070 (2.75)	0.074 (2.90)	0.077 (3.05)	0.081 (3.20)
meters 2 (inches)	5.781 (227.6)	0	0.019 (0.75)	0.026 (1.01)	0.032 (1.27)	0.039 (1.53)	0.045 (1.79)	0.052 (2.05)	0.064 (2.50)	0.072 (2.83)	0.080 (3.16)	0.089 (3.50)	0.095 (3.75)		
meters 3 (inches)	6.076 (239.2)	0	0.021 (0.81)	0.041 (1.63)	0.062 (2.44)	0.083 (3.25)	0.103 (4.06)	0.124 (4.88)	0.145 (5.69)	0.165 (6.50)					
meters 4 (inches)	6.368 (250.7)	0	0.029 (1.14)	0.058 (2.29)	0.087 (3.43)	0.115 (4.54)	0.145 (5.71)	0.174 (6.86)	0.203 (8.00)						
meters 5 (inches)	6.883 (271.0)	0	0.046 (1.83)	0.093 (3.67)	0.140 (5.50)	0.186 (7.33)	0.233 (9.16)	0.279 (11.00)							

3.1.5 Test Procedure

The test procedure for obtaining an acoustic or traverse data point consisted of setting the fan and primary pressures and temperatures required. These were then held constant with automatic pressure and temperature controllers and allowed to stabilize for approximately five minutes. Both acoustic and nozzle operating condition data were then acquired simultaneously. During data acquisition the nozzle operating conditions were closely monitored for fluctuations.

3.2 UTRC LARGE NOZZLE THRUST FACILITY

The static nozzle model aerodynamic tests, conducted with unheated flow, were performed at the United Technologies Research Center in the Large Nozzle Thrust Facility. This facility operates on the blowdown principle and consists of an air supply connected to an apparatus which measures thrust and airflow. Dried air enters the test stand from the $2.758 \times 10^6 \text{ N/m}^2$ (400 psia) blowdown system through a large 1.016 m (40 in) diameter plenum. The high pressure air system, when operated in the blowdown mode, can provide runs of at least a 200 second duration with airflow rates up to 34.05 kg/sec (75 lb/sec) and nozzle exit pressures of 10 atmospheres.

3.2.1 System Description

The United Technologies Large Nozzle Thrust Facility is shown schematically in Figure 3.2-1.

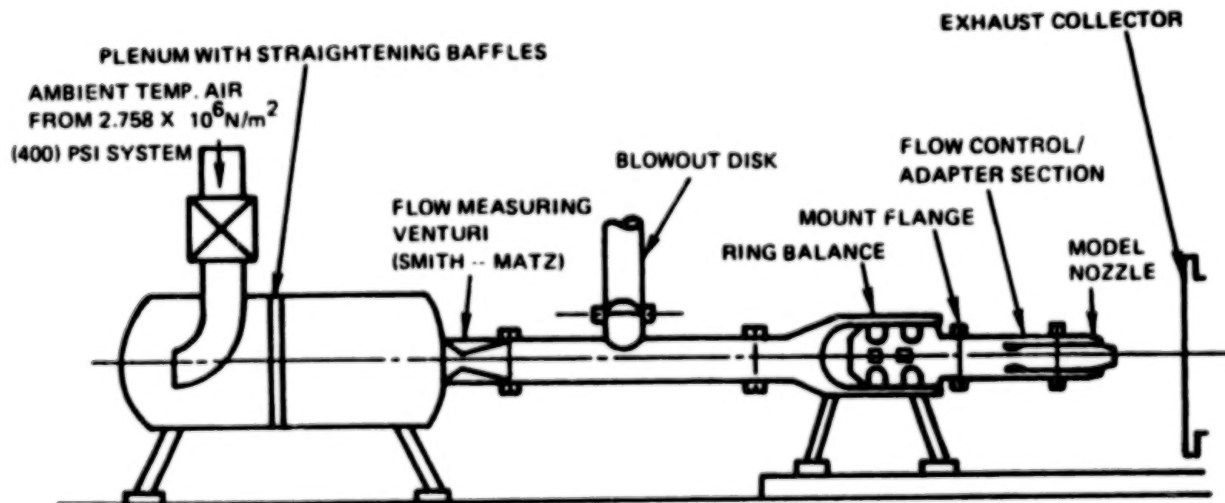


Figure 3.2-1 UTRC Large Nozzle Thrust Facility – Schematic of Overall Installation

Ambient temperature air, throttled from the $2.758 \times 10^6 \text{ N/m}^2$ (400 psig) system, is supplied to the upstream plenum. The flow is straightened in the plenum chamber before passing through a Smith-Matz flow measurement venturi (for total flow measurement) and into a balance section. It then passes through the mount flange into the adapter/flow control section of the model assembly, shown in Figure 3.2-2. The total flow is divided into fan and primary flows at this point. The primary flow is measured by a second venturi. Both fan and primary flows are independently controlled by translating choke plates in each stream which simultaneously serve as flow straighteners and control valves.

Each of these throttle-choke plate assemblies consists of two disks with a series of drilled holes (coincident in the full open position). The flow is regulated by translating one of the disks relative to the other to reduce the flow area. Flow quantity can be adjusted very precisely and with practically no flow distortion over the full range from zero to maximum. The throttled flows then pass through the instrumentation section and exit from the model into the exhaust collector.

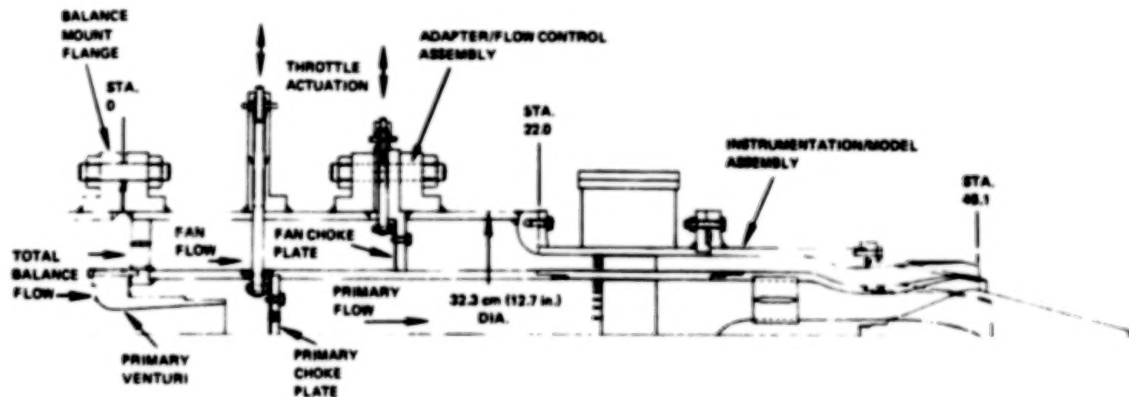


Figure 3.2-2 Aerodynamic Performance Model Assembly

3.2.2 Instrumentation

The charging station instrumentation section, connecting at Station 0.559 m (2.0 in), and model assembly were the same items used in the acoustic test and are described in Section 3.1.3.1.

Total model airflow was measured by the critical flow venturi downstream of the plenum, as shown in Figure 3.2-1. Primary air flow was measured by the critical flow venturi located in the primary flowpath of the aerodynamic performance assembly as indicated in Figure 3.2-2. Fan flow was then determined by subtracting the primary flow from the total measured flow.

Nozzle thrust was measured with a strain gaged six component ring type force balance.

3.2.3 Facility Thrust Balance Calibration

Prior to installation of the aerodynamic performance assembly, the thrust balance was calibrated. The calibration procedure consisted of two steps. First, the thrust facility was capped at the balance mount flange and axial force dead weight testing was performed over a range of internal balance pressures at zero flow conditions to determine sensitivity and pressure tare calibrations. Second, a zero thrust nozzle was installed on the balance mount flange and was tested over a range of flow conditions to define flow tare calibrations. A photograph of the zero thrust nozzle installation is shown in Figure 3.2-3.

To verify overall balance performance, instrumented single flow ASME reference nozzles, shown in Figure 3.2-4, were installed on the balance mount flange and tested over the same range of operating conditions as the test models (pressure ratio of 1.3 to 4.1). The charging station instrumentation used with the ASME nozzles consisted of a nine port area weighted total pressure probe and a single total temperature probe.

Results of the tests were compared to the established level of performance for an ASME nozzle and to previous data to ensure balance repeatability. Both 0.076 m (3 in) and 0.102 m (4 in) diameter ASME nozzles were available for this program. Both were tested to approximate the thrust and flow conditions of the primary only configurations and the coannular models. The level of performance and repeatability of the 0.102 m (4 in) diameter nozzle is illustrated in Figure 3.2-5. As shown, the repeatability of the balance is very good and the data agree well with the established velocity coefficient level.

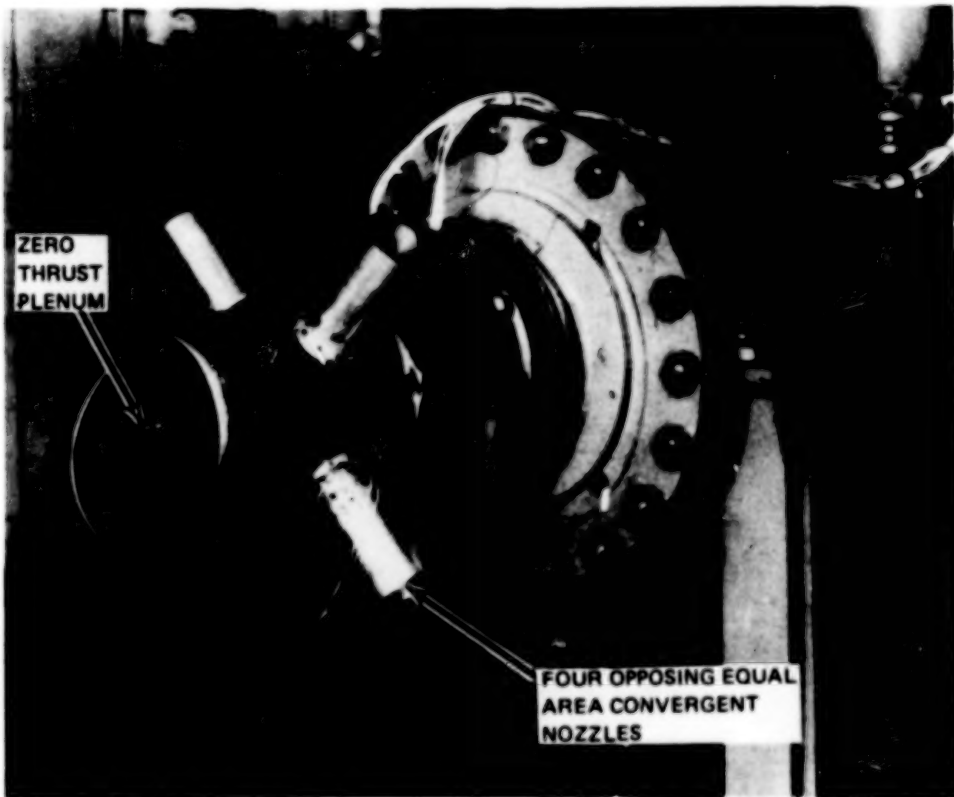


Figure 3.2-3 Zero Thrust Nozzle Installation

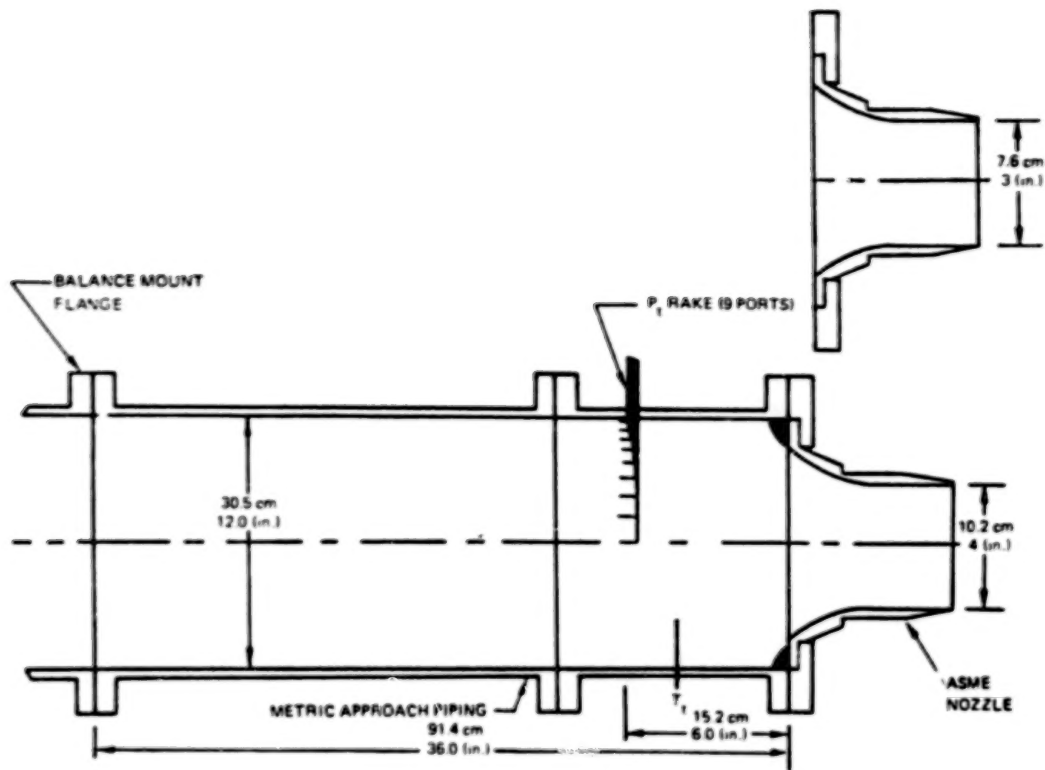


Figure 3.2-4 ASME Reference Nozzle

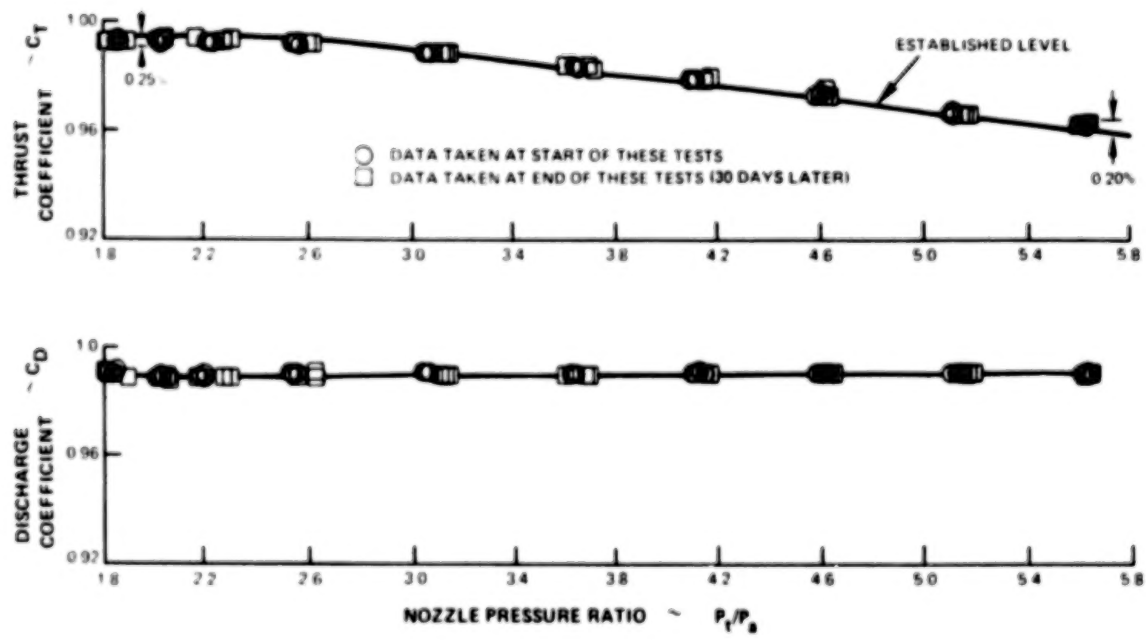


Figure 3.2-5 Performance for 0.102 m (4 in) Diameter ASME Reference Nozzle

After the balance calibrations and ASME nozzle tests were completed, the model adapter/flow control assembly was installed on the balance mount flange and the primary venturi calibrated. This was accomplished by sealing off the fan flow passage and calibrating the primary venturi against the thrust facility standard Smith-Matz type venturi to define the primary flow. The coannular fan flow could then be determined by subtracting the primary flow from the measured balance flow.

The test procedure for a given model configuration consisted of varying the fan nozzle pressure ratio to cover the defined range at a constant value of primary pressure ratio. When this was completed the primary pressure ratio was changed and the process repeated. At each given test point the output of the force balance and the flow metering systems were recorded, along with data from the charging station instrumentation on the model and supporting hardware.

3.2.4 Aerodynamic Performance Test Matrix

The aerodynamic test matrix is shown in Table 3.2-1. This test matrix covers a total of 65 subsonic and supersonic operating points with fan-to-primary velocity ratios smaller and larger than one. Data were taken with primary flow alone and fan flow alone as well as coannular flow conditions. The total pressure ratios listed in Table 3.2-1 were nominal values; nozzle thrust and flow coefficients (C_T and C_D) were calculated using charging station instrumentation area averaged values of pressure and temperature.

TABLE 3.2-1
AERODYNAMIC STATIC TEST MATRIX
(All Data Obtained at Ambient Temperature)

Configurations	Fan Pressure Ratio (P_{tf}/P_a)	Primary Pressure Ratio (P_{tp}/P_a)
A, B, C, D, E	1.3	1.53
	1.8	1.53
	2.5	1.53
	3.2	1.53
	4.1	1.53
	1.3	2.0
	1.8	2.0
	2.5	2.0
	3.2	2.0
	4.1	2.0
B, D	1.3	No Primary Flow
	1.7	No Primary Flow
	2.5	No Primary Flow
	3.2	No Primary Flow
	4.1	No Primary Flow
E	No Fan Flow	1.3
	No Fan Flow	1.8
	No Fan Flow	2.5
	No Fan Flow	3.2
	No Fan Flow	4.1

3.3 NOZZLE MODELS

3.3.1 Configuration Selection

Previous work on inverted velocity profile coannular nozzles had established the reduced noise characteristics of these systems. However, only a preliminary effect of the coannular nozzle geometry on exhaust noise and performance had been identified. The five coannular model configurations used in this program were selected to provide the geometric parameter extensions necessary to develop an engineering design procedure for general application to inverted velocity profile coannular nozzles.

The data base used to determine the necessary parameter extensions was obtained from References 7 through 12. The primary geometric parameters of nozzles tested under these programs are shown in Table 3.3-1. Two nozzles with fan-to-primary area ratios of 0.75 and 1.20 were tested in References 7 and 8. Both configurations had primary nozzles extending slightly downstream from the fan exit plane. Two nozzles with an area ratio of 0.65 were tested as part of References 11 and 12: one nozzle was coplanar, while the other had a significant primary extension and a primary plug. Three acoustic comparisons were made using this data base to determine the effect of nozzle geometry on exhaust noise:

- (1) The 0.75 and 1.20 area ratio nozzles were compared to determine the effect of area ratio.
- (2) The two 0.65 area ratio nozzles were compared to determine the effect of an extended primary and plug on jet noise.
- (3) The 0.75 area ratio nozzle (with $L/H = 2.3$) and 0.65 area ratio coplanar nozzle were compared to determine the effect of a small primary extension on jet noise.

The first comparison showed that an increase in fan area increased the noise generated at all frequencies when total jet area was held constant. High frequency noise for the 1.20 area ratio nozzle was 2 dB higher than the high frequency noise for the 0.75 area ratio nozzle for all operating conditions, while the low frequency noise increase depended upon operating condition. The second comparison showed that a combined plug-primary extension reduced high frequency noise 2.0 dB leaving the low frequency noise unchanged. The third comparison showed that a small primary extension had no effect on jet noise.

This data analysis suggested that certain geometric parameters may be significant. These parameters consist of fan stream and primary stream radius ratio, centerbody length to nozzle annular height ratio, and nozzle area ratio. The evaluation of the five models provided the systematic variation of these potentially important parameters to expand the data base so that an accurate acoustic prediction system could be formulated.

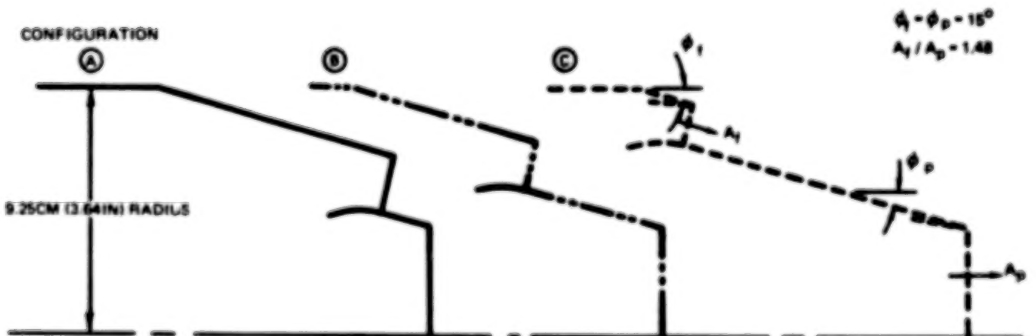
The selected configurations are shown schematically in Figure 3.3-1. Geometric characteristics of the selected configurations, labeled A to E, have already been tabulated in Table 3.1-1. The characteristics of the configurations from previous programs contributing to the data base are tabulated in Table 3.3-1. The parametric extension to the previous data are summarized in the following paragraphs.

TABLE 3.3-1
MODEL GEOMETRIC PARAMETERS FROM
PREVIOUS PROGRAMS

Configuration	Fan				Primary			
	A_f Total m^2 (ft 2)	A_f/A_p	R	L/H	ϕ_f Fan Extension (degrees)	R	L/H	ϕ_p Plug (deg)
Ref. 7,8 0.75 Coannular	0.0126(0.136)	0.75	0.79	2.3	3	-	-	-
Ref. 7,8 1.2 Coannular	0.0126(0.136)	1.20	0.72	1.7	4	-	-	-
Ref. 11, 12 0.65 Coplanar	(1) 0.0183(0.197)	0.65	0.78	-	-	-	-	-
Ref. 11, 12 0.65 Plug	(1) 0.0183(0.197)	0.65	0.91	8.0	13	0.69	7.2	3/15*

(1) Geometry scaled from Figures 1 and 4 of Reference 12 Comprehensive Data Report, Volume I.

*Dual Angle Plug (3 and 15 degrees)



(A) VARIATION OF FAN STREAM RADIUS RATIO



(B) VARIATION OF PRIMARY STREAM RADIUS RATIO

Figure 3.3-1 Schematic of the Selected Test Nozzle Configurations

Area Ratio (A_f/A_p) - A nozzle area ratio of 1.48 was selected for the model designs based on the take-off requirements of the VSCE cycle. Configurations A, B and C (to be compared with the previously tested coannular nozzles) extend the data base from 1.2 to 1.48.

Length to Passage Height (L/H) - With no plug in the primary stream the ratio L/H will increase with fan stream radius ratio if the nozzle area ratio and primary cowl extension angle are held constant. In Configurations A, B, and C, the fan stream L/H ratio increased from 1.0 to 7.7 while the fan stream radius ratio increased from 0.69 to 0.83. Placement of a plug in the primary stream, with nozzle area ratio and cowl extension angles held constant, resulted in a change in primary stream L/H ratio. For Configurations A, D, and E, the fan stream L/H ratio was held constant at 1.0 while the primary stream L/H ratio increased from 0 to 15.27.

Radius Ratios (r_{ID}/r_{OD}) - Fan stream radius ratio effects can be determined from comparisons of Configurations A, B, and C. The relative importance of primary stream radius ratio can be determined from a comparison of Configuration pairs D and B, and E and C.

The minimum fan stream radius ratio was defined by allowing a nominal separation between the fan and primary streams of one fan nozzle annulus height with a fan cowl extension angle of 15 degrees and a conical convergent primary nozzle. The maximum fan stream radius ratio considered was based on a combination of the fan stream jet area, the maximum nacelle diameter for the VSCE-502B and a nominal clearance for actuation mechanisms, etc. These relationships were patterned after the preliminary nozzle design prepared in Reference 18. In other words the maximum radius ratio was obtained when the fan jet was located near the maximum nacelle diameter (allowing the 7.6 cm [3 in] clearance required by the actuation mechanisms).

The five selected configurations were judged to best satisfy the objective of expanding the data base to provide an engineering design procedure within the program limitations.

3.3.2 Model Designs

The geometries of the five test configurations, A through E, are summarized in Table 3.1-1. A photograph of the five model assemblies is shown in Figure 3.3-2. Assembly layouts for the five models appear in Figures 3.3-3 through 3.3-7.

Separate primary cowls and primary plug centerbodies (Configurations D and E) or inner cone fairings (Configurations A, B and C) were required for each model. The inner cone fairings were required in the convergent primary nozzle design to avoid flow separation from the plug centerbody support shaft. It was possible to use the same fan cowl for Configuration B and D, and C and E, so that only three fan cowls were required.

The tests conducted in Reference 7 revealed the presence of fan stream shock screech in the noise spectra of some of the models tested in that program. Since full scale engines do not exhibit this noise characteristic, it was eliminated by adding small screech tabs to the fan cowl trailing edge. The screech tabs were incorporated into the present model fan cowl designs and were machined integrally with the cowls. The eight tabs were equally spaced

around the circumference and had dimensions of 0.007 m (0.265 in) wide by 0.001 m (0.046 in) long, as shown on the Configuration A fan cowl drawing Figure 3.3-8. The tabs were used only for acoustic testing and were machined off to produce a smooth cowl lip for aerodynamic performance testing.

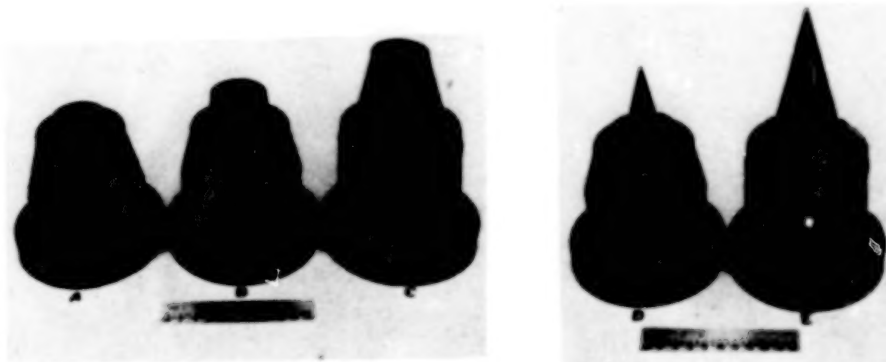
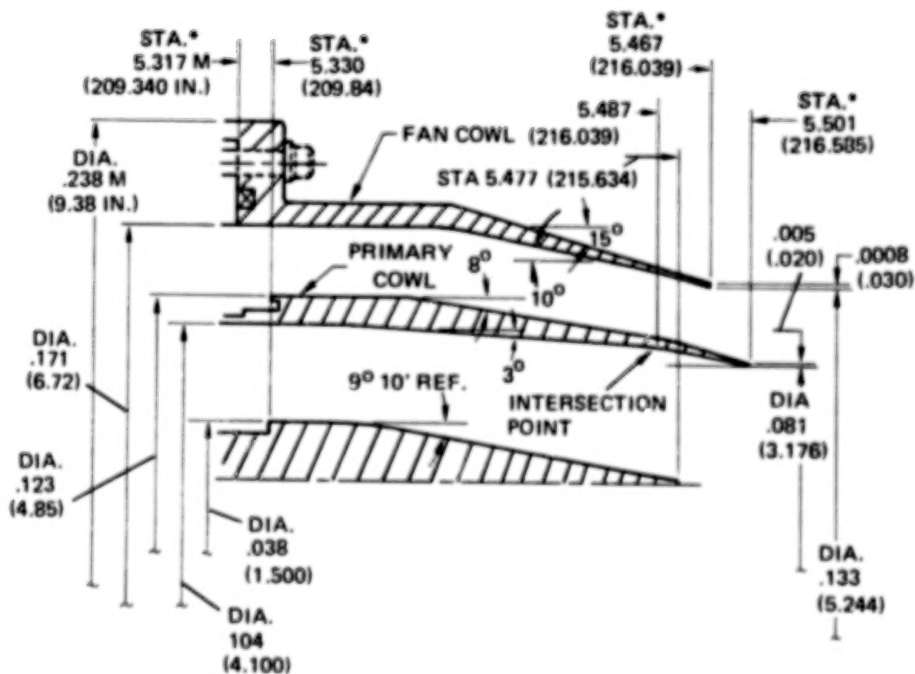
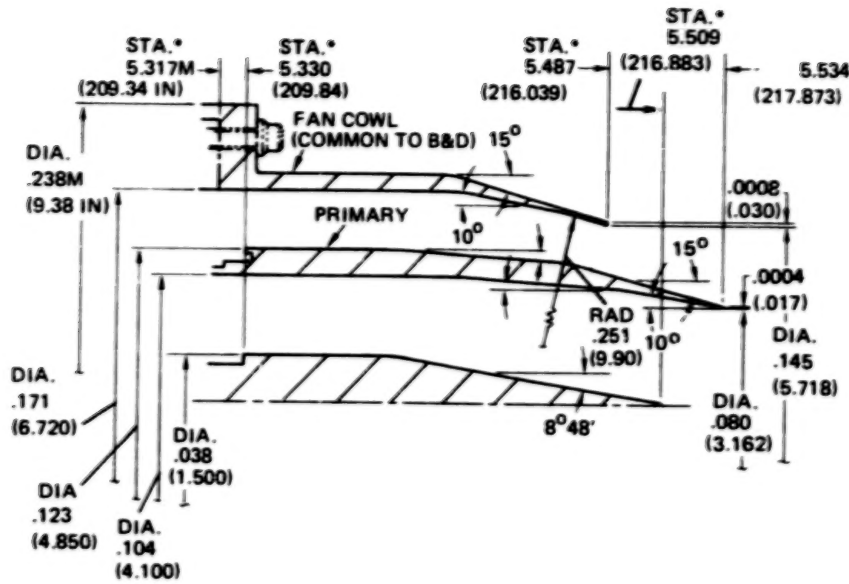


Figure 3.3-2 Test Models



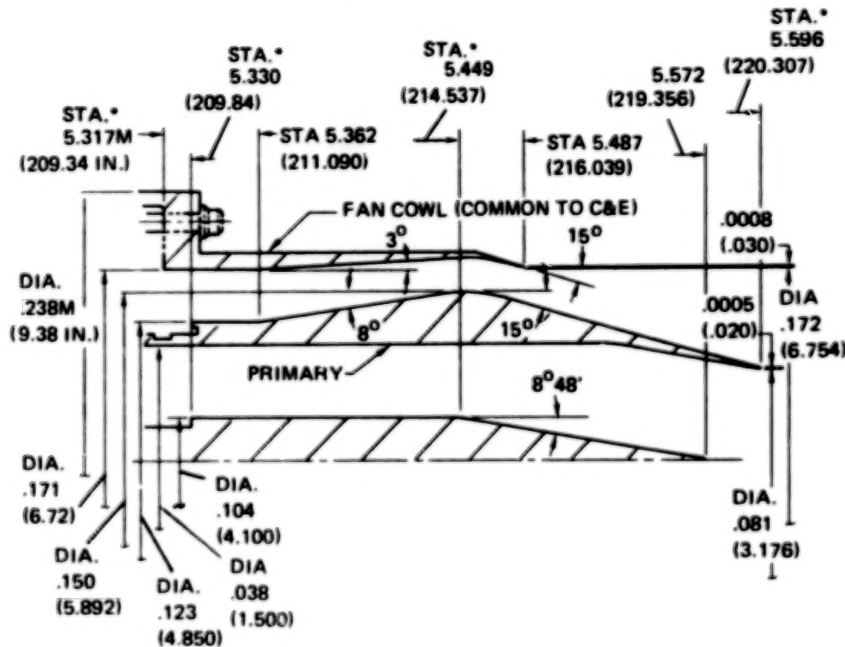
* STATION IDENTIFICATIONS ARE BASED ON LINEAR
STATION DIMENSIONS SHOWN IN FIGURE 3.1-3

Figure 3.3-3 Details of Configuration A



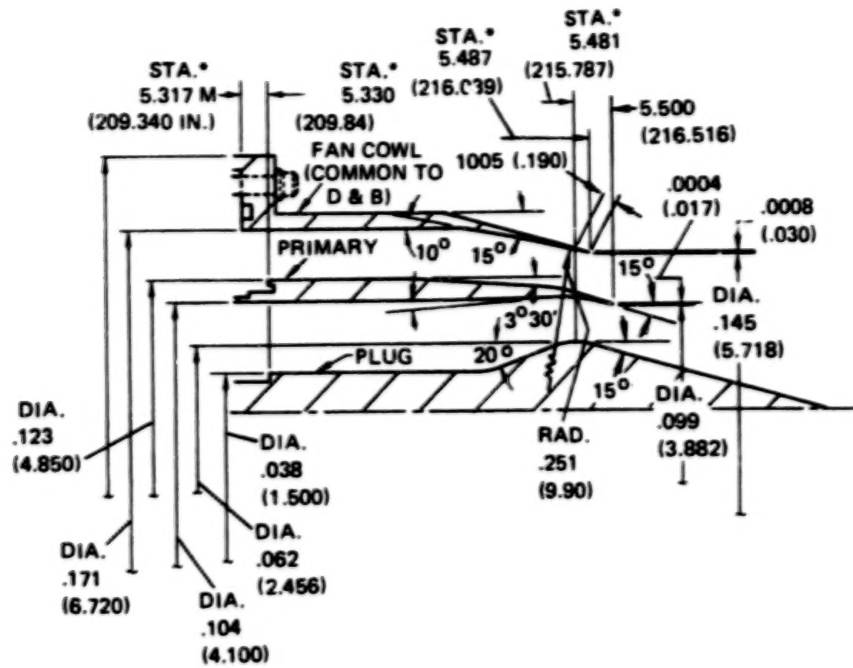
* STATION IDENTIFICATIONS ARE BASED ON LINEAR
STATION DIMENSIONS SHOWN IN FIGURE 3.1-3

Figure 3.3-4 Details of Configuration B



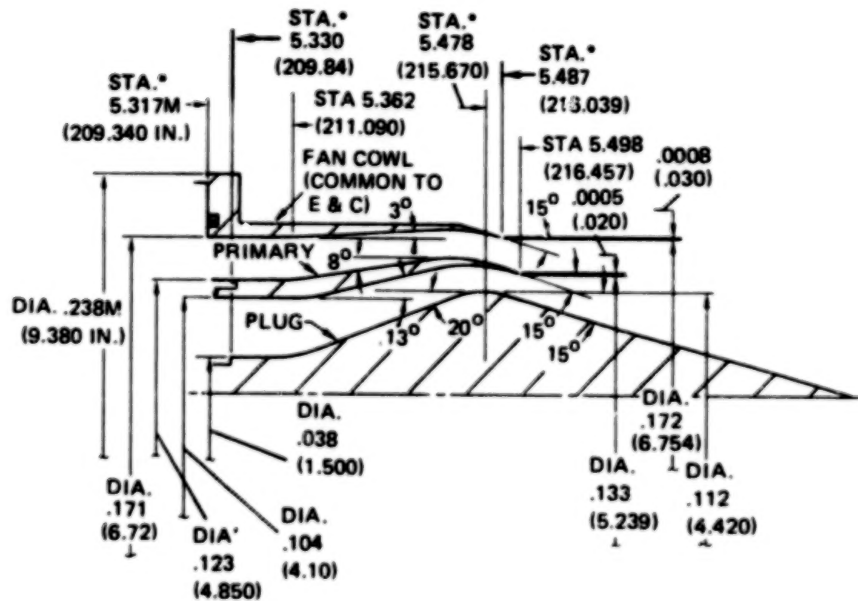
* STATION IDENTIFICATIONS ARE BASED ON LINEAR
STATION DIMENSIONS SHOWN IN FIGURE 3.1-3

Figure 3.3-5 Details of Configuration C



- STATION IDENTIFICATIONS ARE BASED ON LINEAR STATION DIMENSIONS SHOWN IN FIGURE 3.1-3

Figure 3.3-6 Detail of Configuration D



- STATION IDENTIFICATIONS ARE BASED ON LINEAR STATION DIMENSIONS SHOWN IN FIGURE 3.1-3

Figure 3.3-7 Detail of Configuration E

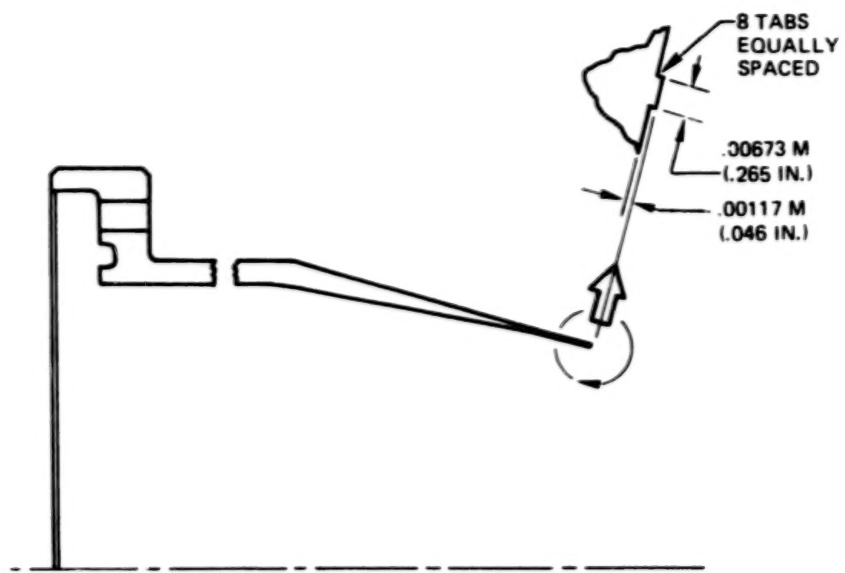


Figure 3.3-8 Model A with Fan Cowl Screech Tabs

SECTION 4.0

TEST DATA

The data obtained from the experimental testing are described in this section along with the test procedure and test matrix showing the conditions at which each of the model configurations was tested. Included are a discussion of the acoustic data and a discussion of the aerodynamic data.

4.1 ACOUSTIC DATA

4.1.1 Acoustic Data Reduction

The measured acoustic signals recorded by the eleven microphone array at 4.57 m (15 ft) radius were corrected, analyzed and converted to full size engine data (12X model size) by the procedure illustrated in Figure 4.1-1. This figure indicates the data outputs available for both the 0.127 m (5 in) equivalent diameter model size and 1.52 m (5 ft) full size scaled engine data. All of the data are available in the companion Comprehensive Data Report (Reference 19).

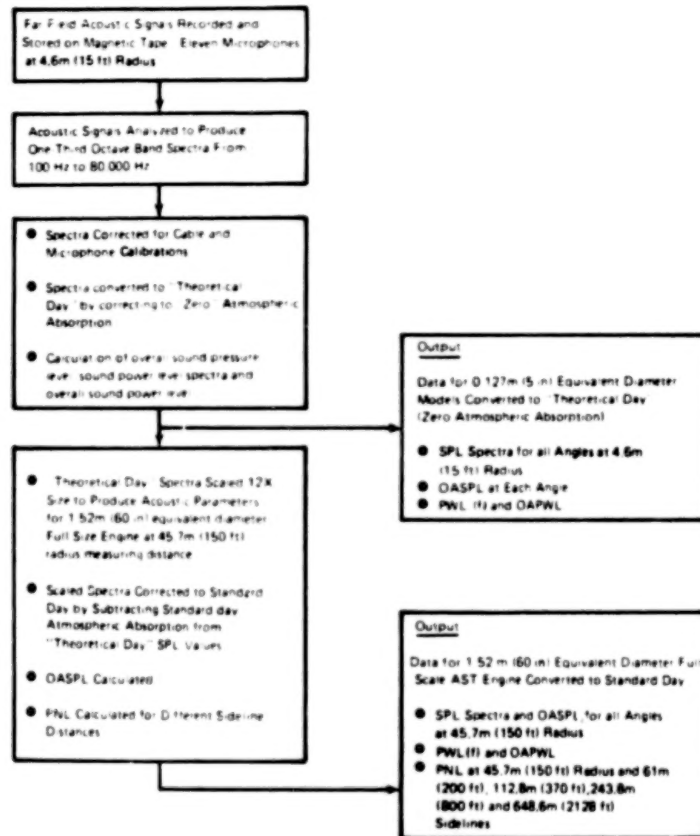


Figure 4.1-1 Acoustic Data Reduction Procedure

The tape recorded far field signals from the eleven microphones were reduced to one-third octave band sound pressure levels by analog/digital analysis performed with a General Radio No. 1921 Analyzer.

The one-third octave band model sound pressure levels, analyzed from 100 Hz to 80,000 Hz band center frequency were corrected for calibrated cable and microphone response. The data were then processed, as shown in Figure 4.1-1, resulting in output tabulations for each test condition. A sample of each output is shown in Tables 4.1-I and 4.1-II.

The two types of data outputs available, indicated by Figure 4.1-1, are theoretical day sound pressure level (SPL) and scaled engine data, described in Sections 4.1.1.1 and 4.1.1.2, respectively. In addition, a tabulation of all model size OASPL's at all angles, including actual operating conditions, is presented in Appendix A. This Appendix also shows the corresponding peak PNL values for the "full-scale" (12X model scale) engine at a 648.6 m side-line distance.

4.1.1.1 Theoretical Day SPL (Model)

The one-third octave band data were transformed into "theoretical day" or "lossless day" data by applying the values of atmospheric absorption defined in Reference 20. This procedure entails adding SPL corrections to measured data. The Δ SPL corrections represent an estimate of the absolute sound absorption for noise in each one-third octave band. The resulting "theoretical day" data represent the noise that would be measured at the microphone if no noise was lost through atmospheric absorption. The formula used in Reference 20 has been verified as accurate only for sound frequencies below 10,000 Hz. However, the formulas were used directly to calculate the values of atmospheric absorption for frequencies up to 80,000 Hz required for the scale model data. A more accurate method was developed in Reference 21 for calculation of atmospheric absorption at frequencies up to 100,000 Hz. An attempt was made to convert the published computer program for use in the present program. However, report results could not be reproduced due to errors in the published computer program. Consequently, the atmospheric absorption corrections in Reference 20 were used.

A sample of the "theoretical day" (lossless) model scale data is shown in Table 4.1-I. At the top of the page are listed the pertinent ambient and nozzle operating parameters in both U.S. Customary Units as well as the International System of Units. The left hand column lists the ambient temperature (TEMP), pressure (PRES), and relative humidity (REL H). Wind direction (WIND D) and wind velocity (WIND V) are not applicable for the indoor test facility.

The center columns list the full scale primary and fan stream exhaust nozzle areas (AREA) as equal to zero to indicate that the noise data are in model scale form. In the same columns are found the stream total to ambient pressure ratio (PR), stream temperature (TEMP), and stream density (RHO), and the ideally expanded velocity (VEL).

The right hand columns list the full scale mass flow (MASS FLOW) as equal to zero to indicate that the noise data are in scale model form. Also listed in this column are the model size ideal thrust (THRUST, IDL), exhaust nozzle areas (AREA MOD), and mass flows (W MODE). Model thrust (THRUST, MEA) is shown to be zero because it was not measured in this part of the experiment.

TABLE 4.1-I

SAMPLE OF ACOUSTIC DATA
(MODEL SIZE; THEORETICAL DAY)

20003F TAPE PT309 NASA VSCE (NAS3-20061) CONFIG. A

15.2049

STAND X206 RIG ID 070530 TEST DATE 03/02/77 SCALE RATIO 12.0/1 RUN NUMBER 20023 CONDITION 83C2															
PRIMARY FAN PRIMARY FAN PRIMARY FAN PRIMARY FAN															
TEMP	77.0(F)	25.0(C)	AREA	SOFT	0.0	0.0	SGM	0.0	0.0	MASS FLOW LB/S	0.0	0.0	KG/S	0.0	0.0
PSFS	30.06IN	1.62BAR	P.R.		1.53	1.79		1.53	1.79	THRUST,IDL LB	91.7	205.5	KN	0.406	0.914
WIND D			TEMP	(R)	1453.7	1264.7	(K)	807.6	702.6	THRUST,MEA LB	0.0	0.0	KN	0.0	0.0
WIND V	0.0MPH	0.0M/S	RHO	LB/FT ³	0.031	0.037	KG/M ³	0.491	0.589	ARLA (MCD) SOFT	0.060	0.060	SGM	0.006	0.007
REL H	70.0%		VEL	FPS	1420.4	1282.5	M/S	432.9	465.9	W (MODEL) LB/S	2.1	4.3	KG/S	0.9	2.0
REL H	70.0%		VEL	FPS	1420.4	1282.5	M/S	432.9	465.9	W (MODEL) LB/S	2.1	4.3	KG/S	0.9	2.0

BAND	1/3 OCTAVE BAND MODEL JET NOISE DATA 15.0FT RADIUS										THEORETICAL DAY SPL - (MODEL)			
	MICROPHONE ANGLES IN DEGREES										POWER			
CENTER FREQ	60	70	80	90	100	110	120	130	140	150	160			
1.00	60.0	60.0	60.0	60.0	60.0	60.0	60.0	60.0	60.0	60.0	60.0	6.0	6.0	6.0
1.03	60.0	60.0	60.0	60.0	60.0	60.0	60.0	60.0	60.0	60.0	60.0	6.0	6.0	6.0
1.10	62.1	64.8	67.5	65.4	60.1	89.2	91.0	93.7	95.1	98.8	102.8	115.3	115.3	115.3
1.125	63.4	67.3	67.5	68.8	90.3	90.8	89.5	94.0	97.6	100.2	103.2	116.4	116.4	116.4
1.165	67.6	64.8	68.6	68.6	86.5	87.6	89.0	96.1	92.7	97.9	102.1	105.3	117.4	117.4
1.200	65.3	66.3	67.6	64.5	90.8	91.6	93.5	95.3	102.0	106.2	108.3	120.7	120.7	120.7
1.250	67.5	60.2	64.6	91.6	92.3	93.5	95.6	99.3	104.4	108.7	110.5	123.1	123.1	123.1
1.210	64.2	69.7	61.4	63.2	94.3	95.8	97.8	102.8	106.8	111.1	113.9	125.8	125.8	125.8
1.400	62.9	45.2	53.9	55.6	46.6	96.6	100.9	105.9	110.8	114.0	116.6	126.8	126.8	126.8
1.500	54.1	94.6	94.9	96.2	96.8	99.3	101.9	107.0	113.0	116.7	115.3	130.4	130.4	130.4
1.530	97.0	92.8	95.4	95.0	94.6	104.9	103.7	109.3	114.2	117.3	116.3	121.9	121.9	121.9
1.550	96.6	96.6	97.4	93.7	94.6	101.4	104.1	109.8	114.7	117.7	116.2	121.9	121.9	121.9
1.600	66.9	97.1	97.2	99.0	100.7	103.0	105.3	109.9	114.4	117.0	116.7	131.7	131.7	131.7
1.625	66.8	65.8	62.5	64.4	106.4	102.7	105.6	109.4	113.1	115.3	115.1	131.5	131.5	131.5
1.650	65.5	96.6	97.8	99.3	106.6	107.7	105.5	109.1	111.5	113.3	113.4	124.2	124.2	124.2
2.00	65.5	95.9	97.7	98.9	104.8	103.0	105.9	108.7	110.1	110.7	110.6	127.9	127.9	127.9
2.20	65.2	95.2	97.4	99.4	101.6	103.5	106.1	108.5	108.9	104.0	110.1	127.4	127.4	127.4
2.45	64.9	95.5	97.1	99.1	100.9	103.5	106.1	107.9	107.6	107.9	104.2	126.7	126.7	126.7
4.00	94.6	95.5	96.8	93.9	100.7	103.5	105.9	107.2	106.6	106.4	106.9	126.1	126.1	126.1
5.00	94.5	94.8	95.1	96.3	100.3	102.8	105.1	106.1	105.1	105.2	105.3	125.1	125.1	125.1
6.25	94.1	94.4	96.0	95.3	100.1	102.8	104.6	109.4	104.2	104.3	103.9	124.3	124.3	124.3
8.00	92.7	94.0	95.8	97.9	94.7	102.6	103.8	104.2	102.8	102.6	101.6	123.6	123.6	123.6
11.0	92.3	93.4	95.2	97.5	94.3	101.8	103.3	103.1	101.9	101.4	94.8	122.9	122.9	122.9
12.5	92.1	92.8	94.7	97.1	94.7	101.1	102.1	102.1	104.4	106.0	97.7	121.9	121.9	121.9
16.0	91.6	92.8	94.7	97.0	98.6	100.6	101.8	101.2	99.6	98.7	98.3	121.6	121.6	121.6
20.0	90.7	92.1	94.1	96.5	98.6	99.9	100.8	100.0	98.3	97.2	94.1	120.4	120.4	120.4
25.0	90.0	91.4	93.5	96.3	97.5	99.8	100.0	98.9	97.3	96.0	93.3	114.8	114.8	114.8
31.5	89.3	91.1	93.6	96.0	97.5	94.1	99.7	98.5	96.7	95.0	91.5	119.3	119.3	119.3
40.0	89.2	91.2	93.6	96.0	97.1	93.2	93.6	96.4	96.1	94.6	91.5	114.0	114.0	114.0
50.0	88.7	90.6	92.8	93.5	96.4	98.7	98.8	97.7	95.3	93.9	91.1	116.6	116.6	116.6
62.0	87.8	89.4	92.1	94.5	95.9	97.8	97.8	96.9	94.4	92.3	90.8	117.6	117.6	117.6
80.0	82.0	89.3	92.2	94.4	96.0	97.3	97.7	96.5	95.1	93.6	91.5	117.7	117.7	117.7
114.0	0.0	0.0	0.0	0.0	0.0	0.0	0.0	0.0	0.0	0.0	0.0	0.0	0.0	0.0

OAPNL = 141.7

DSPL 107.9 108.4 109.8 111.7 113.2 115.4 117.4 120.2 123.1 125.6 125.6

MICROFILMED FROM
BEST AVAILABLE COPY

TABLE 4.1-II

SAMPLE ACOUSTIC DATA
(SCALED TO 1.52 m (60 in.) EQUIVALENT DIAMETER ENGINE)

2003F TAPE PT309 NASA VSCE (NASS-20061) CONFIG. A

15-2049

STAND X206 RIG ID 070530 TEST DATE 03/02/77 SCALE RATIO 12.0/1 RUN NUMBER 2008 CONDITION 8302																	
TEMP	77.0(F)	25.0(G)	AREA	SLFT	PRIMARY FAN			PRIMARY FAN			PRIMARY FAN						
					PRES	1.02BAR	P.M.	1.53	1.79	1.53	1.79	MASS FLOW	LB/S	244.5	627.5	KG/S	135.9
WIND D				TEMP (R)	1455.7	1254.7	(K)	807.6	702.6	THRUST,IDL	LB13211.4	24548.6	NW	56.764	131.661		
WIND V	0.0M/S			WIND V	0.0M/S	0.031	0.037	KG/M3	0.491	0.589	THRUST,MEA	L5	0.0	AL	0.0		
WIND W	0.0M/S			WIND W	0.0M/S	0.031	0.037	KG/M3	0.491	0.589	AREA (M2)	SLFT	0.060	0.060	SUM	0.066	0.067
WIND H	70.0G			WIND H	70.0G	70.0G	70.0G	M/S	432.9	465.9	W (M2D1)	LB/S	2.1	4.3	KG/S	0.9	2.0

FFA DAY

1/3 OCTAVE BAND ENGINE JET NOISE DATA 150.0FT RADIUS

(SCALED ENGINE)

BAND

CENTER FREQ

MICROPHONE ANGLES IN DEGREES

POWER

THHZ

	60	70	80	90	100	110	120	130	140	150	160		
0.00	98.6	97.6	98.0	99.6	100.6	102.5	105.3	110.9	115.8	118.9	117.9		154.7
0.10	93.2	93.2	99.0	100.3	101.2	105.0	105.7	111.4	116.3	119.3	117.8		155.0
0.20	98.5	92.7	98.8	100.6	102.3	104.6	106.9	111.5	116.0	118.6	116.3		154.9
0.30	97.4	98.4	100.1	101.6	102.5	104.3	107.2	110	114.7	118.9	116.7		151.7
0.40	93.1	98.2	99.4	100.9	102.2	104.3	107.1	110.7	115.1	114.9	115.0		152.4
0.50	97.0	97.4	99.2	100.4	102.3	104.5	107.4	110.2	111.6	112.2	117.1		151.1
0.60	96.7	97.6	98.4	100.4	102.5	105.0	107.6	110.6	116.4	116.5	111.6		151.5
0.70	96.4	97.0	98.6	100.6	102.4	105.0	107.6	109.4	109.1	109.4	109.7		149.8
0.80	96.1	97.0	98.3	100.4	102.2	105.0	107.4	108.7	108.1	107.9	106.4		147.2
0.90	95.0	98.3	97.5	99.8	101.6	104.3	105.6	107.6	108.6	108.7	106.8		141.2
1.00	95.5	95.6	97.4	99.7	101.5	104.2	106.6	108.8	108.6	105.7	105.3		147.9
1.10	94.1	95.4	97.2	99.3	101.1	103.4	105.2	105.6	104.2	104.2	103.0		145.0
1.20	93.7	95.6	95.6	98.9	100.7	103.2	104.7	106.7	103.3	102.8	101.2		145.6
1.30	93.4	94.1	95.0	98.4	100.6	102.4	105.7	105.4	101.7	101.3	99.0		144.6
1.40	92.6	94.0	95.9	98.2	99.8	102.0	103.0	102.4	100.8	99.9	97.5		144.2
1.50	91.8	93.2	95.2	97.6	99.1	101.6	101.9	101.1	99.4	98.3	95.2		143.1
2.00	91.1	92.5	94.6	97.4	98.0	100.9	101.1	100.0	98.4	97.1	94.4		147.4
2.50	90.2	92.0	94.5	96.9	96.4	100.0	100.6	99.4	97.6	95.9	92.4		141.8
3.10	89.9	91.4	94.3	95.7	97.7	99.8	99.3	99.1	98.8	95.3	92.2		141.3
4.00	89.2	91.1	93.3	96.0	96.9	99.2	99.3	98.2	95.8	94.4	91.6		140.6
5.00	88.1	89.7	92.4	94.8	96.2	98.1	98.1	97.2	94.7	93.6	91.1		134.6
6.20	88.0	89.3	92.2	94.4	96.0	97.3	97.7	96.5	95.1	93.6	91.5		134.2
8.00	86.0	87.4	90.0	90.0	90.0	90.0	90.0	90.0	90.0	90.0	90.0		0.0
10.0	86.0	86.0	90.0	90.0	90.0	90.0	90.0	90.0	90.0	90.0	90.0		0.0

DAPNL = 163.2

200. SIDELINE											
PNL	112.9	114.4	117.4	119.8	121.0	122.7	122.8	122.1	120.1	118.5	114.1

370. SIDELINE											
PNL	106.8	108.9	111.4	113.8	115.0	116.7	116.8	116.0	114.3	112.6	108.1

440. SIDELINE											
PNL	98.3	100.4	103.6	105.4	106.8	108.3	108.6	108.2	106.5	104.8	100.1

2120. SIDELINE											
PNL	86.6	88.3	90.6	92.9	94.4	96.2	97.1	97.1	95.7	94.0	89.0

Below the parameter listing are the tabulated, model scale one-third octave band sound pressure levels at a 4.57 m (15 ft) polar distance under free field measurement conditions during a "theoretical day". The center frequencies of the 30 measured one-third octave bands from 100 Hz to 80 kHz are listed in the left hand column. Data are not recorded at frequencies of 50 Hz, 63 Hz, or 80 Hz, which is indicated by zeros in Table 4.1-I. The one-third octave band sound pressure levels for each microphone measuring angle, 60, 70, 80, 90, 100, 110, 120, 130, 140, 150, and 160 degrees at each one-third octave band are listed in the appropriate columns.

The one-third octave band power levels (referenced to 10^{-12} watts) are listed at the extreme right hand side of the page. The power level calculation procedure is described in Section 4.1.1.3.

Below the one-third band sound pressure and sound power levels are listed the 4.57 m (15 ft) radius overall sound pressure level, denoted OSPL in the computer printouts, for each angle and the overall sound power level (OAPWL).

4.1.1.2 Scaled Engine Data

The "theoretical day" noise data were scaled to represent a full size engine having linear dimensions corresponding to a 1.52 m (5 ft) equivalent nozzle diameter (12 times model size). Thus, the measured SPL levels were increased by $20 \log 12$ or 21.58 dB and measured frequencies were reduced by a factor of 12 to produce full scale engine noise characteristics. The full scale SPL levels were extrapolated to 45.7 m (150 ft) radius for a standard FAA day ($T_a = 298^\circ\text{K}$ (537°R), REL HUM = 70 percent) by applying the spherical divergence law, $\Delta\text{dB} = 20 \log r_2/r_1$ and the atmospheric attenuation corrections of Reference 20. Overall sound pressure levels (OSPL) were determined by integrating the SPL values from 50 Hz to 6300 Hz. The OSPL calculation is cut off at 6300 Hz because no data were available at higher frequencies when the model data were scaled in frequency to full scale data.

Scaling data in this manner from the test day atmospheric condition to atmospheric conditions on a standard FAA day introduced a small error (less than 0.5 dB) because jet noise is a function of jet velocity divided by the ambient speed of sound. Since the speed of sound is slightly different for test day atmospheric conditions and standard FAA day conditions (unless the ambient air test temperature is 298°K (537°R)), the scaled data will have a different value of the jet velocity divided by the ambient air speed of sound than the original model data.

Perceived noise levels were computed according to Reference 22 from the SPL spectra at various sideline distances at zero altitude with no extra ground attenuations.

A sample of the scaled engine data is shown in Table 4.1-II. The heading at the top of the page is similar to that described in Section 4.1.1.1 with the following exceptions. The left hand columns list the ambient temperature (TEMP) and relative humidity (REL H) corresponding to the FAA standard day (25°C and 77 percent relative humidity) to which the data are scaled.

The center columns list the full scale primary and fan stream exhaust nozzle areas (AREA). The right hand columns list the full scale mass flow (MASS FLOW). Also listed are the full scale ideal thrust (THRUST, IDL).

Below the sound pressure level and sound power level spectra are listed the 45.7 m (150 ft) radius overall sound pressure level (OSPL) for each angle and the overall sound power level (OAPWL). Perceived noise levels (PNL) are listed for each measuring angle at 45.7 m (150 ft) radius and at sideline distances of 60 m (200 ft), 111 m, (370 ft), 244 m (800 ft), and 648.6 m (2128 ft).

Because the characteristics of the test facility ensure far field acoustic signals free from ground reflections, all acoustic values calculated from the measured data are also free field. The extrapolated values do not include extra ground attenuation. The acoustic data from all test points are compiled on computer output sheets in the Comprehensive Data Report (Reference 19).

4.1.1.3 Calculation of Acoustic Power Levels

Sound power level spectra and overall power level were determined individually for the model data and data scaled to full size by spatial integration over the eleven microphone positions from the listed SPL and OSPL values assuming symmetry about the jet axis of the noise generation. Since the theoretical day model scale data represent the noise that would be measured if no atmospheric absorption were present, the power levels represent noise generation at the source under atmospheric conditions equal to those existing during the test. The full scale data, however, represent noise that would be measured on a standard FAA day subject to the scaling error discussed in Section 4.1.1.2. Thus the full scale power levels represent an integration of the far field noise levels on a standard FAA day, reflecting the common method for comparing full scale data. The actual power level calculations employed were:

$$PWL = 10 \log \left(\frac{P}{P_{ref}} \right) = \text{sound power level, in decibels}$$

where: $P = \sum_{k=1}^{11} \frac{P_k^2}{\rho_a c} \Delta \Delta_k = \text{the acoustic power, in watts}$

$$P_{ref} = 10^{-12} \text{ watts} = \text{the reference power level}$$

$$P_k = 10^{\left(\frac{SPL}{10} \right)} P_{ref}^2 = \text{mean square sound pressure}$$

$$P_{ref} = 20 \times 10^{-6} \text{ N/m}^2 = \text{reference acoustic pressure}$$

$$\rho_a = \text{atmospheric density}$$

$$c_a = \text{atmospheric speed of sound}$$

11 = number of microphones

ΔA_k = surface area of spherical segment associated with i^{th} microphone

for the first microphone,

$$\Delta A_k = 2\pi r^2 \left[\cos \theta_1 - \cos \left(\frac{\theta_1 + \theta_2}{2} \right) \right].$$

for intermediate microphones,

$$\Delta A_k = 2\pi r^2 \left[\cos \left(\frac{\theta_{k-1} + \theta_k}{2} \right) - \cos \left(\frac{\theta_k + \theta_{k+1}}{2} \right) \right].$$

and for the last microphone,

$$\Delta A_{11} = 2\pi r^2 \left[\cos \left(\frac{\theta_{10} + \theta_{11}}{2} \right) - \cos \theta_{11} \right].$$

where r is the distance of the microphone from the nozzle.

4.1.2 Acoustic Results and Discussion

Selected results obtained during the program are presented in this section in order to illustrate the effects of nozzle geometry and operating condition on the acoustic characteristics of inverted velocity profile coannular exhaust systems. Only limited data are presented since detailed correlations of the acoustic data with nozzle geometry and operating condition are contained in Section 5.0. In Section 5.0 it was determined that the most significant nozzle geometry parameters affecting the acoustic data were fan stream and primary stream radius ratios. The ratio H/L , where H is the annulus height of the fan stream and L is the primary nozzle exit plane and fan nozzle exit plane separation distance, was not a significant noise correlation parameter, as discussed in Section 5.2.1.2. Consequently, the effect of nozzle geometry on the acoustic data in this section is discussed in terms of fan stream and primary stream radius ratio. The complete acoustic (model size and scaled 12 times to engine size) and aerodynamic data tabulations are contained in the Comprehensive Data Report (Reference 19).

The following topics are discussed in this section: comparison of convergent nozzle data with SAE predictions, unsuppressed coannular nozzle results, definition of the acoustic characteristics of a single stream plug nozzle, and definition of the acoustic characteristics of a coannular nozzle with primary flow leakage.

4.1.2.1 Comparison of Convergent Nozzle Data With SAE Predictions

To obtain the reference convergent nozzle data, the primary nozzle from Configuration B was tested at four operating conditions, test points 15 – 18, defined in Section 3.1.4. This reference nozzle has an inner plug terminating at a sharp point 0.0224 m (0.0735 ft) or 0.28 throat diameters upstream from the nozzle exit plane. Two operating conditions consisted of supersonic flows and two operating conditions consisted of subsonic flows. Figure 4.1-2 contains comparisons at 90 and 150 degrees of the measured data, scaled by a factor of 12, with the SAE prediction (Reference 23) for a subsonic nozzle pressure ratio of 1.8. Since the noise measurements were obtained in an anechoic environment and considered to be free field levels, they were compared with free field noise level predictions. The spectral peaks of the measured data agreed with predicted values to within 1.0 dB. Figure 4.1-3 contains comparisons at 90 and 150 degrees of the scaled data with a prediction for a nozzle pressure ratio of 3.2. The prediction at this supersonic pressure ratio was obtained by adding the SAE prediction, which includes only jet exhaust mixing noise, to a shock noise prediction made using the Harper-Bourne and Fisher theory (Reference 24). At 150 degrees, the mixing noise prediction dominated the shock noise prediction, and the prediction agreed with the measured data to within 1.0 dB at the spectral peaks. At 90 degrees, the shock noise is a significant factor in the total noise spectrum. At the spectrum peak, the measured data and prediction agree to within 2.0 dB. The measured and predicted data illustrated in Figures 4.1-2 and 4.1-3 agreed well within the ± 2 dB accuracy attributed to the SAE prediction method, except at very high frequencies where the measured data were higher than the SAE predictions. The origin of the high frequency difference between the data and SAE predictions is unknown and at the present cannot be attributed to instrumentation errors. Appendix B contains a summary of the procedure used to verify the instrumentation accuracy and data-acquisition procedure.

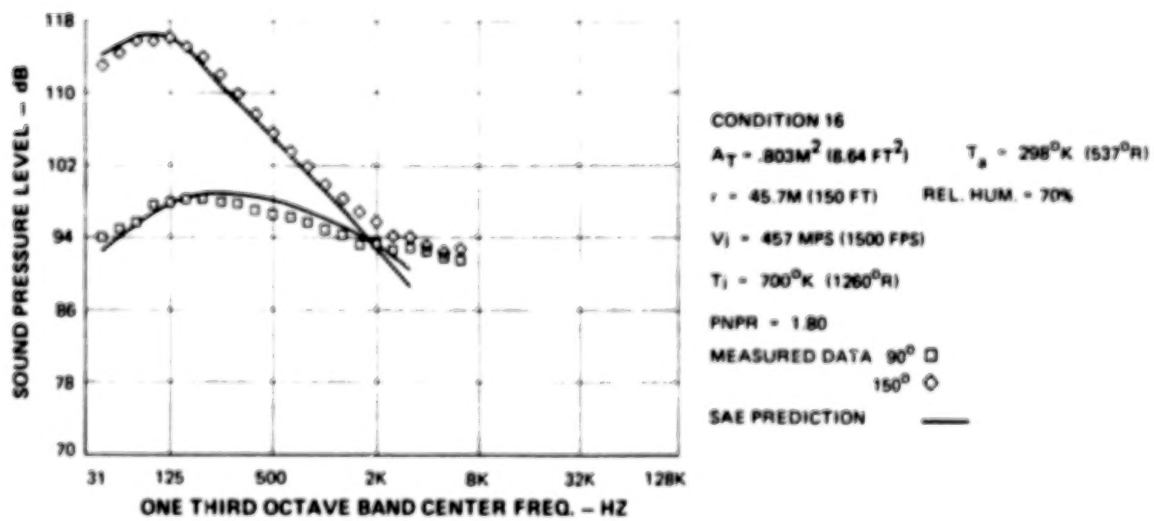


Figure 4.1-2 Comparison of Measured Data, Scaled to Engine Size, with SAE Predictions for a Convergent Nozzle at Subsonic Conditions

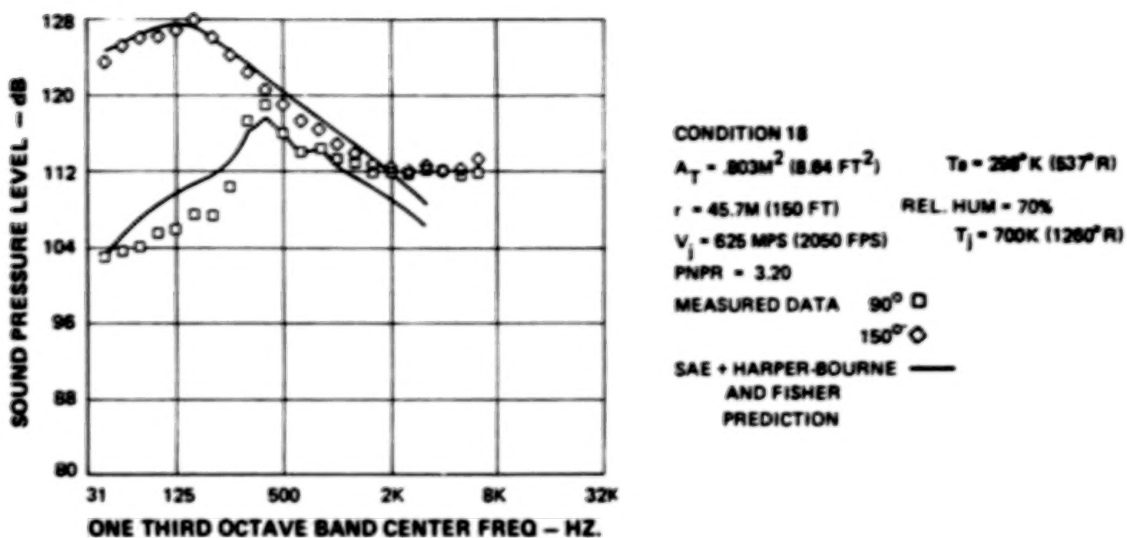


Figure 4.1-3 Comparison of Measured Data, Scaled to Engine Size, with SAE Predictions for a Convergent Nozzle at Supersonic Conditions

4.1.2.2 Unsuppressed Coannular Nozzle Results

The effects on the acoustic characteristics of coannular nozzles of nozzle operating condition and geometry were investigated in this program. The noise characteristics of the models tested are presented in terms of peak perceived noise level, perceived noise level directivity, and one-third octave band sound pressure levels. The noise characteristics also were correlated with the plume aerodynamic data obtained in this program and are presented in this section of the report. Appendix A contains a complete listing of acoustic power levels, OASPL directivity, and perceived noise level directivity for all test conditions.

Definition of the Effect of Nozzle Operating Condition on Inverted Velocity Profile Coannular Nozzle Acoustic Characteristics

Since the fan stream jet tended to control the total measured jet noise for most of the selected inverted velocity profile test range, the ideally expanded fan jet velocity was selected as the main parameter for presentation of the acoustic data. Perceived noise level (PNL) at the angle of peak sideline noise level, 120 degrees in most cases, is shown as a function of fan velocity in Figure 4.1-4 for Configuration A with a constant primary velocity of 427 m/sec (1400 ft/sec) and primary temperature of 811°K (1460°R). The construction details of Configuration A are illustrated in Figure 3-3-3. An increase in PNL can be noted with increasing fan velocity. Figure 4.1-5 contains a similar set of curves for Configuration A with the second primary operating condition used in the test, a primary velocity of 539 m/sec (1770 ft/sec) and a primary temperature of 811°K (1460°R).

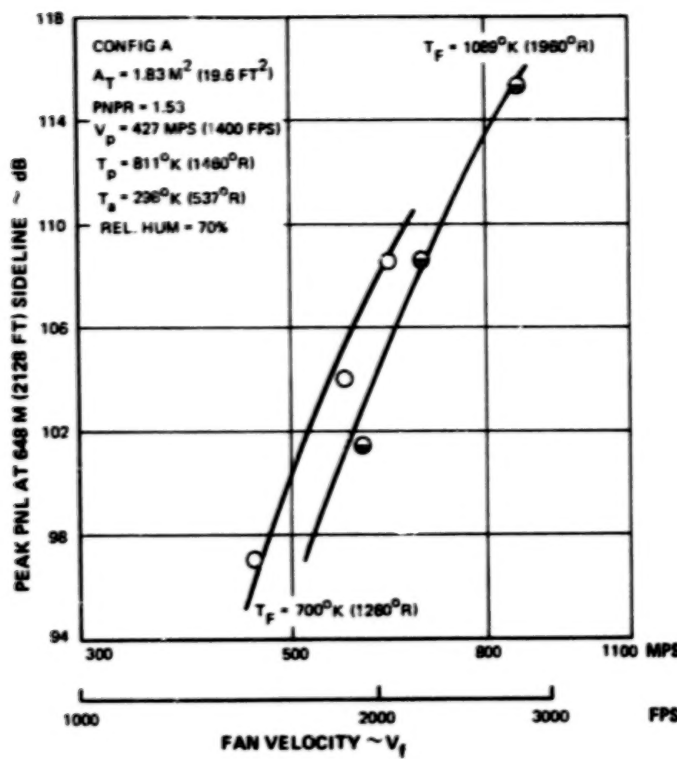


Figure 4.1-4 Peak PNL for Configuration A

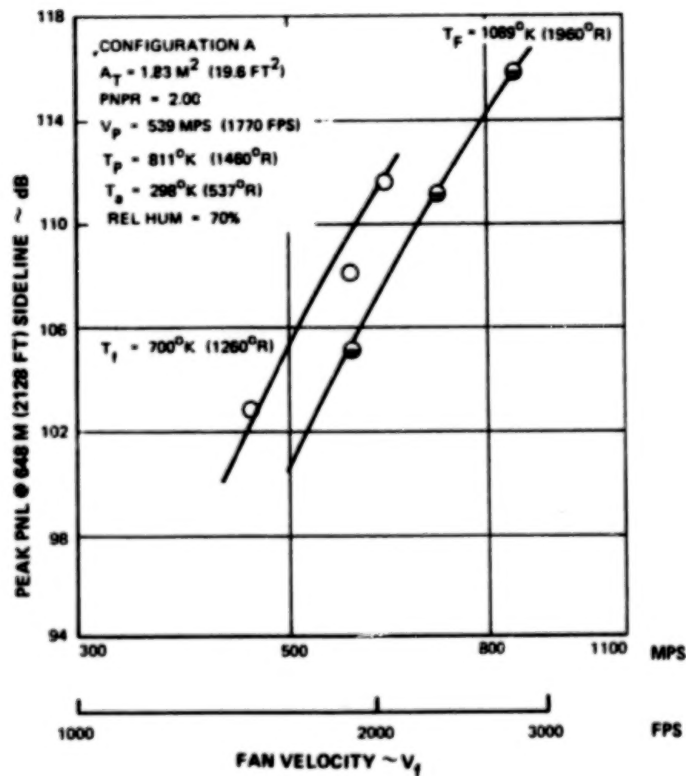


Figure 4.1-5 Peak PNL for Configuration A

The noise directivity characteristics obtained for Configuration A are illustrated in Figure 4.1-6, which contains sideline PNL as a function of measurement angle for a series of fan jet velocities. At angles forward of 90 degrees at the supersonic fan operating conditions (fan nozzle pressure ratios of 2.5 and 3.2), shock noise was present in the measured noise spectra resulting in a very slight change of directivity.

One-third octave band spectra for Configuration A at 150 and 90 degree angles are contained in Figures 4.1-7 and 4.1-8, respectively, for fan to primary velocity ratios of 1.34, 1.66 and 2.00. The data in these figures were obtained for subsonic primary nozzle pressure ratio (1.53) and fan nozzle pressure ratios of 1.8, 2.5 and 4.1. The spectrum for the 1.34 velocity ratio data at 150 degrees shows a double peak that is characteristic of the noise from inverted velocity profile jets. The noise generated at a higher fan to primary velocity ratio of 1.66 exhibits a high frequency peak that is similar in level to the low frequency peak, and the separation of the high and low frequency peaks is less pronounced than the peaks for the 1.34 velocity ratio data. The noise generated at a fan to primary velocity ratio of 2.00 is also dominated by the low frequency peak. As can be observed by comparing the spectra for the 1.34, 1.66 and 2.00 velocity ratios, an increase in fan stream velocity while maintaining a constant primary subsonic velocity caused the low frequency spectrum peak to progressively dominate the spectrum. This result (see Section 5.0) was predicted to be due to the noise produced by the merged region of the flow.

Figure 4.1-8 contains one-third octave band spectra at 90 degrees for the same operating conditions illustrated in Figure 4.1-7. The data trends are similar to those observed at the 150 degree angle except that the spectra are broad and do not exhibit two distinct noise peaks. At 150 degrees, the spectra were dominated by jet exhaust mixing noise, and there was no evidence of shock noise at the supersonic fan nozzle pressure ratios of 2.5 and 4.1. At 90 degrees, however, shock noise is visible, at the supersonic operating conditions, at a frequency of 5000 Hz. At the fan nozzle pressure ratio of 2.5 the spectrum shape is slightly different than that for the subsonic pressure ratio of 1.8 which indicates the presence of shock noise. At the fan nozzle pressure ratio of 4.1, the shock noise is a significant factor in the total noise spectrum.

Figures 4.1-9 and 4.1-10 contain one-third octave band data at the 150 and 90 degree angles, respectively, for Configuration A for two coannular nozzle operating conditions with the same fan stream conditions but with different primary stream conditions. The data in Figures 4.1-9 and 4.1-10 were obtained for a subsonic fan nozzle pressure ratio of 1.8. The fan to primary flow velocity ratios of the two sets of data were 1.06 and 1.34. At both the 150 and 90 degree angles, as the primary stream velocity was increased, the low frequency noise increased while the high frequency noise was unchanged. Although the primary nozzle pressure ratio was supersonic for the 1.06 velocity ratio data, jet exhaust mixing noise dominated the spectra in Figures 4.1-9 and 4.1-10, and shock noise generated by the primary stream was not visible.

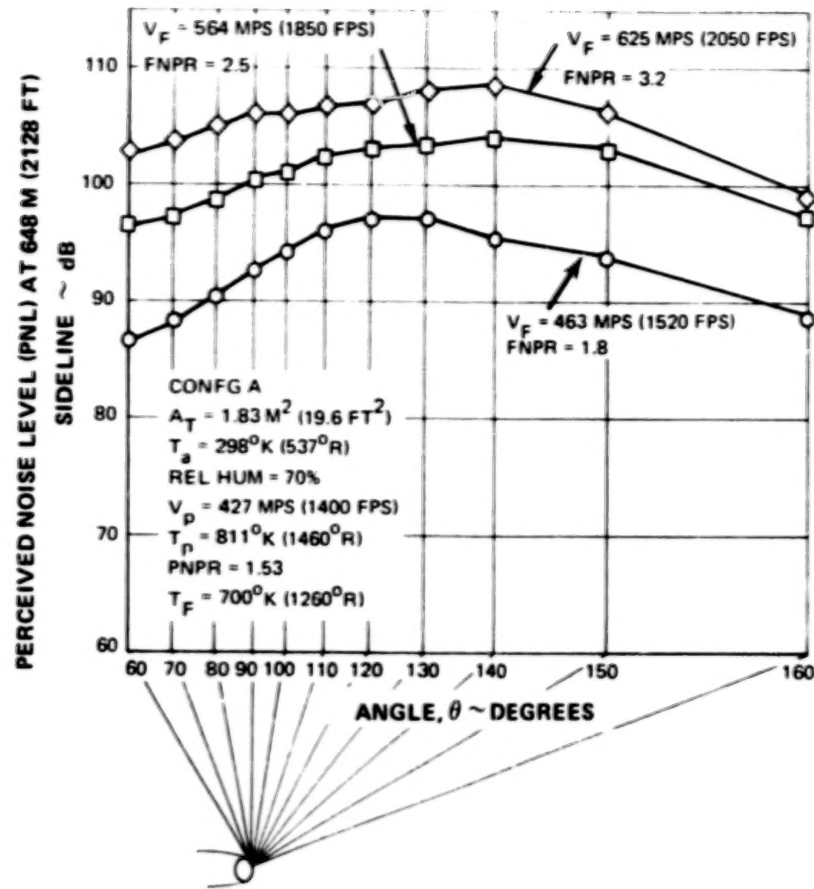


Figure 4.1-6 Effect of Fan Velocity on the PNL Directivity of Inverted Velocity Profile Coannular Nozzles

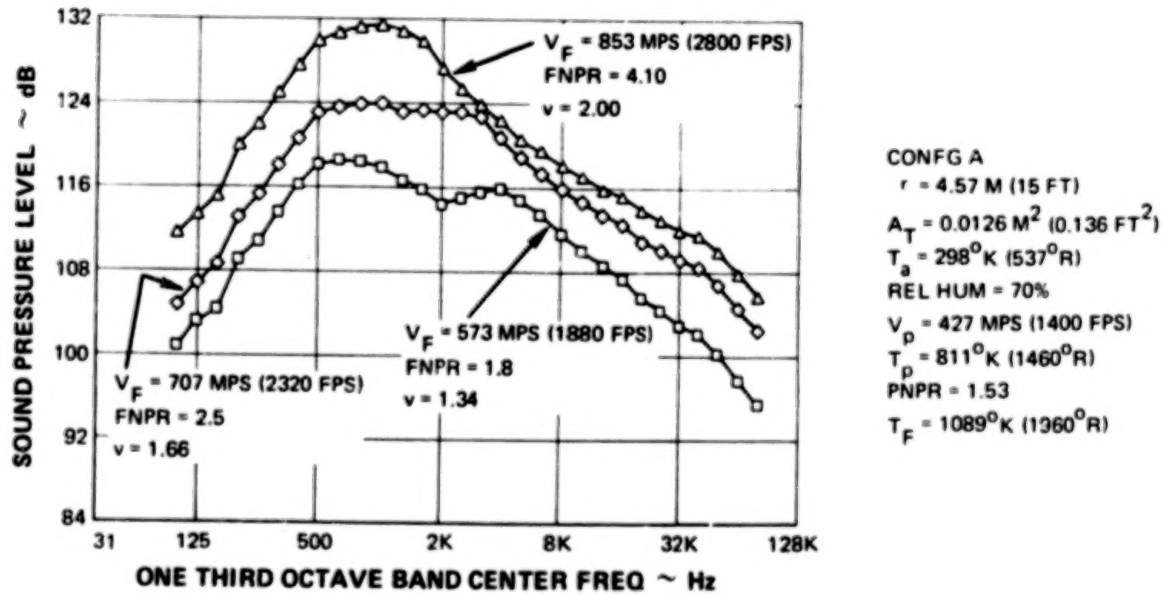


Figure 4.1-7 Effect of Increasing Fan Velocity on Inverted Velocity Profile SPL Spectra at 150 Degrees

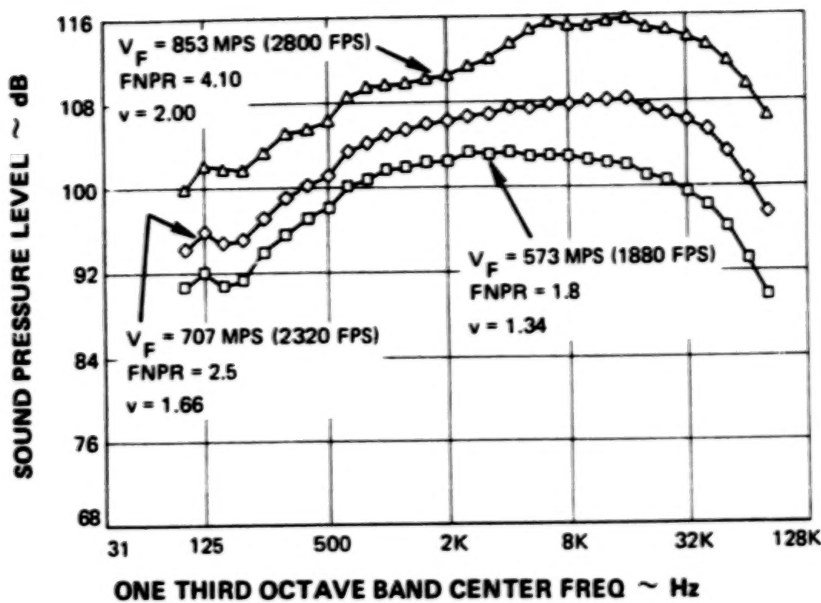


Figure 4.1-8 Effect of Increasing Fan Velocity on Inverted Velocity Profile SPL Spectra at 90 degrees

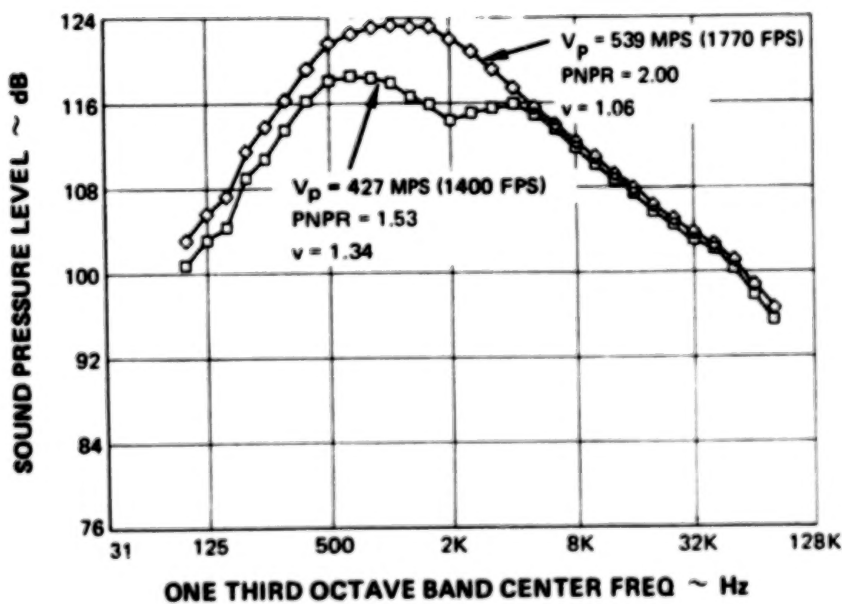


Figure 4.1-9 Effect of Increasing Primary Velocity on Inverted Velocity Profile SPL Spectra at 150 Degrees

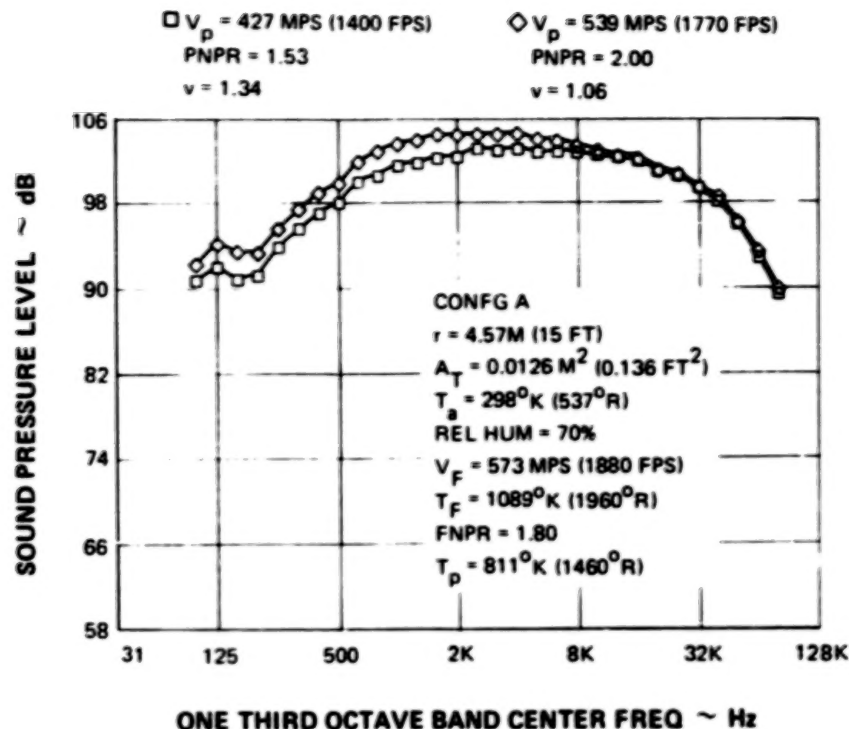


Figure 4.1-10 Effect of Increasing Primary Velocity on Inverted Velocity Profile SPL Spectra at 90 Degrees

Figure 4.1-11 contains measured plume aerodynamic data that illustrate the effect on the peak mean flow velocity of increasing the primary stream velocity, while maintaining a constant fan stream velocity. The peak mean flow velocity was the maximum mean flow velocity obtained in a radial traverse of the jet plume at a fixed axial position and was calculated from total pressure, static pressure, and total temperature measurements as discussed in Section 4.2.1.2. The peak mean flow velocity at a given axial position in the flow was plotted in Figure 4.1-11 versus the axial position normalized by a diameter, D_t , defined as $D_t = 2 \sqrt{A_t/\pi}$, where A_t is the total nozzle area. As primary velocity was increased from 427 m/sec (1400 ft/sec) to 539 m/sec (1770 ft/sec), the rate of decay with axial distance of the peak mean velocity was reduced. In the initial region of the flow (0 to 2 diameters downstream from the fan nozzle exit plane), the decay rates of the two flows are similar, and thus the high frequency noise produced by these regions of the flow should be similar for both operating conditions as was illustrated in Figures 4.1-9 and 4.1-10. In the flow region 4 to 11 diameters downstream from the fan nozzle exit plane, the peak mean velocity for the low velocity ratio operating condition was higher than that for the high velocity ratio operating condition. Therefore, the low frequency noise produced in this region was predicted to be less, as illustrated in Figures 4.1-9 and 4.1-10, for the high velocity ratio operating condition than for the low velocity ratio operating condition. Thus, the aerodynamic measurements were consistent with the data trends observed in Figures 4.1-9 and 4.1-10.

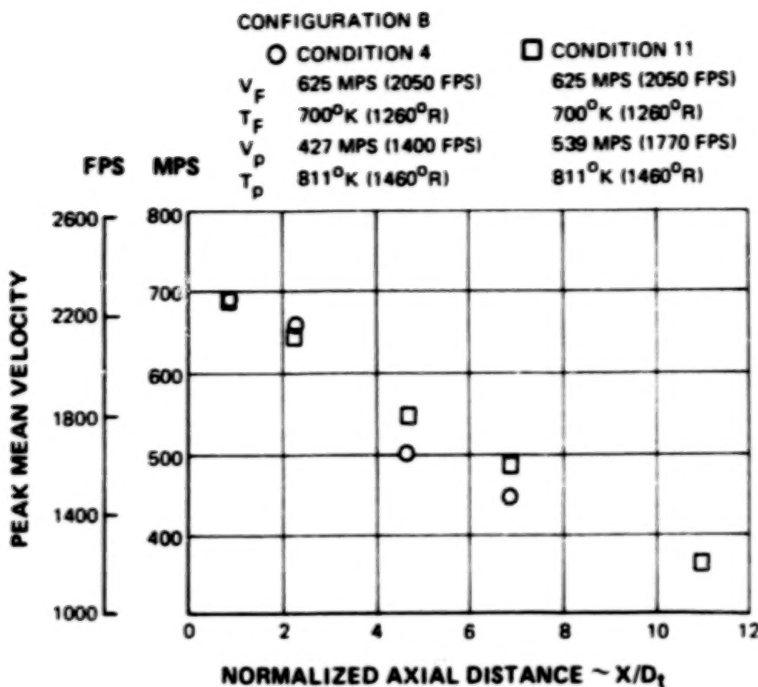


Figure 4.1-11 Comparison of the Peak Mean Velocity Decay for Configuration B, Test Conditions 4 and 11

Definition of the Effect of Nozzle Geometry on Inverted Velocity Profile Coannular Nozzle Acoustic Characteristics

The test configurations defined in Section 3.3 provided independent variation of fan stream and primary stream radius ratios for which fan-to-primary area ratio was held constant; for Configurations A, B, and C the fan radius ratio was increased from 0.69 to 0.83, while the primary radius ratio was held constant. The primary radius ratio for Configurations B and D was increased from zero to 0.60, while fan radius ratio was held constant at 0.75, and the primary radius ratio for Configurations C and E was increased from zero to 0.81, while fan radius ratio was held constant at 0.83.

The effects of nozzle geometry on perceived noise level (PNL) at the angle of peak noise level, 120 degrees, are shown in Figure 4.1-12 for a primary velocity of 427 m/sec (1400 ft/sec) and in Figure 4.1-13 for a primary velocity of 539 m/sec (1770 ft/sec). At fan velocities near 610 m/sec (2000 ft/sec), an increase in fan radius ratio from 0.69 to 0.83 reduced peak PNL 2 to 3 dB, and an increase in primary radius ratio from 0 to 0.81 (fan radius ratio was constant at 0.83) reduced peak PNL an additional 0 to 1 dB. As the fan velocity was increased, the noise reductions were less. At a fan velocity of 853 m/sec (2800 ft/sec), an increase in fan radius ratio from 0.69 to 0.83 did not reduce peak PNL levels while an increase in primary radius ratio from 0 to 0.81 reduced peak PNL levels 0 to 1.0 dB.

The changes in noise directivity characteristics due to geometry variations are illustrated in Figure 4.1-14, which shows PNL as a function of measurement angle at fixed operating condition. The angle of peak PNL did not change over the range of conditions illustrated in Figure 4.1-14.

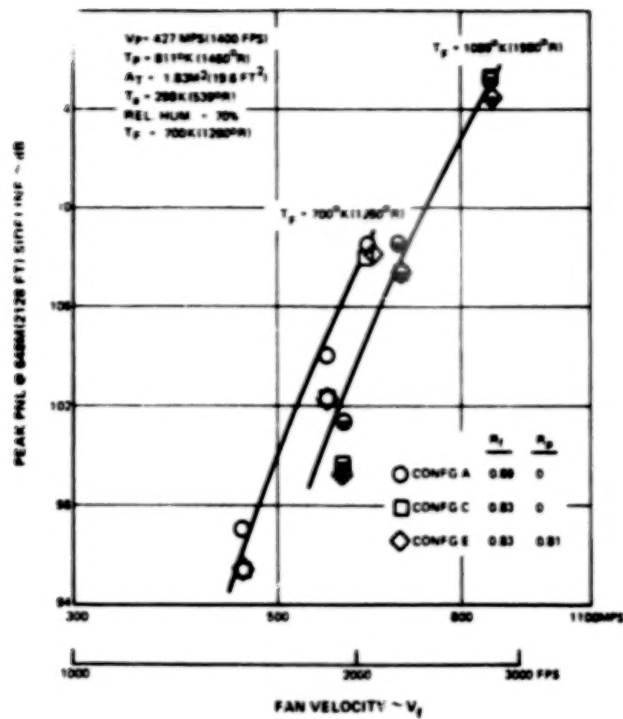


Figure 4.1-12 Comparison of Peak PNL for Configurations A, C, and E at a Primary Velocity of 427 m/sec (1400 ft/sec)

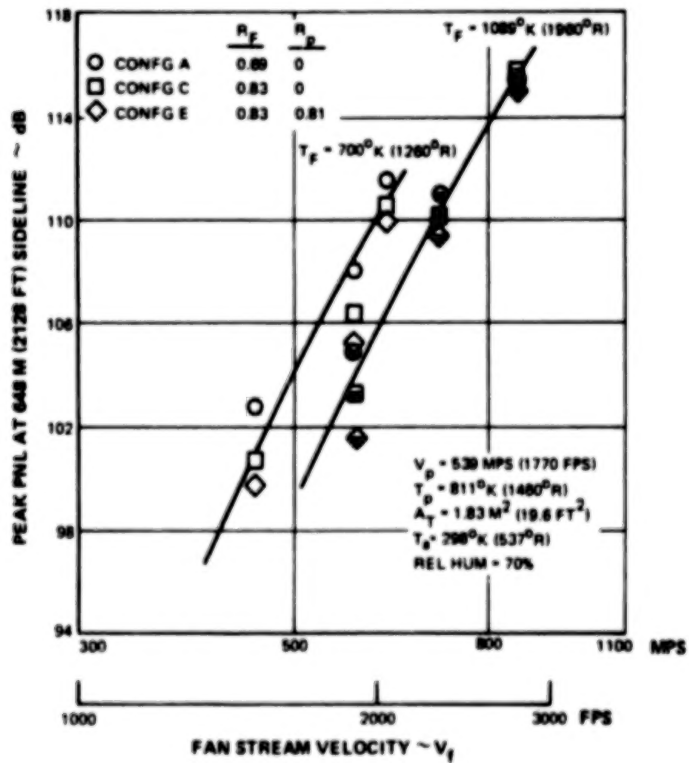


Figure 4.1-13 Comparison of Peak PNL for Configurations A, C, and E at a Primary Velocity of 539 m/sec (1770 ft/sec)

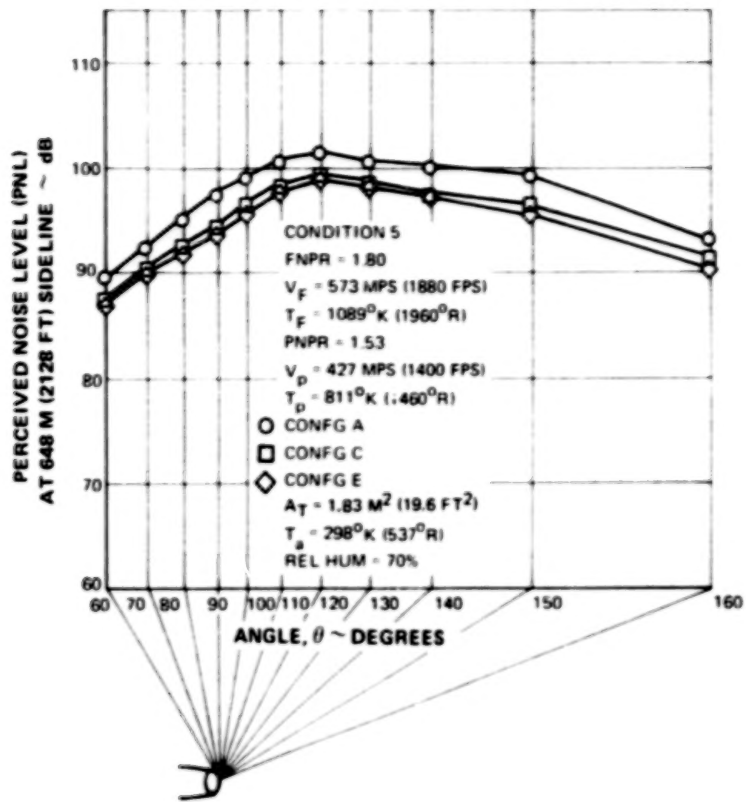


Figure 4.1-14 Comparison of PNL Directivity for Configurations A, C, and E

One-third octave band spectra at the 150 and 90 degree angles for Configurations A, C, and E are contained in Figures 4.1-15 and 4.1-16, respectively, for subsonic primary and fan stream operating conditions ($\text{PNPR} = 1.53$ and $\text{FNPR} = 1.80$) and show a peak PNL reduction of 2.7 dB, as discussed in the preceding paragraph. The model geometries of Configurations A, C, and E are illustrated in Figures 3.3-3, 3.3-5, and 3.3-7. The spectra in Figures 4.1-15 and 4.1-16 show that an increase in fan radius ratio or primary radius ratio reduced the high frequency noise but did not change the low frequency noise. An increase in fan stream radius ratio from 0.69 to 0.83 (with primary stream radius ratio equal to zero) reduced the high frequency noise levels 4.0 dB at 150 degrees and 6.0 dB at 90 degrees while an increase in primary stream radius ratio from 0 to 0.81 (with fan stream radius ratio held constant at 0.83) reduced the high frequency noise zero and 1.0 dB at 90 degrees and 150 degrees, respectively.

One-third octave band spectra at 150 and 90 degree angles for Configurations B and D are contained in Figures 4.1-17 and 4.1-18 for the same operating condition as the data in Figures 4.1-15 and 4.1-16. The model geometries of Configurations B and D are illustrated in Figures 3.3-4 and 3.3-6; Configurations B and D have the same fan stream radius ratios, 0.75, but primary stream radius ratios of 0 and 0.60, respectively. The data in Figures 4.1-17 and 4.1-18 demonstrate that the increase in primary stream radius ratio from 0 to 0.60 did not reduce the noise level of Configuration D relative to that of Configuration B.

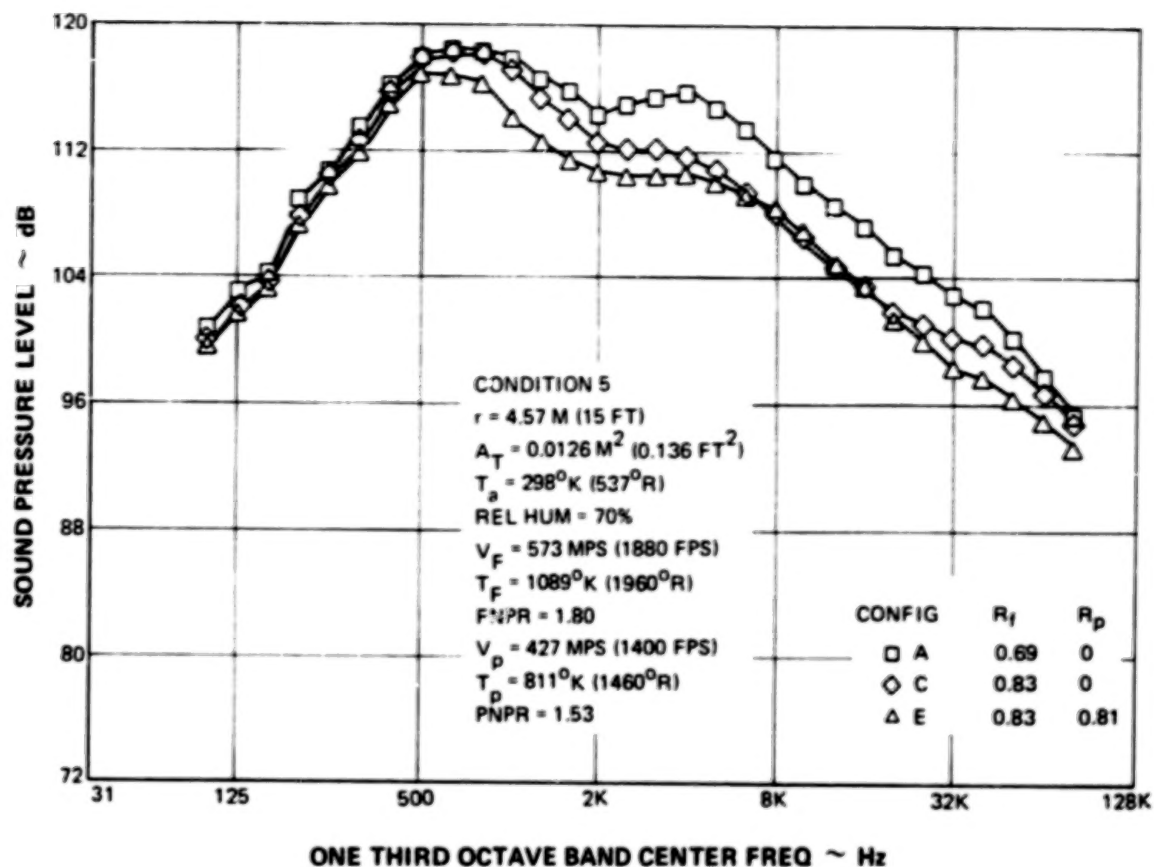


Figure 4.1-15 Effect of Nozzle Geometry on Inverted Velocity Profile SPL Spectra at 150 Degrees for a Subsonic Fan Stream Operating Condition

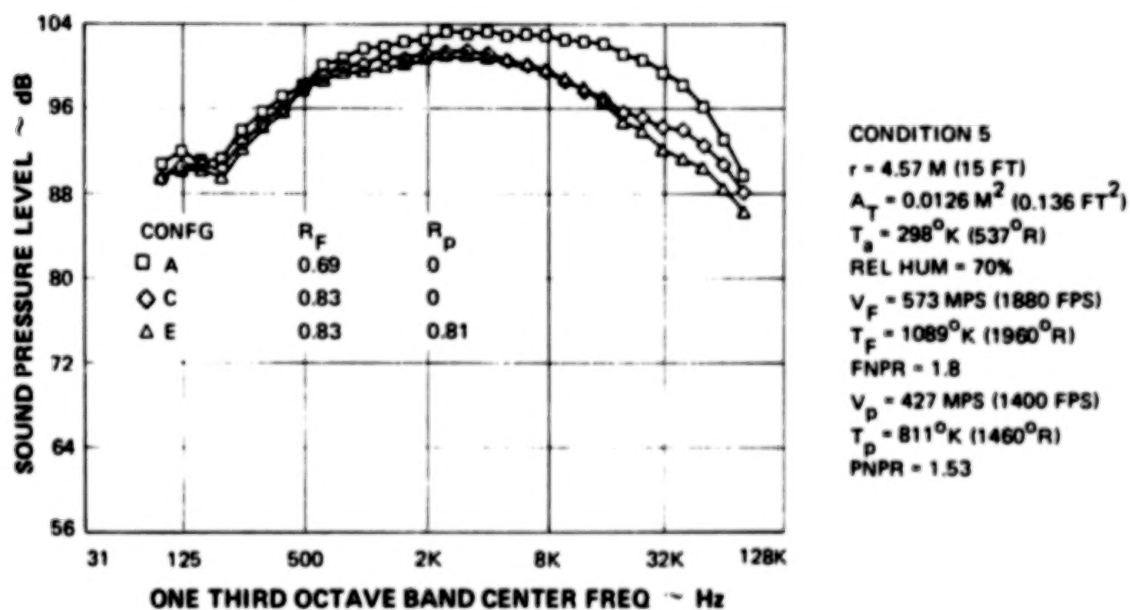


Figure 4.1-16 Effect of Nozzle Geometry on Inverted Velocity Profile SPL Spectra at 90 Degrees for a Subsonic Fan Stream Operating Condition

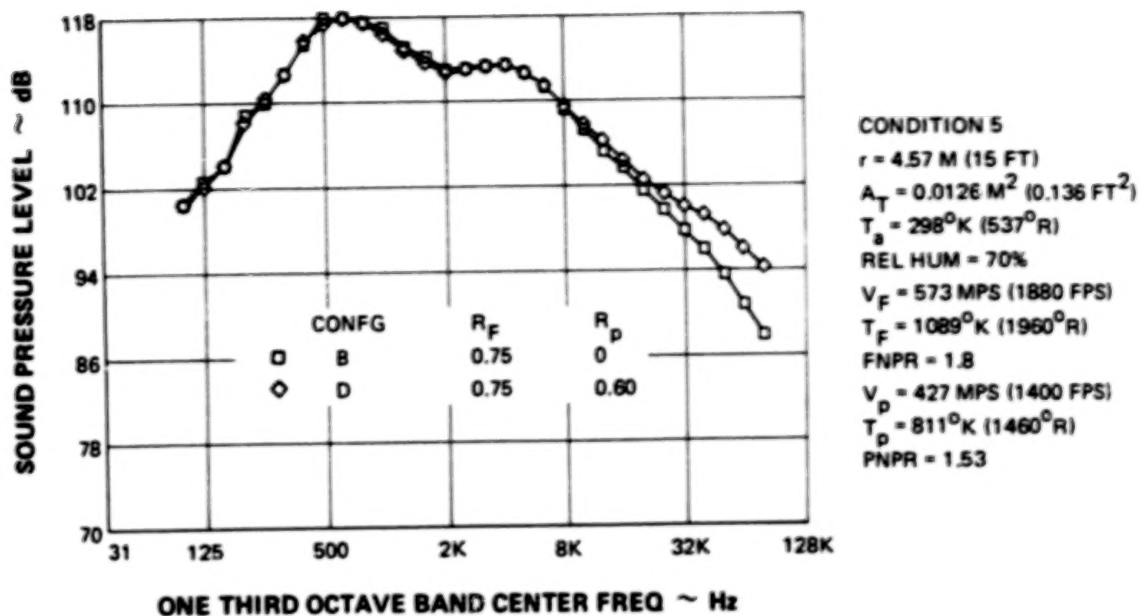


Figure 4.1-17 Effect of Nozzle Geometry on Inverted Velocity Profile SPL Spectra at 150 Degrees for a Subsonic Fan Stream Operating Condition

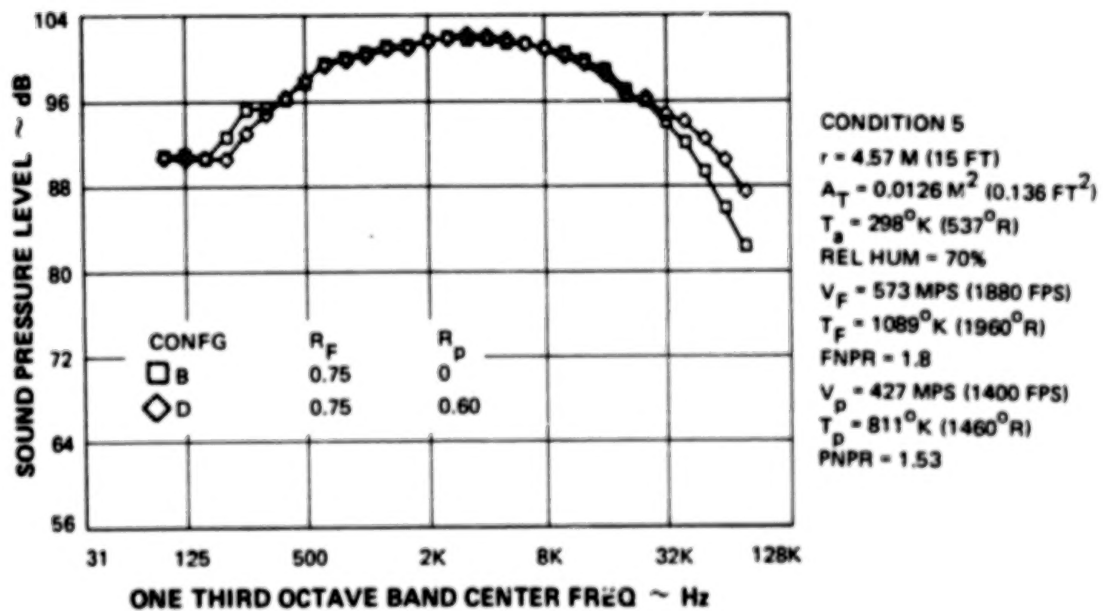


Figure 4.1-18 Effect of Nozzle Geometry on Inverted Velocity Profile SPL Spectra at 90 Degrees for a Subsonic Fan Stream Operating Condition

Figures 4.1-19 and 4.1-20 contain spectra for Configurations A, C and E at 150 and 90 degrees, respectively, with a subsonic primary flow ($PNPR = 1.53$) and supersonic fan flow ($FNPR = 4.1$). The 150 degree spectra were dominated by a low frequency noise peak and were not affected significantly by the changes in fan or primary stream radius ratio that were tested.

The 90 degree spectra, however, were affected by changes in fan stream and primary stream radius ratio. At 90 degrees the total noise spectrum was not dominated by the low frequency noise component, and the high frequency noise component was reduced 3.0 dB by an increase in fan stream radius ratio from 0.69 to 0.83 (with primary stream radius ratio equal to zero) and reduced an additional 1.0 dB by an increase in primary stream radius ratio from 0 to 0.81 (with fan stream radius ratio held constant at 0.83).

One-third octave spectra at the 150 and 90 degree angles for Configurations B and D are contained in Figures 4.1-21 and 4.1-22 for the same operating condition as the data in Figures 4.1-19 and 4.1-20. Configuration B and D have the same fan stream radius ratio but primary stream radius ratios of 0 and 0.60, respectively. The data at 150 degrees in Figure 4.1-21 demonstrate that only a small (approximately 1.0 dB) noise reduction was obtained by increasing the primary stream radius ratio from 0 to 0.60. At 90 degrees there was no reduction in mixing noise by the increase in radius ratio although the shock noise level increased as radius ratio increased.

The data in Figures 4.1-15 through 4.1-22 demonstrate that an increase in fan stream or primary stream radius ratio decreased the high frequency jet exhaust noise and did not affect the low frequency mixing noise. Furthermore, an increase in fan stream radius ratio reduced the high frequency noise more than an increase in primary stream radius ratio.

Shock noise was not consistently reduced or increased by an increase in fan and primary stream radius ratios. The data in Figure 4.1-22 suggest that an increase in primary stream radius ratio caused an increase in shock noise generated by a supersonic fan stream. The data in Figure 4.1-23 demonstrate that this was not generally true. In Figure 4.1-23, Configurations A, B, C, and D produced approximately the same shock noise while Configuration E produced the least shock noise. In general, the shock noise levels for all five configurations were within ± 2 dB at fixed operating condition. This result is discussed further in Section 5.2.2.

Figure 4.1-24 contains aerodynamic measurements for Configurations A, C and E at an operating condition for which a small PNL reduction (1.0 dB) was noted for Configuration E as compared with Configuration A. In Figure 4.1-24, the peak mean velocity axial decay is demonstrated to be the same for the three configurations. Consequently, they should have produced approximately the same noise levels as was observed.

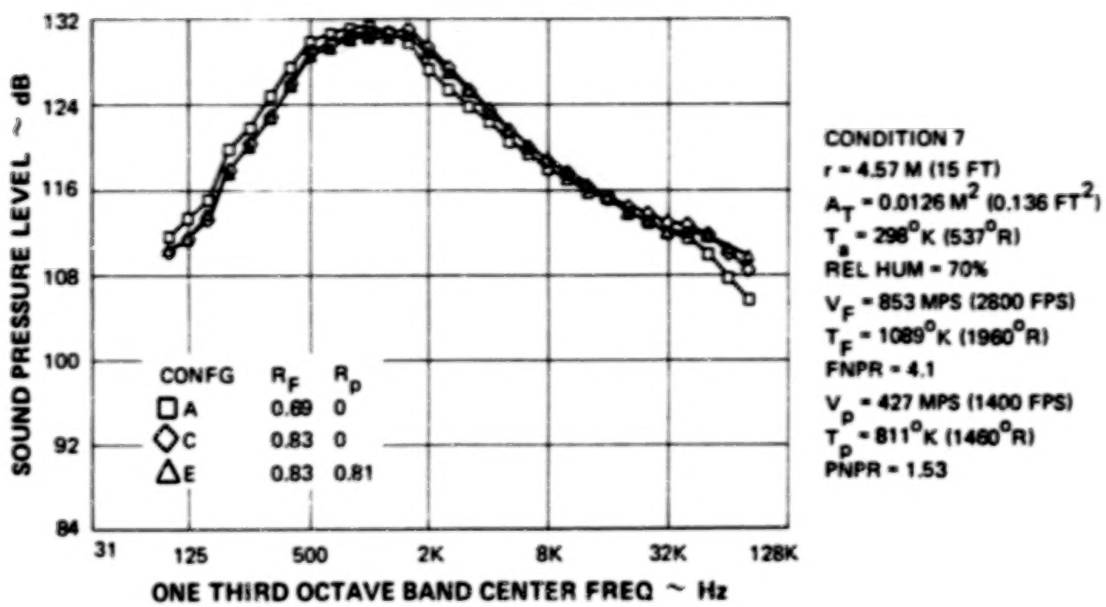


Figure 4.1-19 Effect of Nozzle Geometry on Inverted Velocity Profile SPL Spectra at 150 Degrees for a Supersonic Fan Stream Operating Condition

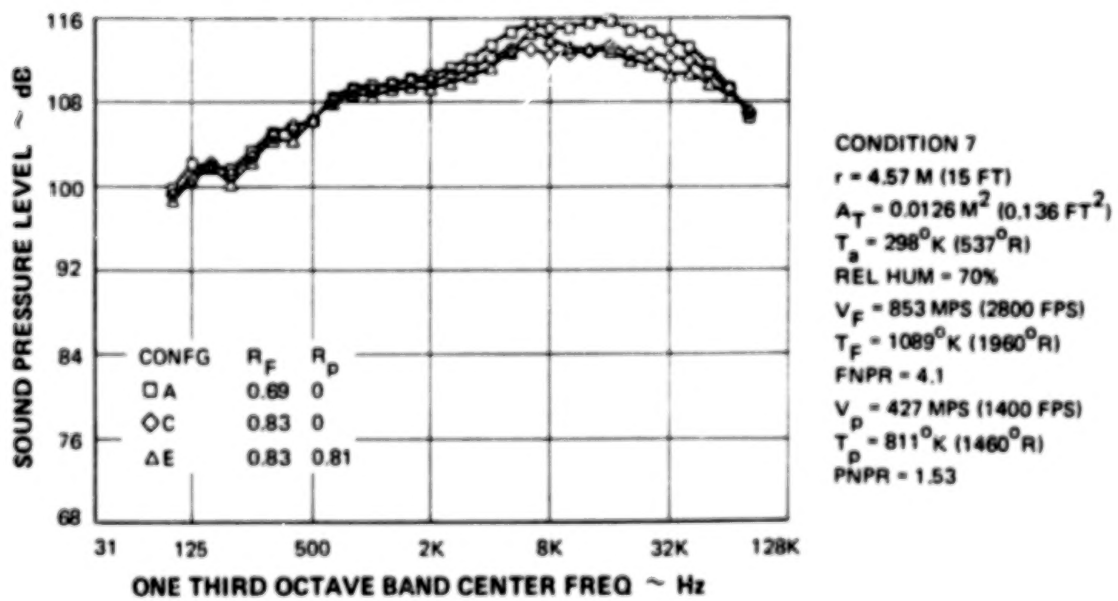


Figure 4.1-20 Effect of Nozzle Geometry on Inverted Velocity Profile SPL Spectra at 90 Degrees for a Supersonic Fan Stream Operating Condition

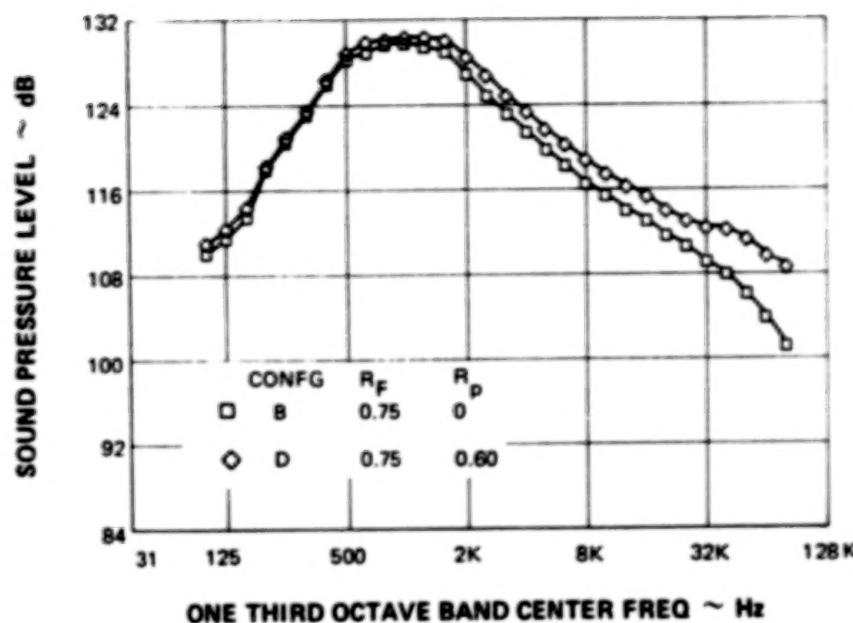


Figure 4.1-21 Effect of Nozzle Geometry on Inverted Velocity Profile SPL Spectra at 150 Degrees for a Supersonic Fan Stream Operating Condition

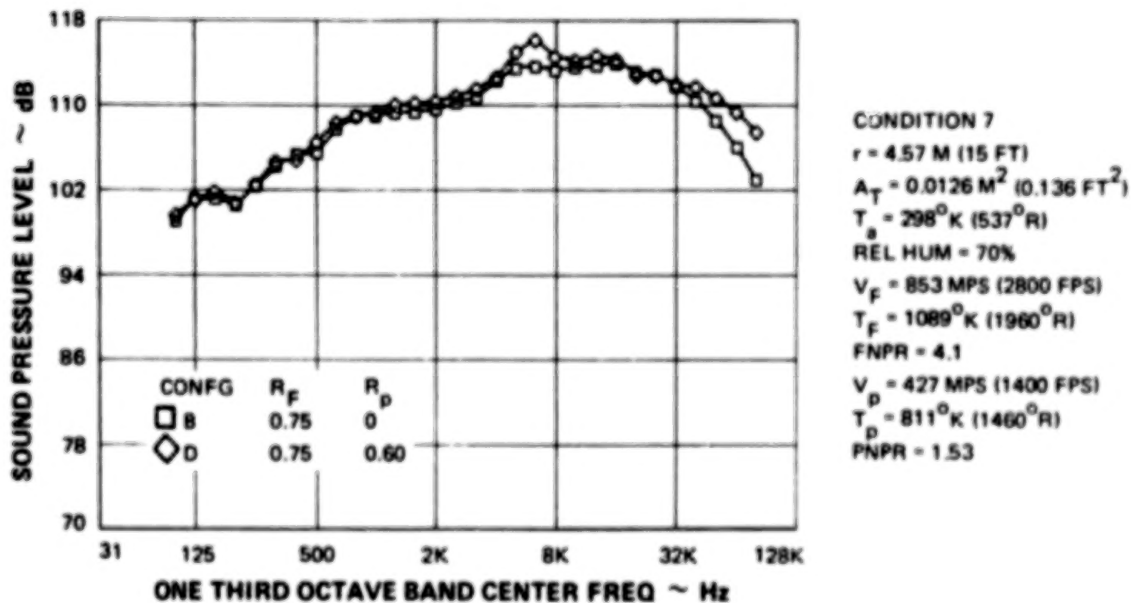


Figure 4.1-22 Effect of Nozzle Geometry on Inverted Velocity Profile SPL Spectra at 90 Degrees for a Supersonic Fan Stream Operating Condition

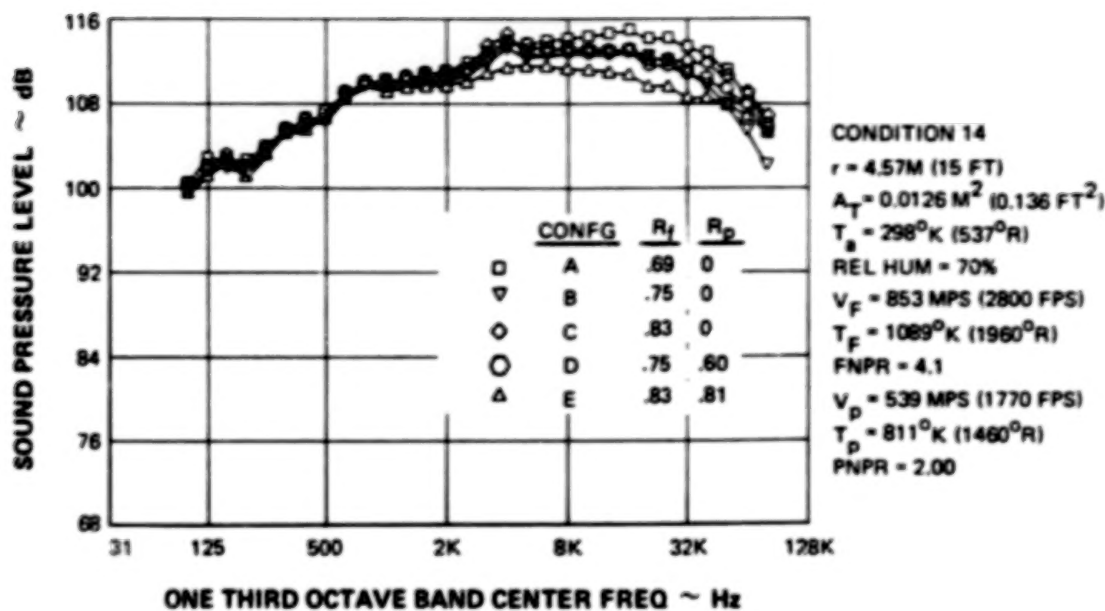


Figure 4.1-23 Comparison of Shock Noise Levels Produced By Configurations A, B, C, D, and E for Supersonic Fan Stream and Primary Stream Operating Conditions

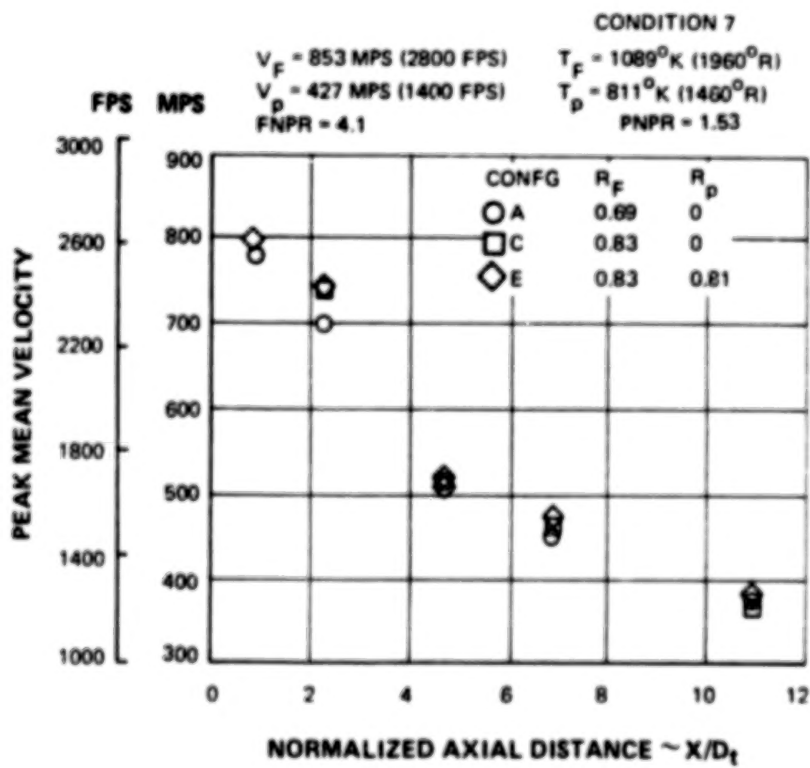


Figure 4.1-24 Effect of Nozzle Geometry on the Aerodynamic Development of an Inverted Velocity Profile Coannular Nozzle

4.1.2.3 Definition of the Acoustic Characteristics of a Single Stream Plug Nozzle

The effects of a plug on the acoustic characteristics of a single stream convergent nozzle were investigated by comparing data from Configuration E with Configuration B when both nozzles were operated only with a primary flow; both nozzles had the same total flow area (see Figures 3.3-4 and 3.3-7). Configuration E contained a plug whereas Configuration B did not. The effect of a plug on perceived noise level (PNL) at the peak noise angle is illustrated in Figure 4.1-25. Peak PNL with the plug installed was 2 to 4 dB lower than the levels from the nozzle without the plug. The larger noise reduction was obtained at low jet velocities, and the noise reduction decreased as jet velocity was increased. Figure 4.1-26 contains PNL directivity plots for both the convergent nozzle and plug nozzle at two operating conditions. For the subsonic operating condition ($PNPR = 1.8$), PNL was lowered uniformly at all angles by the addition of a plug. At the supersonic operating condition ($PNPR = 3.2$) PNL was only slightly lower with the plug nozzle for angles greater than 140 degrees, but was substantially lower at angles from 60 to 130 degrees. This was due to lower levels of shock noise with the plug installed, as can be seen from the spectra. The effect of flow separation at the plug may alter these results. In addition the noise reduction obtained by the addition of a plug may vary with radius ratio.

One-third octave band comparisons at 150 degrees between Configuration B and E are contained in Figure 4.1-27 for range of nozzle velocities between 314 m/sec (1030 ft/sec) and 625 m/sec (2050 ft/sec) at a temperature of 700°K (1260°R). At the low velocity, the noise from the plug nozzle was lower over a range of frequencies from the peak frequency of the spectrum to the highest frequency measured (80 kHz). At the largest velocity, the noise from the plug nozzle was about the same as that from the nozzle without a plug, although at the peak PNL angle (see Figure 4.1-26) the plug nozzle noise levels were 2.0 dB lower than the noise levels from Configuration B. Figure 4.1-28 contains data at 90 degrees for the same nozzles and operating conditions as Figure 4.1-27. At low velocities, the noise was lower by similar amounts to those observed at 150 degrees while at the supersonic conditions (nozzle pressure ratio >1.89), shock noise levels were much lower with the plug installed. This was not observed at 150 degrees because at these supersonic conditions mixing noise dominates the spectrum at this angle. Therefore, it was concluded that the effect of a plug in a convergent nozzle was to reduce mixing noise at low nozzle velocities and reduce shock noise at supersonic operating conditions.

Figure 4.1-29 contains plume aerodynamic data obtained at a supersonic operating condition for Configuration E, the nozzle containing a plug. In contrast to a convergent nozzle, for which the peak mean velocity at a given axial station is constant through the end of the potential core (approximately five nozzle diameters), the peak mean velocity began to decrease 2 to 4 diameters downstream from the nozzle exit plane. This is consistent with the lower noise levels observed from Configuration E.

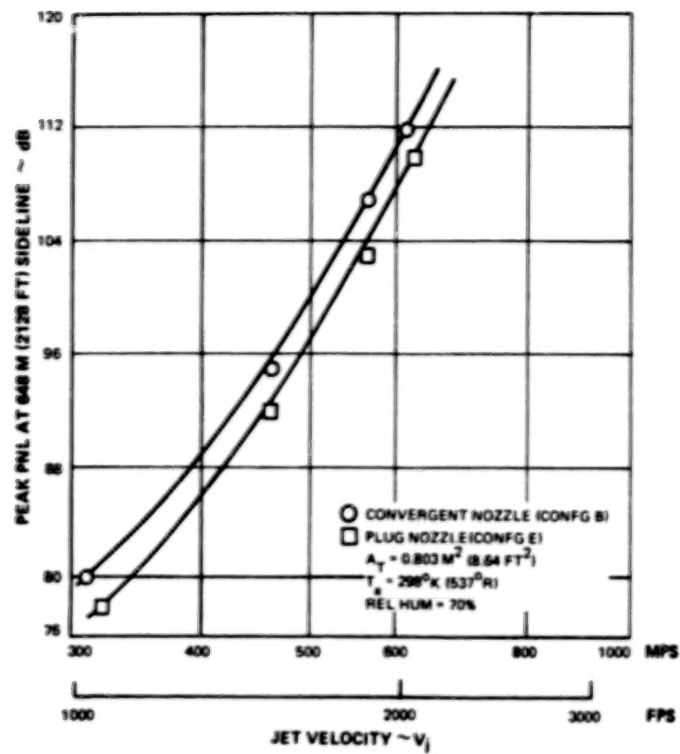


Figure 4.1-25 Comparison of Peak PNL for Single Stream Convergent and Plug Nozzles

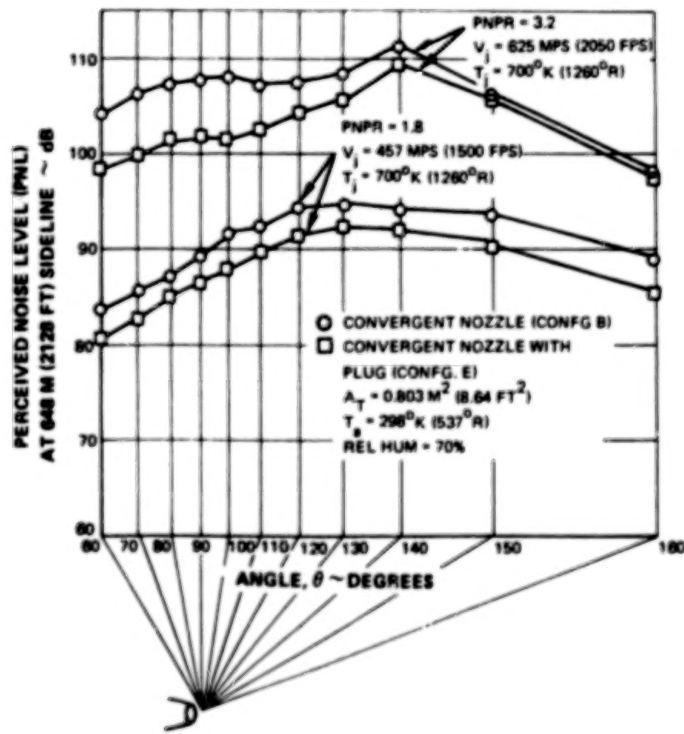


Figure 4.1-26 Effect of Plug on Single Stream Convergent Nozzle PNL Directivity

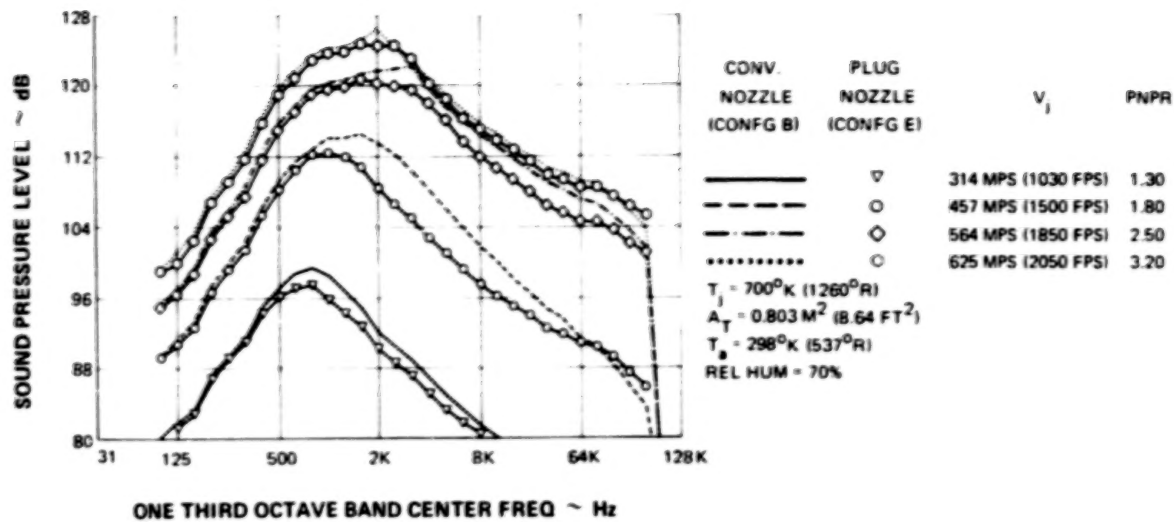


Figure 4.1-27 Effect of a Plug on Single Stream Convergent Nozzle SPL Spectra at 150 Degrees

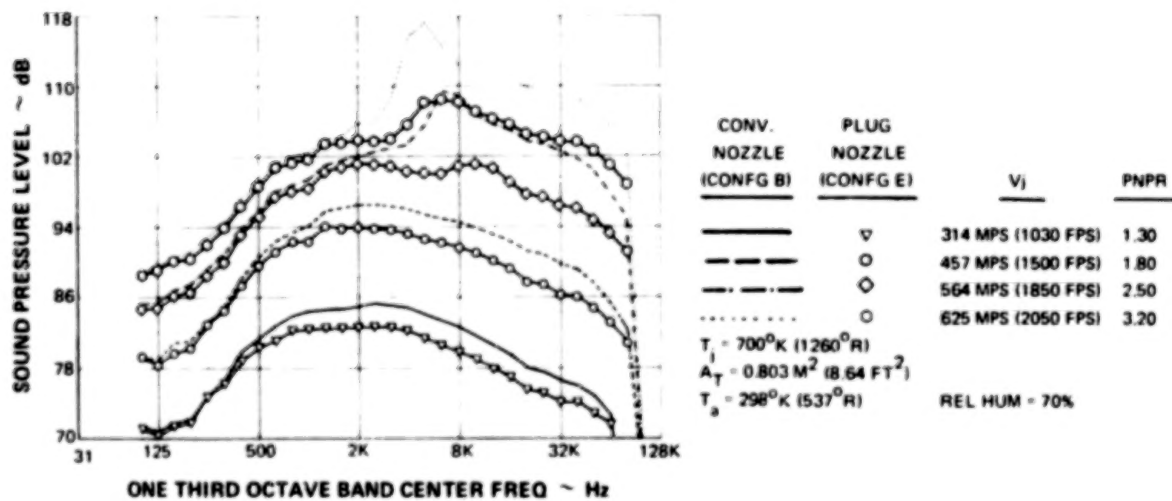


Figure 4.1-28 Effect of a Plug on Single Stream Convergent Nozzle SPL Spectra at 90 Degrees

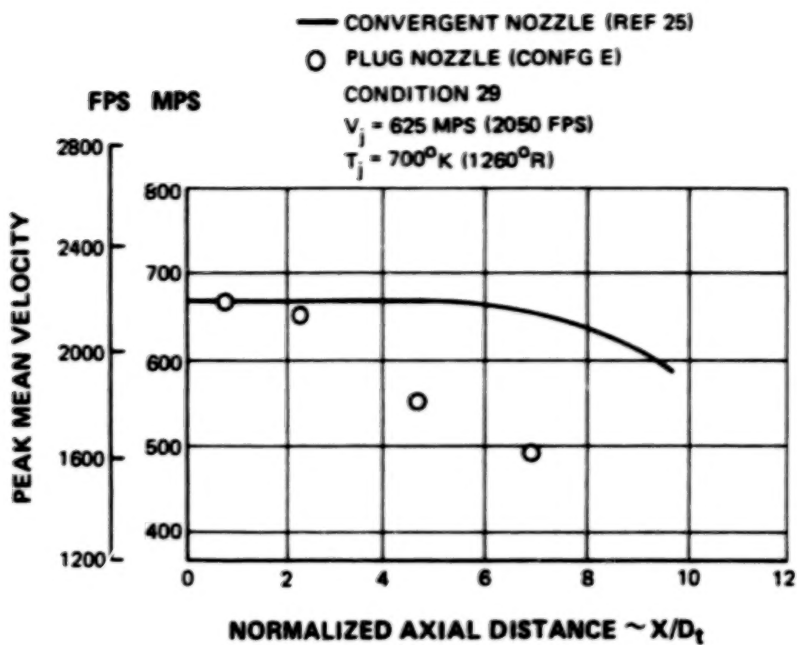


Figure 4.1-29 Comparison of the Peak Mean Velocity Decay for Single Stream Convergent and Plug Nozzles

4.1.2.4 Definition of the Acoustic Characteristics of a Coannular Nozzle with Primary Flow Leakage

Configurations B and D were operated as annular nozzles by turning the primary flow off. The acoustic data obtained for these nozzles actually represent data obtained for high fan to primary velocity ratio coannular jets because the primary nozzle was not physically sealed by a plug, and a small amount of air was entrained through the primary nozzle. Figure 4.1-30 contains a comparison between the peak PNL obtained for Configuration B with the primary flow turned off and the peak PNL for Configuration B with a primary velocity of 427 m/sec (1400 ft/sec). The annular jet with primary leakage flow produced more noise on a PNL basis than the coannular nozzle with a primary velocity of 427 m/sec (1400 ft/sec). A similar trend, illustrated in Figure 4.1-31, was observed by comparing annular jet noise data from Configuration D with Configuration D data obtained with a primary velocity of 427 m/sec (1400 ft/sec). Figure 4.1-32 contains PNL directivity plots for Configuration B operated as a conventional IVP coannular nozzle and an annular nozzle with primary leakage flow. Data for two sets of operating conditions, one with a supersonic fan stream ($\text{FNPR} = 3.2$) and one with a subsonic fan stream ($\text{FNPR} = 1.8$), are included in Figure 4.1-32. At the subsonic fan stream operating condition, the configuration with the primary leakage flow produced 1.6 dB less noise at the peak PNL angle than the configuration producing an inverted velocity profile. At the supersonic fan stream condition, the configuration with the primary leakage flow produced 3.2 dB more noise at the peak PNL angle than the configuration producing an inverted velocity profile.

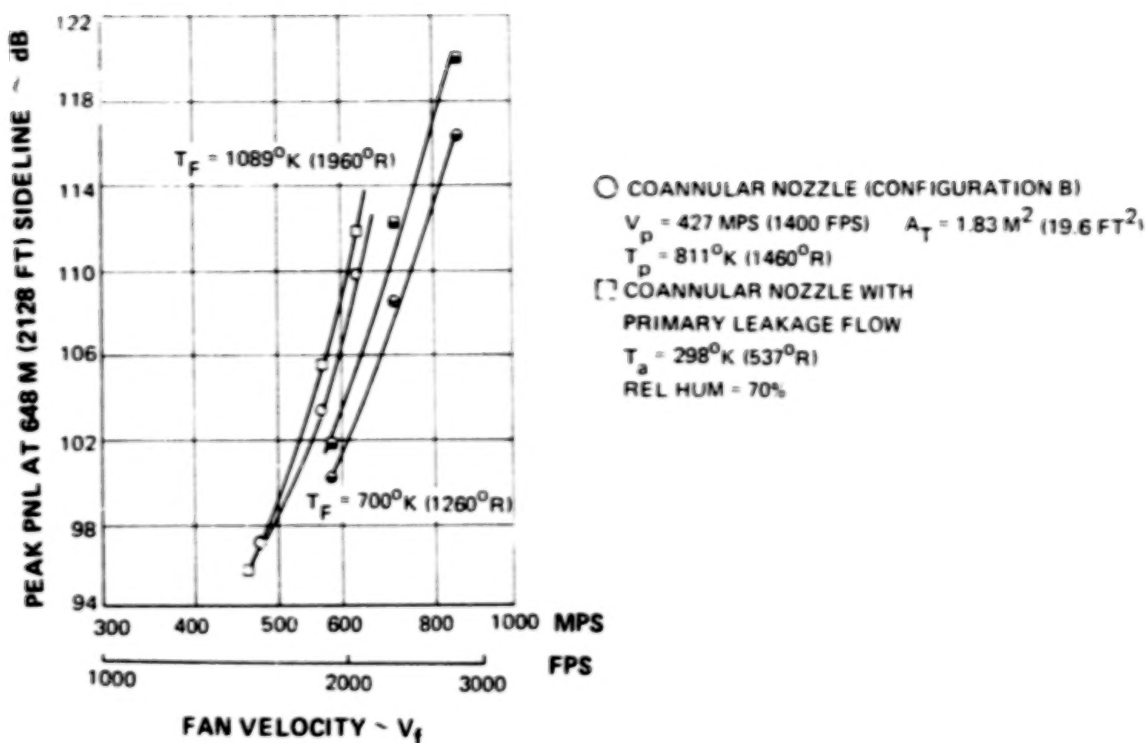


Figure 4.1-30 Comparison of Peak PNL for an Annular Nozzle ($V_p \approx 0$) and a Coannular Nozzle ($V_p = 427 \text{ mps (1400 fps)}$)

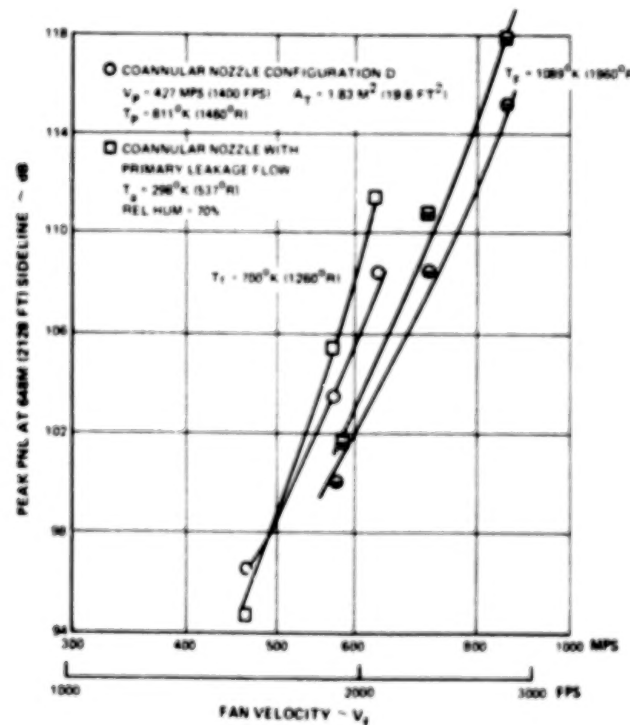


Figure 4.1-31 Comparison of Peak PNL for an Annular Nozzle ($V_p \approx 0$) and a Coannular Nozzle ($V_p = 427 \text{ mps (1400 fps)}$)

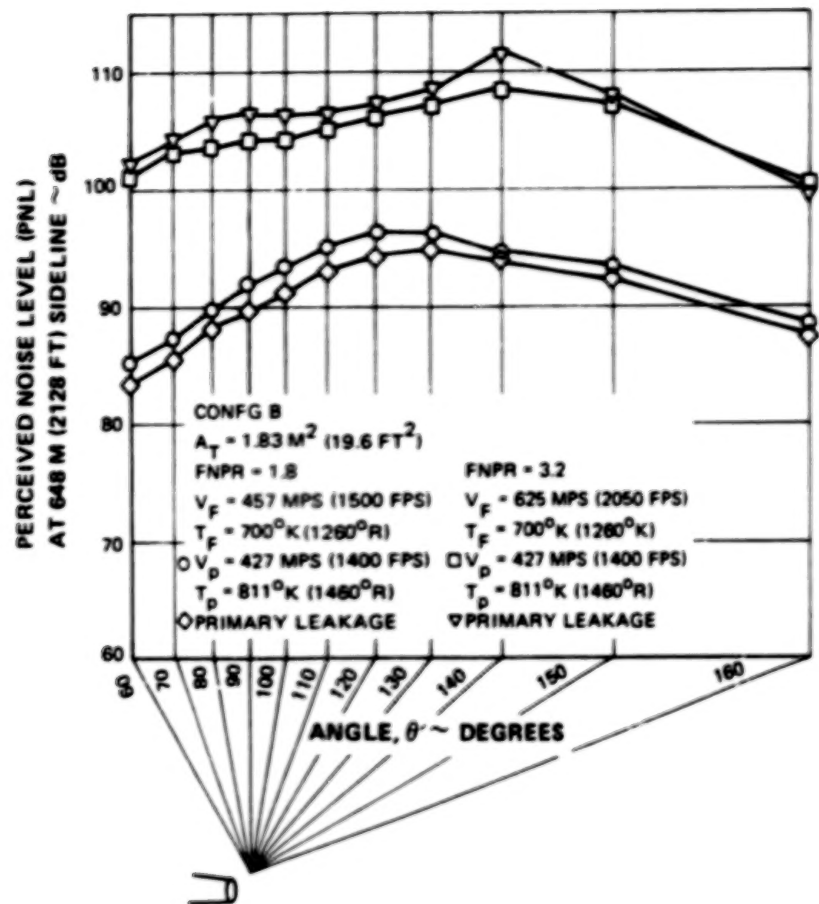


Figure 4.1-32 Comparison of PNL Directivity for an Annular Nozzle ($V_p \geq 0$) and a Coannular Nozzle ($V_p = 427 \text{ m/sec (1400 ft/sec)}$) for Subsonic and Supersonic Annular Flow Conditions

One-third octave band spectra at 150 and 90 degrees are contained in Figures 4.1-33 and 4.1-34 for the inverted velocity profile configuration and the primary leakage flow configuration. The operating conditions for the data in these two figures are the same as those for the data in Figure 4.1-32. For both 150 and 90 degrees, at the subsonic operating condition (FNPR = 1.8) the primary leakage configuration produced mixing noise levels that were 2.0 dB lower at the spectral peak than the mixing noise levels produced by the inverted velocity profile configuration. At the supersonic operating condition (FNPR = 3.2), the mixing noise levels were the same for both configurations but the primary leakage flow configuration produced more shock noise than the inverted velocity profile configuration.

The peak mean velocity axial decay is illustrated in Figure 4.1-35 for Configuration B, operated both as an IVP coannular nozzle with a primary velocity of 427 m/sec (1400 ft/sec) and as an annular nozzle with primary leakage flow. The flow development initially was the same (through 1 diameter) but the peak mean velocity of the annular jet in a region approximately 5 diameters downstream from the nozzle exit plane was larger than that for the IVP coannular jet configuration. This observation was consistent for both Configurations B and D. Data were not available for comparison at the last two axial measurement planes.

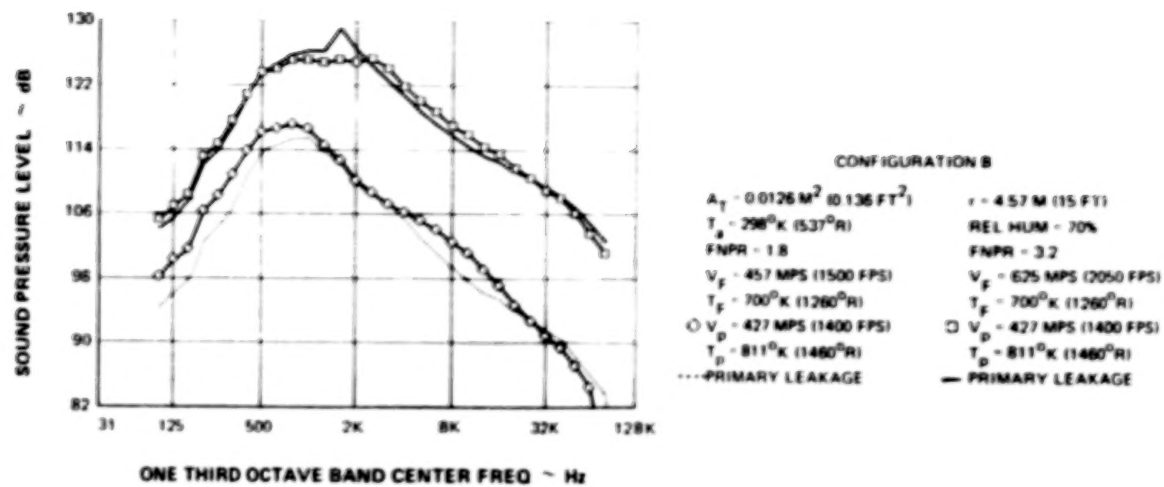


Figure 4.1-33 Comparison of SPL Spectra at 150 Degrees for an Annular Nozzle ($V_p \geq 0$) and a Coannular Nozzle ($V_p = 427 \text{ m/sec (1400 ft/sec)}$) for Subsonic and Supersonic Annular Stream Operating Conditions

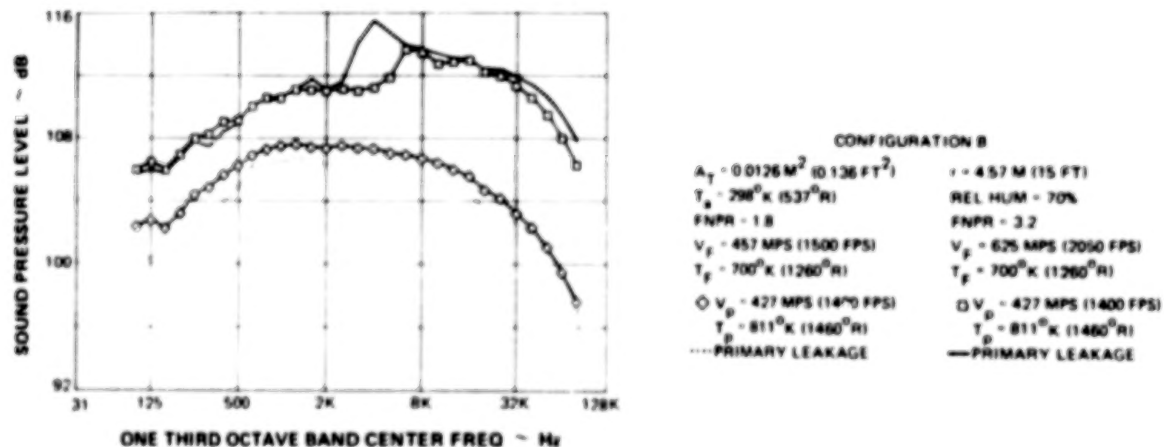


Figure 4.1-34 Comparison of SPL Spectra at 90 Degrees for an Annular Nozzle ($V_p \geq 0$) and a Coannular Nozzle ($V_p = 427 \text{ m/sec (1400 ft/sec)}$) for Subsonic and Supersonic Annular Stream Operating Conditions

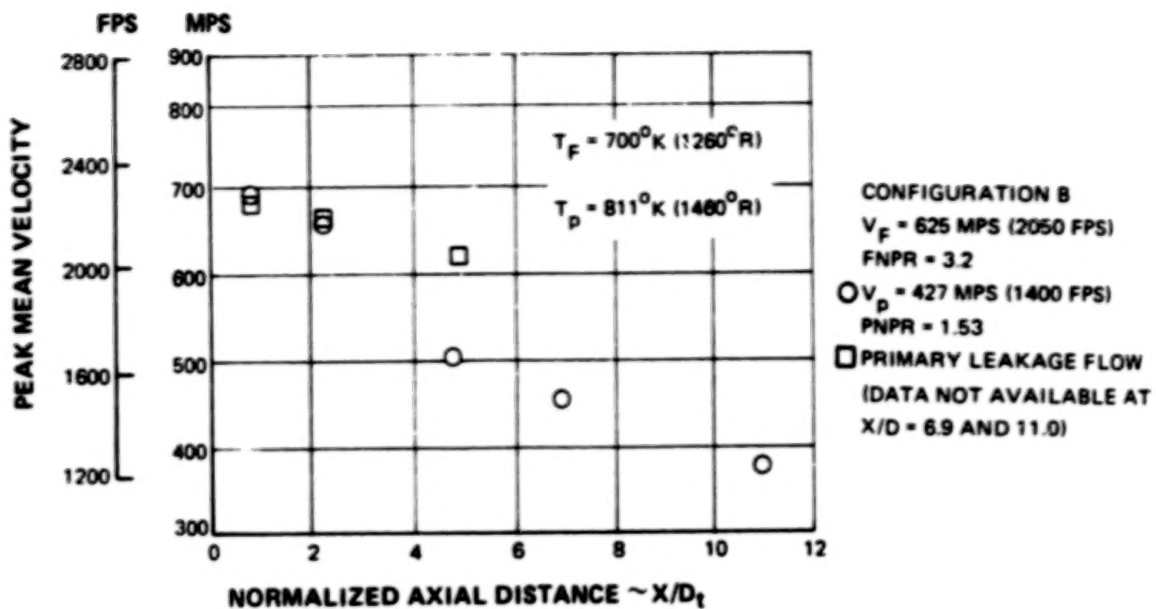


Figure 4.1-35 Comparison of the Peak Mean Velocity Decay for an Annular Nozzle ($V_p \approx 0$) and a Coannular Nozzle ($V_p = 427 \text{ m/sec}$ (1400 ft/sec)) for a Supersonic Annular Stream Operating Condition

4.2 AERODYNAMIC DATA

4.2.1 Aerodynamic Data Reduction

Measured aerodynamic data will be discussed in two categories:

- (1) Thrust and flow coefficients
- (2) Nozzle exit profiles

4.2.1.1 Thrust and Discharge Coefficient Data Reduction

By definition, the thrust coefficient of a nozzle is the ratio of the actual nozzle thrust (as measured by the test stand balance) and the ideal thrust (which is based on the thermodynamics properties of the flow entering the nozzle).

$$C_T = \frac{F_t}{F_{id_t}}$$

where F_t = measured thrust
 F_{id_t} = total ideal thrust
 $= F_{id}(\text{primary}) + F_{id}(\text{fan})$

The ideal thrust (F_{id}) of each stream is calculated by the equation:

$$F_{id} = P_t A^* \sqrt{\frac{2\gamma^2}{\gamma-1} \left(\frac{2}{\gamma+1} \right)^{\frac{\gamma+1}{\gamma-1}} \left[1 - \left(\frac{P_a}{P_t} \right)^{\frac{\gamma-1}{\gamma}} \right]} \quad \text{Eq. (4-1)}$$

where:

P_t = area weighted average total pressure at instrumentation station (N/m² (psia))

$$A^* = \frac{W_t}{P_t} \sqrt{\frac{T_t \bar{R}}{g_c \gamma}} \left(1 + \frac{\gamma-1}{2} \right)^{\frac{\gamma+1}{2(\gamma-1)}} \quad \text{Eq. (4-2)}$$

A^* = Nozzle thrust area

and W_t = Total measured air flow rate (kg/sec, (lbm/sec))

T_t = Total temperature at instrumentation station (°K, (°R))

γ = Specific heat ratio

\bar{R} = Gas constant = 88.51 Nm/kg °K (53.3 lbf ft/lbm °R)

g_c = Conversion factor ≈ 1.0 kg m/N sec² (32.174 lbm ft/lbf sec²)

The nozzle flow coefficient for each stream is calculated by the equation:

$$C_D = \frac{W_t}{W_{id}} \quad \text{Eq. (4-3)}$$

where:

$$W_{id} = \frac{P_t A}{\sqrt{T_t}} M \sqrt{\frac{\gamma g_c}{\bar{R}}} \left(1 + \frac{\gamma-1}{2} M^2 \right)^{\frac{(\gamma+1)}{2(\gamma-1)}} \quad \text{Eq. (4-4)}$$

(kg/sec(lbm/sec))

A = Nozzle exit area in each stream (m²(ft²))

$$M = 1.0 \text{ if } P_t/P_a > 1.8929$$

$$M = \sqrt{\frac{2}{\gamma - 1}} \left(\left(\frac{P_t}{P_a} \right)^{\frac{\gamma - 1}{\gamma}} - 1 \right) \quad \text{if } P_t/P_a \leq 1.8929$$

Data from the thrust test stand were recorded with the UTRC Wide-Band System for Acquiring and Recording Data (WISARD), an automatic data acquisition system which digitizes up to 20 analog input signals and stores the binary equivalents on magnetic tape. Data were reduced by the IBM 370 computer. An example of the reduced data in final format is given in Table 4.2-1.

TABLE 4.2-1
TYPICAL PERFORMANCE DATA - MODEL B

Configuration 8
Run 1337

TP	PNPR	FNPR	CT	CD _p	CD _f
3	1.53	4.25	.973	.893	.980
4	1.53	4.24	.972	.880	.984
5	1.54	3.78	.975	.853	.980
6	1.53	3.78	.975	.854	.979
7	1.54	3.30	.978	.736	.975
8	1.54	3.31	.976	.769	.930
9	1.54	2.90	.980	.690	.974
10	1.53	2.90	.983	.700	.972
11	1.53	2.87	.982	.688	.974
12	1.54	2.56	.980	.765	.980
13	1.54	2.56	.980	.771	.977
14	1.54	2.24	.980	.805	.977
15	1.54	2.24	.979	.808	.976
16	1.54	1.82	.977	.877	.971
17	1.54	1.81	.977	.878	.971
18	1.53	1.50	.976	.916	.965
19	1.53	1.50	.975	.921	.965
20	1.53	1.36	.979	.931	.960
21	1.53	1.36	.978	.930	.960

Where: TP = Test Point Number
 PNPR = Primary Nozzle Pressure Ratio
 FNPR = Fan Nozzle Pressure Ratio
 CT = Thrust Coefficient
 CD_p = Primary Discharge Coefficient
 CD_f = Fan Discharge Coefficient

4.2.1.2 Traverse Data Reduction

Nozzle exit temperature and velocity distributions were determined from traverse data obtained in the X-206 stand. The calibrated traverse probe measured static pressure, total pressure, and total temperature at each traverse matrix test point, as described in Sections 3.1.3.2 and 3.1.3.3.

Complete traverse data are contained in the Comprehensive Data Report (Reference 19). A sample of the printout format is shown in Table 4.2-II for Configuration D. Radius (r), total temperature (T_t), and velocity (V) are tabulated for each axial traverse location (X).

Velocity was determined from the following expression:

$$V = \sqrt{\left(\frac{\gamma g_c \theta T_t M^2}{1 + \frac{\gamma-1}{2} M^2} \right)} \quad \text{m/sec (ft/sec)} \quad \text{Eq. (4-5)}$$

where:

$$M = \sqrt{\frac{2}{\gamma-1} \left(\left(\frac{P_t}{P_s} \right)^{\frac{\gamma-1}{\gamma}} - 1 \right)} \quad \text{Eq. (4-6)}$$

4.2.2 Aerodynamic Results and Discussion

Selected aerodynamic data are presented in this section, including nozzle thrust coefficient, nozzle discharge coefficient, and nozzle velocity and temperature profiles. A complete set of aerodynamic data is contained in the Comprehensive Data Report (Reference 19).

4.2.2.1 Thrust Coefficient

The model performance was evaluated in the United Technologies Research Center's Large Nozzle Test Facility (LNTF), as discussed in Section 3.2. The reader is referred to a brief review of the model configuration (Figure 3.3-1) to facilitate understanding of the following discussion.

TABLE 4.2-H
SAMPLE TRAVERSE DATA TABULATION - CONFIGURATION D

Config. D
Cond. 8592

X-mm (in.)	.11 (4.5)			.30 (11.6)			.57 (22.3)			.88 (34.7)			1.40 (55)		
r	T ₁	V	r	T ₁	V	r	T ₁	V	r	T ₁	V	r	T ₁	V	
2.959(1.1648)	716 (1289)	361 (1184)	0	814 (1446)	374 (1226)	0	797 (1435)	399 (1308)	0	694 (1249)	385 (1263)	27.676(10.8960)	321 (577)	0	
3.577(1.4082)	702 (1264)	459 (1506)	1.680(0.4415)	792 (1425)	424 (1290)	1.839(0.7236)	739 (1331)	410 (1345)	2.473(1.0525)	619 (1114)	330 (1083)	23.005 (9.0569)	332 (598)	2 (6)	
3.952(1.5559)	667 (1202)	459 (1506)	2.494(0.9818)	750 (1350)	409 (1342)	3.926(1.5455)	586 (1055)	326 (1070)	5.590(2.2008)	508 (914)	229 (752)	18.302 (7.2054)	361 (650)	17 (55)	
4.332(1.7057)	651 (1173)	467 (1533)	3.313(1.3042)	700 (1260)	406 (1332)	5.967(2.3491)	491 (884)	220 (722)	8.457(3.3296)	447 (804)	134 (438)	13.734 (5.4070)	292 (705)	60 (187)	
4.718(1.8575)	572 (1030)	413 (1354)	4.126(1.6245)	604 (1087)	410 (1346)	8.012(3.1545)	434 (782)	113 (372)	11.286(4.4435)	395 (711)	49 (161)	9.263 (3.6468)	430 (774)	126 (413)	
5.094(2.0072)	506 (911)	361 (987)	4.945(1.9470)	532 (957)	310 (1017)	10.063(3.9619)	379 (683)	42 (138)	14.263(5.6153)	352 (634)	12 (40)				
5.470(2.1535)	474 (853)	201 (661)	5.753(2.3647)	470 (846)	212 (697)	12.137(4.7784)	337 (607)	0	17.163(6.7571)	332 (597)	4 (13)				
5.852(2.3038)	417 (750)	106 (328)	6.495(2.5572)	421 (757)	124 (407)	14.206(5.5930)	323 (582)	0	20.057(7.8964)	322 (580)	0				
6.224(2.4501)	376 (676)	28 (92)	6.945(2.7343)	407 (732)	73 (238)	16.360(6.4014)		0							
6.610(2.6025)	339 (611)	0.3 (1)	7.782(3.0639)	371 (667)	18 (59)										
6.987(2.7508)	335 (603)		8.651(3.4058)	344 (620)	2.4 (8)										
7.364(2.8991)	330 (594)	0	9.284(3.6550)	339 (610)	0										
7.997(3.1483)	328 (590)	0													
8.625(3.3953)	328 (590)	0													

When Cond = Test point #

- r = Radius - cm (inches)
- X = Axial position from fan nozzle exit plane - meter (inches)
- T₁ = Total temperature "K ("R)
- V = Velocity - m/sec (ft/sec)

Thrust coefficient (CT) data are shown for the five tested models in Figures 4.2-1 through 4.2-5 for two primary nozzle pressure ratios (PNPR) over a range of fan nozzle pressure ratios (FNPR). The data are smooth and consistent.

Figure 4.2-6 shows combined CT data for all five configurations at PNPR 1.53 and 2.0. Data points were removed for clarity. Configuration A exhibited the best performance, having a CT of approximately 0.985 between FNPR 2.5 and 4.1. Comparison of Configuration A with the other zero primary radius ratio nozzles, B and C, indicates a successive reduction in CT of from 1 percent at FNPR of 2.5 to 2 percent at FNPR of 4.0. Since fan radius ratio increased from 0.69 (Configuration A) to 0.83 (Configuration C), it must be concluded that the increased radius ratio and resulting increasing primary cowl length (L/H) is detrimental to nozzle performance. This is logical since the internal and external nozzle wetted surface area increases with increasing radius ratio resulting in a higher internal pressure loss and friction drag loss. This has been verified analytically and is discussed further in the performance prediction discussion of Section 6.0.

The performance reduction with an increase in radius ratio was also observed in the comparison of the plug nozzles D and E. Configuration E (with fan and primary radius ratios of 0.83 and 0.81, respectively) has approximately 0.8 percent lower CT than Configuration D (with fan and primary radius ratio of 0.75 and 0.60, respectively).

There was one apparent exception to the radius ratio — performance trend. Configuration B displayed a rapid drop-off in CT above FNPR 3.0. This is explained by the fact that Configuration B experienced a higher expansion loss than Configurations A and C as a result of the fan nozzle area ratio (A_f/A^*), as discussed in Section 6.3. The over-expansion loss for Configuration B more than compensated for the radius ratio effect so that the fact that Configuration B has lower CT than Configuration C at the higher FNPR does not contradict the trend. The overexpansion effect was factored into the performance prediction system and will be discussed further in Section 6.0.

Note that at the lower FNPR the performance reduction with increasing radius ratio is more pronounced at PNPR 1.53 than at 2.0. This occurs because the thrust contribution of the fan nozzle is a smaller percentage of the total exhaust system thrust at PNPR 2.0. Consequently, for a given level of fan stream loss, overall system CT will be less affected by radius ratio at PNPR 2.0. At the very high FNPR, the fan stream thrust contribution dominates and the radius ratio effect appears to be the same for both PNPR 1.53 and 2.0.

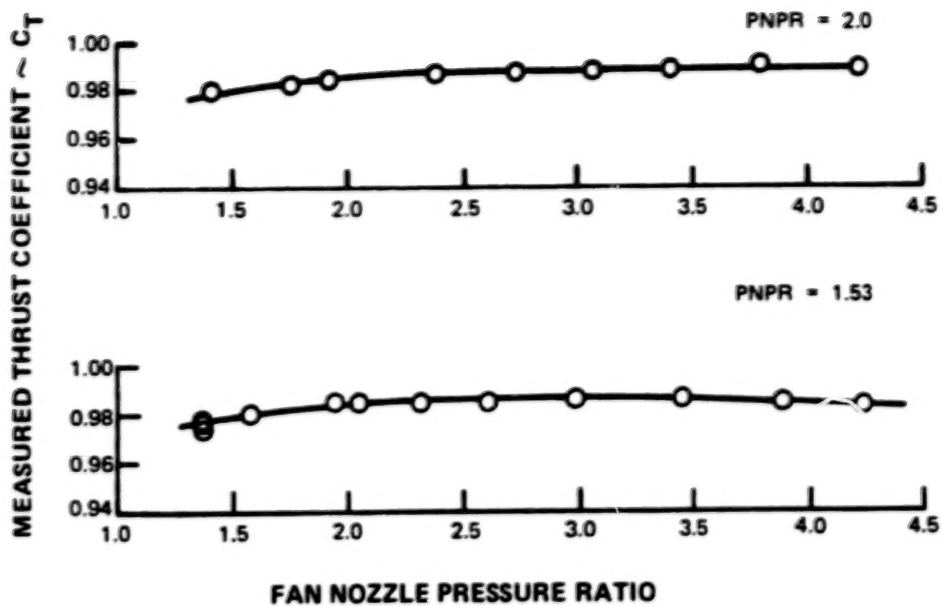


Figure 4.2-1 Nozzle Thrust Coefficient for Configuration A

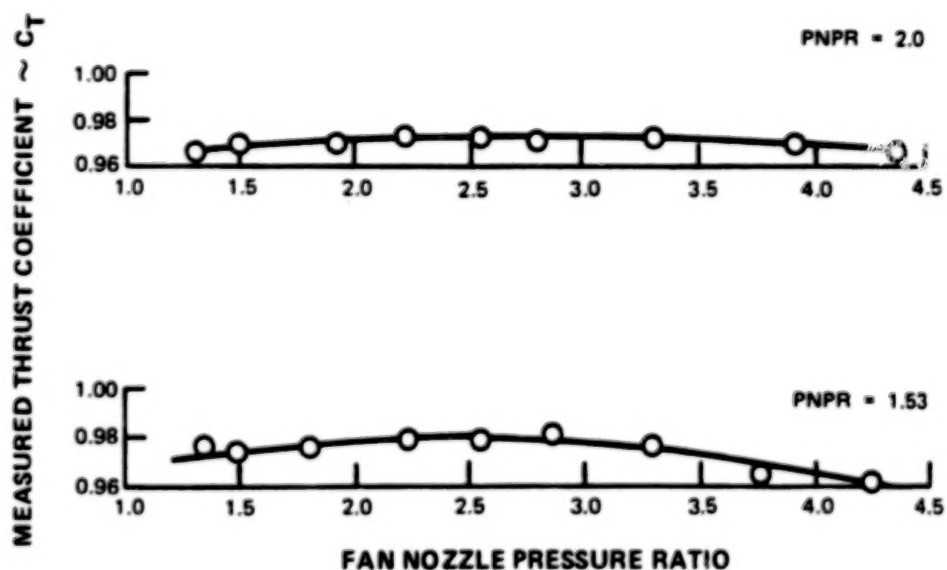


Figure 4.2-2 Nozzle Thrust Coefficient for Configuration B

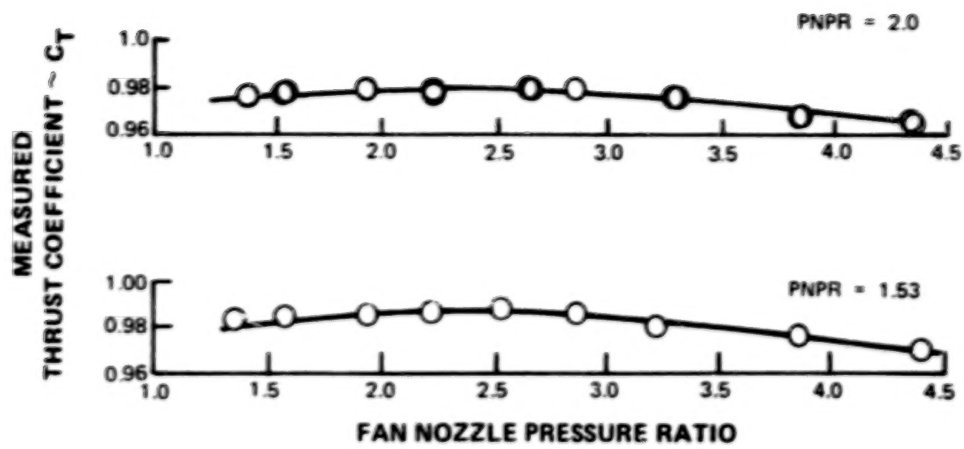


Figure 4.2-3 Nozzle Thrust Coefficient for Configuration C

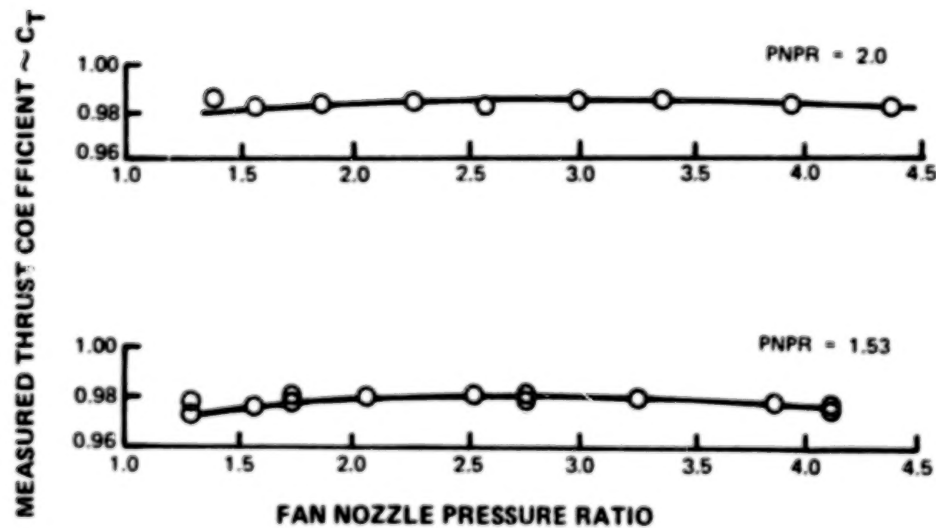


Figure 4.2-4 Nozzle Thrust Coefficient for Configuration D

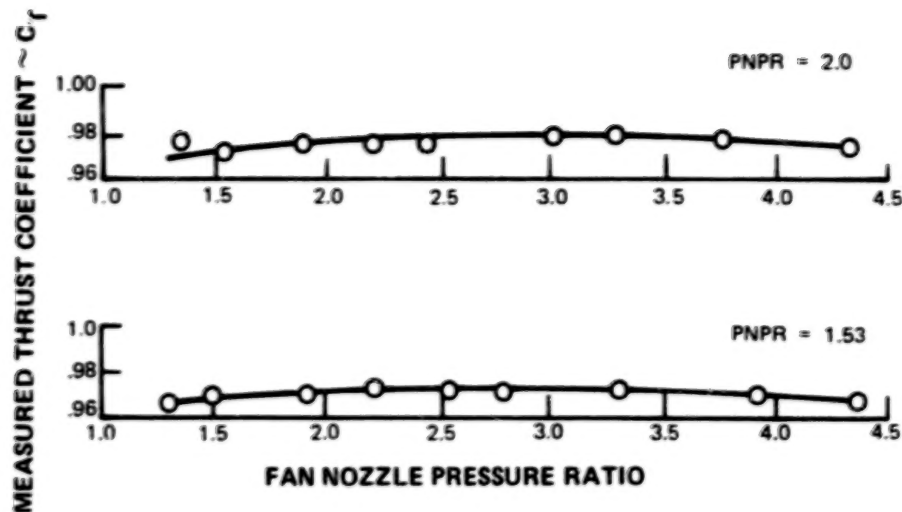


Figure 4.2-5 Nozzle Thrust Coefficient for Configuration E

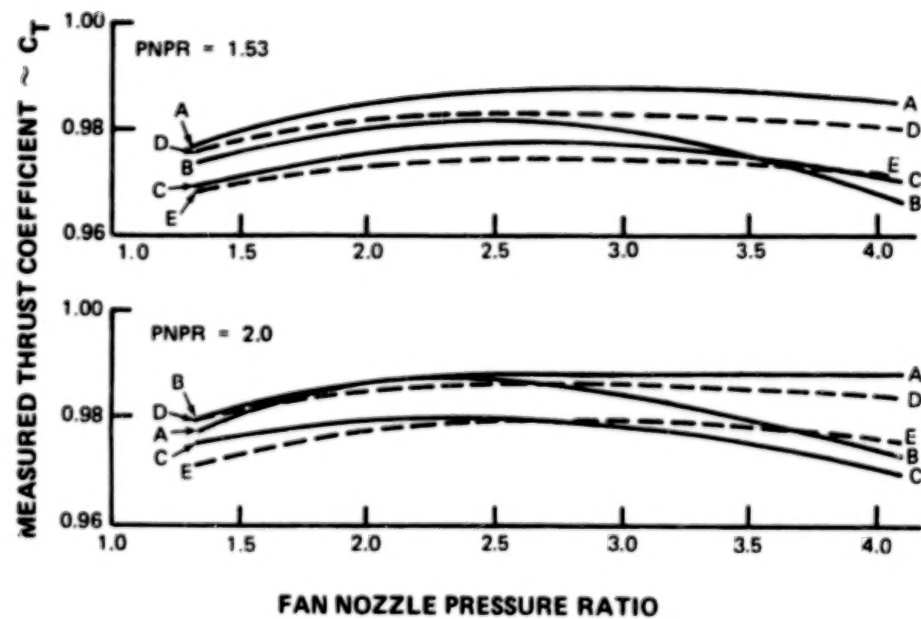


Figure 4.2-6 Comparison of Measure Thrust Coefficients

4.2.2.2 Discharge Coefficient

The fan and primary discharge coefficients are shown for each configuration at PNPR 2.0 in Figures 4.2-7 through 4.2-11 and at PNPR 1.53 in Figures 4.2-12 through 4.2-16.

The data are consistent. Fan discharge coefficients, CD_f , are compared for all models at PNPR 1.53 and 2.0 in Figure 4.2-17. CD_f increased with FNPR for all configurations to FNPR = 3.0 and was essentially flat at higher FNPR. Comparisons of PNPR = 1.53 and PNPR = 2.0 data model by model indicated that CD_f were unaffected by changes in PNPR. This suggests that the fan to primary offsets (see Figure 3.3-1) are sufficient to ensure that the primary stream does not affect CD_f .

The maximum spread in CD_f for all models is approximately 1.5 percent. This has no practical significance to the VSCE cycle since Configuration A ($CD_f = .97$ @ FNPR = 3.0, $CD_f = .96$ @ FNPR = 2.0) could be sized 1.5 percent larger to provide the same fan flow as Configurations C and E.

Primary discharge coefficients, CD_p , are compared for all configurations in Figure 4.2-18. The zero primary radius ratio configurations (A, B, and C), showed a significant decrease in discharge coefficient (flow restriction) as FNPR increased. The severity of this flow restriction increased with reduction in PNPR which was an indication that the fan stream was impinging upon the primary flow and was the cause of the restriction. The effect is largest for Configuration C, which has highest radius ratio and highest fan-primary offset.

The flow restriction is also present in the plug Configurations D and E, but to a much smaller degree. Comparison of Configurations B and D, which have the same fan radius ratio, showed that the zero primary radius ratio Configuration B showed more severe flow restriction which suggested that the problem might be offset oriented. However, comparison of Configurations A and D, which have the same offset, suggested that there may be another contributing factor. Since all models were designed with a 15 degree cowl angle, the presence of the plugs in Configurations D and E reduced the fan-primary stream interaction by reducing the fan to primary impingement angle.

It is clear that the strong primary flow restriction exhibited by Configurations B and C would result in a much higher than desired mechanical area to meet flow requirements for practical engine designs. Design modifications to improve discharge coefficients for this type of nozzle might include: (1) a significant reduction in primary cowl angle, (2) a convergent-divergent primary (3) utilization of an isentropic contour on the inner fan stream to reduce fan to primary impingement angle, (4) use of a plug primary, or (5) some combination of these approaches.

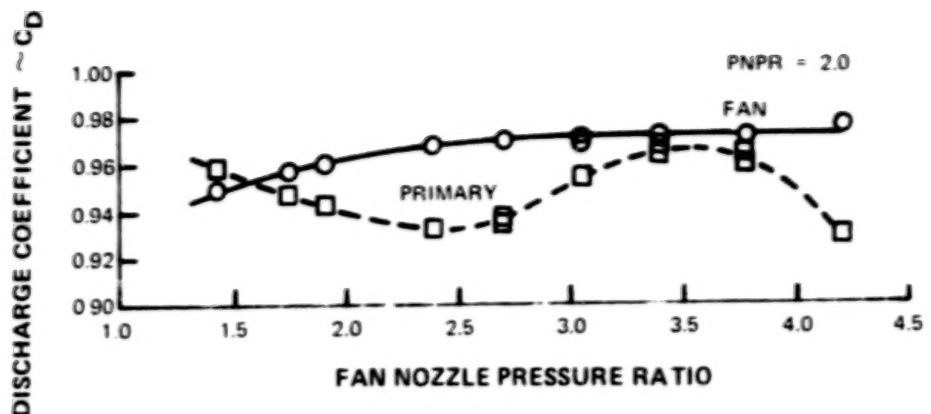


Figure 4.2-7 Nozzle Discharge Coefficients for Configuration A at PNPR 2.0

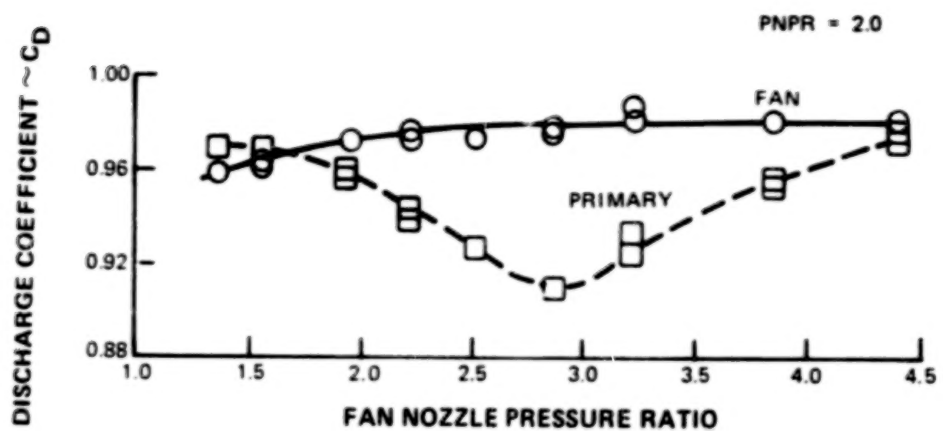


Figure 4.2-8 Nozzle Discharge Coefficients for Configuration B at PNPR 2.0

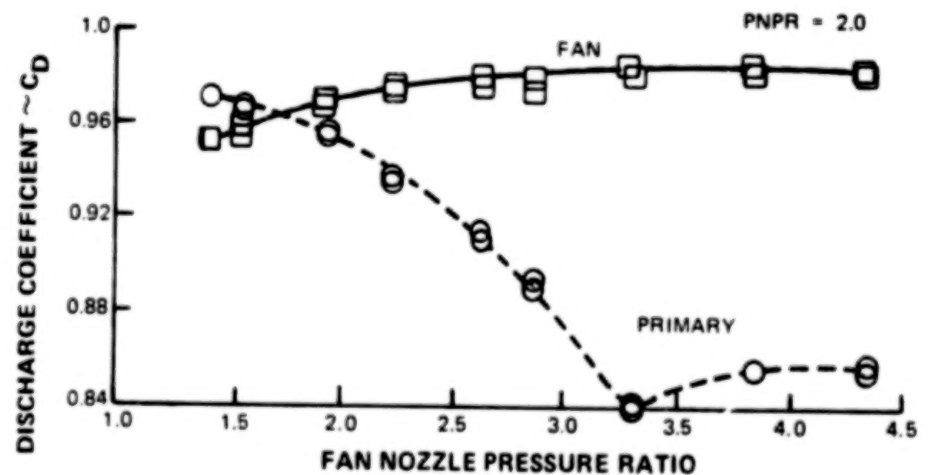


Figure 4.2-9 Nozzle Discharge Coefficients for Configuration C at PNPR 2.0

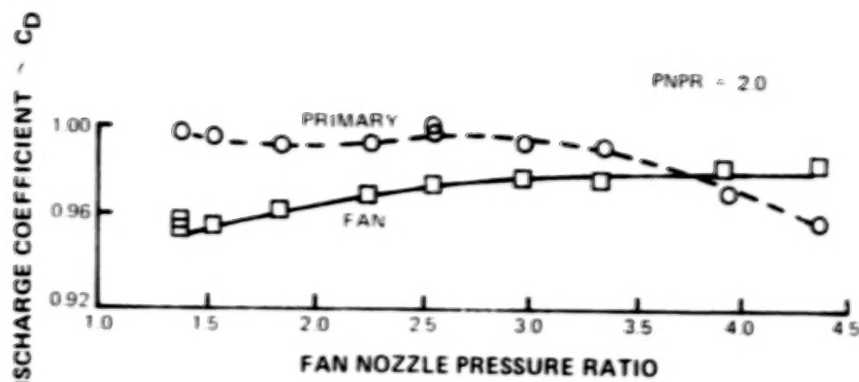


Figure 4.2-10 Nozzle Discharge Coefficients for Configuration D at PNPR 2.0

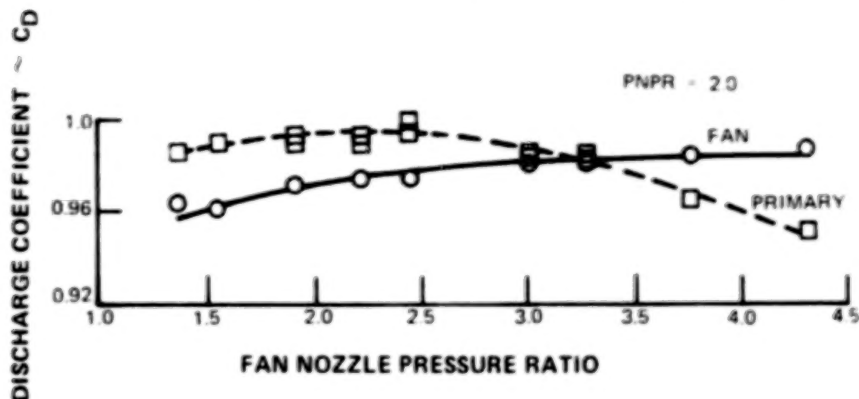


Figure 4.2-11 Nozzle Discharge Coefficients for Configuration E at PNPR 2.0

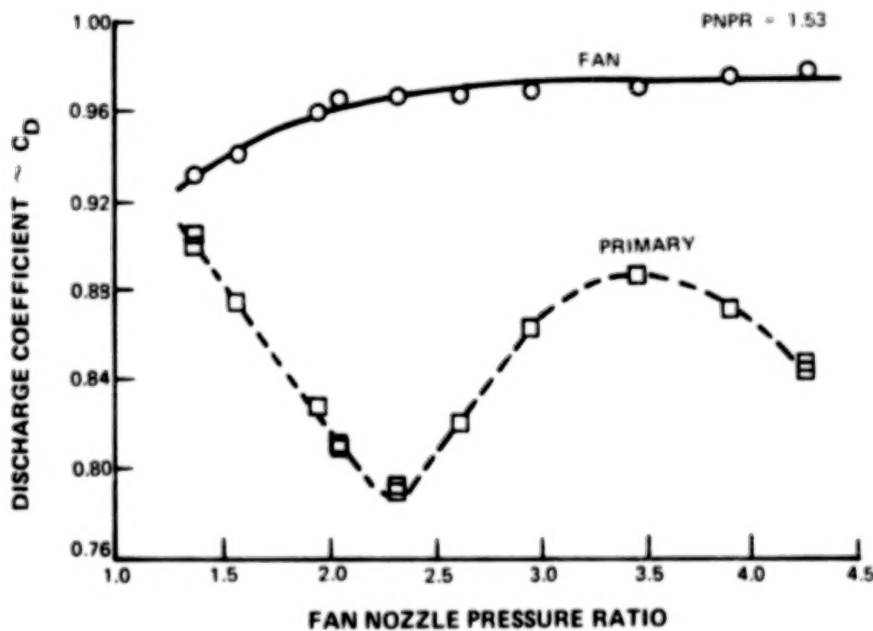


Figure 4.2-12 Nozzle Discharge Coefficient for Configuration A at PNPR 1.53

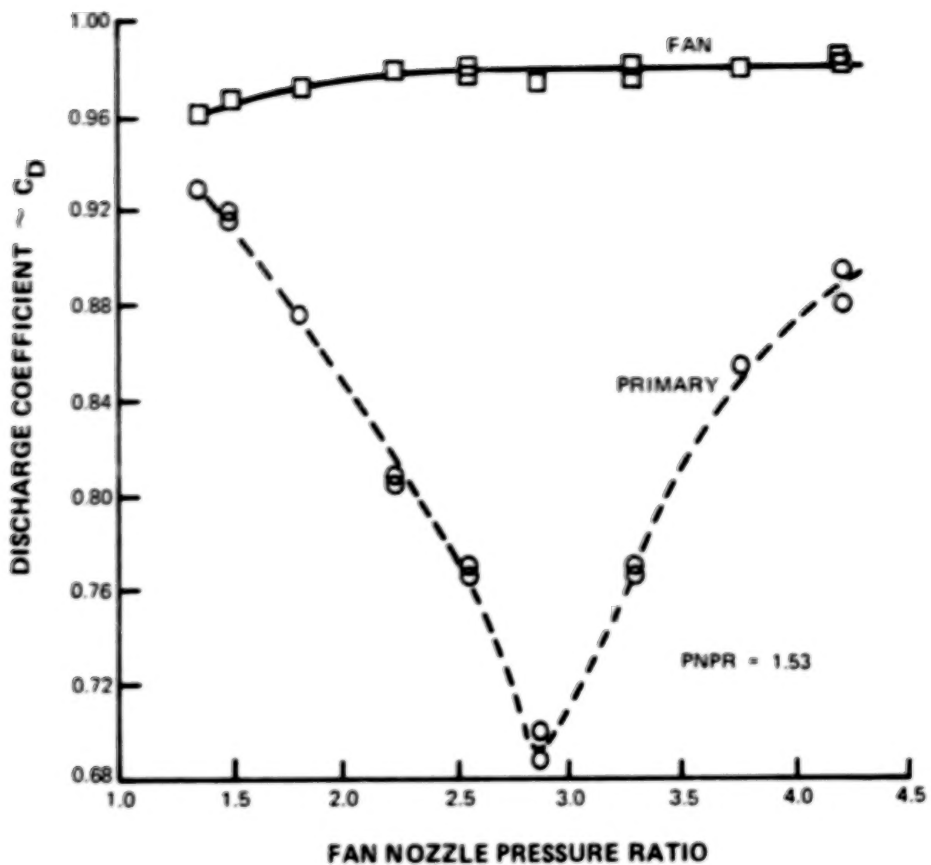


Figure 4.2-13 Nozzle Discharge Coefficients for Configuration B at PNPR 1.53

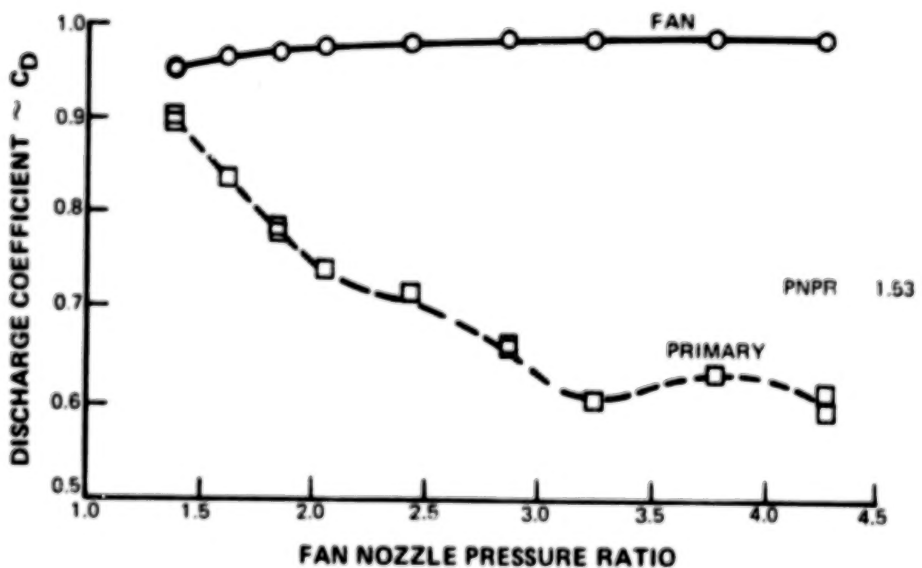


Figure 4.2-14 Nozzle Discharge Coefficients for Configuration C at PNPR 1.53

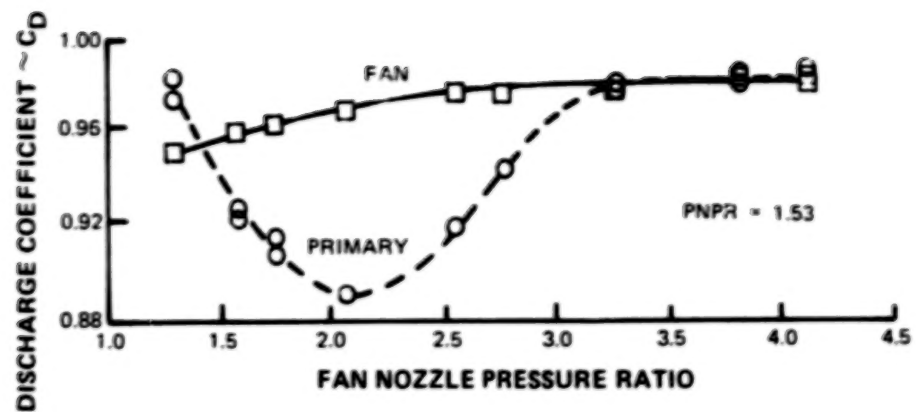


Figure 4.2-15 Nozzle Discharge Coefficients for Configuration D at PNPR 1.53

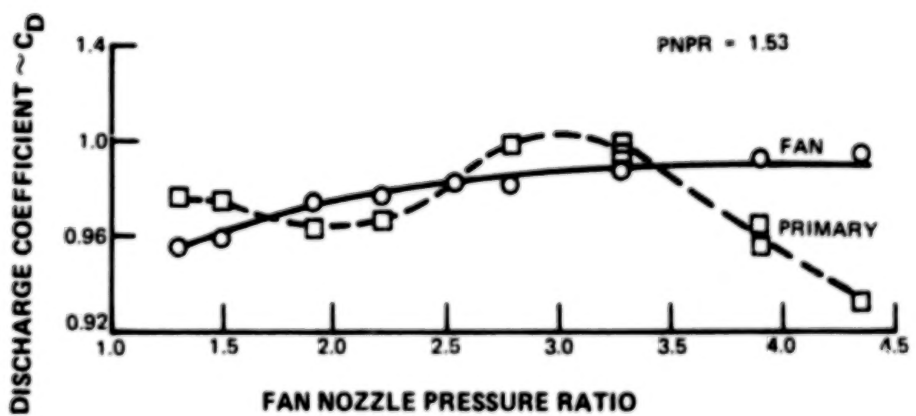


Figure 4.2-16 Nozzle Discharge Coefficients for Configuration E at PNPR 1.53

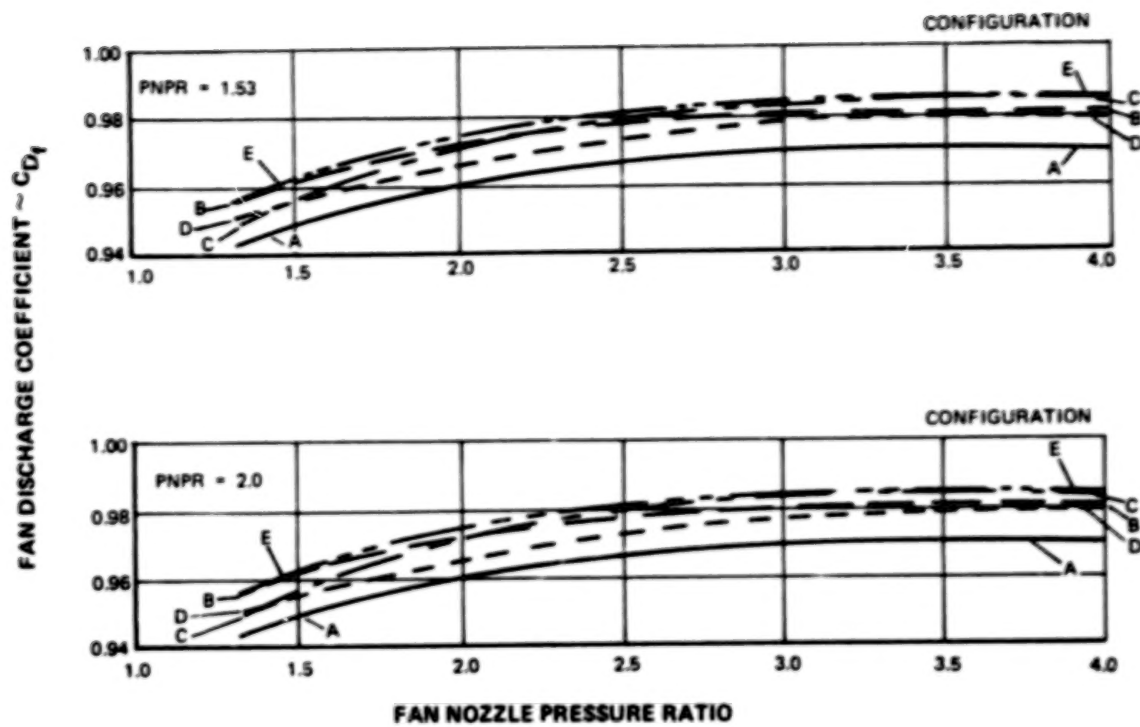


Figure 4.2-17 Comparison of Measured Fan Nozzle Discharge Coefficients

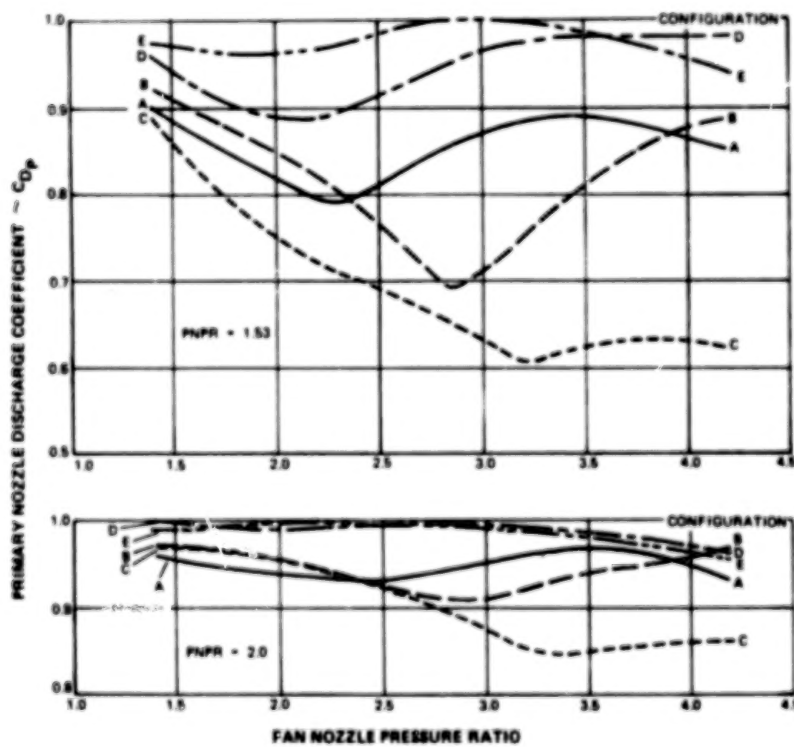


Figure 4.2-18 Comparison of Measured Primary Nozzle Discharge Coefficients

4.2.2.3 Nozzle Velocity and Temperature Profiles

Aerodynamic traverse data (total pressure, static pressure and total temperature) were obtained for each of the 16 operating conditions defined in Table 3.1-III. Fan nozzle pressure ratios ranged from 1.8 to 3.2 with a temperature range from 700°K (1260°R) to 1089°K (1960°R). Primary nozzle pressure ratios were 1.53 or 2.0 at 811°K (1460°R). Radial traverses at 5 axial stations were taken to define the nozzle discharge plume for each model as described in Section 3.1.4. The Comprehensive Data Report, Reference 19, contains all traverse data obtained in this program.

Scaled velocity profiles are shown for Configurations A, B, and D in Figures 4.2-19, 4.2-20, and 4.2-21. The profiles for Configurations A and C (lowest and highest radius ratio plugless configurations) are compared in Figure 4.2-22. Velocity and temperature profiles for Configurations C and E (high fan radius ratio, zero primary radius ratio and plug configurations) are compared in Figures 4.2-23 and 4.2-24.

As expected, all of the traverses showed a sharp distinction between the fan and primary streams at traverse stations 1 and 2. (Note that station 1 traverses do not go to the nozzle centerline because of mechanical interference between the nozzle and traverse mechanism.) At station 3, in Figure 4.2-19, the effects of stream mixing became evident as indicated by the reduction in peak velocity from station 2 to 3 (701 m/sec (2300 ft/sec) to 518 m/sec (1700 ft/sec)). The two streams have essentially merged by stations 4 and 5 where the velocity peak of 384 m/sec (1260 ft/sec) occurred at the nozzle centerline.

A comparison of the velocity profiles for the lowest and highest fan radius ratio, zero primary radius ratio configurations (Configurations A and C) are shown in Figure 4.2-22. The profile comparison indicates the effect of radius ratio on the radial location of the peak jet velocity. The peak velocity of the higher radius ratio configuration, Configuration C, tends to occur nearer the flow centerline than the peak velocity of Configuration A. This trend is observed in both the initial, unmixed portion of the coannular jet and further downstream in the merged flow region. The comparison at station 3 also indicates that the core region of high velocity flow of Configuration C is smaller than that of Configuration A. The comparison also indicates that increasing fan radius ratio reduces peak core velocity. The peak velocity observed for Configuration C is lower relative to Configuration A. This was consistent with the reduced high frequency noise measured for Configuration C in the acoustic results section 4.1.2.

The velocity profile comparison of zero primary radius ratio and plug nozzles at constant fan radius ratio (Configurations C and E) is shown in Figure 4.2-23. The comparison indicates that the zero primary radius ratio Configuration C showed the same radial inward shift of velocity peak relative to plug Configuration E as Configuration A did relative to C in the previous comparison. There does not appear to be any significant difference in the velocity peak decay rate between the plug and zero primary radius ratio Configurations C and E. This was substantiated by the acoustic results (Section 4.1.2) which indicated relatively small differences between the two configurations.

The temperature profile comparison of Configurations C and E (shown in Figure 4.2-24) indicates very small difference between the two models except at station 1. The station 2 profiles were practically identical. The stations 3, 4, and 5 temperature comparison are similar to the velocity traverse of Figure 4.2-23.

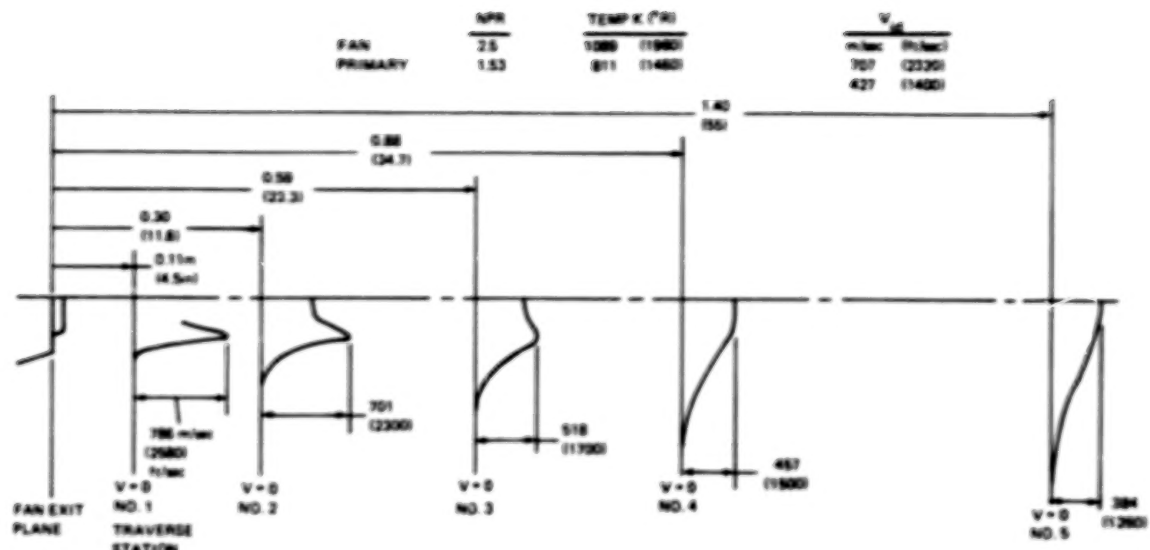


Figure 4.2-19 Configuration A Plume Traverse ~ Velocity Profile

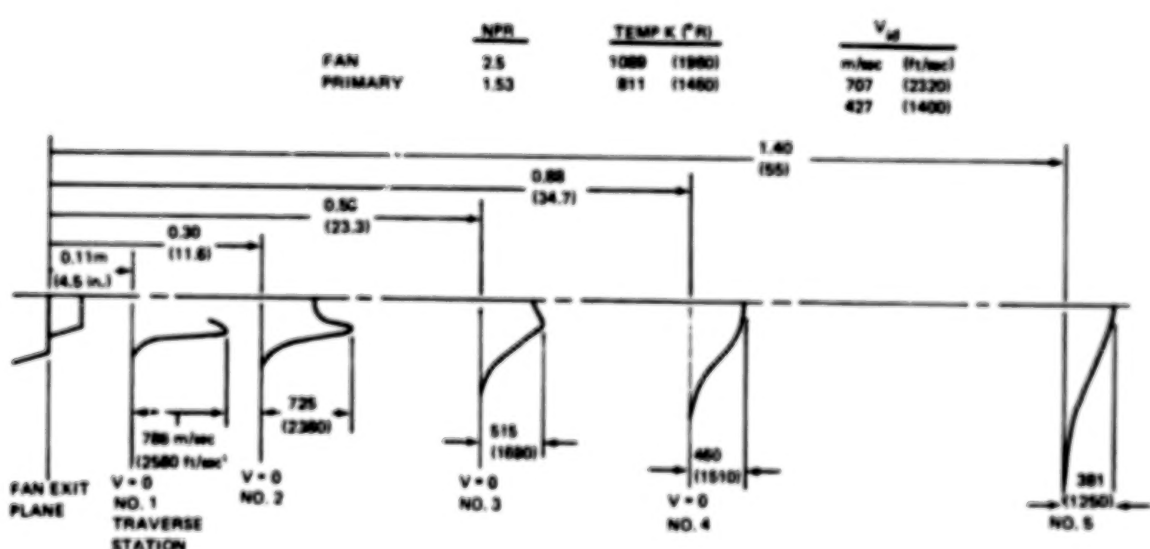


Figure 4.2-20 Configuration B Plume Traverse ~ Velocity Profile

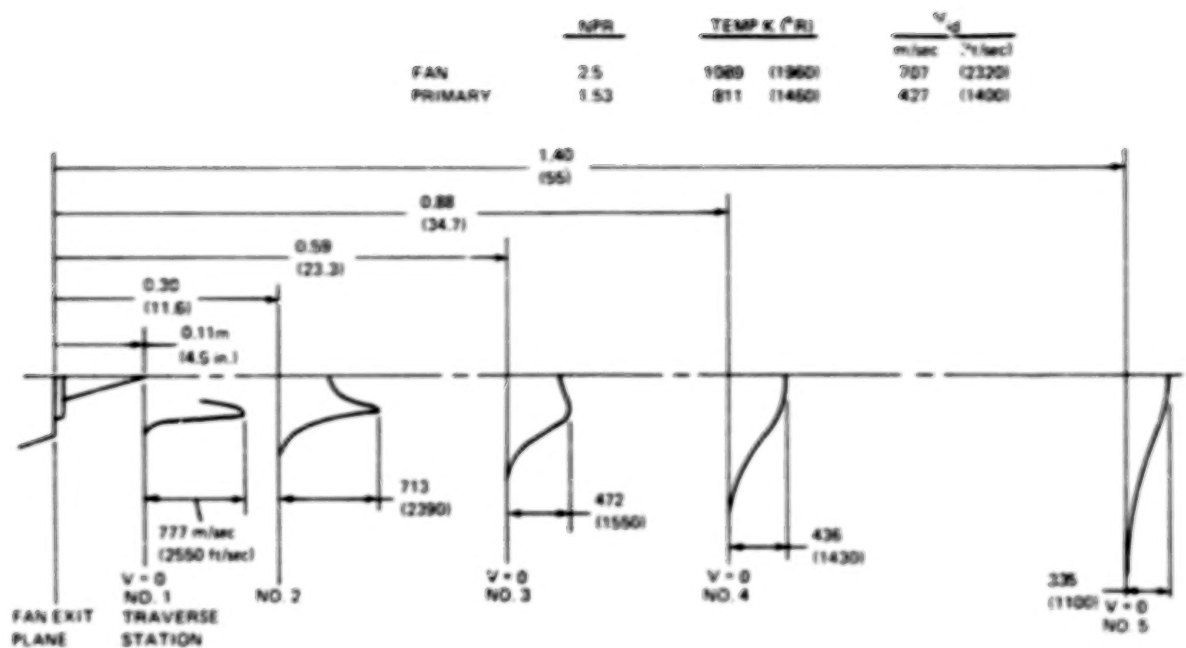


Figure 4.2-21 Configuration D Plume Traverse ~ Velocity Profile

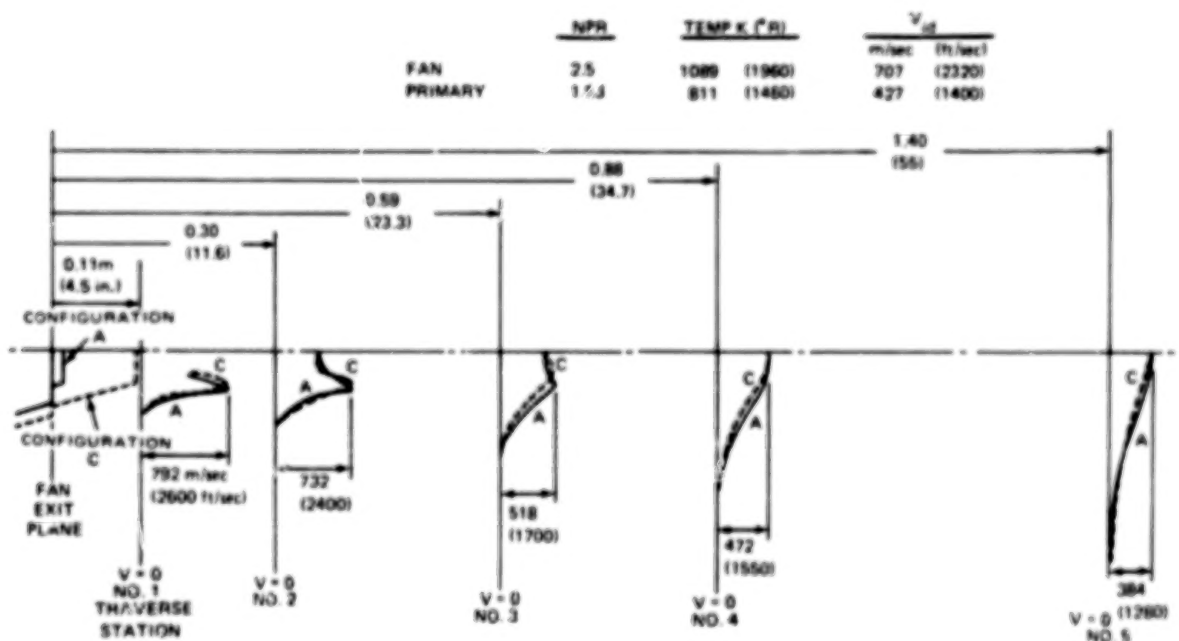


Figure 4.2-22 Plume Velocity Profile Traverse Comparison for Configurations A & C

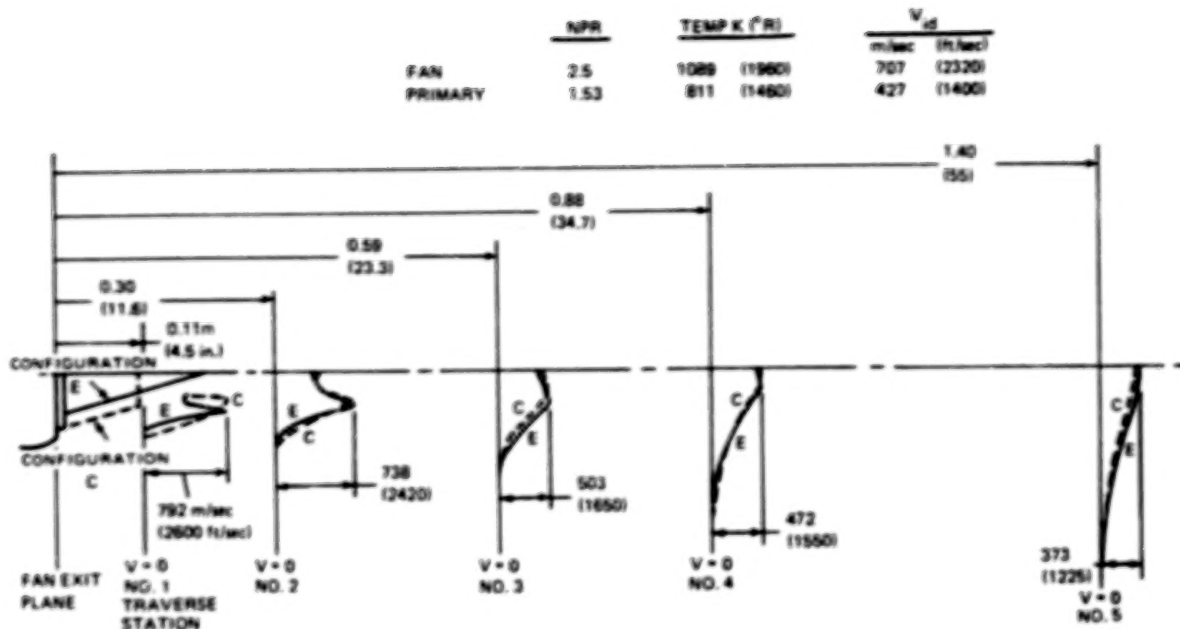


Figure 4.2-23 Plume Velocity Profile Traverse Comparison for Models C & E

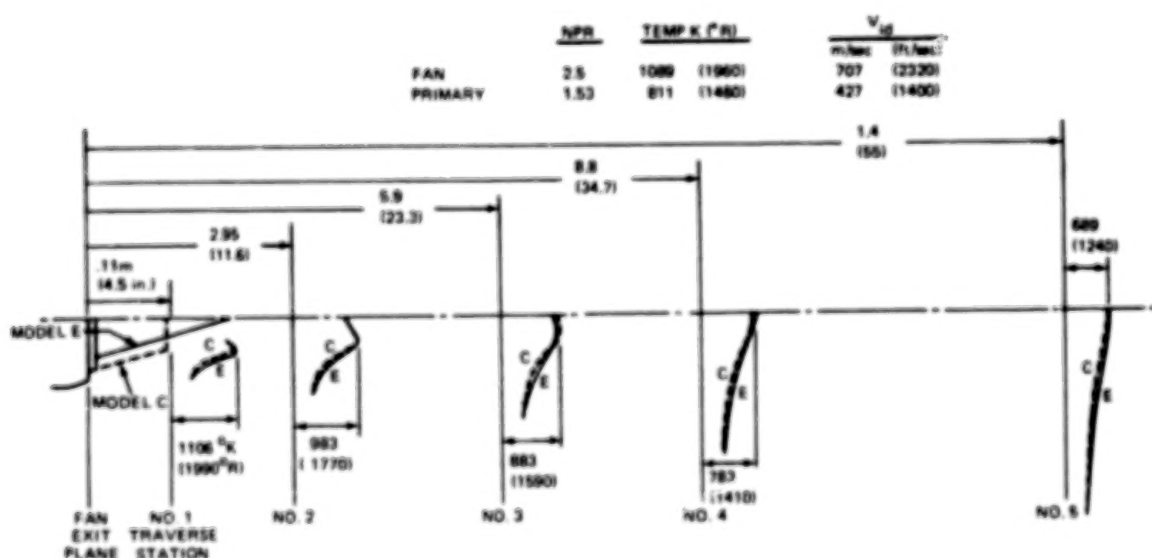


Figure 4.2-24 Plume Temperature Profile Comparison for Models C & E

**AERODYNAMIC AND ACOUSTIC
INVESTIGATION OF INVERTED VELOCITY
PROFILE COANNULAR EXHAUST NOZZLE
MODELS AND DEVELOPMENT OF
AERODYNAMIC AND ACOUSTIC
PREDICTION PROCEDURES**

TABLE OF CONTENTS

		<i>Page</i>
SECTION 1.0	SUMMARY	1 1/A12
SECTION 2.0	INTRODUCTION	3 1/A14
	2.1 Background	3 1/A14
	2.2 Program Description	4 1/B1
	2.2.1 Test Matrices	5 1/B2
	2.2.2 Test Program Description	5 1/B2
	2.2.3 Aerodynamic and Acoustic Prediction Procedure	6 1/B3
SECTION 3.0	APPARATUS – MODEL TEST AND TEST FACILITIES	7 1/B4
	3.1 Jet Noise Test Facility (X-206 Stand)	7 1/B4
	3.1.1 Test Chamber	7 1/B4
	3.1.2 Acoustic Data Acquisition System	10 1/B7
	3.1.3 Pressure and Temperature Instrumentation	10 1/B7
	3.1.3.1 Nozzle Operating Condition Instrumentation	10 1/B7
	3.1.3.2 Nozzie Exhaust Plume Traverse Instrumentation	12 1/B10
	3.1.3.3 Exhaust Plume Traverse System Description	12 1/B10
	3.1.3.4 Data Acquisition Equipment	15 1/B13
	3.1.4 Acoustic Test Matrix	15 1/B13
	3.1.5 Test Procedure	19 1/C6
	3.2 UTRC Large Nozzle Thrust Facility	19 1/C6
	3.2.1 System Description	19 1/C6
	3.2.2 Instrumentation	20 1/C7
	3.2.3 Facility Thrust Balance Calibration	21 1/C8
	3.2.4 Aerodynamic Performance Test Matrix	23 1/C10
	3.3 Nozzle Models	24 1/C11
	3.3.1 Configuration Selection	24 1/C11
	3.3.2 Model Designs	26 1/C13
SECTION 4.0	TEST DATA	31 1/D4
	4.1 Acoustic Data	31 1/D4
	4.1.1 Acoustic Data Reduction	31 1/D4
	4.1.1.1 Theoretical Day SPL (Model)	32 1/D5
	4.1.1.2 Scaled Engine Data	35 1/D10
	4.1.1.3 Calculation of Acoustic Power Levels	36 1/D11
	4.1.2 Acoustics Results and Discussion	37 1/D12
	4.1.2.1 Comparison of Convergent Nozzle Data With SAE Predictions	38 1/D13
	4.1.2.2 Unsuppressed Coannular Nozzle Results	39 1/D14
	4.1.2.3 Definition of the Acoustic Characteristics of a Single Stream Plug Nozzle	54 1/F1

TABLE OF CONTENTS (Cont'd)

		Page
	4.1.2.4 Definition of the Acoustic Characteristics of a Coannular Nozzle with Primary Flow Leakage	57 1/F4
4.2 Aerodynamic Data		61 1/F8
	4.2.1 Aerodynamic Data Reduction	61 1/F8
	4.2.1.1 Thrust and Discharge Coefficient Data Reduction	61 1/F8
	4.2.1.2 Traverse Data Reduction	64 1/F11
4.2.2 Aerodynamic Results and Discussion		64 1/F11
	4.2.2.1 Thrust Coefficient	64 1/F11
	4.2.2.2 Discharge Coefficient	70 1/G4
	4.2.2.3 Nozzle Velocity and Temperature Profiles	76 1/G10
SECTION 5.0	ACOUSTIC ENGINEERING PREDICTION PROCEDURE	81 2/A5
	5.1 General Approach	81 2/A5
	5.1.1 Description of the Acoustic Data Base	81 2/A5
	5.1.2 Definition of Spectral Decomposition	84 2/A8
	5.1.3 Definition of Acoustic Models Used in Developing the Prediction Procedure	90 2/A14
	5.1.4 Definition of Characteristic Velocity, Temperature, and Area for Initial and Merged Regions	91 2/B1
5.2 Static Jet Exhaust Noise Prediction Procedure		93 2/B3
	5.2.1 Development of Mixing Noise Data Correlations	93 2/B3
	5.2.1.1 Merged Region Mixing Noise	98 2/B8
	5.2.1.2 Initial Region Mixing Noise	109 2/C5
	5.2.2 Development of Shock Noise Data Correlations	117 2/C13
	5.2.2.1 Development of Fan Stream Shock Noise Data Correlations	117 2/C13
	5.2.2.2 Development of Primary Stream Shock Noise Data Correlations	125 2/D7
5.3 Flight Jet Exhaust Noise Prediction Procedure		130 2/D12
	5.3.1 General Background	130 2/D12
	5.3.2 Definition of the Effect of Flight on Mixing Noise	132 2/D14
	5.3.2.1 Definition of the Effect of Flight on the Low Frequency Mixing Noise Component	134 2/E2
	5.3.2.2 Definition of the Effect of Flight on the High Frequency Mixing Noise Component	136 2/E4
	5.3.3 Definition of the Effect of Flight on the Shock Noise Component	138 2/E6

TABLE OF CONTENTS (Cont'd)

	Page	
5.4 Summary of Acoustic Prediction Procedure	139	2/E7
5.4.1 General Approach	139	2/E7
5.4.2 Summary of the Static Acoustic Prediction Procedure	140	2/E8
5.4.2.1 Low Frequency Mixing Noise Component	140	2/E8
5.4.2.2 High Frequency Mixing Noise Component	141	2/E9
5.4.2.3 Fan Stream Shock Noise	142	2/E10
5.4.2.4 Primary Stream Shock Noise	143	2/E11
5.4.3 Summary of the Flight Acoustic Prediction Procedure	144	2/E12
5.4.3.1 Low Frequency and High Frequency Mixing Noise Components	145	2/E13
5.4.3.2 Fan Stream and Primary Stream Shock Noise Components	145	2/E13
5.5 Sample Calculation	146	2/E14
5.5.1 Inputs Required for the Acoustic Prediction	147	2/F1
5.5.2 Prediction of the Static Jet Exhaust Noise	147	2/F1
5.5.2.1 Low Frequency Mixing Noise	147	2/F1
5.5.2.2 High Frequency Mixing Noise	148	2/F2
5.5.2.3 Fan Stream Shock Noise	149	2/F3
5.5.2.4 Primary Stream Shock Noise	149	2/F3
5.5.3 Prediction of the Flight Jet Exhaust Noise	151	2/F5
5.5.3.1 Low Frequency and High Frequency Mixing Noise Components	151	2/F5
5.5.3.2 Fan Stream and Primary Stream Shock Noise Components	151	2/F5
5.6 Comparison of Data with Predictions Using the Acoustic Prediction Procedure	152	2/F6
5.6.1 Comparison of IVP Coannular Nozzle Noise Predictions with Measured Data	153	2/F7
5.6.2 Analysis of the Accuracy of the Prediction Procedure	165	2/G5
SECTION 6.0	STATIC AERODYNAMIC PERFORMANCE PREDICTION PROCEDURE	
6.1 Approach	167	2/G7
6.1.1 Subsonic and Supersonic Nozzle Loss Mechanisms	167	2/G7
6.1.2 Prediction Procedure Concept	167	2/G7
6.2 Viscous Losses	168	2/G8
6.2.1 Internal Duct Loss	168	2/G8
6.2.2 External Scrubbing Loss	170	2/G10
6.2.3 Correlation of Subsonic Model Performance	171	2/G11

TABLE OF CONTENTS (Cont'd)

	Page
6.3 Shock Loss	172 2/G12
6.3.1 Plug Nozzle Operating Characteristics	172 2/G12
6.3.2 Off-Design Shock Loss	173 2/G13
6.4 Application of the Aerodynamic Performance Prediction Procedure	176 3/A6
6.4.1 Procedural Steps and Input Requirements	176 3/A6
6.4.2 Numerical Example of the Procedure Use	179 3/A9
6.5 Evaluation of the Static Aerodynamic Performance Prediction Procedure	182 3/A12
 SECTION 7.0	
SUMMARY OF RESULTS AND CONCLUSIONS	187 3/B3
7.1 Acoustic Results and Conclusions	187 3/B3
7.1.1 Acoustic Prediction Procedure	187 3/B3
7.1.2 Acoustic Test Results	188 3/B4
7.2 Aerodynamic Performance Results and Conclusions	188 3/B4
7.2.1 Static Aerodynamic Performance Prediction Procedure	188 3/B4
7.2.2 Aerodynamic Performance Test Results	189 3/B5
7.3 Prediction System Accuracy	190 3/B6
 APPENDIX A	191 3/B7
 APPENDIX B	205 3/D5
 LIST OF SYMBOLS	211 3/D11
 REFERENCES	214 3/D14

SECTION 5.0

ACOUSTIC ENGINEERING PREDICTION PROCEDURE

A jet exhaust noise engineering prediction procedure for inverted velocity profile (IVP) coannular jets was developed during this program and is presented in this section. With this prediction procedure, the IVP coannular jet noise spectrum is decomposed into four components: a low frequency mixing noise component, a high frequency mixing noise component, and inner-stream and outer-stream shock noise components. The high frequency mixing noise component is generated in the *initial region* of the IVP coannular nozzle aerodynamic flow in which the fan and primary mixing layers develop independently. The low frequency mixing noise component is generated in the *merged region* of the flow in which the fan and primary mixing layers have merged. Shock noise is generated by the passage of turbulent eddies through the flow shock structure and is generated if either the fan stream or primary stream is supersonic. Data correlations were developed for each noise component for both static and flight conditions.

In Section 5.1, the general approach used in developing the prediction procedure is described. The static prediction procedure is described in Section 5.2, and in Section 5.3 the effects of flight are described. Section 5.4 contains a flow chart using the prediction procedure, and Section 5.5 contains a sample calculation using the prediction procedure. Sample predictions using the prediction procedure are shown in Section 5.6 along with a description of the accuracy and limitations of the empirical prediction procedure. The normalized data plots developed during this program are contained in the Comprehensive Data Report (Reference 19).

5.1 GENERAL APPROACH

Acoustic tests of IVP coannular nozzles were conducted over a wide range of nozzle geometries and operating conditions. This data base was used to develop the acoustic empirical prediction system. In the following sections, the data base is defined and the method is described for decomposing the total noise spectrum into its four components. Noise generation models are then developed for each noise component.

The following topics are described in this section: definition of the acoustic data base; definition of the spectral decomposition; definition of the acoustic models used in developing the prediction procedure; and definition of the characteristic velocity, temperature, and area for the initial and the merged regions.

5.1.1 Description of the Acoustic Data Base

The data base consisted of data obtained during three NASA-sponsored programs: NAS3-17866 (References 7, 8, 9, 10), NAS3-18008 (References 11, 12), and NAS3-20061 (present program). Table 5.1-I contains a summary of the nozzles and operating conditions tested in each program. Coannular nozzles, with slight primary extensions, without center plugs were tested in References 7, 8, 9 and 10. These nozzles had fan to primary area ratios of 0.75 and 1.20. The 0.75 area ratio nozzle had a fan radius ratio of 0.79 and a primary radius ratio of zero, and the 1.20 area ratio nozzle had a fan radius ratio of 0.72 and a primary radius ratio

of zero. These nozzles were tested statically over a range of operating conditions, including variations in fan to primary velocity ratio between 1.03 and 2.80 and variations in fan to primary temperature ratio between 0.36 and 2.76. In addition to the static tests, the nozzles also were tested in a free jet wind tunnel to simulate flight velocities up to 129.5 m/sec (425 ft/sec). Two nozzles were tested in References 11 and 12. Both nozzles had a fan to primary area ratio of 0.65 and the same total area; one, however, had coplanar fan and primary nozzles while the other had a plug in the primary nozzle and a fan-primary exit plane separation. The coplanar nozzle had a fan radius ratio of 0.78 and a primary radius ratio of zero while the second nozzle had a fan radius ratio of 0.91 and a primary radius ratio of 0.69. In References 11 and 12 most test conditions were set with fan to primary velocity ratios of either 1.50 or 2.00, and fan to primary temperature ratios ranged between 0.8 and 1.96. Five additional nozzles were tested as part of the present program. All nozzles had a fixed area ratio of 1.48 and the same total area. Three of the nozzles had a fixed primary radius ratio of zero (no plug) but different fan radius ratios of 0.69, 0.75, 0.83. The other two nozzles contained plugs in the primary stream; one had a fan radius ratio of 0.75 and a primary radius ratio of 0.60 while the other had a fan radius ratio of 0.83 and a primary radius ratio of 0.81. In the present program, nozzle operating conditions were varied parametrically with fan to primary velocity ratios between 1.07 and 2.00 and temperature ratios between 0.86 and 1.34.

TABLE 5-1-4
SUMMARY OF NOZZLE PARAMETERS AND OPERATING
CONDITIONS IN THE DATA BASE

Configuration	A _T Total	Fan-Pri Area Ratio	Fan Radius Ratio	Pri Radius Ratio	Fan-Pri Velocity Ratio	Fan-Pri Temperature Ratio
References 7, 8 (NASA Contract NAS3-17866) Static Test						
0.75 Coannular	0.0126 m ² (0.136 ft ²)	0.75	0.79	0	1.03 - 2.80	0.36 - 2.76
1.20 Coannular	0.0126 m ² (0.136 ft ²)	1.20	0.72	0		
References 9, 10 (NASA Contract NAS3-17866) Flight Test						
0.75 Coannular	0.0057 m ² (0.0618 ft ²)	0.75	0.79	0	1.00 - 2.10	1.00 - 3.20
1.20 Coannular	0.0057 m ² (0.0618 ft ²)	1.20	0.72	0		
References 11, 12 (NASA Contract NAS3-18008)						
0.65 Coplanar	0.0183 m ² (0.197 ft ²)	0.65	0.79	0	1.5 and	0.80 - 1.96
0.65 Plug	0.0183 m ² (0.197 ft ²)	0.65	0.90	0.66	2.0	
Present Program (Contract NAS3-20061)						
Model A	0.0126 m ² (0.136 ft ²)	1.48	0.69	0		
Model B	0.0126 m ² (0.136 ft ²)	1.48	0.75	0		
Model C	0.0126 m ² (0.136 ft ²)	1.48	0.83	0	1.07 - 2.00	0.86 - 1.34
Model D	0.0126 m ² (0.136 ft ²)	1.48	0.75	0.60		
Model E	0.0126 m ² (0.136 ft ²)	1.48	0.83	0.81		

Since the data base consisted of data from three different programs and test facilities, the consistency of the data base must be established. Convergent nozzle data from References 7, 8, 9, and 10 and the present program can be compared directly because identical reference convergent nozzle operating conditions were used and both contracts were conducted by Pratt & Whitney Aircraft. Figure 5.1-1 presents a comparison of the data at the peak noise angle from the static jet noise facilities used in these two programs. Agreement between the two sets of data is within approximately 1.0 dB at the spectral peaks. Data from References 11 and 12, which were obtained by the General Electric Corporation, cannot be compared directly with data from the other two programs because identical convergent nozzle operating conditions were not available from this contract and the other two obtained by Pratt & Whitney Aircraft. The data can be assessed, however, by comparing measured convergent nozzle data from all three contracts with SAE predictions (Reference 23) for the same operating conditions. Figure 5.1-2 contains a comparison of the measured and predicted peak SPL at the peak noise angle for these three test programs. Data from References 7, 8, 11, and 12 and the present program are consistent with each other and with the SAE predictions, while data from References 9 and 10 are approximately 2.0 dB higher than the SAE predictions. A similar trend was observed at other angles. The data from References 11 and 12 were consistently higher than the SAE predictions and higher than the data from the other two programs; therefore, a correction factor (2.0 dB) was subtracted from the former data set.

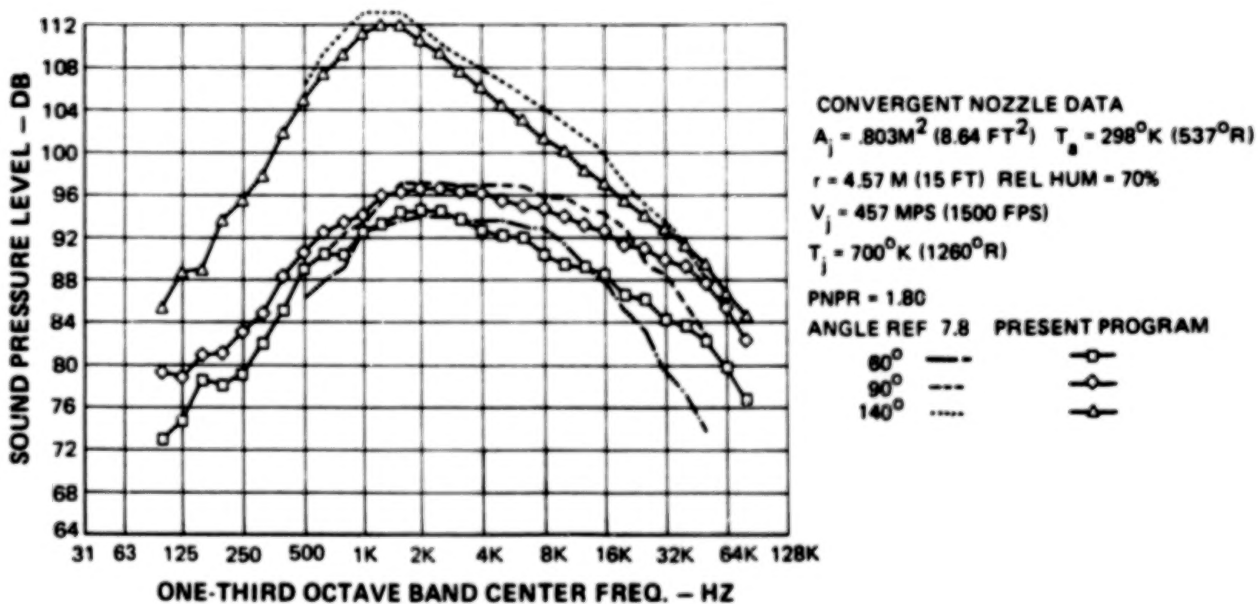


Figure 5.1-1 Comparison of Convergent Nozzle SPL Spectra from the Present Program and References 7 and 8

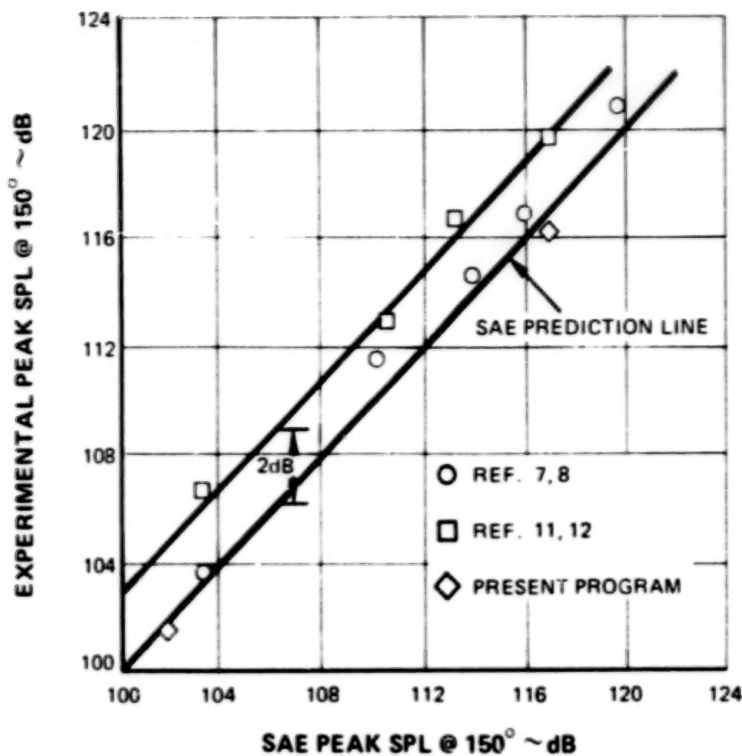


Figure 5.1-2 Comparison of SAE Predictions with Measured SPL Spectra from References 7, 8, 11 and 12 and the Present Program

5.1.2 Definition of Spectral Decomposition

A typical spectrum produced by an IVP coannular jet is illustrated in Figure 5.1-3. It contains a shock noise component and a broad, often double peaked, jet mixing noise component. The shock noise component was present only if the fan stream or primary stream was supersonic and is discussed in Section 5.2.2. Shock noise is produced by the convection of turbulent eddies through the shock structure of either a supersonic fan stream or primary stream (Reference 24). The mixing noise portion of the spectrum is generated by aerodynamic quadrupoles in the fan and primary jet shear layers and is discussed in Section 5.2.1.

A typical aerodynamic flow that generates the type of acoustic spectrum described in the preceding paragraph is illustrated in Figure 5.1-4. In Figure 5.1-4, the peak mean velocity is plotted as a function of axial distance from the fan nozzle exit plane. The aerodynamic flow can be divided into two regions: an *initial region*, in which the fan mixing layer and primary mixing layer develop independently, and a *merged region*, in which the individual character of the two mixing layers is lost. The initial and merged regions are both characterized by a region of constant velocity followed by a region of rapid velocity decay. The large difference between the peak mean velocity in the initial and merged regions suggests that the high and low frequency portions of the mixing noise spectrum should be analyzed separately in terms of the parameters characteristic of each region of the flow. Consequently, the mixing noise produced by an IVP coannular nozzle was divided into two components: one generated by the initial region and one generated by the merged region.

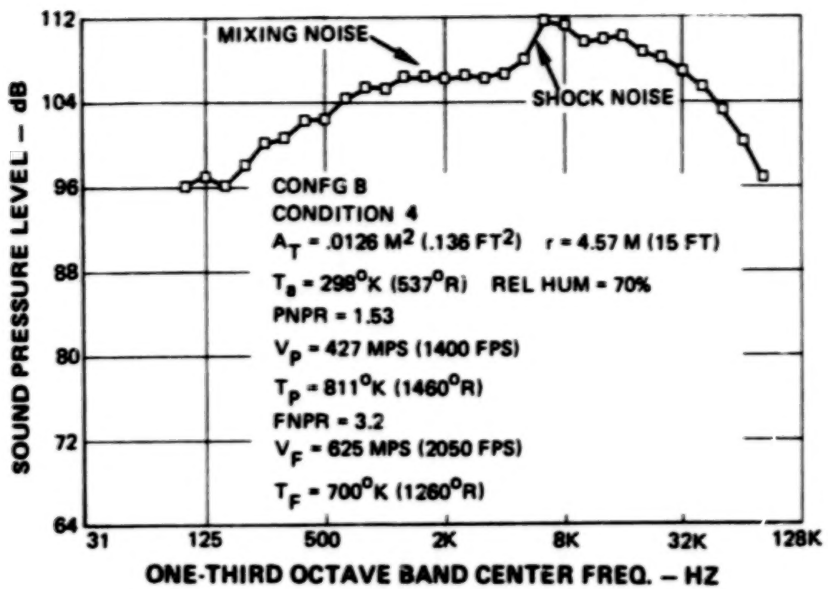


Figure 5.1-3 *Typical Inverted Velocity Profile Coannular Nozzle SPL Spectra at 90 Degrees*

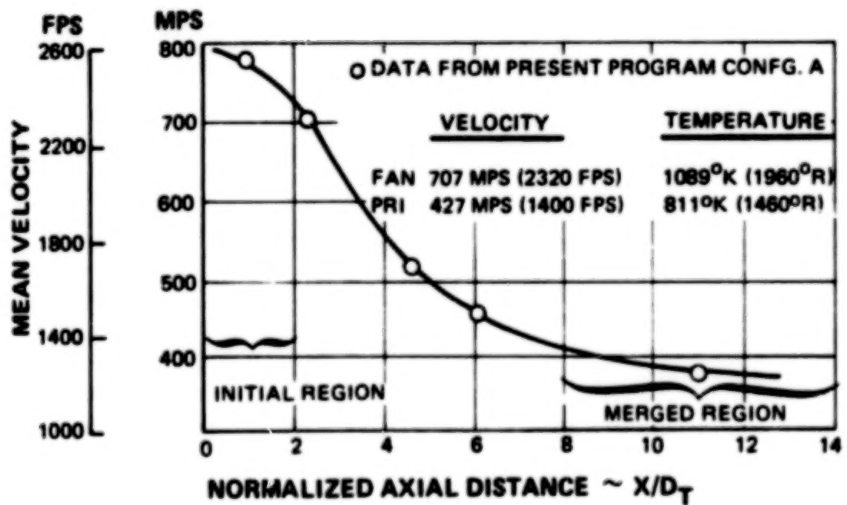


Figure 5.1-4 *Peak Mean Velocity Decay of an Inverted Velocity Profile Coannular Nozzle*

Since the velocity and turbulence levels in the shear layer between the fan flow and ambient air are greater than the corresponding levels in the shear layer between the fan flow and primary flow, the fan shear layer is the dominant source of mixing noise in the initial region. High frequency mixing noise is generated in the fan shear layer close to the nozzle exit plane and low frequency mixing noise is generated in the shear layer of the merged region further downstream. Therefore, the initial region can be associated with the high frequency mixing noise component, and the merged region can be associated with the low frequency mixing noise component. This correspondence is illustrated in Figure 5.1-5.

Shock noise is also produced by the aerodynamic flow if the fan stream or the primary stream is supersonic. Therefore, there are, in general, four noise components that comprise an inverted velocity profile coannular nozzle noise spectrum. These include a high frequency mixing noise component, a low frequency mixing noise component, a fan stream shock noise component, and a primary stream shock noise component.

The procedure used to divide a measured IVP coannular nozzle noise spectrum into the different components consisted of: (1) to inspect the spectrum to identify a fan stream or primary stream shock noise component and, if present, logarithmically subtract it from the total measured noise using the shock noise spectral shape obtained from convergent nozzle data; and (2) to divide the resulting mixing noise spectrum into high frequency and low frequency noise components using a mixing noise spectral shape obtained from convergent nozzle data. The mixing components were separated by first determining the dominant component (e.g., if the low frequency levels dominate the spectrum, the merged noise component is the dominant component) and then logarithmically subtracting the dominant mixing noise component from the total mixing noise component to define the other mixing noise component.

An example of this decomposition process is illustrated in Figure 5.1-6. In the total noise spectrum in Figure 5.1-6a, there was only one shock noise component because only the fan stream was supersonic ($FNPR = 2.5$). The shock noise component was first logarithmically subtracted from the total noise spectrum, assuming the shock noise spectrum shape was the same as that produced by a single stream convergent nozzle (see Section 5.2.2). This procedure results in the definition of the shock noise component and mixing noise component, which are illustrated in Figure 5.1-6b. Since the resulting mixing noise spectrum in Figure 5.1-6b was dominated by the high frequency noise component, this component was inserted into the spectrum, as illustrated in Figure 5.1-6c, and the low frequency noise component was defined by logarithmically subtracting the high frequency mixing noise component from the total mixing noise spectrum. This procedure results in the two mixing noise components illustrated in Figure 5.1-6d. The process of defining one mixing noise component by logarithmically subtracting the other mixing noise component from the total mixing noise spectrum ensured that the logarithmic sum of the shock noise and mixing noise components would reproduce the original total noise spectrum. When one of the shock noise or mixing noise components did not dominate the total noise spectrum, the decomposition procedure was iterated until noise components were obtained which, when logarithmically added, reproduced the original noise spectrum. In Figure 5.1-6e, the logarithmic sum of the three noise components is compared with the original data contained in Figure 5.1-6a.

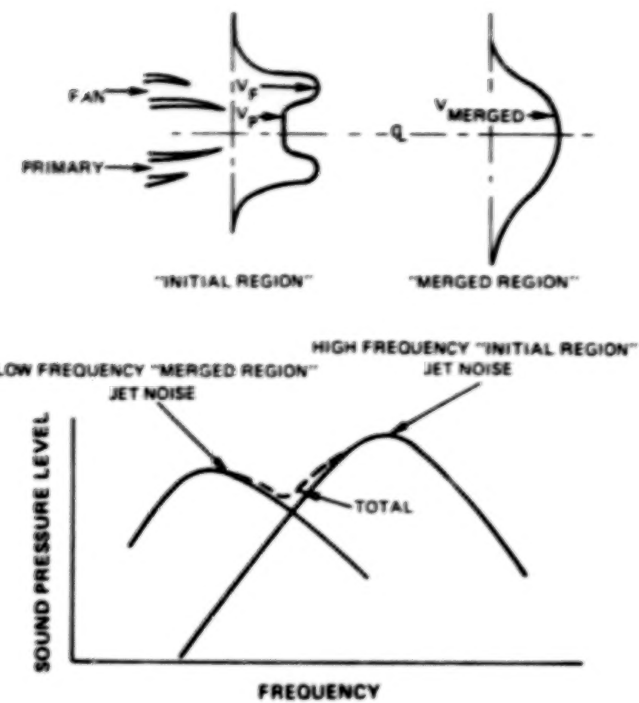


Figure 5.1-5 Physical Basis of the Prediction Procedure for the Mixing Noise Components of the SPL Spectrum

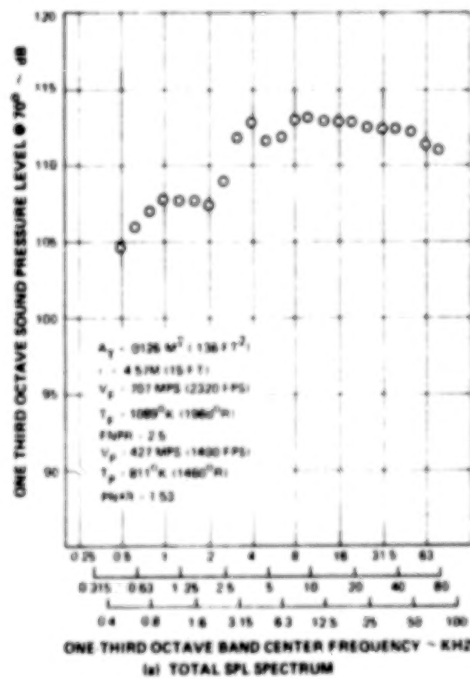
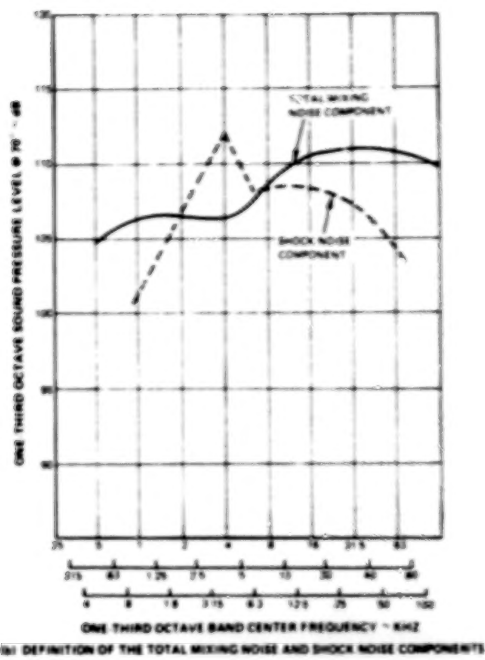


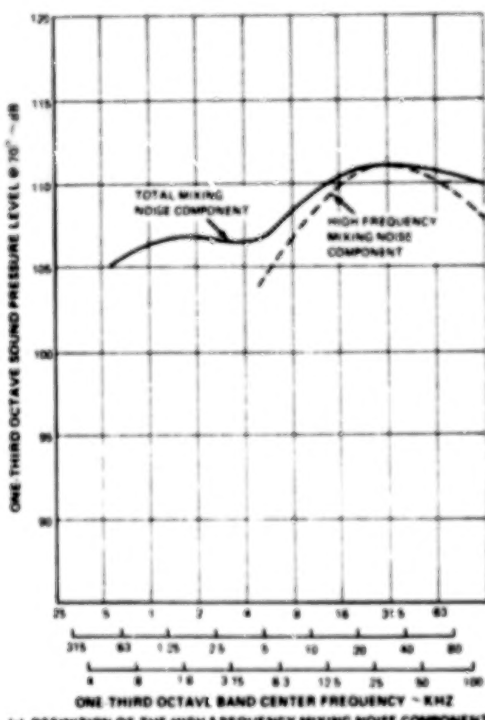
Figure 5.1-6 Example of the Procedure Used to Decompose a Total Noise Spectrum Into the High Frequency Mixing Noise, Low Frequency Mixing Noise, and Shock Noise Components



(a) DEFINITION OF THE TOTAL MIXING NOISE AND SHOCK NOISE COMPONENTS

Figure 5.1-6

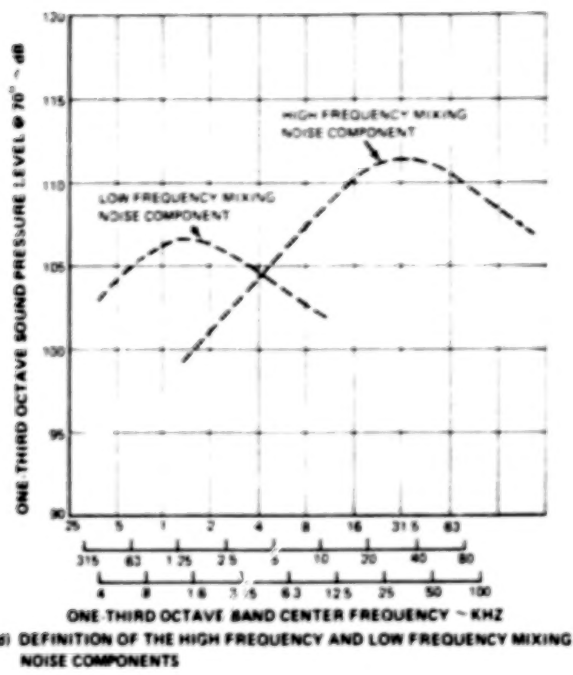
Example of the Procedure Used to Decompose a Total Noise Spectrum Into the High Frequency Mixing Noise, Low Frequency Mixing Noise, and Shock Noise Components (Cont'd)



(b) DEFINITION OF THE HIGH FREQUENCY MIXING NOISE COMPONENTS

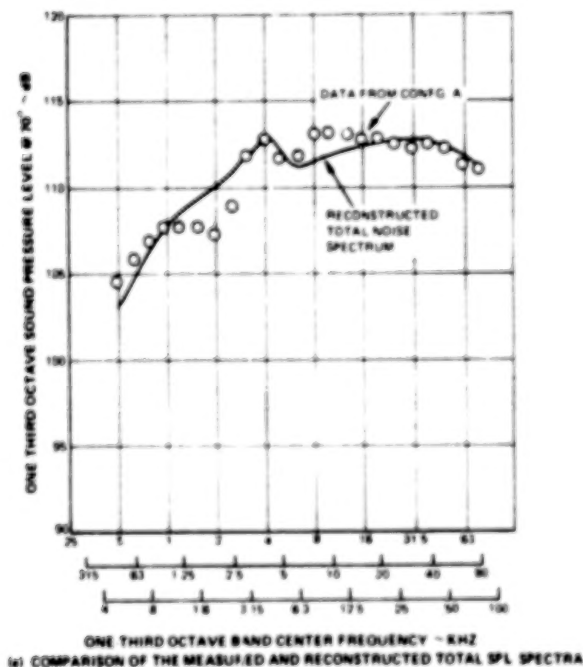
Figure 5.1-6

Example of the Procedure Used to Decompose a Total Noise Spectrum Into the High Frequency Mixing Noise, Low Frequency Mixing Noise, and Shock Noise Components (Cont'd)



(d) DEFINITION OF THE HIGH FREQUENCY AND LOW FREQUENCY MIXING NOISE COMPONENTS

Figure 5.1-6 Example of the Procedure Used to Decompose a Total Noise Spectrum Into the High Frequency Mixing Noise, Low Frequency Mixing Noise, and Shock Noise Components (Cont'd)



(e) COMPARISON OF THE MEASURED AND RECONSTRUCTED TOTAL SPL SPECTRA

Figure 5.1-6 Example of the Procedure Used to Decompose a Total Noise Spectrum Into the High Frequency Mixing Noise, Low Frequency Mixing Noise, and Shock Noise Components (Cont'd)

The spectral decomposition process is summarized in Figure 5.1-7. The process led to a definition of a characteristic Fan Stream Shock Noise Sound Pressure Level (FSNSPL) and Fan Stream Shock Noise Frequency (FSNF); a characteristic Primary Stream Shock Noise Sound Pressure Level (PSNSPL) and Primary Stream Shock Noise Frequency (PSNF); a characteristic High Frequency Sound Pressure Level (HFSPL) and High Frequency (HF), and a characteristic Low Frequency Sound Pressure Level (LFSPL) and Low Frequency (LF).

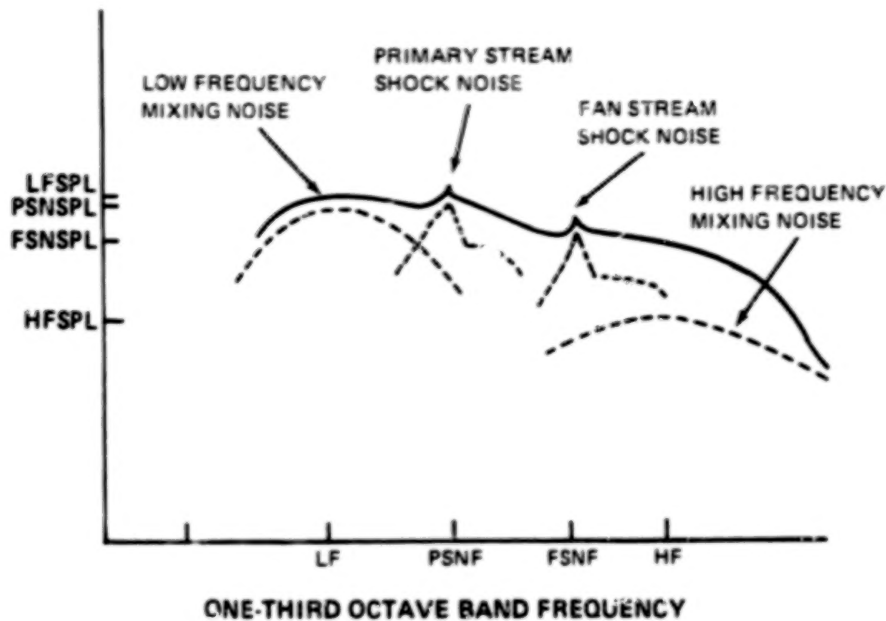


Figure 5.1-7 *Definition of the Low Frequency Mixing Noise, High Frequency Mixing Noise, Fan Stream Shock Noise, and Primary Stream Shock Noise Components*

5.1.3 Definition of Acoustic Models Used in Developing the Prediction Procedure

Noise generation models for the noise components defined in Section 5.1.2 were developed based on the physics of the IVP coannular nozzle flow development and noise generation. The mixing noise model was based on the IVP coannular nozzle mean flow field development illustrated in Figure 5.1-4 in which the initial and merged regions both consisted of a region of constant velocity followed by a region of rapid axial decay. The flow in each region behaves in a manner similar to that of a single convergent nozzle; that is, the peak mean velocity at a given axial position in the flow from a convergent nozzle is constant until the end of the potential core at which point it decays. This suggests that the mixing noise produced by the initial region and merged region can be regarded as equivalent to that generated by two separate convergent nozzles, each operated at a characteristic velocity, temperature, and area appropriate for each flow region. Based on this approach, both the high and low frequency mixing noise levels were normalized with respect to nozzle operating conditions using the correlation factors discussed in Reference 23. That is, the mixing noise components were normalized with respect to temperature by the factor $10 \omega \log (T/T_a)$ and correlated with $\log V/c_a$, where ω is the SAE density exponent, T_a is the ambient air temperature, c_a is the ambient speed of sound, and V and T are the characteristic velocity and temperature, respectively, for either the initial or the merged region.

The shock noise scaling parameters were based on the Harper-Bourne and Fisher theory (Reference 24) of shock noise developed for convergent nozzles. The noise scaling parameters developed in this theory were modified in the present analysis to obtain scaling parameters for the shock noise produced by coannular nozzles. In the Harper-Bourne and Fisher theory, shock noise is generated by the passage of turbulent eddies through the jet shock structure.

Convergent nozzle shock noise is a function of the parameter $(L_s/r)^2$, where L_s is the characteristic shock cell spacing and r is the acoustic measurement radius, and Mach number. For a convergent nozzle, L_s is defined by

$$L_s = 1.1 D \sqrt{M^2 - 1},$$

where M is the Mach number of the flow and D is the jet diameter. Therefore, convergent nozzle shock noise is a function of $(D/r)^2$ and $\sqrt{M^2 - 1}$ or, equivalently, A/r^2 and $\sqrt{M^2 - 1}$, where A is the area of the nozzle. A Strouhal number, S , can be defined for convergent nozzle shock noise as

$$S = \frac{f L_s \left\{ (1 + M_c \cos \theta)^2 + (0.19 M_c)^2 \right\}^{1/2}}{V_c},$$

where f is the characteristic frequency of noise radiated at an angle θ , and M_c is the turbulent eddy convection velocity, V_c , divided by the ambient speed of sound. The angle θ is measured with respect to the upstream jet axis. The expression in curly brackets is a Doppler factor arising from the relative motion of a fixed observer and moving source. In the original Harper-Bourne and Fisher theory, only the Doppler factor $(1 + M_c \cos \theta)$ appeared in the Strouhal number expression. As the turbulent eddy Mach number, M_c , approaches unity, this Doppler factor must be modified to account for the finite eddy lifetime. The modification to the Doppler factor, the term $0.19 M_c$, was determined in Reference 26.

The shock noise model for IVP coannular nozzle was based on these convergent nozzle scaling parameters. Since either the fan stream or primary stream can be a source of shock noise, a Strouhal number and Mach number were defined for each based on the characteristic flow properties appropriate for either flow stream.

5.1.4 Definition of Characteristic Velocity Temperature, and Area for Initial and Merged Regions

In order to correlate noise generated by the initial and merged regions of the flow, a characteristic velocity, temperature, and area associated with each region must be defined. The characteristic velocity and temperature for each region were obtained by: (1) identifying the characteristic frequency generated by each region from the mixing spectrum, as defined in Section 5.1.2; (2) determining the location in the aerodynamic flow field that each frequency is generated; and (3) defining the local flow parameters in the appropriate region of the flow as the characteristic parameters. This procedure is illustrated in Figure 5.1-8. In Figure

5.1-8a, a noise spectrum at 150 degrees, measured with respect to the upstream jet axis, was used to identify the characteristic frequency of noise generated by the initial and merged regions of the flow. The axial distribution of frequencies, in terms of the acoustic power spectrum, generated by the aerodynamic flow of an inverted velocity profile coannular nozzle, was determined by the method described in Reference 15 and is illustrated in Figure 5.1-8b. In Reference 15 a flow prediction procedure developed by P.T. Harsha (Reference 27) was used to predict the mean flow produced by an IVP coannular nozzle, as illustrated in Figure 5.1-8c. The frequency of noise, $f(X)$, generated at any axial position in the flow, was then determined from the relation

$$f(X) = .3 \frac{V(X)}{b(X)} \sqrt{\frac{T(X)}{T_a}} \quad \text{Eq. (5-1)}$$

where $V(X)$ and $T(X)$ are the peak mean velocity and temperature, respectively, at a distance X from the nozzle exit plane, and $b(X)$ is the local mixing layer thickness of the fan stream mixing layer. The mixing layer width, $b(X)$, was defined as the distance between the radial positions where the mean velocity was 5 percent and 95 percent of the peak mean velocity. Source location techniques have demonstrated that a given frequency of noise is actually generated over a finite region of the aerodynamic flow. In the present analysis, this distribution of sources was approximated by assuming that each frequency was generated at only one location in the flow; this location would correspond to the peak of the actual source distribution. The relationship in Equation (5-1) was experimentally determined in Reference 26 for unheated convergent nozzle flows ($T(X) = T_a$). This expression was assumed to be locally valid in an IVP coannular nozzle flow and was empirically extended to heated flows with the factor $\sqrt{T(X)/T_a}$. From Figure 5.1-8b, the axial locations of the frequencies HF and LF were determined. These axial locations were defined as $(X/D)_i$ and $(X/D)_m$, respectively, where the axial distance X was measured from the fan nozzle exit plane and D is an equivalent diameter calculated from the total nozzle area. The characteristic velocities for the initial and merged regions were then defined by the use of Figure 5.1-8c, which contains a plot of the peak mean velocity at a given axial position as a function of axial position. The local mean velocities at $(X/D)_i$ and $(X/D)_m$, denoted as V_i and V_m , respectively, were defined as the initial region and merged region characteristic velocities. The characteristic temperatures for the initial region and merged region were defined in a similar manner.

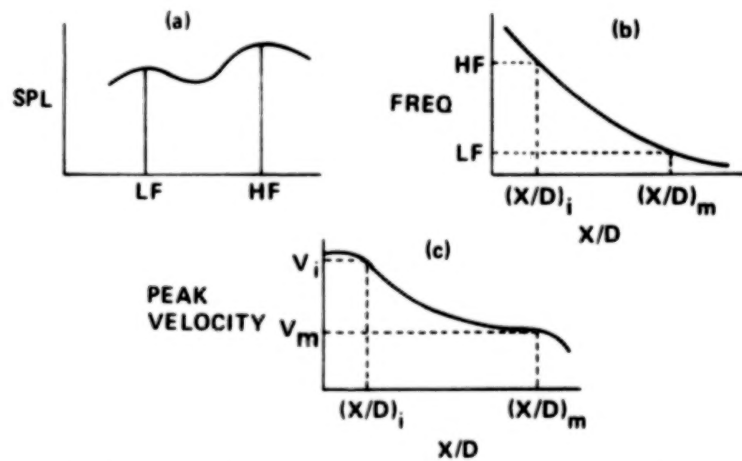


Figure 5.1-8 *Definition of the Procedure Used to Define the Characteristic Velocity and Temperature for Initial and Merged Regions*

As an example of this procedure, consider the acoustic spectrum in Figure 5.1-9. The characteristic frequencies for the initial region and merged region (Figure 5.1-9a) are 80 Hz and 315 Hz, respectively. The plot of frequency versus axial distance for the operating condition in Figure 5.1-9a is shown in Figure 5.1-9b; the axial location for the frequencies of 80 Hz and 315 Hz are $(X/D_t)_i = 1.5$ and $(X/D_t)_m = 7.0$. The plot of peak mean velocity versus axial distance is shown in Figure 5.1-9c for the operating condition in Figure 5.1-9a. At $(X/D_t)_i = 1.5$, the characteristic velocity for the initial region is 571 m/sec (2200 ft/sec); and at $(X/D_t)_m = 7.0$, the characteristic velocity for the merged region is 463 m/sec (1520 ft/sec).

The procedure outlined in the preceding paragraph was used to define the characteristic velocity and temperature for a number of nozzle operating conditions. In order to predict the characteristic parameters for any operating condition, empirical relationships were then determined (see Section 5.2) expressing the initial and merged region characteristic velocity and temperature as a function of the operating conditions and geometry of the coannular nozzle.

The characteristic areas for the initial and merged regions were defined as the physical fan nozzle area and total nozzle area, respectively. The characteristic velocity, temperature, and area for each region were used to determine correlations for the mixing noise generated by the initial and merged regions, as described in Section 5.2.

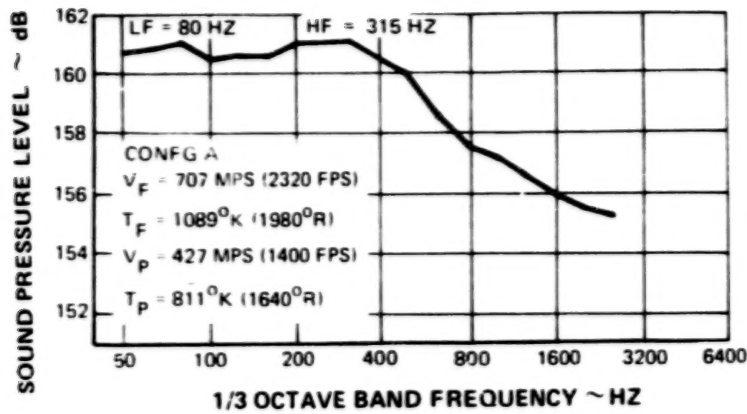
5.2 STATIC JET EXHAUST NOISE PREDICTION PROCEDURE

In this section, the methods used to normalize the four noise components with respect to nozzle operating condition and geometry are presented. The following topics are discussed: development of the mixing noise data correlations and development of the shock noise data correlations.

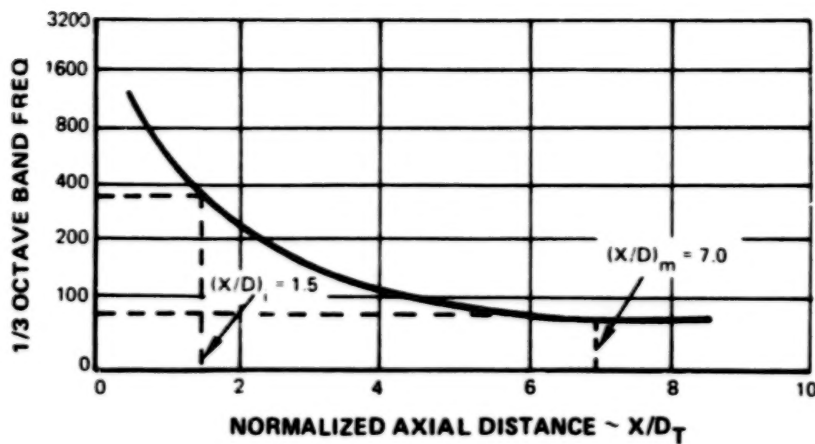
5.2.1 Development of Mixing Noise Data Correlations

The low frequency mixing noise component and high frequency mixing noise component were correlated with nozzle operating condition and nozzle geometry. The mixing noise correlations with nozzle operating condition were developed using the noise model described in Section 5.1.3 in which the noise generated by the initial or merged region was modeled as that generated by an equivalent convergent nozzle operated at the characteristic velocity, temperature, and area for each region. The high frequency and low frequency characteristic peak SPL values (defined as HFSPL and LFSPL, respectively, in Section 5.1.2) were normalized with respect to temperature by the relation

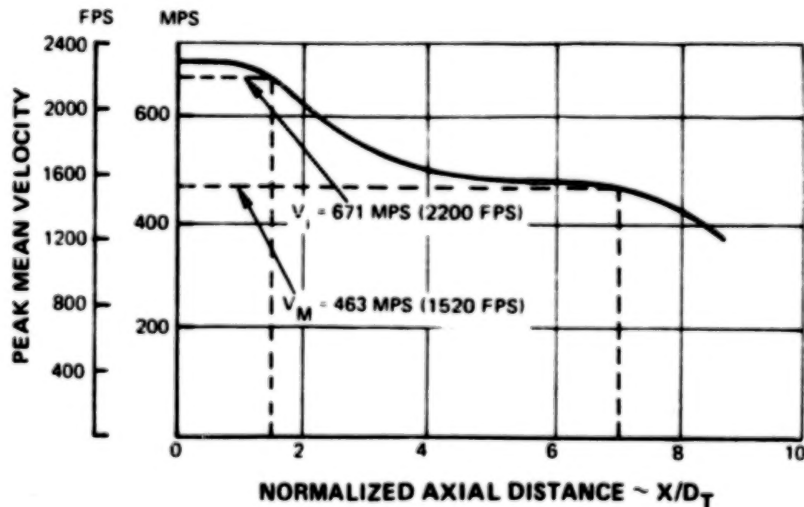
$$SPL_{corr} = SPL + 10 \omega \log \left(\frac{T}{T_a} \right), \quad \text{Eq. (5-2)}$$



(a) Definition of the Characteristic Frequencies LF and HF



(b) Definition of the Locations in the Aerodynamic Flow That Generate the Frequencies LF and HF



(c) Definition of the High Frequency and Low Frequency Characteristic Velocities

Figure 5.1-9 Example of the Procedure Used to Define the Characteristic Velocities for Initial Region and Merged Region

where SPL is either the high frequency or low frequency noise component, SPL_{corr} is the SPL noise component normalized with respect to temperature, T is the initial or merged region static temperature for the noise component, T_a is the ambient air temperature, and ω is the SAE density exponent (Reference 23). For purely quadrupole noise sources, the temperature appearing in Eq (5-2) is the static temperature. However, use of matched asymptotic expansions (Ref. 36) or Lilley's equation (Ref. 37) to determine a rigorous scaling law for aerodynamic noise with jet flow density(or temperature) has demonstrated that the acoustic power radiated by a jet has the scaling law.

$$PWL \propto V_j^8 \left(\rho_j^2 + B \frac{\rho_a^2}{V_j^4} C_a^4 \right),$$

where ρ_j is the jet density, ρ_a is the ambient air density, and B is a constant, or

$$PWL \propto \rho_{eff}^2 V_j^8$$

where

$$\rho_{eff} = \rho_j (1 + B/M^2),$$

and M is the Mach number of the flow. Then an effective temperature can be defined

$$T_{eff} = T/(1 + B/M^2),$$

and jet noise will then follow the scaling law

$$PWL \propto \frac{1}{T_{eff}^2} V_j^8$$

Then use of Eq (5-2) as an equation for normalizing jet noise data with respect to temperature requires use of T_{eff} in place of T. Use of the static temperature in Eq (5-2) will not include the jet noise Mach number dependence derived above. Because the coefficient B is not accurately known (see Reference 36 for an order of magnitude estimate), T_{eff} also cannot be used in Eq 5-2. As a result, the total temperature was used as an estimate of T_{eff} because the total temperature has the corrective relative trend variation with Mach number.

Figure 5.2-1 contains a plot of ω versus V/c_a , where V is the appropriate initial or merged region velocity and c_a is the ambient speed of sound. The normalization in Equation (5-2) is that which could be expected if the initial and merged regions of the flow generate noise levels equivalent to those from a convergent nozzle operated at the characteristic temperature and velocity of the appropriate region. The data were corrected for temperature by use of Equation (5-2) and SPL_{corr} was correlated with $\log V/c_a$ as discussed in Section 5.2.1.1.

After the mixing noise components were normalized with respect to nozzle operating condition, they were normalized with respect to nozzle geometry. This normalization can be expressed algebraically by the equation

$$SPL_{nor} = SPL_{corr} + f(A/r'^2, R_f, R_p).$$

Eq. (5-3)

where SPL_{nor} is the completely normalized SPL for either the initial region or merged region, A is the characteristic area for either the initial or merged region, r' is the appropriate measurement distance, R_f is the fan radius ratio, and R_p is the primary radius ratio. The function f was determined empirically from the experimental data, as discussed in Section 5.2.1.2.

In addition to the normalization of the HFSPL and LFSPL with respect to nozzle operating condition and geometry, the characteristic frequencies (HF and LF) were normalized by defining a Strouhal number based on the characteristic velocity and area for each region.

The measurement radius from an observation point to the jet noise low frequency source (denoted r_m) or high frequency source (denoted r_i) differ since the two noise sources are located in different regions of the flow. The initial region noise was assumed to be generated at a location near the nozzle exit plane and the merged region noise was assumed to be generated farther downstream as an approximation to the detailed source distribution.

From Figure 11 of Reference 15, for the initial region $X_i \approx 1.5 D_t$ and for the merged region $X_m \approx 7.0 D_t$, then from Figure 5.2-2, with the definition $\theta_m \leq \theta$ and $\theta_i \leq \theta$,

$$r_m = r \sqrt{1 + 49 \left(\frac{D_t}{r}\right)^2 - 14 \frac{D_t}{r} \cos(180^\circ - \theta)},$$

Eq. (5-4)

$$\theta_m = \arcsin \left[\frac{r}{r_m} \sin(180^\circ - \theta) \right].$$

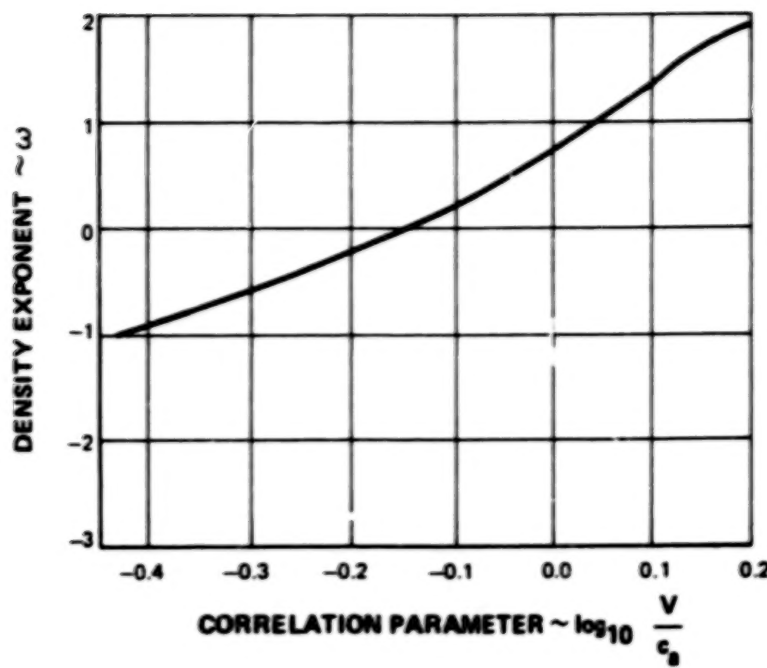


Figure 5.2-1 *Definition of the SAE Density Exponent (Reference 23)*

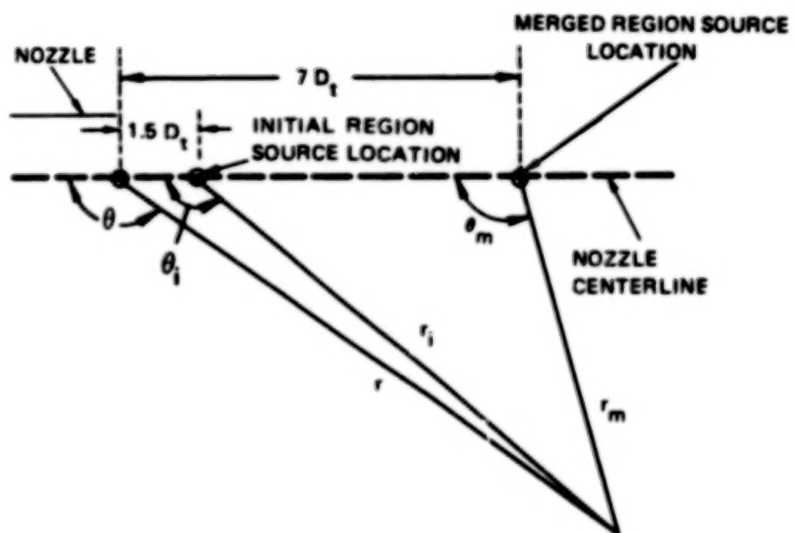


Figure 5.2-2 *Definition of the Merged Region, Initial Region, and Nozzle Exit Plane Coordinates*

$$\text{and } r_i = r \sqrt{1 + 2.25 \left(\frac{D_t}{r}\right)^2 - 3 \left(\frac{D_t}{r}\right) \cos(180^\circ - \theta)}, \quad \text{Eq. (5-5)}$$

$$\theta_i = \arcsin \left[\frac{r}{r_i} \sin(180^\circ - \theta) \right].$$

Figure 5.2-3 contains plots of distance correction, $20 \log r/r_i$, and angle correction, $\Delta\theta_i \equiv \theta - \theta_i$ versus θ ; and Figure 5.2-4 contains plots of $20 \log r/r_m$ and $\Delta\theta_m \equiv \theta - \theta_m$ versus θ using $D_t/r = 0.028$, which is correct for the facilities from References 7 and 8 and the present program. As illustrated in Figure 5.2-3, the level and angle corrections were small for the initial region source, and $r_i \approx r$ and $\theta_i \approx \theta$. Therefore, noise generated in the initial region, the high frequency noise component, was not corrected for source location. However, the angle corrections were on the order of ten degrees and the level corrections were 1 to 2 dB for the merged region source, and, therefore, source location must be incorporated in the prediction of the merged region noise. The application of the source location angle and level corrections for the merged region is discussed in Section 5.2.1.1.

The detailed developments of the mixing noise correlations are discussed in Section 5.2.1.1 for the low frequency noise component and in Section 5.2.1.2 for the high frequency noise component.

5.2.1.1 Merged Region Mixing Noise

The merged region characteristic velocity and temperature were defined using the procedure described in Section 5.1.4. The merged region characteristic velocity and temperature were defined for a limited set of nozzle operating conditions, as described in Section 5.1.4. The merged region characteristic velocity and temperature were found to vary with nozzle operating condition in a manner similar to the mass flow averaged velocity and temperature, but the absolute levels of the merged region characteristic parameters were lower than the mass averaged parameters by a factor of 0.86. In addition, the merged region parameters were a stronger function of primary to fan stream temperature ratio and fan to primary stream area ratio than were the mixed flow parameters. The resulting expressions for the merged region velocity and temperature are

$$V_m = 0.86 V_p \frac{1 + a^{1/2} \frac{V_f}{V_p} \sqrt{\frac{T_{tp}}{T_{tf}}}}{1 + a^{1/2} \sqrt{\frac{T_{tp}}{T_{tf}}}}, \quad \text{Eq. (5-6)}$$

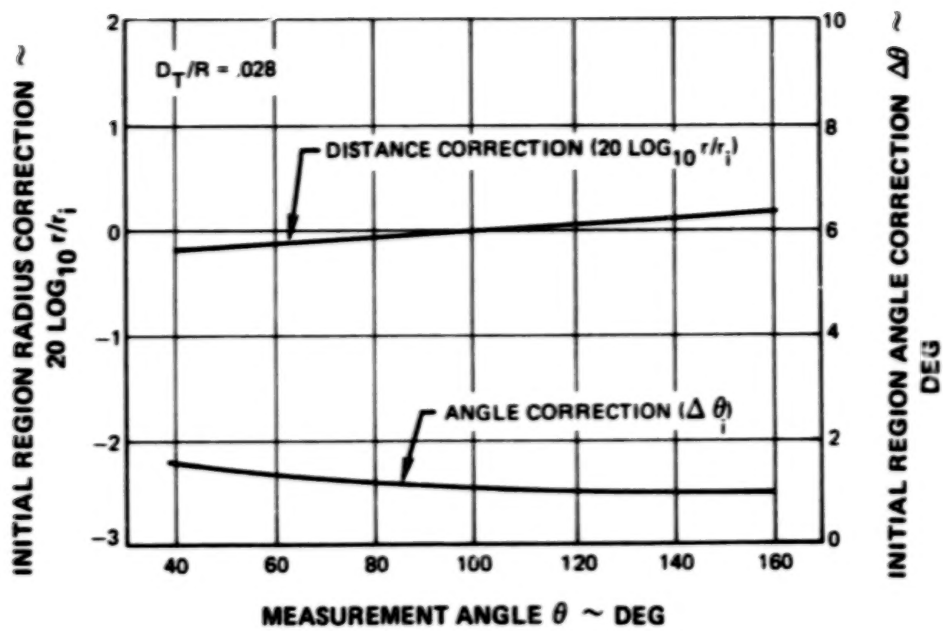


Figure 5.2-3 Angle and Distance Corrections for the Initial Region

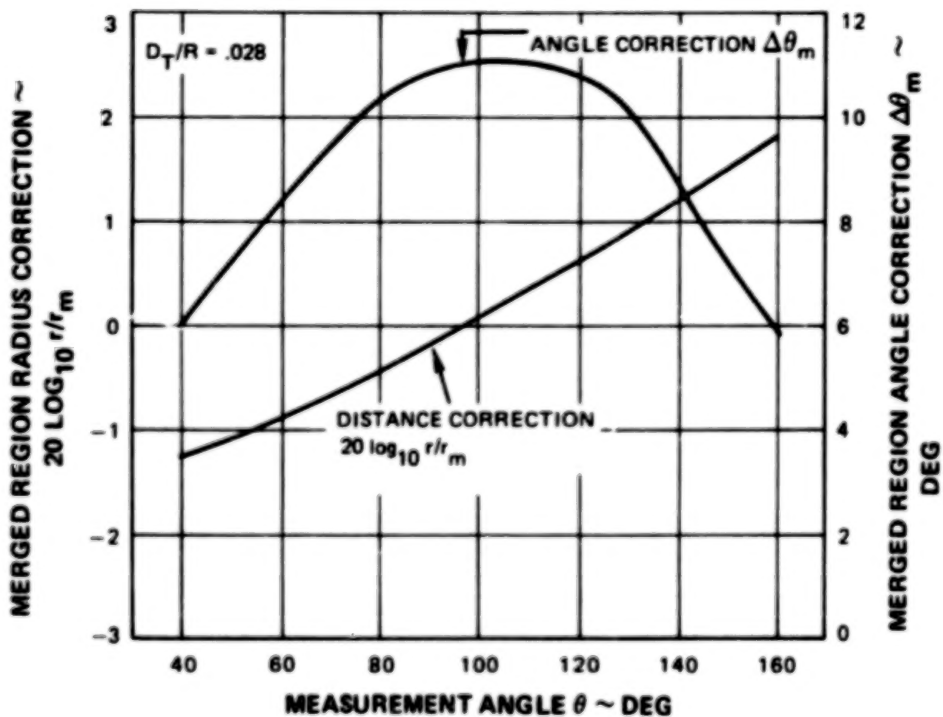


Figure 5.2-4 Angle and Distance Corrections for the Merged Region

and

$$T_{tm} = 0.86 T_{tp} \frac{1 + a^{1.2} \frac{T_{tf}}{T_{tp}} \sqrt{\frac{T_{tp}}{T_{tf}}}}{1 + a^{1.2} \sqrt{\frac{T_{tp}}{T_{tf}}}} \quad \text{Eq. (5-7)}$$

where V_f and T_{tf} are the ideally expanded fan velocity and total temperature, respectively, V_p and T_{tp} are the ideally expanded primary velocity and total temperature, respectively, V_m and T_m are the characteristic velocity and temperature for the merged region, respectively, and a is the fan to primary area ratio. If the exponent of the area ratio was 1.0 and the two nozzles have equal exit pressures, then the merged region velocity and temperature would be a factor of 0.86 lower than the mass averaged velocity and temperature.

For each nozzle geometry, the low frequency spectrum peak, LFSPL, was corrected for temperature by the expression

$$LFSPL_{corr} = LFSPL + 10 \omega \log \frac{T_{tm}}{T_a} \quad \text{Eq. (5-8)}$$

and $LFSPL_{corr}$ was plotted versus $\log V_m/c_a$ as described in Section 5.2.1. Figure 5.2-5 contains a plot of $LFSPL_{corr}$, versus $\log V_m/c_a$, for data obtained from References 7 and 8, at a measurement angle of $\theta_m = 143$, ($\theta = 150$) degrees measured with respect to the upstream jet axis. The angle θ_m is that measured with respect to the merged region source location while θ is that measured with respect to the nozzle exit plane for a radius of 4.57 m (15 ft). The data collapse obtained in Figure 5.2-5 demonstrates that the low frequency data can be collapsed to a single line, with respect to operating condition for fixed geometry, using the model described in Section 5.1.3.

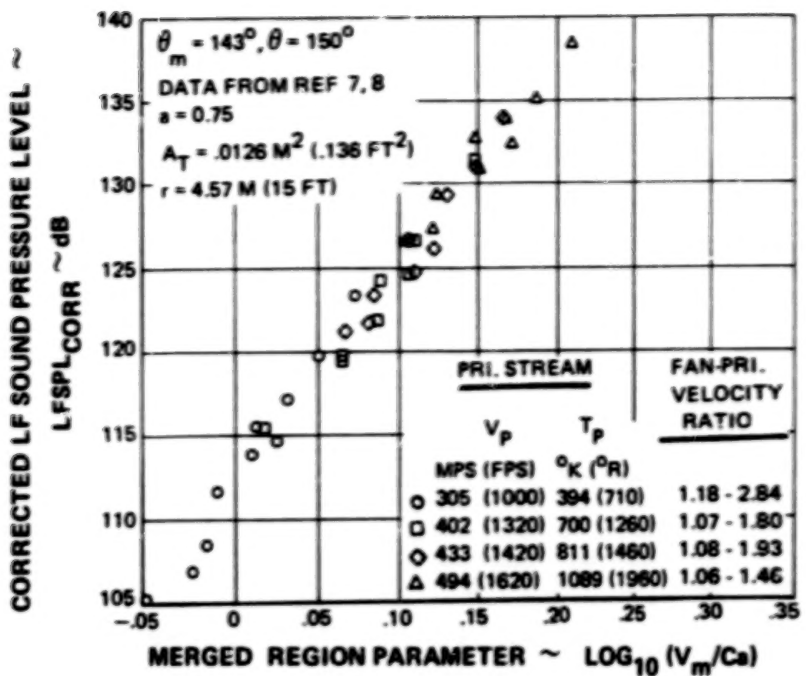


Figure 5.2-5 Normalization of the Low Frequency Mixing Noise Data at $\theta_m = 143^\circ (\theta = 150^\circ)$ With Respect to Nozzle Operating Condition

Figure 5.2-6 contains a plot of LFSPL_{corr} versus V_m/ca at an angle of $\theta_m = 79$ ($\theta = 90$) degrees. The data collapsed to two lines, one corresponding to fan to primary velocity ratios of less than 2.0 and the other corresponding to velocity ratios greater than 2.0. This suggests that data trends are not uniform at all angles since the parameters defined in Equations (5-6) and (5-7) did collapse the data at $\theta_m = 143$ ($\theta = 150$) degrees. These different results do not appear to be a result of the normalization parameters defined in Equations (5-6) and (5-7) but a fundamental data trend. The origin of this effect is uncertain but may be due to non-isotropic radiation by the quadrupole sources in the fan stream shear layer or complex refraction effects due to the developing velocity and temperature gradients in the flow. To remove the disparity between the high velocity ratio data and the low velocity ratio data, the parameters in Equations (5-6) and (5-7) were modified to

$$V_m = \alpha V_p \frac{1 + a^{1.2} \frac{V_f}{V_p} \sqrt{\frac{T_{tp}}{T_{tf}}}}{1 + a^{1.2} \sqrt{\frac{T_{tp}}{T_{tf}}}} \quad , \quad \text{Eq. (5-9)}$$

and

$$T_{tm} = \alpha T_{tp} \frac{1 + a^{1/2} \sqrt{\frac{T_{tp}}{T_{tf}}}}{1 + a^{1/2} \sqrt{\frac{T_{tp}}{T_{tf}}}} \quad . \quad \text{Eq. (5-10)}$$

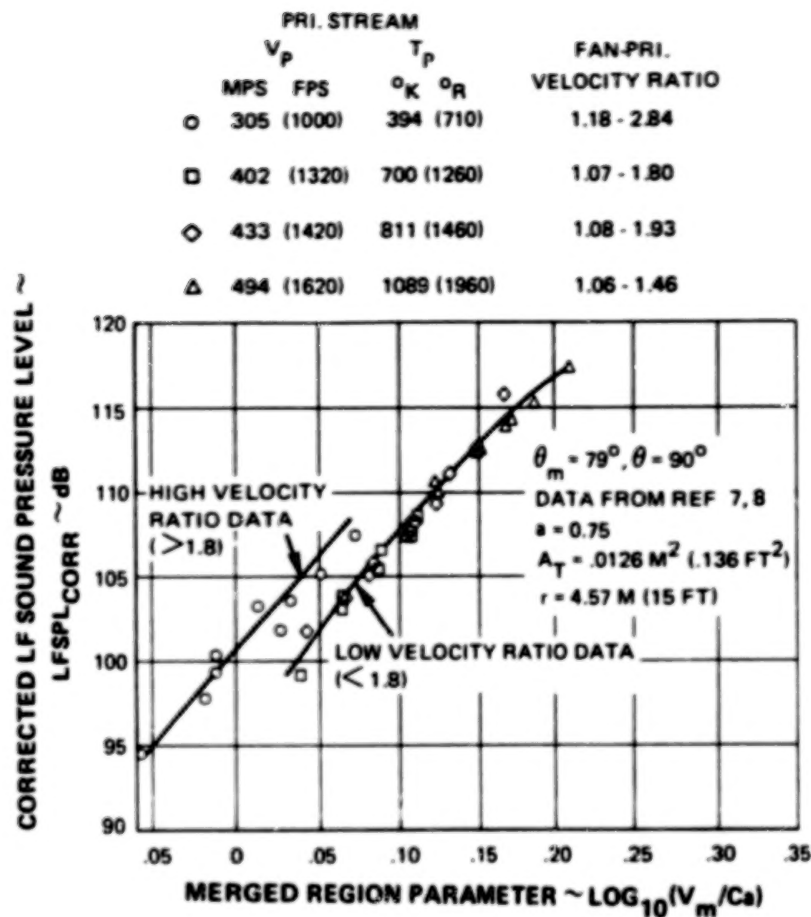


Figure 5.2-6 Normalization of the Low Frequency Mixing Noise Data at $\theta_m = 79^\circ$ ($\theta = 90^\circ$) With Respect to Nozzle Operating Condition

where α is defined by:

$$\begin{aligned}
 51^\circ \leq \theta_m \leq 80^\circ \quad \alpha &= \begin{cases} 0.86 & \text{if } v < 1.8 \\ 0.23 + 0.35 v & \text{if } 1.8 \leq v \leq 2.0 \\ 0.93 & \text{if } v > 2.0 \end{cases} \\
 80^\circ < \theta_m \leq 120^\circ \quad \alpha &= \begin{cases} 0.86 & \text{if } v < 1.8 \\ 0.23 + 0.35 v & \text{if } 1.8 \leq v \leq 2.2 \\ 1.0 & \text{if } v > 2.2 \end{cases} \\
 120^\circ < \theta_m \quad \alpha &= 0.86
 \end{aligned} \tag{Eq. (5-11)}$$

where v is the fan to primary velocity ratio. At angles of $\theta_m = 121$ ($\theta = 130$) degrees to $\theta_m = 155$ ($\theta = 160$) degrees the parameters in Equations (5-9) and (5-10) reduce to those in Equations (5-6) and (5-7). The correlation of $LFSPL_{corr}$ versus $\log V_m/c_a$ at $\theta_m = 79$ ($\theta = 90$) degrees is illustrated in Figure 5.2-7 for the revised parameters defined in Equations (5-9) and (5-10). Figure 5.2-7 demonstrates that the high and low velocity ratio data can be collapsed to a single line.

$LFSPL_{corr}$ can be normalized with respect to nozzle geometry by the expression

$$LFSPL_{nor} = LFSPL_{corr} - 10 \log A_t/r_m^2. \tag{Eq. (5-12)}$$

where A_t is the total nozzle area, r_m is the measurement radius from the merged region source location, and $LFSPL_{nor}$ is the completely normalized low frequency noise component. Implicit in Equation (5-12) is the assumption that the low frequency mixing noise can be scaled to any engine size by the correction $10 \log A_t/r_m^2$. There appears to be no additional dependence of the low frequency noise component on fan or primary stream radius ratio. $LFSPL_{nor}$ is plotted versus $\log V_m/c_a$ for angles of $\theta_m = 51$ ($\theta = 60$), $\theta_m = 79$ ($\theta = 90$), $\theta_m = 109$ ($\theta = 120$) and $\theta_m = 143$ ($\theta = 150$) degrees in Figures 5.2-8 through 5.2-11. Additional correlations are contained in the Comprehensive Data Report (Reference 19). Included in all figures are data from References 7 and 8 and the present program. The data from References 11 and 12, corrected by 2.0 dB as discussed in Section 5.1.1, are also included in Figures 5.2-9 and 5.2-11. The data from References 11 and 12 were obtained at different angles θ_m than those in References 7 and 8 and the present program. The data from References 11 and 12 were interpolated to the angle θ_m appropriate for the data in References 7 and 8. The standard deviation of the data collapse associated with each angle is indicated on each figure. The data collapse demonstrates that Equation (5-12) provides normalization of the low frequency IVP coannular jet noise component with respect to nozzle geometry and operating condition. The standard deviation of this normalization varies between ± 1.0 dB and ± 1.5 dB.

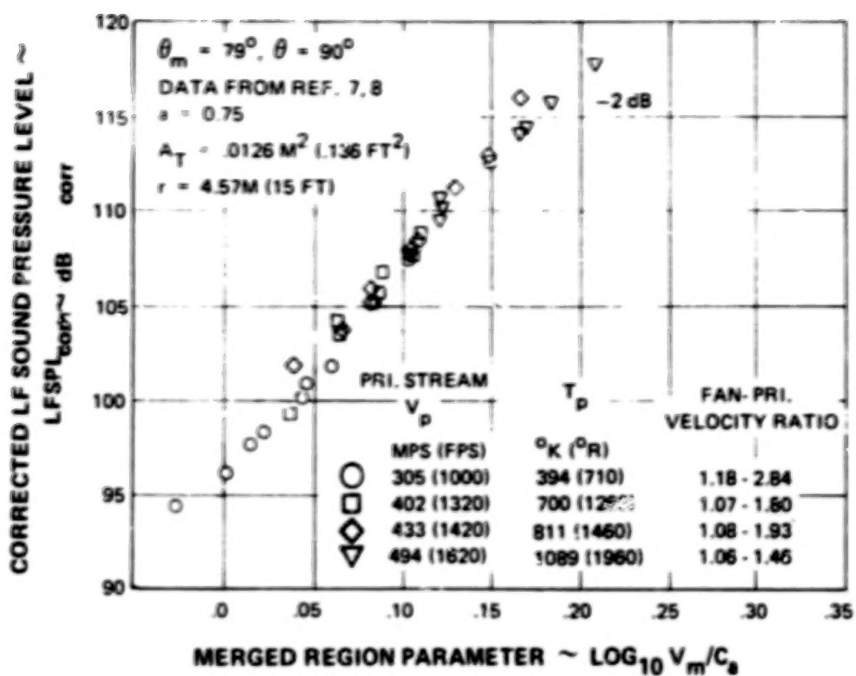


Figure 5.2-7 Normalization of the Low Frequency Mixing Noise Data at $\theta_m = 79^\circ$ ($\theta = 90^\circ$) With Respect to Nozzle Operating Condition Using the Revised Parameters

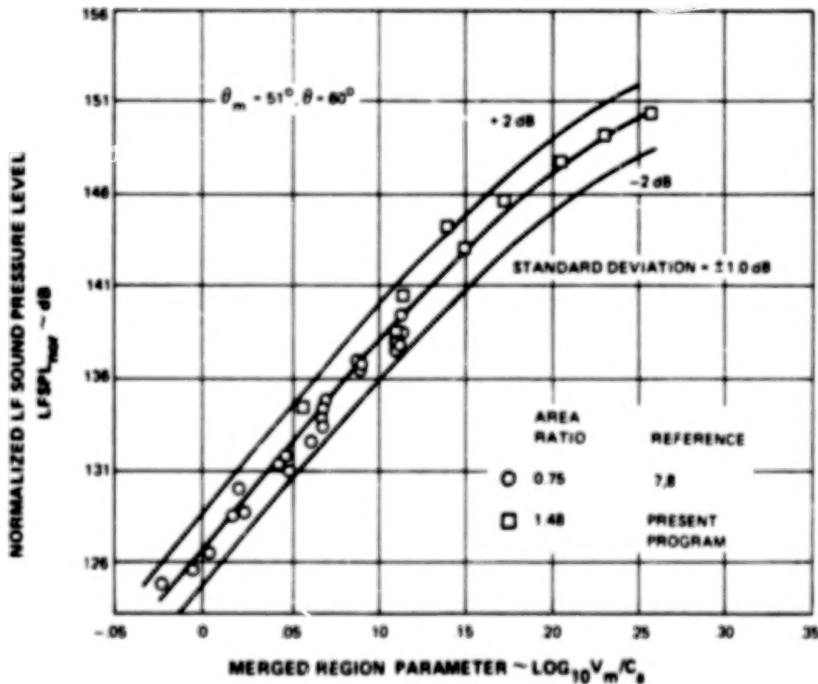


Figure 5.2-8 Normalization of the Low Frequency Noise Component at $\theta_m = 51^\circ$ ($\theta = 60^\circ$) With Respect to Nozzle Operating Condition and Geometry

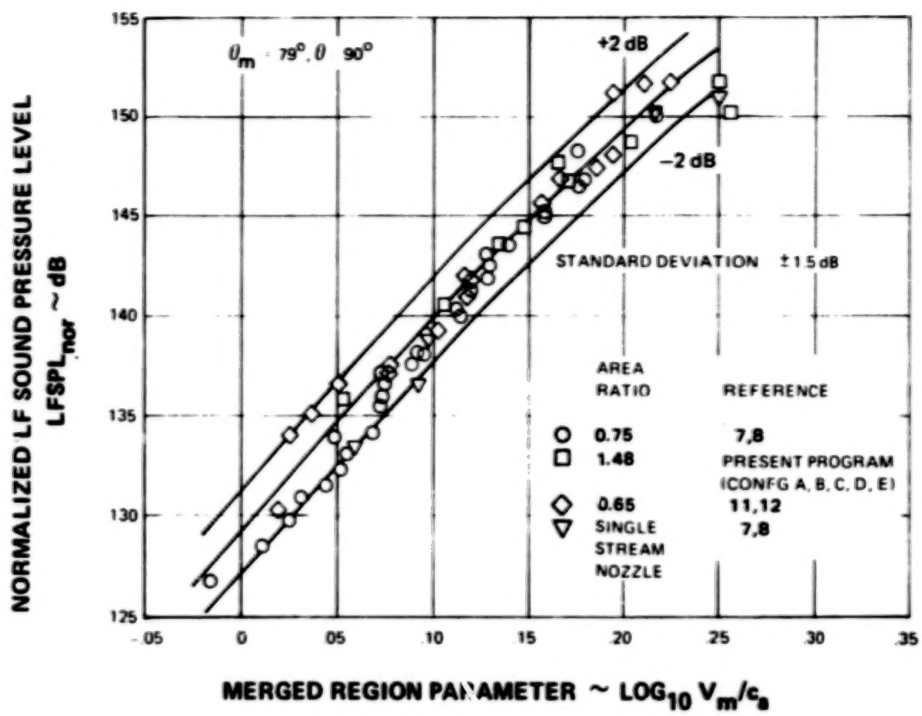


Figure 5.2-9 Normalization of Low Frequency Data at $\theta_m = 79^\circ$ ($\theta = 90^\circ$) With Respect to Nozzle Operating Condition and Geometry

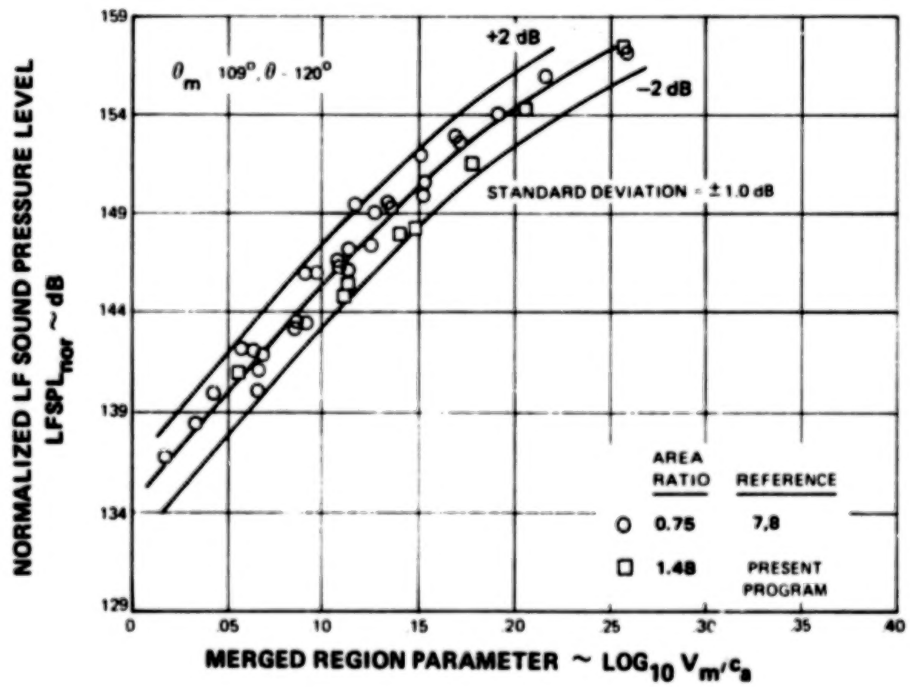


Figure 5.2-10 Normalization of the Low Frequency Mixing Noise Component at $\theta_m = 109^\circ$ ($\theta = 120^\circ$) With Respect to Nozzle Operating Condition and Geometry

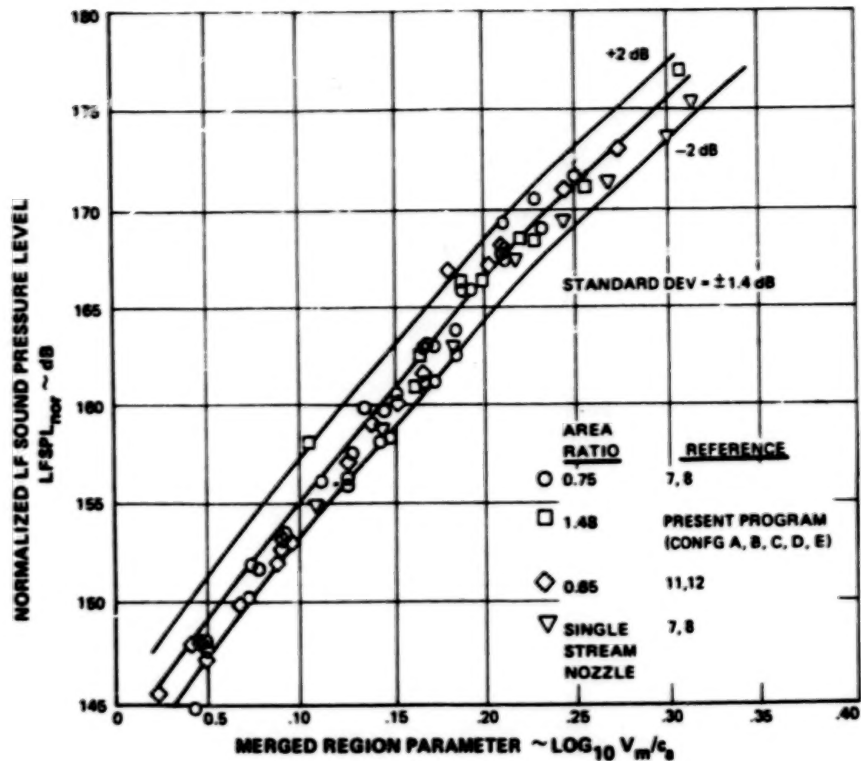


Figure 5.2-11 Normalization of Low Frequency Data at $\theta_m = 143^\circ$ ($\theta = 150^\circ$) With Respect to Nozzle Operating Condition and Geometry

Figures 5.2-9 and 5.2-11 also contain $LFSPL_{nor}$ levels for a single stream convergent nozzle data from References 7 and 8. For a convergent nozzle, the fan to primary velocity ratio and temperature ratio are 1.0, and Equations (5-9) and (5-10) reduce to

$$V_m = 0.86 V_f,$$

and

Eq. (5-13)

$$T_{tm} = 0.86 T_{tf}.$$

That is, the peak low frequency noise generating region for a convergent nozzle is near the end of the potential core of the jet where the characteristic velocity and temperature is 0.86 of the initial exit plane values. The data from Reference 25 show that these characteristic values are obtained approximately five diameters downstream from the nozzle exit plane.

Figure 5.2-12 contains a set of summary curves for the normalized mixing noise component, $LFSPL_{nor}$, as a function of $\log V_m/ca$ for angles from $\theta_m = 51$ degrees to $\theta_m = 155$ degrees, measured with respect to the upstream jet axis.

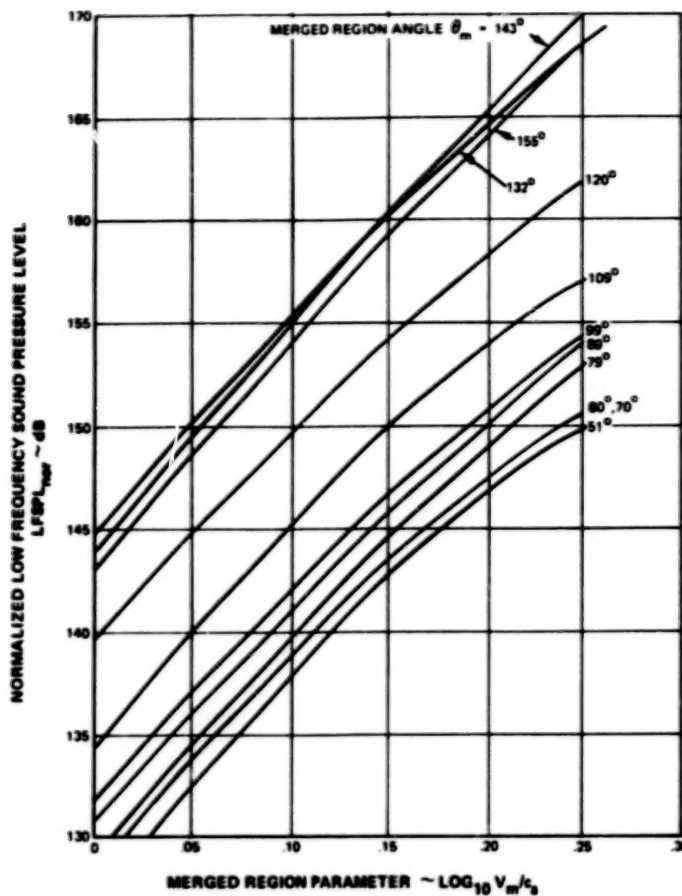


Figure 5.2-12 Normalized Prediction Curves for The Low Frequency Mixing Noise Component

The characteristic frequency of noise generated by the merged region, defined as LF, was normalized by the expression

$$S_m = \frac{(LF) D_t}{V_m} , \quad \text{Eq. (5-14)}$$

where

$$D_t = 2 \sqrt{A_t/\pi},$$

and S_m is the low frequency noise component Strouhal number, D_t is a diameter calculated from the total nozzle area, and V_m is the merged velocity. The Strouhal number was 0.2 at an angle of $\theta_m = 143$ degrees and increased to 0.65 at $\theta_m = 79$ degrees, as illustrated in Figure 5.2-13. This is similar to the behavior observed for the Strouhal number of a convergent nozzle. The data collapse in Figure 5.2-13 demonstrates that Equation (5-14) provides a frequency normalization to within $\pm 1/3$ octave band. Figure 5.2-14 contains the normalized low frequency spectra for angles of $\theta_m = 51$ degrees through $\theta_m = 155$ degrees.

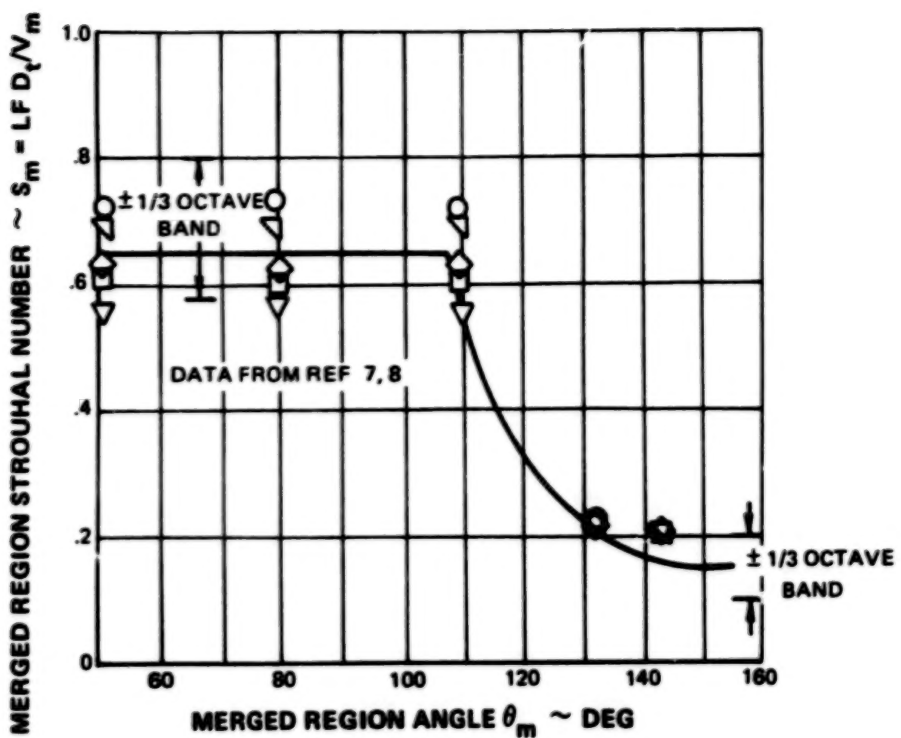


Figure 5.2-13 *Definition of the Low Frequency Mixing Noise Component Strouhal Number*

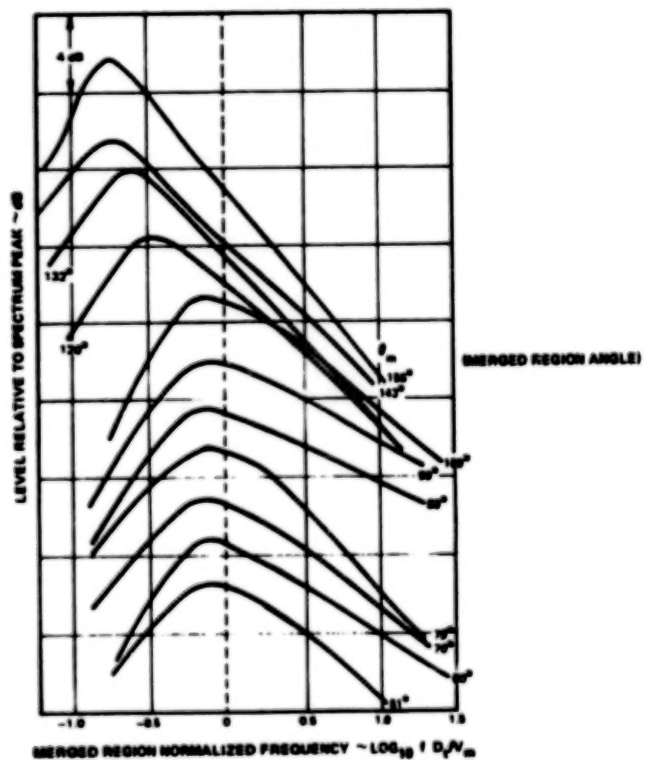


Figure 5.2-14 *Normalized Spectral Shapes for the Low Frequency Mixing Noise Component*

The curves in Figures 5.2-12 and 5.2-14 are defined with respect to the angle θ_m , measured with respect to the merged region source location. If predictions are desired at a given angle θ , measured with respect to the nozzle exit plane, the following procedure should be followed: (1) determine the angle θ_m corresponding to θ using Equation (5-4), (2) interpolate the spectra in Figure 5.2-14 and the levels in Figure 5.2-12 to the angle θ_m , and (3) calculate the low frequency noise component at θ_m, r_m (corresponding to θ, r) using Equations (5-8) and (5-12). This noise component is then added to the other noise components calculated at (θ, r) .

Figures 5.2-12 through 5.2-14, along with Equations (5-4) and (5-8) through (5-12), can be used to predict the low frequency noise component. The ideally expanded fan and primary stream conditions can be used to calculate V_m and T_m . These values, along with the ambient air conditions, can be used to calculate the absolute noise level, LFSPL, from Equations (5-8) and (5-12), and Figure 5.2-12. Figure 5.2-13 and Figure 5.2-14 can be used to obtain the correct frequency, LF, and spectral shape for the low frequency noise component. A sample prediction is contained in Section 5.5.

5.2.1.2 Initial Region Mixing Noise

The initial region characteristic velocity and temperature were defined using the procedure described in Section 5.1.4. The results are

$$V_i = V_f \frac{1 + 0.1 \frac{V_p}{V_f} \sqrt{\frac{T_{tf}}{T_{tp}}}}{1 + 0.1 \sqrt{\frac{T_{tf}}{T_{tp}}}}, \quad \text{Eq. (5-15)}$$

and

$$T_{ti} = T_{tf} \frac{1 + 0.1 \frac{V_p}{V_f} \sqrt{\frac{T_{tf}}{T_{tp}}}}{1 + 0.1 \sqrt{\frac{T_{tf}}{T_{tp}}}}, \quad \text{Eq. (5-16)}$$

The initial region characteristic parameters are approximately the same as the fan stream ideally expanded operating conditions. Generally, the ratios of V_i/V_f and T_{ti}/T_{tf} are greater than 0.90. Use of the fan stream exit plane conditions, however, do not provide good data collapse of the high frequency mixing noise component, and use of the expressions in Equations (5-15) and (5-16) is required.

For a single nozzle geometry, the high frequency spectrum peak, HFSPL, was corrected for temperature by the expression

$$HFSPL_{corr} = HFSPL + 10 \omega \log (T_{tj}/Ta), \quad Eq. (5-17)$$

where ω is a function of V_j/c_a , and $HFSPL_{corr}$ was plotted versus $\log V_j/c_a$. Figures 5.2-15 and 5.2-16 contain plots of $HFSPL_{corr}$ for data obtained from References 7 and 8 at angles of 90 and 150 degrees; as discussed in Section 5.2.1, acoustic data generated by the initial region were not corrected for source location. All data in these two figures were obtained for a 0.75 area ratio nozzle operated over a wide range of operating conditions. The data at 150 degrees, shown in Figure 5.2-16, collapsed along a line which shows a change in slope near $\log V_j/c_a = 0.2$. As velocity is increased, jet mixing noise must approach an asymptotic V^3 behavior, where V is a characteristic flow velocity, because of the constraint that acoustic energy cannot be larger than the kinetic energy of the flow. This change in slope at large jet velocities has also been observed for convergent nozzles. The data collapse obtained in Figures 5.2-15 and 5.2-16 demonstrates that the high frequency noise component can be normalized with respect to nozzle operating condition using the model described in Section 5.1.3.

The high frequency noise component was predicted to be a function of fan nozzle area, fan stream radius ratio, and primary stream radius ratio. The high frequency noise component was normalized with respect to nozzle geometry by plotting the quantity $HFSPL_{corr} - 10 \log A_f/r^2$, where A_f is the fan stream area and r is the measurement radius from the nozzle exit plane, versus fan stream radius ratio, R_f , for various primary stream radius ratios, R_p , at fixed $\log V_j/c_a$. A typical result, obtained at 150 degrees, is illustrated in Figure 5.2-17. As either R_f or R_p was increased, the high frequency noise component was reduced, and the amount of reduction was a function of the parameter $\log V_j/c_a$. Additional curves of this type are contained in the Comprehensive Data Report (Reference 19).

Another parameter that could affect the high frequency noise component is the ratio H/L where H is the annulus height and L is the primary nozzle – fan nozzle separation distance. The high frequency noise component was also plotted versus this parameter, and a sample result is illustrated in Figure 5.2-18. This figure demonstrates that the ratio H/L was not a good correlation parameter for the high frequency noise component. The data do not collapse to a single line. Consequently, the ratio H/L was not used in the analysis of the high frequency noise component.

The normalized high frequency noise component, $HFSPL_{nor}$, was defined as

$$HFSPL_{nor} = HFSPL_{corr} - 10 \log A_f/r^2 + \Delta SPL (R_f, R_p, \log V_j/c_a), \quad Eq. (5-18)$$

where the function ΔSPL was determined empirically from correlations such as those contained in Figure 5.2-17. Implicit in Equation (5-18) is the assumption that the high frequency mixing noise can be scaled to any engine size by the correction $10 \log A_f/r^2$. The function ΔSPL is summarized in Table 5.2-1.

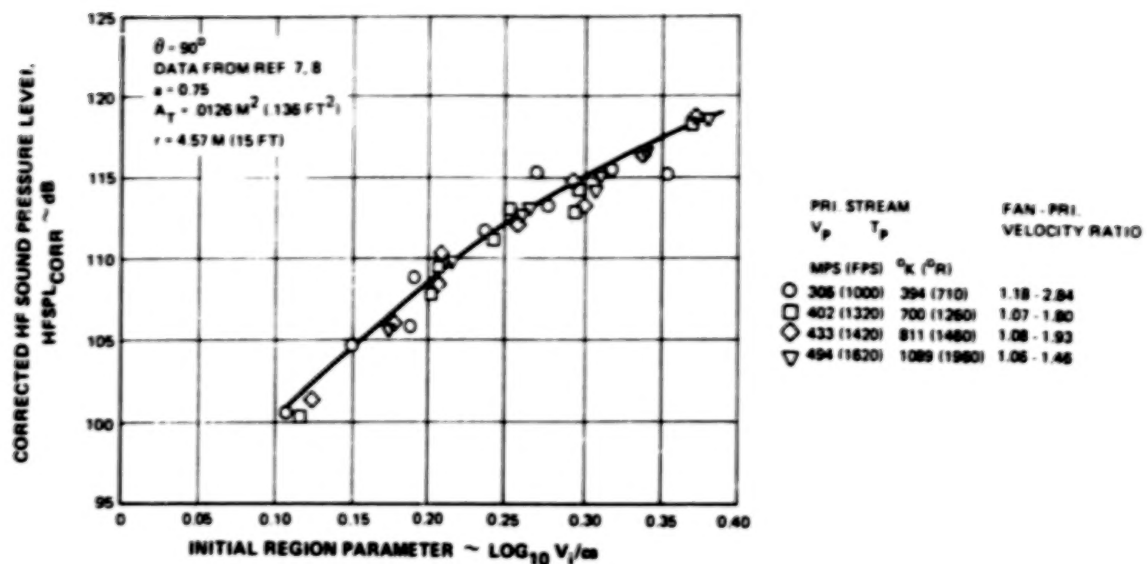


Figure 5.2-15. Normalization of the High Frequency Mixing Noise Component at 90° With Respect to Nozzle Operating Condition

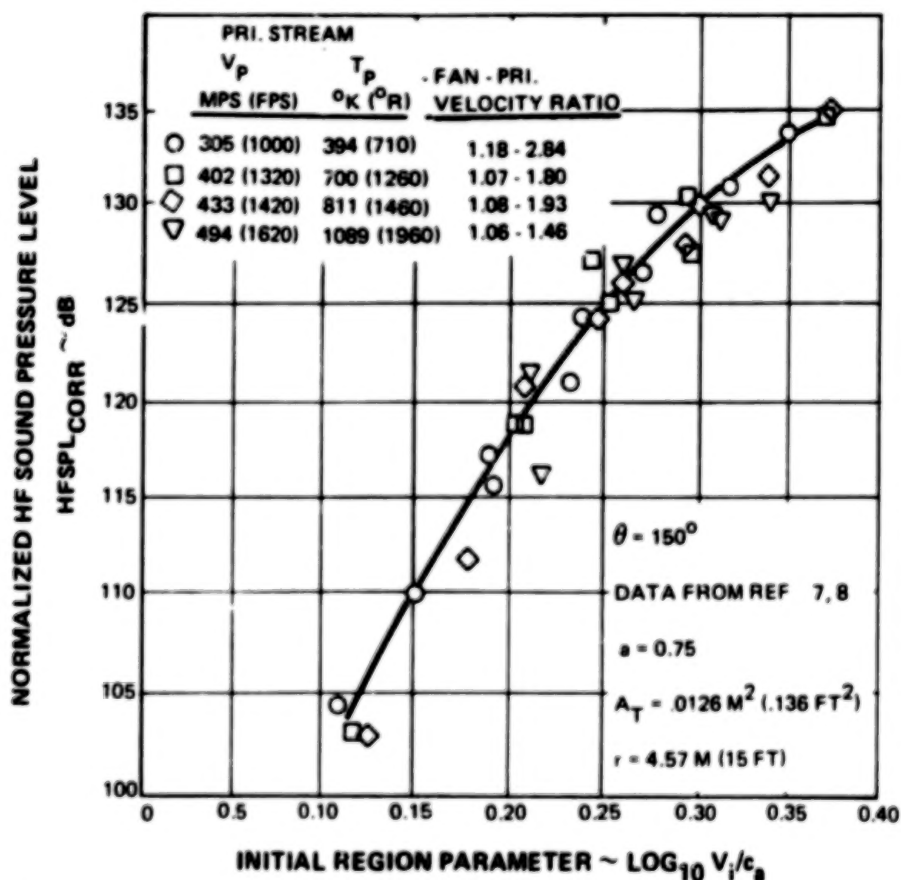


Figure 5.2-16 Normalization of the High Frequency Mixing Noise Component at 150° With Respect to Nozzle Operating Condition

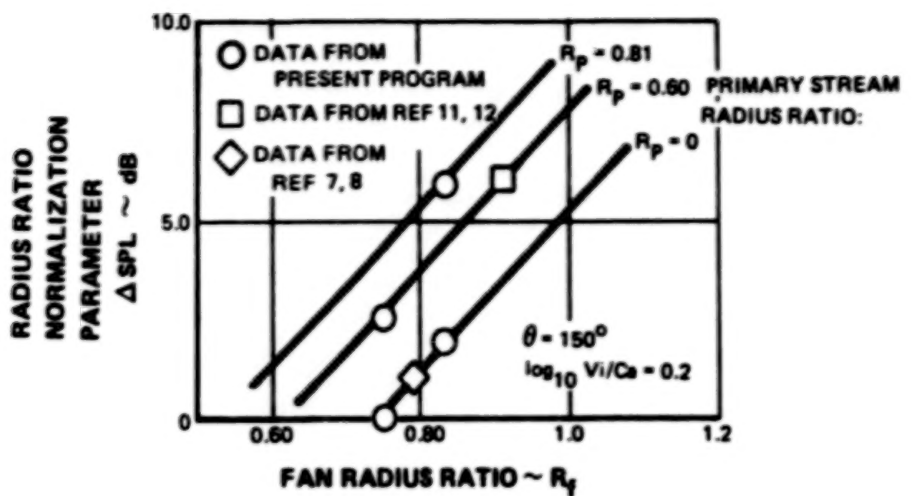


Figure 5.2-17 Definition of ΔSPL as a Function of Fan Stream Radius Ratio and Primary Stream Radius Ratio

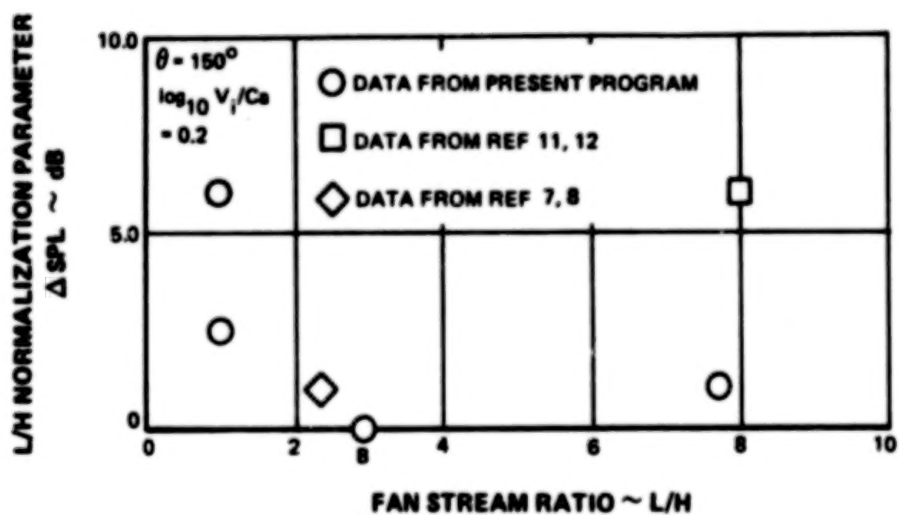


Figure 5.2-18 Definition of ΔSPL as a Function of Fan Stream Ratio L/H

TABLE 5.2-1
SUMMARY OF THE FUNCTION Δ SPL
FOR THE INITIAL REGION MIXING NOISE

θ (Deg.)	Δ SPL ~ dB
$60 \leq \theta < 75$	$-(222.2 \log \frac{V_i}{c_a} - 95.1)(R_f - 0.69)$
$75 \leq \theta < 95$	$-(99.7 \log \frac{V_i}{c_a} - 44.9)(R_f - 0.69)$
$95 \leq \theta < 115$	$-(94.4 \log \frac{V_i}{c_a} - 35.9)(R_f - 0.69)$
$115 \leq \theta < 135$	$-(151.8 \log \frac{V_i}{c_a} - 57.7)(R_f - 0.69) - (16.7 \log \frac{V_i}{c_a} - 6.3)R_p$
$135 \leq \theta < 160$	$-(131.1 \log \frac{V_i}{c_a} - 49.8)(R_f - 0.69) - (12.3 \log \frac{V_i}{c_a} - 4.7)R_p$

The normalized high frequency noise component, $HFSPL_{nor}$, was plotted versus $\log V_i/c_a$ for angles of 70, 90, 110, 130, and 150 degrees in Figures 5.2-19 through 5.2-23. Additional figures are contained in the Comprehensive Data Report (Reference 19). Included in Figures 5.2-20, 5.2-22, and 5.2-23 are data from References 11 and 12 (corrected by 2.0 dB as discussed in Section 5.1.1), References 7 and 8, and the present program. Figure 5.2-19 and 5.2-21 contain data only from the present program. The standard deviations associated with each angle are indicated in each figure. The data collapse in these figures demonstrates that Equations (5-15) through (5-18) provide a normalization of the high frequency noise component with respect to nozzle geometry and operating condition. The standard deviation of this normalization varies between ± 1.5 dB and ± 2.4 dB.

Figure 5.2-24 contains a set of summary curves for the normalized high frequency noise component, $HFSPL_{nor}$, as a function of $\log V_i/c_a$ for angles from 60 to 160 degrees.

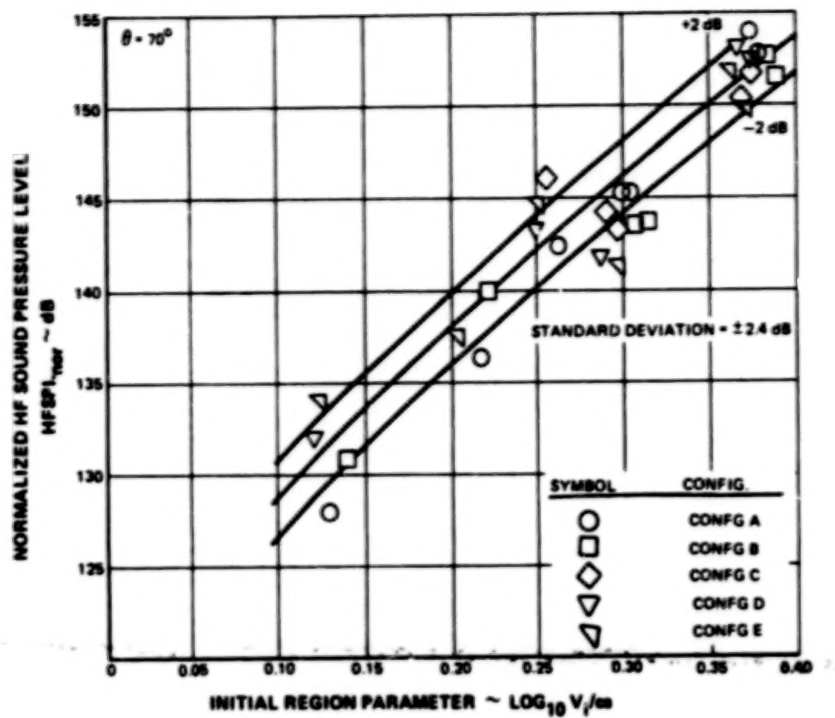


Figure 5.2-19 Normalization of the High Frequency Mixing Noise Component at $\theta = 70^\circ$ With Respect to Nozzle Operating Condition and Geometry

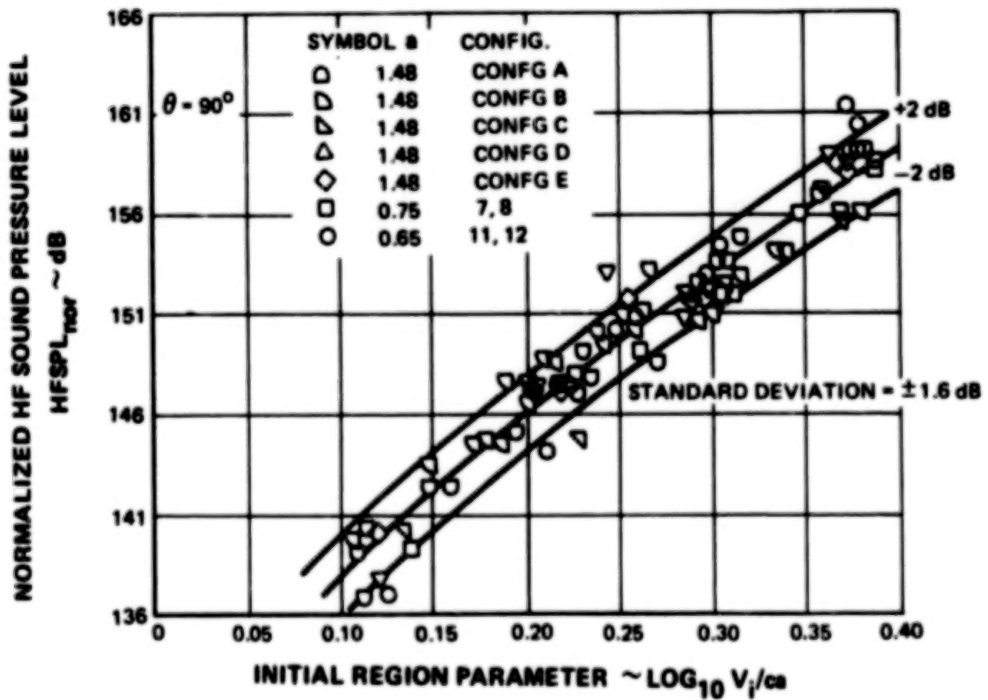


Figure 5.2-20 Normalization of the High Frequency Mixing Noise Component at $\theta = 90^\circ$ With Respect to Nozzle Operating Condition and Geometry

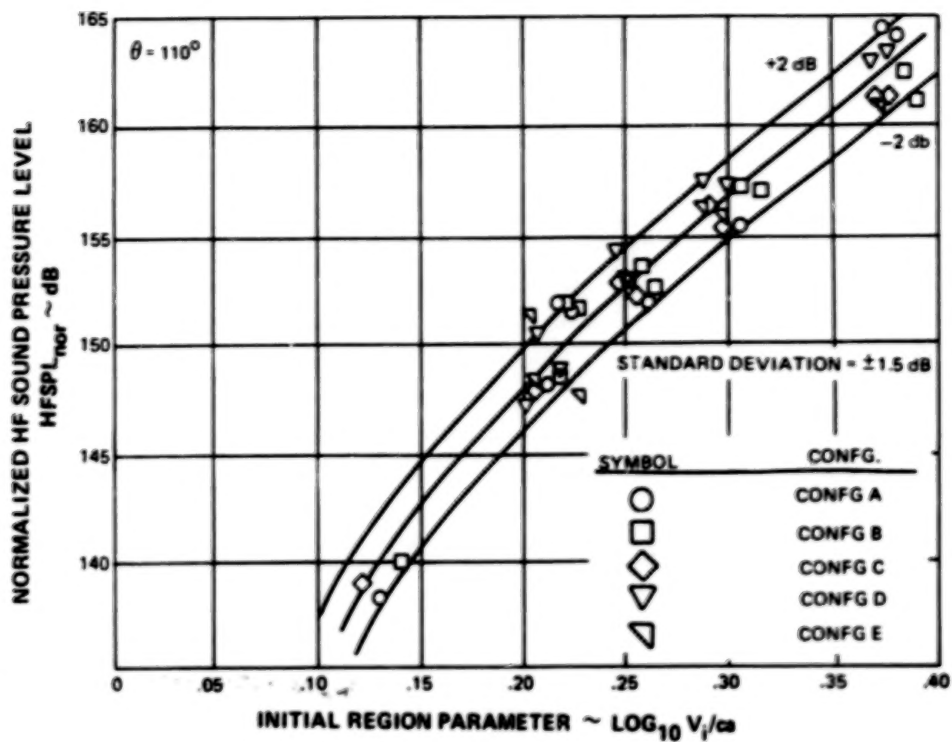


Figure 5.2-21 Normalization of the High Frequency Mixing Noise Component at $\theta = 110^\circ$ With Respect to Nozzle Operating Condition and Geometry

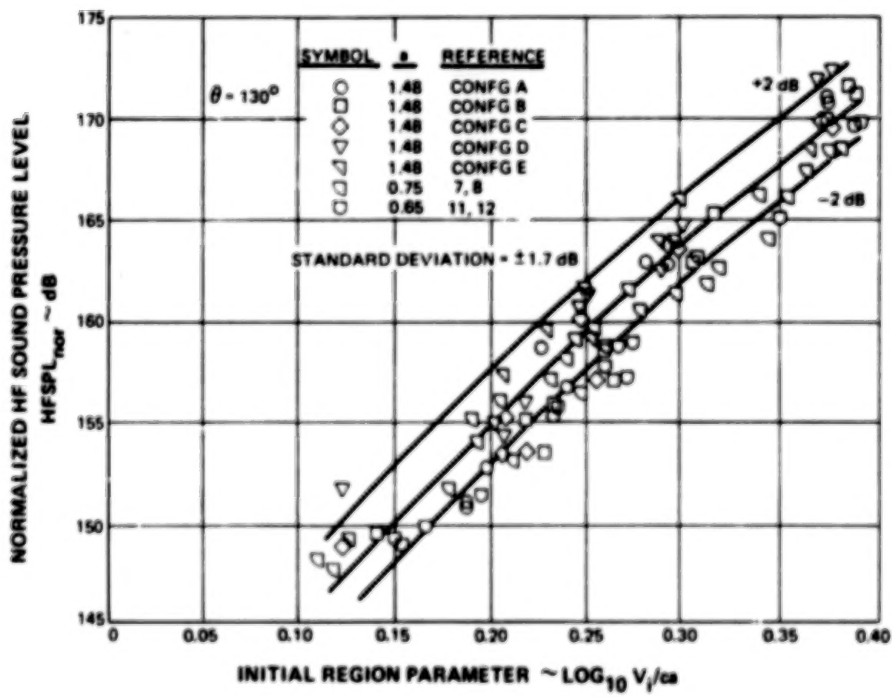


Figure 5.2-22 Definition of the High Frequency Mixing Noise Component at $\theta = 130^\circ$ With Respect to Nozzle Operating Condition and Geometry

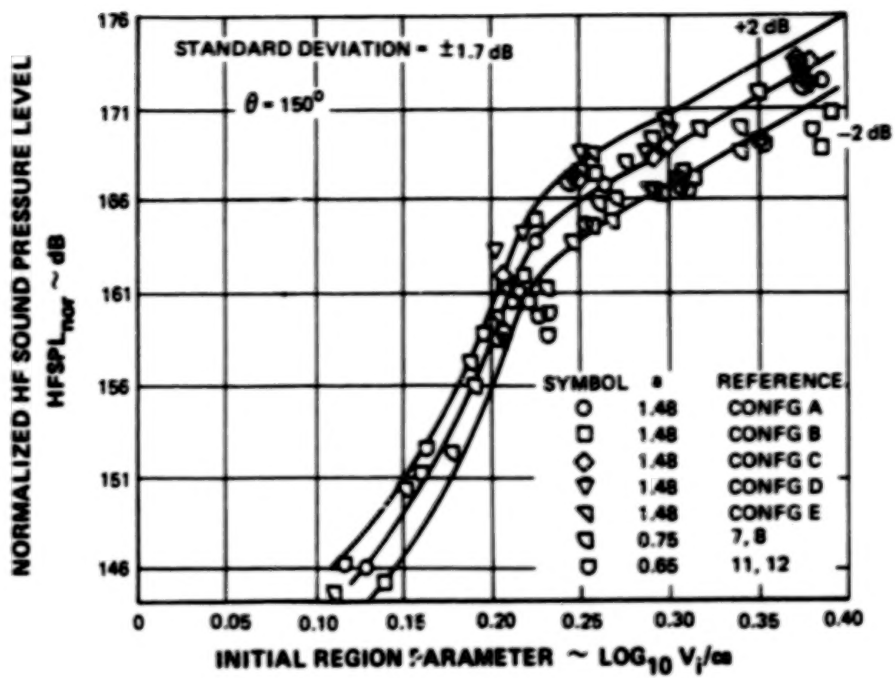


Figure 5.2-23 *Definition of the High Frequency Mixing Noise Component at $\theta = 150^\circ$ With Respect to Nozzle Operating Condition and Geometry*

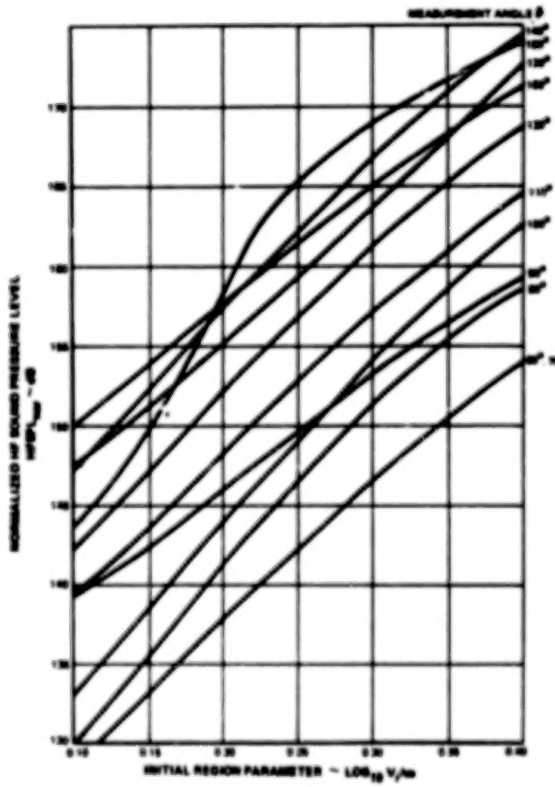


Figure 5.2-24 *Normalized High Frequency Mixing Noise Component Prediction Curves*

The spectra for $HFSPL_{nor}$ were normalized with respect to operating condition by the definition of a Strouhal number, S_i , based on the initial region characteristic parameter. The Strouhal number was defined as

$$S_i = \frac{(HF) H}{V_i}, \quad \text{Eq. (5-19)}$$

where HF is the characteristic frequency, and H is the annulus height of the fan stream. The Strouhal number was found to be a weak function of operating condition as illustrated in Figure 5.2-25. The frequency of the initial region noise is predicted by Equation (5-19) to within \pm one 1/3 octave band. The high frequency noise component spectral shapes are summarized in Figure 5.2-26.

Figures 5.2-24, 5.2-25 and 5.2-26, along with Equations (5-15) through (5-18), can be used to predict the high frequency noise component for an IVP coannular nozzle. The ideally expanded fan and primary stream conditions can be used to calculate the characteristic parameters V_i and T_{t_i} . These values, along with the ambient air conditions, can be used to calculate the absolute noise level $HFSPL$, from Equations (5-17) and (5-18), and Figures 5.2-25 and 5.2-26 can be used to define the spectral shape and frequency HF of the high frequency noise component. A sample prediction is contained in Section 5.5.

5.2.2 Development of Shock Noise Data Correlations

The shock noise model described in Section 5.1.3 was used to develop data correlation parameters for shock noise generated by either a supersonic fan stream or supersonic primary stream. The fan stream shock noise parameters are discussed in Section 5.2.2.1 and the primary stream shock noise parameters are described in Section 5.2.2.2.

5.2.2.1 Development of Fan Stream Shock Noise Data Correlations

For a supersonic fan stream, the coannular nozzle shock noise was correlated with the function of the shock noise parameters based on the fan stream conditions. That is, shock noise was a function of A_f/r^2 and $\sqrt{M_i^2 - 1}$, where M_i is a Mach number calculated from the initial region parameters V_i and T_{t_i} . The Mach number was obtained from perfect gas, isentropic compressible flow tables (see Reference 28, for example) using the initial region velocity, V_i , and temperature, T_{t_i} . For example, an ideally expanded velocity of 786 m/sec (2580 ft/sec) and temperature of 1089°K (1960°R) correspond to a Mach number of 1.405. For a fixed primary pressure ratio (1.53), fan stream temperature (1089°K (1960°R)), primary stream temperature (700°K (1260°R)), and observation angle (60 degrees), the shock noise levels were plotted versus $\log_{10} \sqrt{M_i^2 - 1}$ in Figure 5.2-27. The data in Figure 5.2-27 were obtained from References 7 and 8. The data collapsed to a straight line of slope 4.0, indicating that the shock noise correlation parameter $\sqrt{M_i^2 - 1}$ provides a first approximation to the correlation parameter for a coannular nozzle.

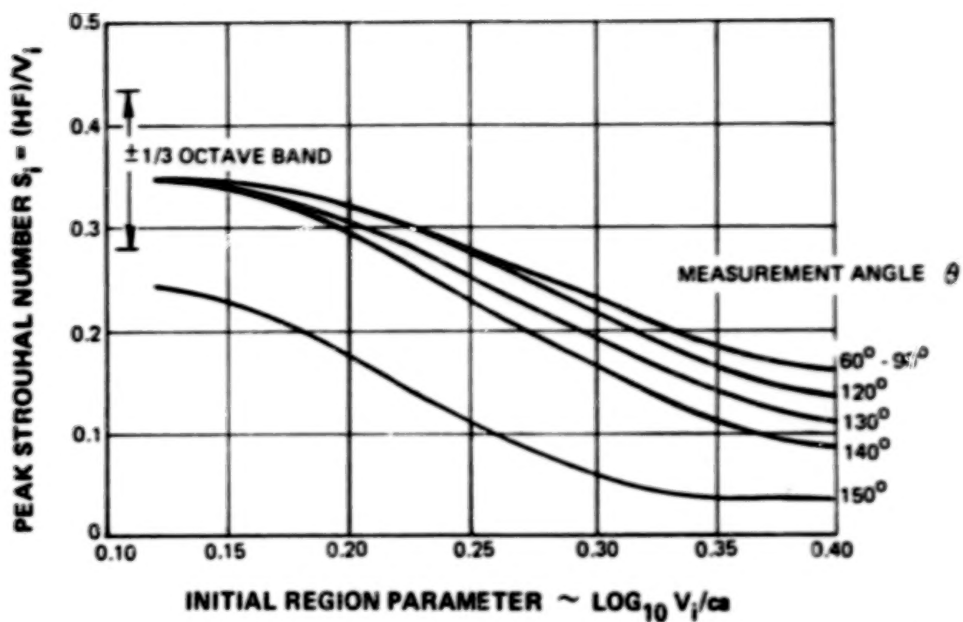


Figure 5.2-25 Definition of the High Frequency Mixing Noise Component Strouhal Number with Angle and Initial Region Velocity Parameter

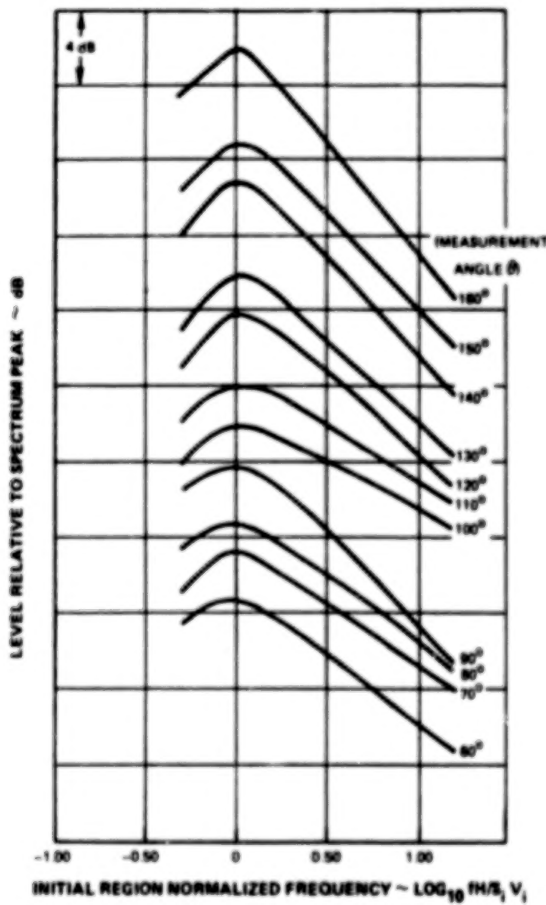


Figure 5.2-26 Definition of the High Frequency Mixing Noise Component Spectral Shapes

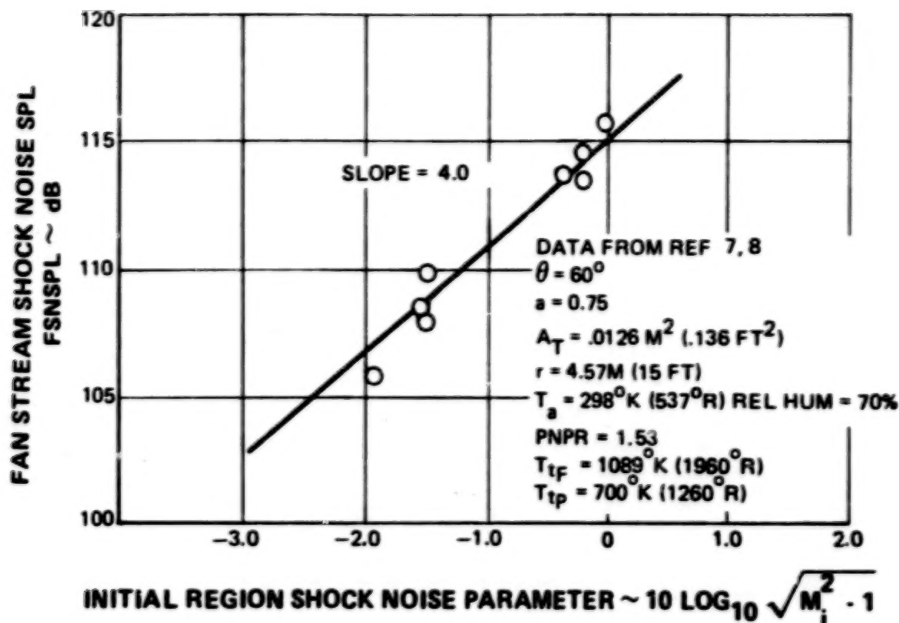


Figure 5.2-27 Correlation of Fan Stream Shock Noise Data with the Theoretical Shock Noise Parameter

While the correlation illustrated in Figure 5.2-27 collapsed shock noise data for fixed primary pressure ratio, fan temperature, and observation angle, IVP coannular nozzle shock noise in general is also a function of these three variables. Figures 5.2-28 and 5.2-29 illustrate the effect on fan stream shock noise of changes in primary pressure ratio and fan temperature. As primary pressure ratio or the fan temperature increased, with primary temperature held constant, the fan stream shock noise decreased. This demonstrates that the shock noise structure is a function of these two variables. Empirical correlations were developed to normalize shock noise with respect to fan temperature and primary pressure ratio. These corrections were established using data from References 7 and 8 and are illustrated in Figures 5.2-30 and 5.2-31. In Figure 5.2-30, shock noise data are plotted versus the fan temperature for two fan pressure ratios. The data trends are the same for both fan pressure ratios, and therefore the effect of fan temperature is independent of fan pressure ratio. In Figure 5.2-31, shock noise data are plotted versus primary pressure ratio. Included in Figure 5.2-31 are data from References 7 and 8, Reference 6, and the present program. Although the data are limited, shock noise levels are consistently reduced with increased primary pressure ratio.

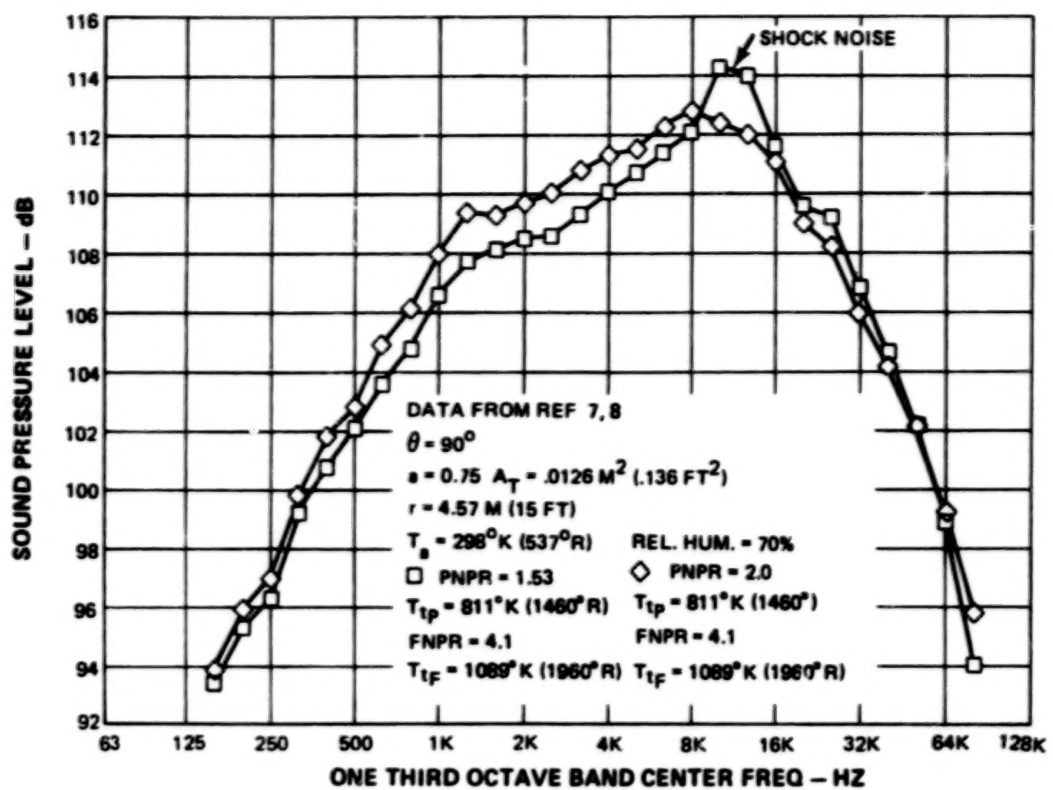


Figure 5.2-28 Definition of the Effect of PNPR on Fan Stream Shock Noise

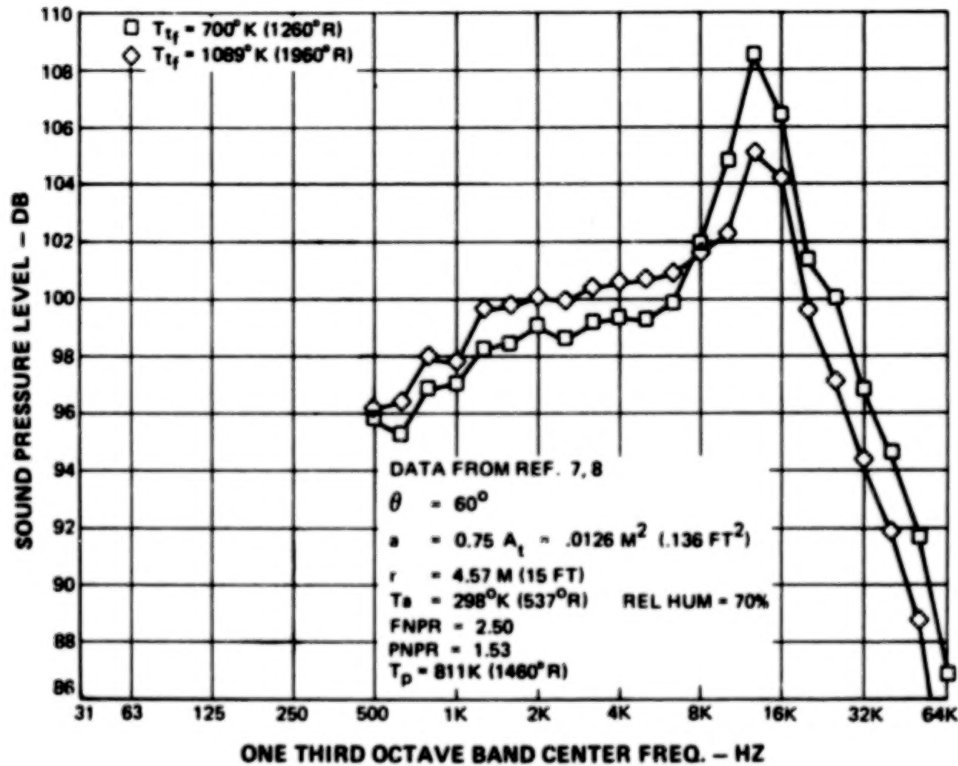


Figure 5.2-29 Example of the Effect of Fan Temperature on Fan Stream Shock Noise

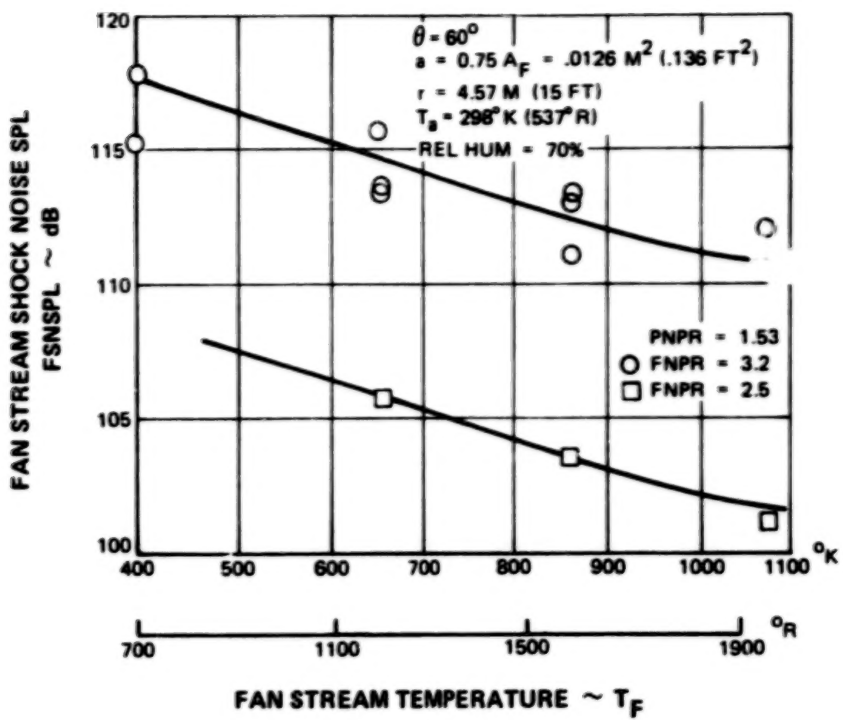


Figure 5.2-30 Correlation of FSNSPL at 60° with Fan Temperature

- FAN PRESSURE RATIO = 3.2, $\theta = 70^\circ$, $T_{fF} = 700^\circ\text{K}$ (1260°R), REF. 7, 8
- ◇ FAN PRESSURE RATIO = 3.04, $\theta = 90^\circ$, $T_{fF} = 589^\circ\text{K}$ (1060°R), REF. 6
- ▽ FAN PRESSURE RATIO = 2.5, $\theta = 70^\circ$, $T_{fF} = 1089^\circ\text{K}$ (1960°R), PRESENT PROGRAM

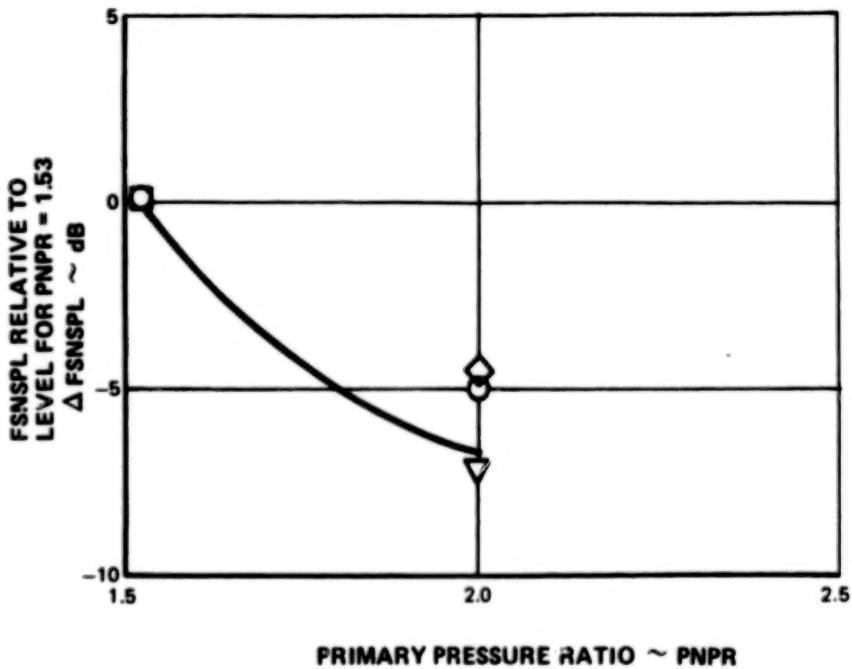


Figure 5.2-31 Correlation of Fan Stream Shock Noise SPL with Primary Primary Ratio

The data in Reference 6 consisted of a series of coannular nozzle acoustic tests. In addition to acoustic data, shadowgraphs of the flow shock structure were also obtained for selected operating conditions. Most of the acoustic data analysis was conducted on a power level or overall power level basis. Consequently, the conclusions in this study cannot directly be applied to the current investigation in which the characteristics of IVP coannular mixing noise and shock noise were investigated separately and on an SPL basis. Since the power level of the total spectrum can be dominated by the shock noise component at some operating conditions and by the mixing noise component at other operating conditions, conclusions about the behavior of shock noise based on analysis of the power spectrum alone can be misleading. As indicated in Figure 5.2-31, however, the data from Reference 6 are consistent with the results of the present investigation. It should be emphasized that only limited data could be compared between Reference 6 and the present program because the test matrices for the two programs did not overlap extensively. Data from Reference 6 were not available over a large enough range of fan temperatures to be included in Figure 5.2-30.

The shock noise component from the fan stream at 90 degrees can be normalized with respect to nozzle operating condition by the expression

$$FSNSPL_{nor} = FSNSPL - 10 \log A_f/r^2 + \Delta SPL (PNPR) + \Delta SPL (T_{tf}/T_a)$$

Eq. (5-20)

where the Fan Shock Noise Sound Pressure Level is denoted FSNSPL, the normalized Fan Shock Noise Sound Pressure Level is denoted FSNSPL_{nor}, ΔSPL (PNPR) is the correction for primary pressure ratio obtained from Figure 5.2-31, and ΔSPL (T_{tf}/T_a) is the correction for fan temperature obtained from Figure 5.2-30.

The necessity of relying on empirical corrections for primary pressure ratio and fan temperature introduces an uncertainty when predictions are made for parameters not included in the data base; that is, for primary pressure ratios less than 1.53 or greater than 2.5 and for fan temperatures greater than 1089°K (1960°R). Experimental evidence was not available to verify the procedure outside this range. The data that would be required to extend the Harper-Bourne and Fisher theory to IVP coannular nozzles include: (1) data on the change in shock structure with fan and primary temperatures and pressure ratios, (2) data on the shock strength as a function of fan and primary temperatures and pressure ratios, and (3) data on the turbulence properties of eddies convected through the shock structure. Extrapolations to fan temperatures and primary pressure ratios outside of the data base can be made using the formulas in Table 5.2-II, which were developed from Figures 5.2-30 and 5.2-31. A discussion of the accuracy of the extrapolations is contained in Section 5.4.

Shock noise data from References 7, 8, 9, and 10 and the present program, normalized by Equation (5-20), are correlated versus $\log \sqrt{M_f^2 - 1}$ in Figure 5.2-32. The data from References 11 and 12 were corrected by 2.0 dB, as discussed in Section 5.1.1. The data collapsed to a straight line with a standard deviation of ± 2.0 dB.

TABLE 5.2-II
DEFINITION OF FAN SHOCK NOISE NORMALIZATION FACTORS

$$\Delta \text{SPL} (\text{PNPR}) = 60.2 \log \left(\frac{\text{PNPR}}{1.53} \right) \text{ dB}$$

$$\Delta \text{SPL} (T_{tf}/T_a) = 12.5 \log (T_{tf}/T_a) \text{ dB}$$

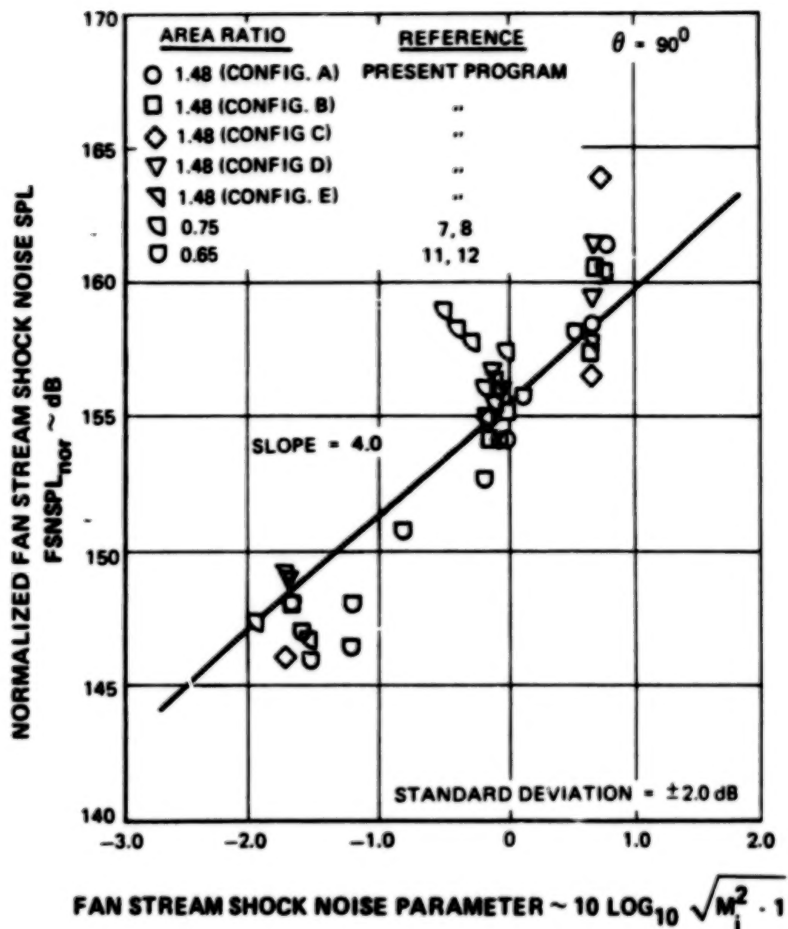


Figure 5.2-32 Definition of the Normalized Fan Stream Shock Noise Component Peak SPL at 90°

The shock noise from IVP coannular nozzles appeared to have a distinct directivity pattern as opposed to the shock noise from single stream convergent nozzles which tends to be omnidirectional. Figure 5.2-33 contains shock noise correlations for several different angles using data from References 7 and 8. The data in Figure 5.2-33 were used to define the directivity curve in Figure 5.2-34. Shock noise levels in Figure 5.2-34 are referenced with respect to those levels at 90 degrees.

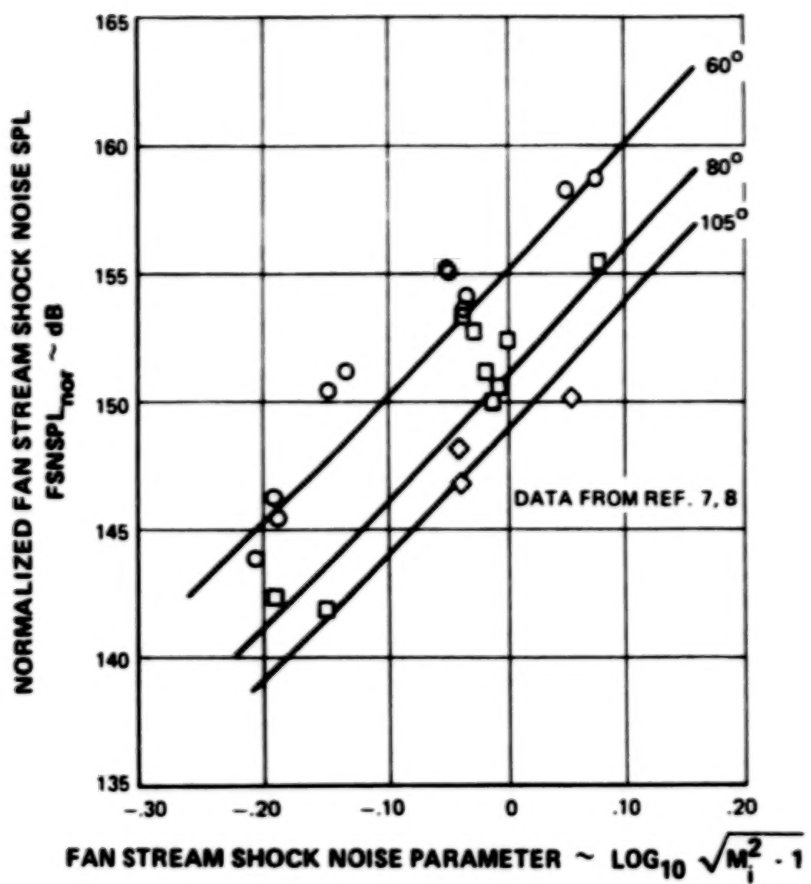


Figure 5.2-33 Comparison of the Normalized Fan Stream Shock Noise Component Peak SPL at 60° , 80° , and 105°

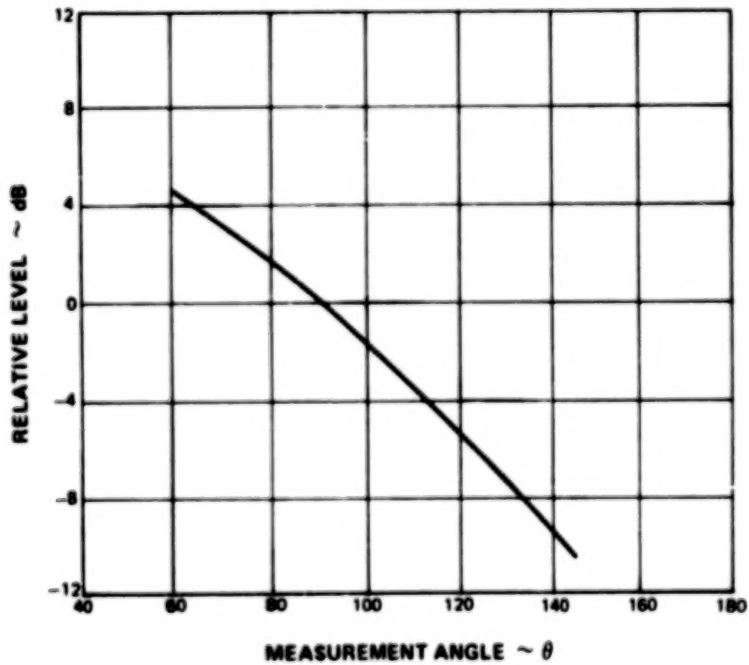


Figure 5.2-34 Directivity Factor for Fan Stream Shock Noise

A Strouhal number for the fan stream shock noise, S_{FSN} , was defined using the expression from Section 5.1.3, as

$$S_{FSN} = \frac{FSNF \cdot \frac{\{(1 + M_{ci} \cos \theta)^2 + (0.19 M_{ci})^2\}^{1/2} L_{sf}}{V_{ci}}}{}, \quad \text{Eq. (5-21)}$$

where L_{sf} is defined as

$$L_{sf} = 1.10H \sqrt{M_i^2 - 1}, \quad \text{Eq. (5-22)}$$

and

$$V_{ci} = 0.7 V_i. \quad \text{Eq. (5-23)}$$

The quantity **FSNF** was used to denote the characteristic Fan Shock Noise Frequency, and M_{ci} is the velocity V_{ci} divided by the ambient speed of sound. The shock noise Strouhal number was determined to be 0.52. As illustrated in Figure 5.2-35, the expression in Equation (5-20) can be used to calculate the peak shock noise frequency to within \pm one 1/3 octave frequency band. The normalized shock noise spectral shape is illustrated in Figure 5.2-36.

The shock noise peak level at any angle can be predicted from Equation (5-20), Figure 5.2-32, Table 5.2-II, and Figure 5.2-34. The correct peak frequency at each angle is defined in Equation (5-21) and the spectrum shape is defined in Figure 5.2-36. A sample prediction is contained in Section 5.5.

5.2.2.2 Development of Primary Stream Shock Noise Data Correlations

As the primary pressure ratio was increased, the fan stream shock noise was reduced in level, as illustrated in Figure 5.2-28. Along with this decrease in fan stream shock noise was an increase in primary stream shock noise. This effect is illustrated in Figure 5.2-37. As the primary pressure ratio increased from 1.53 to 2.00, the fan stream shock noise was reduced. A further increase in primary pressure ratio to 2.5 caused the primary stream shock noise, generated at a lower frequency, to dominate the total noise spectrum. The reduction in shock noise frequency as the primary flow becomes supersonic suggests that the shock structure, instead of being based on the annulus height of the fan stream, is generated across the primary flow. Shadowgraphs from Reference 6 demonstrate that as nozzle operating conditions were varied the shock structure also changed. Consequently, for primary pressure ratios greater than 1.89, a shock noise component based on the primary stream conditions was defined.

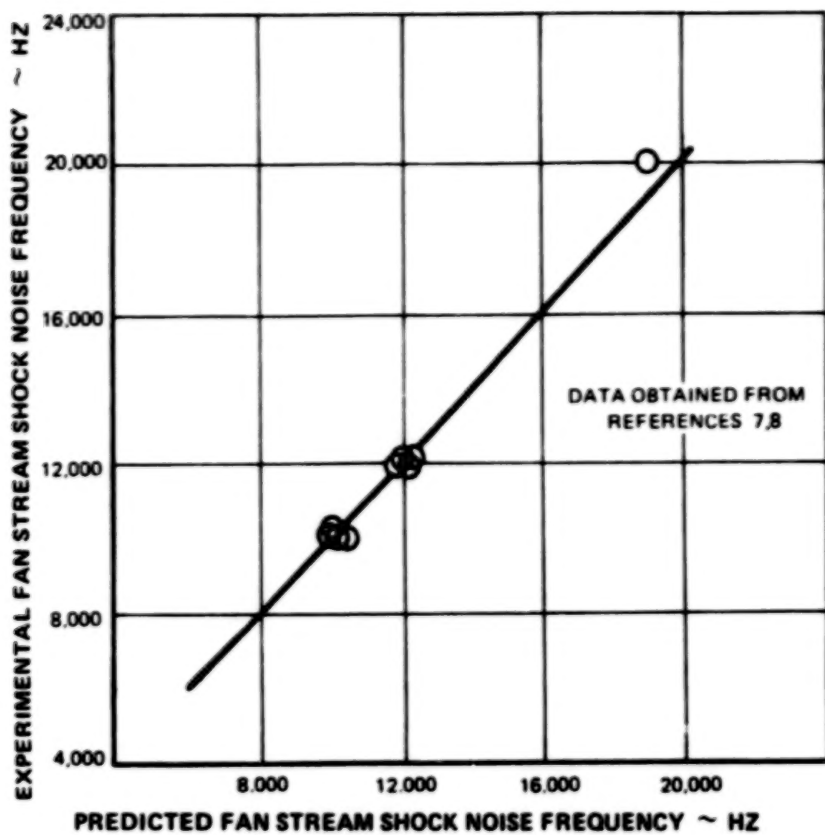


Figure 5.2-35 Comparison of the Predicted Fan Stream Shock Noise Peak Frequency with Experimental Values

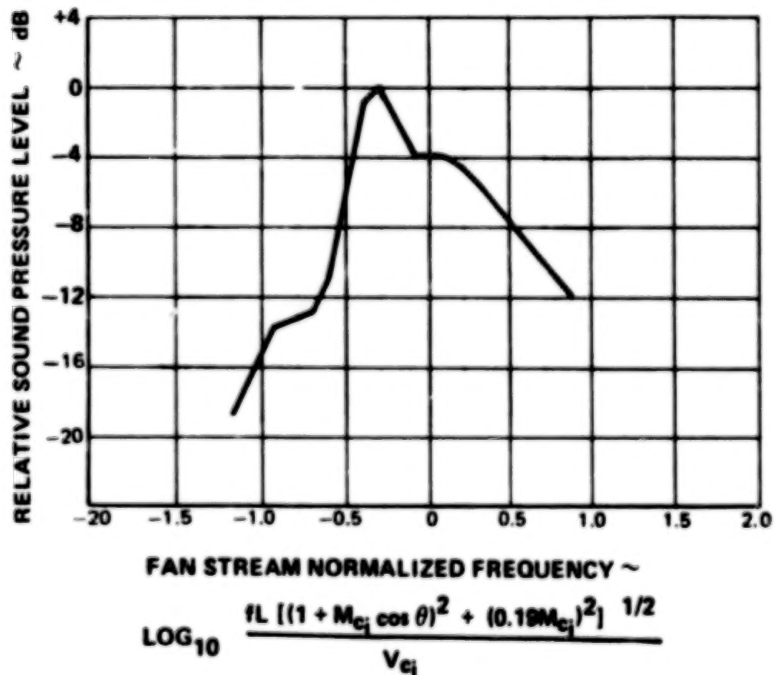


Figure 5.2-36 Definition of the Fan Stream Shock Noise Spectral Shape for All Angles

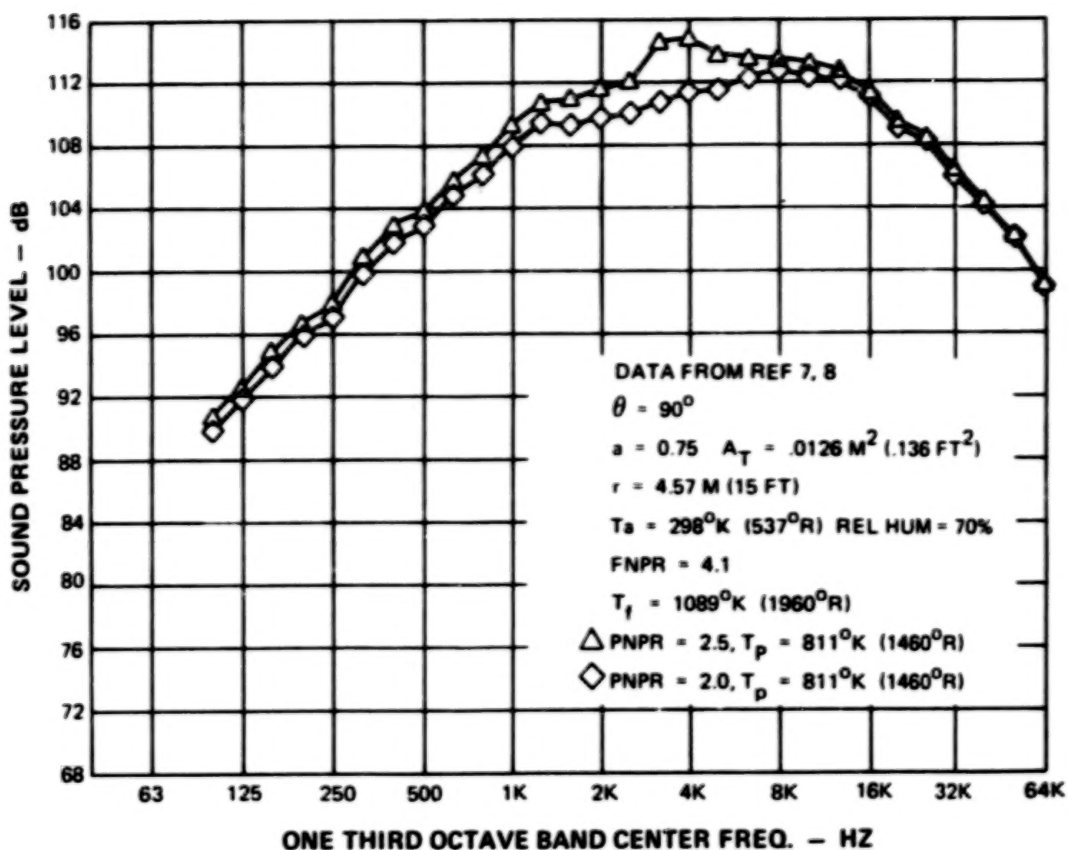


Figure 5.2-37 Example of Shock Noise Generated by a Supersonic Primary Flow

The Primary Shock Noise Sound Pressure Level, PSNSPL, was normalized by the expression

$$PSNSPL_{nor} = PSNSPL - 10 \log \frac{A_p}{r^2}, \quad \text{Eq. (5-24)}$$

where $PSNSPL_{nor}$ is the Primary Shock Noise Sound Pressure Level normalized with respect to nozzle geometry, and plotted versus the shock noise parameter $\sqrt{M_p^2 - 1}$, where M_p is the primary stream Mach number. Figure 5.2-38 contains a plot of the normalized shock noise component versus $\log \sqrt{M_p^2 - 1}$. Data from References 7 and 8 and the present program are contained in this figure. The data collapsed to a straight line with a standard deviation of ± 1.3 dB. The approximate slope of the line is 4.0.

A Strouhal number for the primary stream shock noise, S_{PSN} , was defined as

$$S_{PSN} = \frac{PSNF}{V_{cp}} \frac{\{(1 + M_{cp} \cos \theta)^2 + (0.19 M_{cp})^2\}^{1/2} L_{sp}}{V_{cp}}, \quad \text{Eq. (5-25)}$$

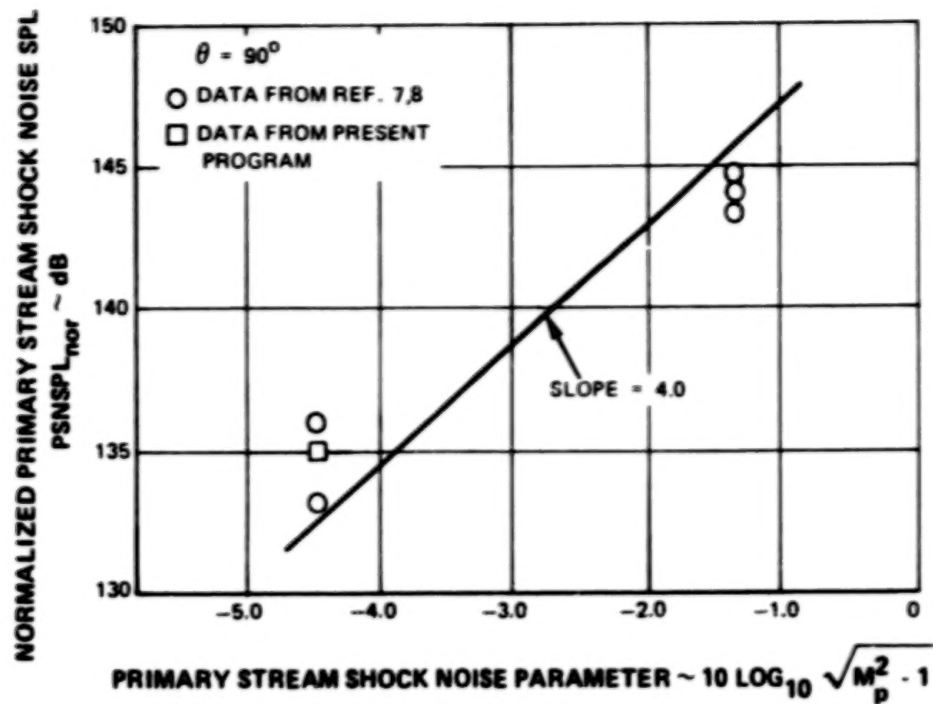


Figure 5.2-38 Correlation of the Normalized Primary Stream Shock Noise Levels with the Theoretical Shock Noise Parameter

where

$$L_{sp} = 1.1 D_p \sqrt{M_{cp}^2 - 1}, \quad \text{Eq. (5-26)}$$

$$D_p = 2 \sqrt{A_p / \pi},$$

and

$$V_{cp} = 0.7 V_p. \quad \text{Eq. (5-27)}$$

The quantity PSNF was used to denote the characteristic Primary Shock Noise Frequency, and M_{cp} is the velocity V_{cp} divided by the ambient speed of sound. The shock noise Strouhal number was determined to be 0.91. As illustrated in Figure 5.2-39, the expression in Equation (5-24) can be used to calculate the peak shock noise frequency to within \pm one 1/3 octave band. The spectrum shape and directivity for the primary stream shock noise are summarized in Figures 5.2-40 and 5.2-41.

The IVP coannular nozzle shock noise generated by the primary stream can be calculated from Equations (5-24), (5-25), and (5-26) and Figures 5.2-38, 5.2-40 and 5.2-41. A sample prediction is contained in Section 5.5.

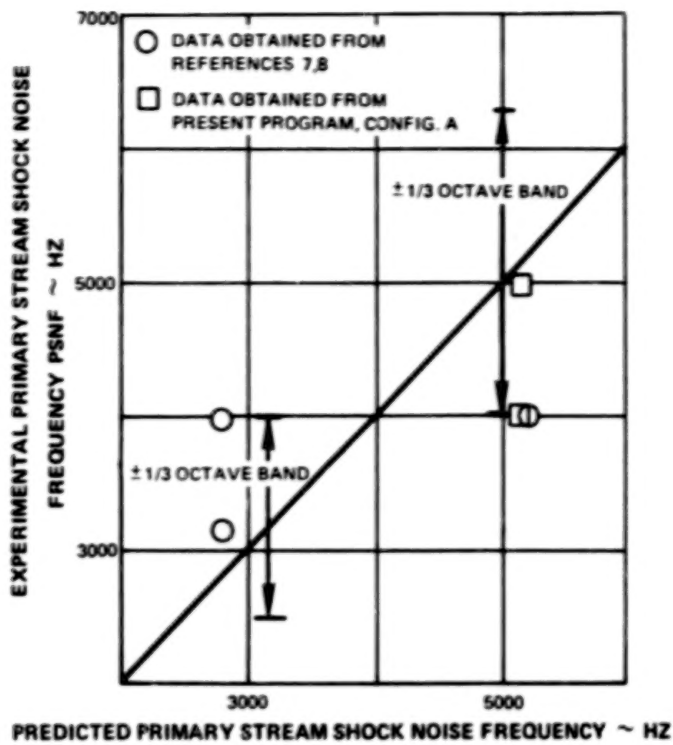


Figure 5.2-39 Comparison of the Predicted Primary Stream Shock Noise Peak Frequency with Experimental Values

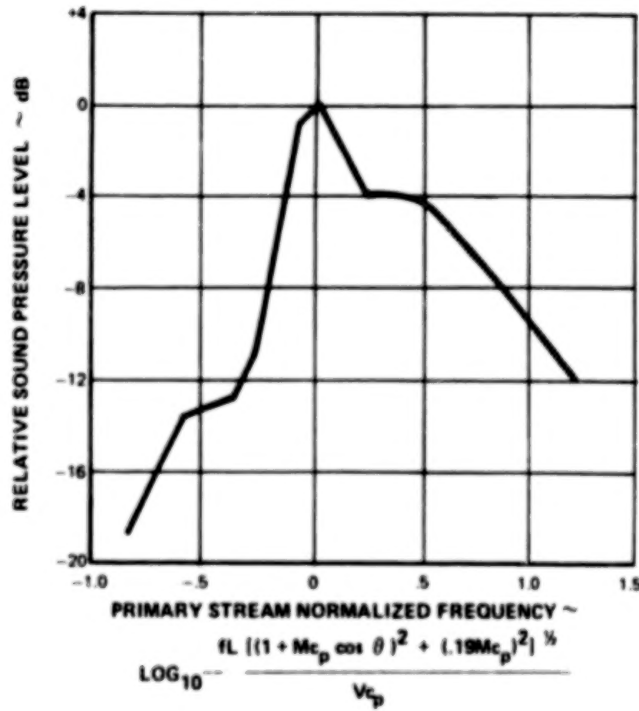


Figure 5.2-40 Definition of the Primary Stream Shock Noise Spectral Shape for All Angles

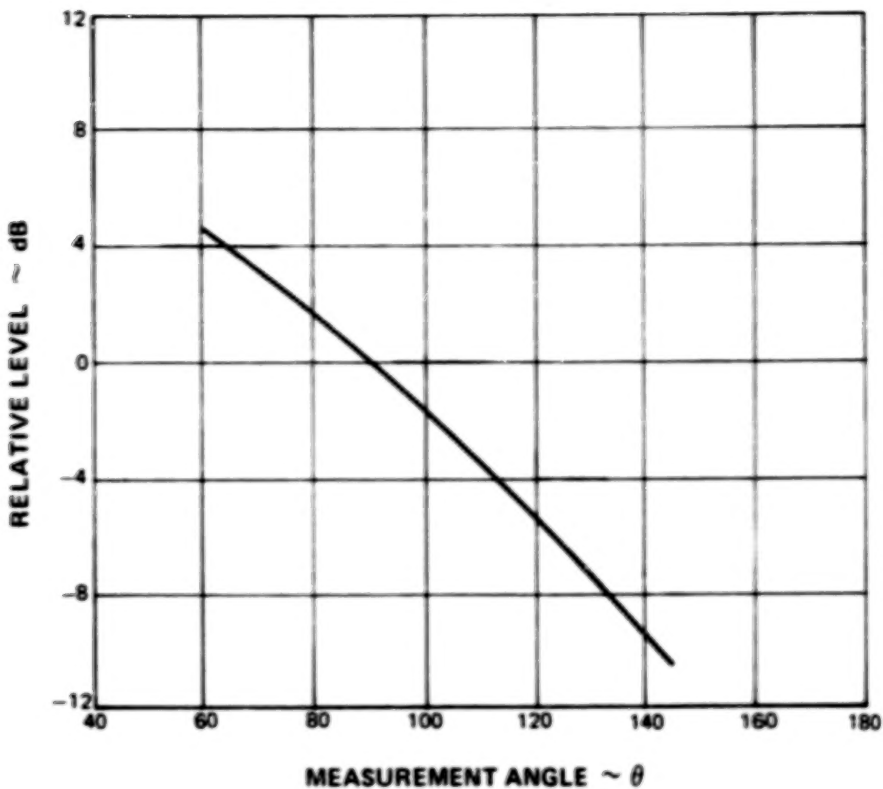


Figure 5.2-41 Directivity Factor for Primary Stream Shock Noise

5.3 FLIGHT JET EXHAUST NOISE PREDICTION PROCEDURE

The effect of flight on IVP jet exhaust noise was simulated in the United Technologies Research Center free jet wind tunnel (Reference 29) as reported in References 9 and 10. Simulated forward flight data were obtained for the 0.75 and 1.2 area ratio nozzles for a limited set of nozzle operating conditions. The simulated forward flight data were decomposed into four noise components in the same manner as described in Section 5.1-2. The effect of flight was then determined for each noise component. The following topics are discussed in Section 5.3: general background, definition of the effect of flight on mixing noise and definition of the effect of flight on shock noise.

5.3.1 General Background

A free jet wind tunnel was used to simulate the effect of flight on jet noise in References 9 and 10. The free jet wind tunnel is illustrated in Figure 5.3-1. Data were obtained in References 9 and 10 for an inverted velocity profile coannular nozzle placed in a free jet wind tunnel which simulated flight velocities from 0 to 129.5 m/sec (425 ft/sec). In References 9 and 10 two corrections were applied to the measured data to account for the wind tunnel shear layer refraction and the convection of sound by the wind tunnel flow. The shear layer refraction correction accounts for sound wave refraction by the wind tunnel shear layer. This correction is discussed in detail in Reference 20. Data corrected in this manner represent data measured in a frame of reference fixed with respect to the coannular nozzle

in an infinite air stream. Data obtained in this frame of reference correspond to data obtained by microphones moving with an aircraft. In this frame of reference, the air stream that extends to infinity convects the sound wave as it propagates from the source. The second correction applied to the data removes this convection of sound by the transformation

$$\tan \theta = \frac{\sin \theta_e}{\cos \theta_e - M_0} \quad \text{Eq. (5-28)}$$

where θ_e is the angle, measured with respect to the upstream jet axis, corresponding to the retarded angle of noise emission. The transformation in Equation (5-28) associates data at an angle θ with a retarded noise emission angle, θ_e .

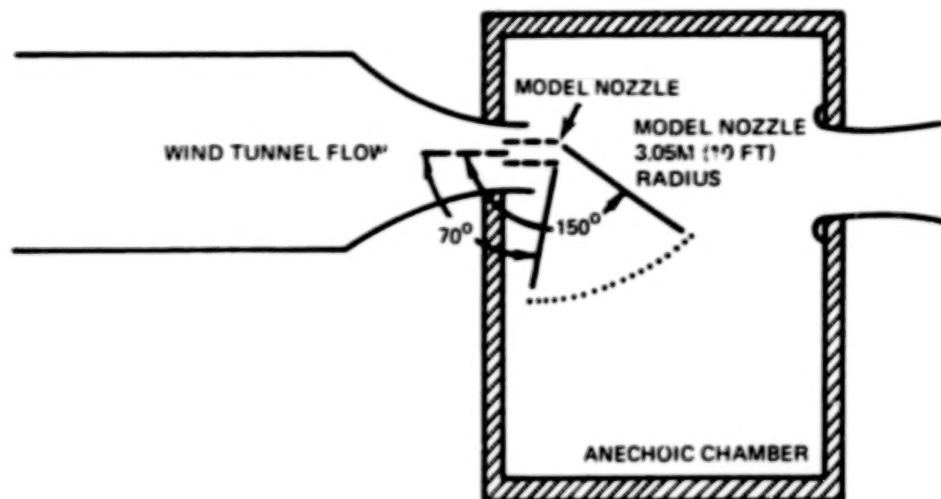


Figure 5.3-1 Free Jet Wind Tunnel Facility Used to Simulate the Effect of Forward Flight on Jet Exhaust Noise

Free jet wind tunnel simulated forward flight data corrected for the wind tunnel shear layer and transformed to the θ_e coordinate system correspond to data measured in an aircraft flyover test, except for a Doppler shift in frequency, when the flyover data are referenced to the retarded aircraft location. The Doppler shift in frequency is not exactly simulated, however, because the relative motion of source and observer is not simulated in a free jet wind tunnel. The Doppler shift that must be applied to the data is

$$f_{FLIGHT} = \frac{f_{FLIGHT_IM}}{1 - M_0 \cos \theta_e} \quad \text{Eq. (5-29)}$$

Free jet wind tunnel data corrected for the wind tunnel shear layer and convection and Doppler shifted in frequency thus are equivalent to aircraft flyover data with respect to the retarded noise emission aircraft location. This equivalence can be expressed as

$$SPL_{FLIGHT} (\theta_e, f_{FLIGHT}) = SPL_{FLIGHT SIM} (\theta_e, \frac{f_{FLIGHT SIM}}{1 - M_0 \cos \theta_e}) \quad \text{Eq. (5-30)}$$

5.3.2 Definition of the Effect of Flight on Mixing Noise

The effect of simulated forward flight on the noise is characterized in terms of a relative velocity exponent, n , given by

$$n = \frac{SPL_s (\theta) - SPL_{FLIGHT SIM} (\theta_e)}{10 \log \frac{V_j}{V_j - V_0}} \quad \text{Eq. (5-31)}$$

where SPL_s is the SPL generated under static conditions, $SPL_{FLIGHT SIM}$ is the SPL generated at a simulated forward flight velocity of V_0 and V_j is the jet velocity. In the model developed for the mixing noise produced by the initial region and merged region of the flow (see Section 5.1), the noise radiated by each region was defined in terms of the noise radiated by a convergent nozzle operated at the characteristic velocity, temperature, and area for each region. Therefore, Equation (5-31) was used to define relative velocity exponents for both the initial region and merged region using the appropriate initial or merged characteristic velocity in place of V_j in Equation (5-31).

The Doppler shift in frequency between static data and flight data includes the transformation between static and simulated flight and between simulated flight and flight data. If f_c is the frequency of noise generated by a turbulent eddy in its convected frame of reference (see Reference 26)

$$f_s = \frac{f_c}{[(1 + M_c \cos \theta)^2 + (0.19 M_c)^2]^{1/2}} \quad ,$$

and

$$f_{FLIGHT SIM} = \frac{f_c}{[(1 + (M_c - M_0) \cos \theta_e)^2 + (0.19 M_c)^2 \rightarrow (0.19 (M_c - M_0))^2]^{1/2}} \quad ,$$

where M_c is the eddy Mach number defined with respect to the ambient speed of sound. Then using these expressions and Equation (5-29),

$$f_{FLIGHT} = \frac{1}{1 - M_0 \cos \theta_e} \left[\frac{(1 + M_c \cos \theta)^2 + (0.19 M_c)^2}{(1 + (M_c - M_0) \cos \theta_e)^2 + (0.19 (M_c - M_0))^2} \right]^{1/2} f_s.$$

The expression in square brackets cannot in general be evaluated because M_c is not known for the complicated flow generated by an inverted velocity profile coannular nozzle. However, if $M_0 \ll M_c$ this expression is unity, and

$$f_{FLIGHT} = \frac{1}{1 - M_0 \cos \theta_e} f_s. \quad \text{Eq. (5-32)}$$

If the frequencies are Doppler shifted as indicated in Equation (5-32), SPL levels in flight can be calculated from the relation

$$SPL_{FLIGHT} (\theta_e) = SPL_s (\theta) - 10 \log \left(\frac{V}{V - V_0} \right)^n, \quad \text{Eq. (5-33)}$$

where V is the appropriate velocity for the initial region or merged region. The results of the free jet wind tunnel forward flight simulation thus can be used to predict noise levels in flight using Equations (5-32) and (5-33) along with the static prediction procedure.

The flow development of an IVP coannular nozzle is affected by an external flow as was discussed in Reference 15. In Reference 26 it was determined that the potential core of a convergent nozzle is lengthened by a factor $\sqrt{1 + m}/(1 - m)$, where m is the ratio of the external flow velocity divided by the jet velocity. Therefore, as a first approximation, the change in source location of the initial and merged regions due to external flow is

$$X_m = 7.0 \frac{\sqrt{1 + m_m}}{1 - m_m} D_t,$$

and

$$X_i = 1.5 \frac{\sqrt{1 + m_i}}{1 - m_i} D_t.$$

where m_m and m_i are defined as

$$m_m = \frac{V_o}{V_m}$$

and

$$m_i = \frac{V_o}{V_i}$$

Unless very high external flow velocities are required, the approximation $X_i \approx 1.5 D_t$ can be used for the initial region source location, and therefore, $r_i \approx r$ and $\theta_i \approx \theta$.

5.3.2.1 Definition of the Effect of Flight on Low Frequency Mixing Noise Component

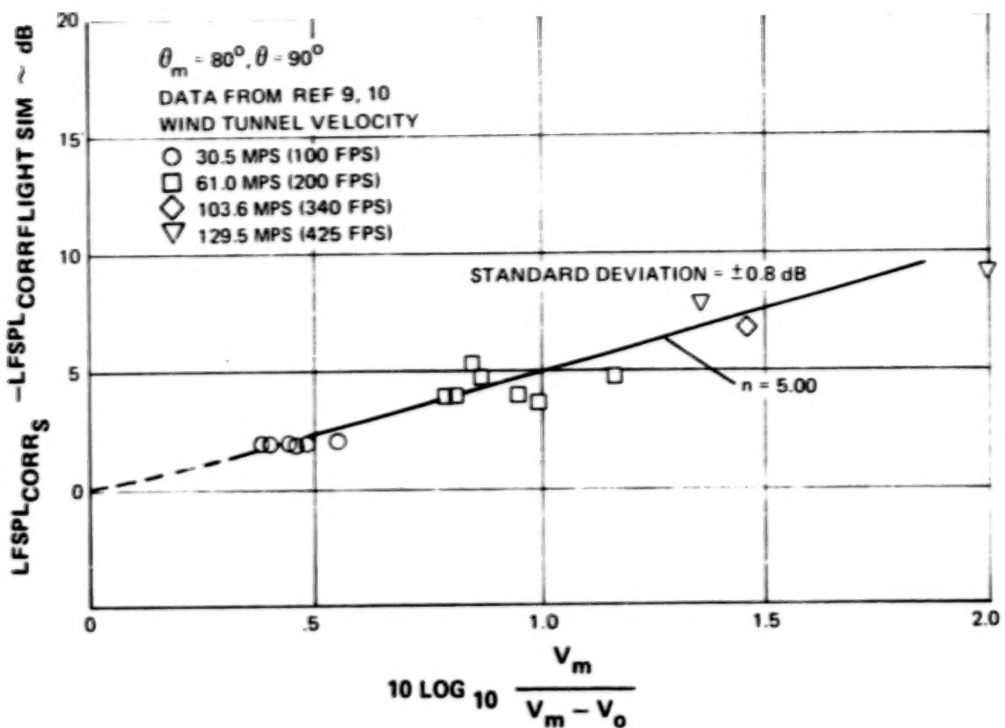
The effect of external flow velocity on the low frequency noise component, $LFSPL_{corr}$, is illustrated in Figures 5.3-2 and 5.3-3. In these figures, the noise component $LFSPL_{corr}$ is plotted versus $\log [V_m/(V_m - V_o)]$ for angles of $\theta_m = 80(\theta = 90)$ degrees and $\theta_m = 144(\theta = 150)$ degrees, respectively. The angle θ_m , measured with respect to the merged region source location, was calculated from Equation (5-5) using an average value of 0.24 for m_m in Equation (5-34). The free jet velocity, V_o , was varied between static conditions and 129.5 m/sec (425 ft/sec). The data collapse demonstrates that the effect can be correlated on the basis of the relative velocity parameter $\log [V_m/(V_m - V_o)]$. The standard deviations associated with each angle are contained in Figure 5.3-1 and 5.3-2; in both figures the standard deviation is ± 0.8 dB.

The flight exponents are actually a weak function of frequency as can be observed in Reference 30 in which high frequency noise reductions are slightly less than low frequency reductions. Since exponents were calculated only for the spectral peaks of the initial region and merged region mixing noise components, a small error is introduced at other frequencies. As evidenced by the comparisons between predictions and data discussed in Section 5.6, these errors are small.

It should be noted that the angle θ corresponds to the angle θ_m , measured with respect to the merged region source location, as discussed in Section 5.2.1. Therefore, θ_m should be used in Equation (5-28) to calculate a retarded angle θ_{em} which in general, will be different than the angle θ_e corresponding to θ . In general, the static prediction must be iterated to an angle θ_m which, when transformed using Equation (5-28), yields an angle θ_{em} that is the same as θ_e .

A summary of the relative velocity exponents for the merged region velocity noise component, defined as n_m , is contained in Figure 5.3-4. The flight correction for the parameter $LFSPL$ is then defined as

$$LFSPL_{FLIGHT}(\theta_e) = LFSPL_s(\theta) - 10 \log \left(\frac{V_m}{V_m - V_o} \right)^{n_m} \quad . \quad \text{Eq. (5-35)}$$



MERGED REGION FLIGHT CORRELATION PARAMETER ~

Figure 5.3-2 Correlation of the Low Frequency Mixing Noise Component at $\theta_m = 80$ ($\theta = 90$) Degrees with Relative Velocity

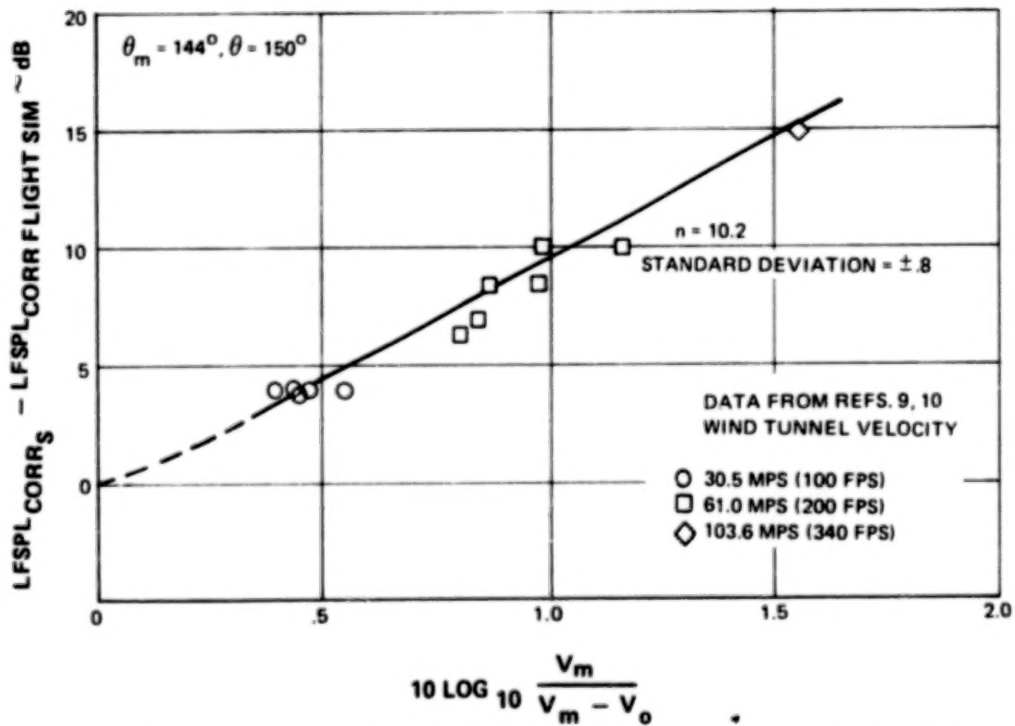


Figure 5.3-3 Correlation of the Low Frequency Mixing Noise Component at $\theta_m = 144$ ($\theta = 150$) Degrees with Relative Velocity

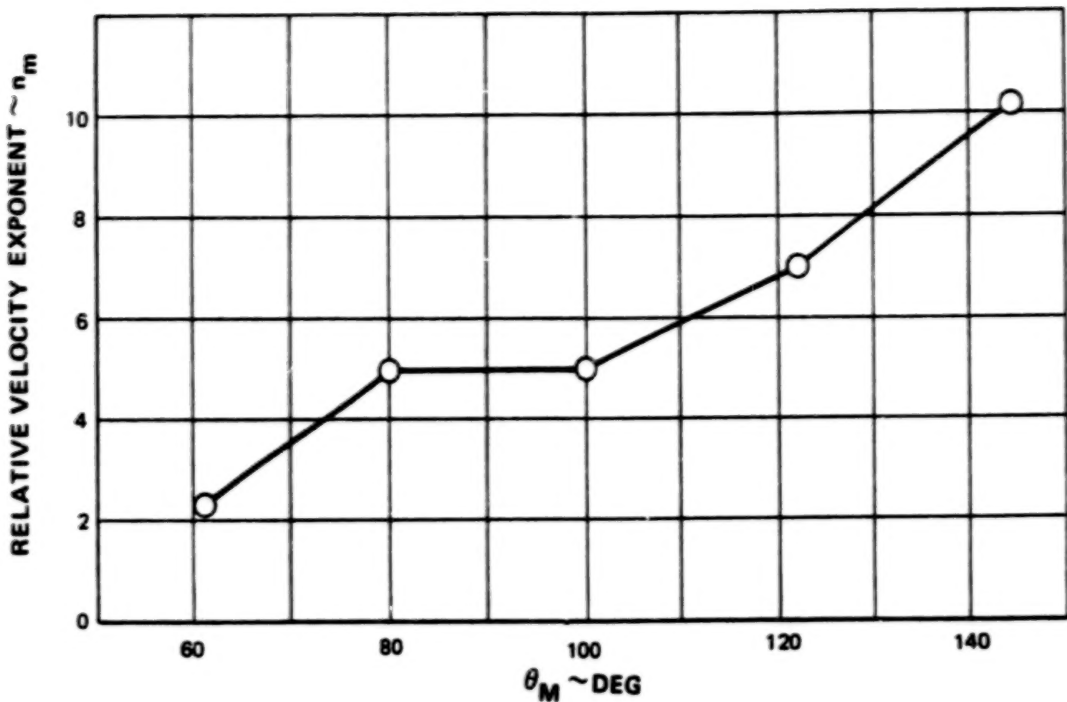


Figure 5.3-4 Definition of the Relative Velocity Exponent for the Low Frequency Mixing Noise Component

5.3.2.2 Definition of the Effect of Flight on the High Frequency Mixing Noise Component

The effect of external flow velocity on the high frequency noise component, $HFSPL_{corr}$, is illustrated in Figures 5.3-5 and 5.3-6. In Figures 5.3-5 and 5.3-6 the noise component $HFSPL_{corr}$ is plotted versus $\log [V_i/(V_i - V_o)]$ for angles of 90 and 150 degrees. The data collapse indicates that the effect of flight can be correlated on the basis of the relative velocity parameter $\log V_i/(V_i - V_o)$. The standard deviations associated with each angle are contained in Figures 5.3-5 and 5.3-6; at 90 degrees the standard deviation is ± 2.0 dB and at 150 degrees the standard deviation is ± 2.7 dB. The larger standard deviation for the initial region data collapse may be a result of the change in source location as wind tunnel velocity is increased. Since source location changes as wind tunnel velocity increases, the angle θ_i also changes. In the analysis of the data it was assumed that $\theta_i \approx \theta$, and as a result this assumption may introduce an error at high wind tunnel velocities.

A summary of the relative velocity exponents for the initial region velocity noise component, defined as n_i , is contained in Figure 5.3-7. The flight correction for the parameter $HFSPL_{corr}$ is then defined as

$$HFSPL_{FLIGHT}(\theta_e) = HFSPL_s(\theta) - 10 \log \left(\frac{V_i}{V_i - V_o} \right)^{n_i} \quad . \quad \text{Eq. (5-36)}$$

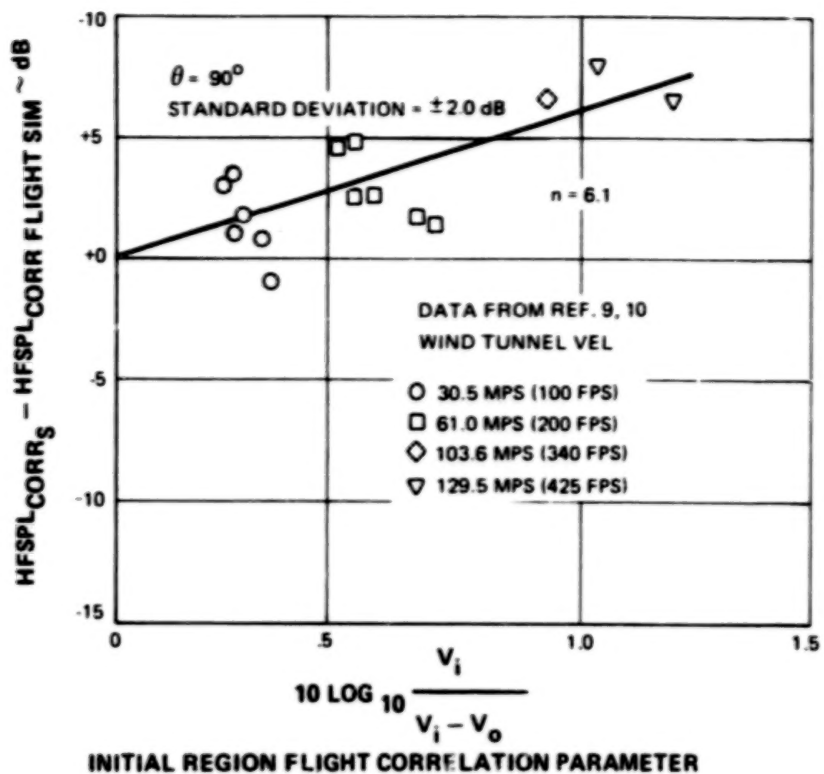


Figure 5.3-5 Correlation of the High Frequency Mixing Noise Component at 90° with Relative Velocity

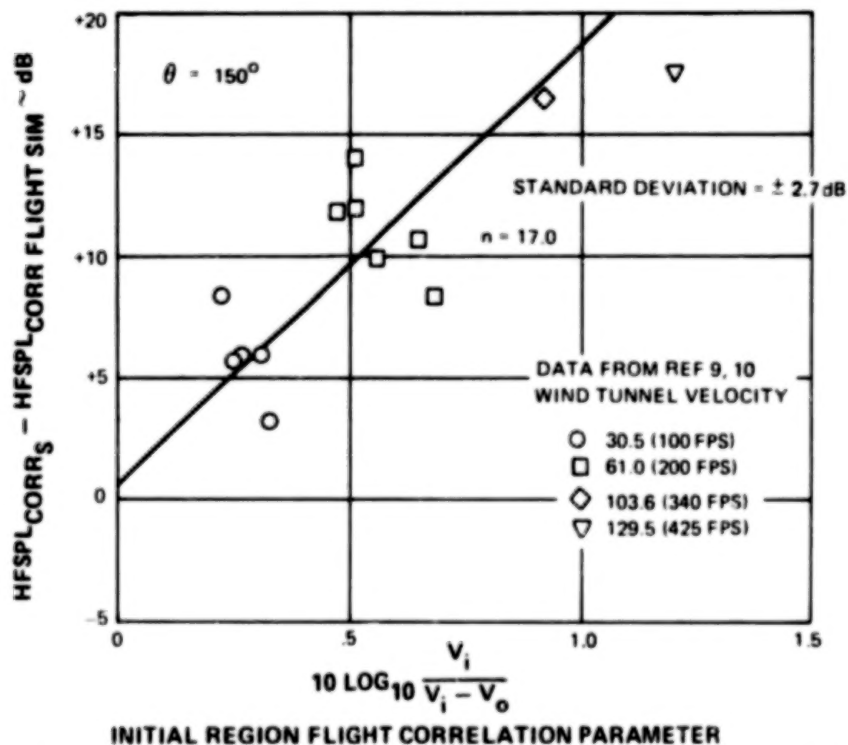


Figure 5.3-6 Correlation of the High Frequency Mixing Noise Component at 150° with Relative Velocity

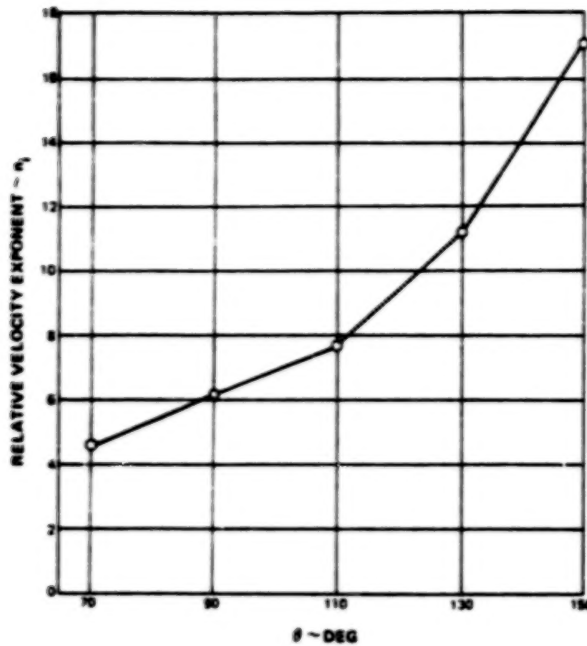


Figure 5.3-7 *Definition of the Relative Velocity Exponents for the High Frequency Mixing Noise Component*

A comparison of the initial region and merged region exponents in Figures 5.3-4 and 5.3-7 shows that the initial region exponents are larger than the merged region exponents at 150 degrees and approach the merged region exponents at 90 degrees. This behavior is consistent with the change of jet velocity observed in Reference 30 in the exponents of a convergent nozzle. As described in Reference 30, as the jet velocity of a convergent nozzle increased, the relative velocity exponent also increased. Since, on the average, the initial region velocities are higher than the merged region velocities, it would be expected on the basis of the data in Reference 30 that the initial region exponents would be larger than the merged region exponents.

5.3.3 Definition of the Effect of Flight on the Shock Noise Component

If shock noise is generated by a stationary source, the convective amplification factor for it should be of the form $(1 - M_0 \cos \theta)^{\text{exponent}}$ (Reference 31), where M_0 is the flight Mach number calculated with respect to the ambient speed of sound. Convective amplification is a factor arising from the relative motion of the source, medium, and observer, and the exponent is a function of the multipole character of the sources (Reference 31, for example). Figure 5.3-8 contains a plot of the shock noise level in the free jet wind tunnel measured with respect to the static noise levels, versus $\log(1 - M_0 \cos \theta)$. The data collapse to a line with a standard deviation of ± 0.6 dB. The slope of the line, 4.0, is the exponent. Then, the shock noise lever in flight can be calculated from the relation

$$\text{SNSPL}_{\text{FLIGHT}}(\theta_e) = \text{SNSPL}_s(\theta) - 10 \log(1 - M_0 \cos \theta_e)^{4.0}. \quad \text{Eq. (5-37)}$$

This expression applies to shock noise generated by either a supersonic fan stream or a supersonic primary stream.

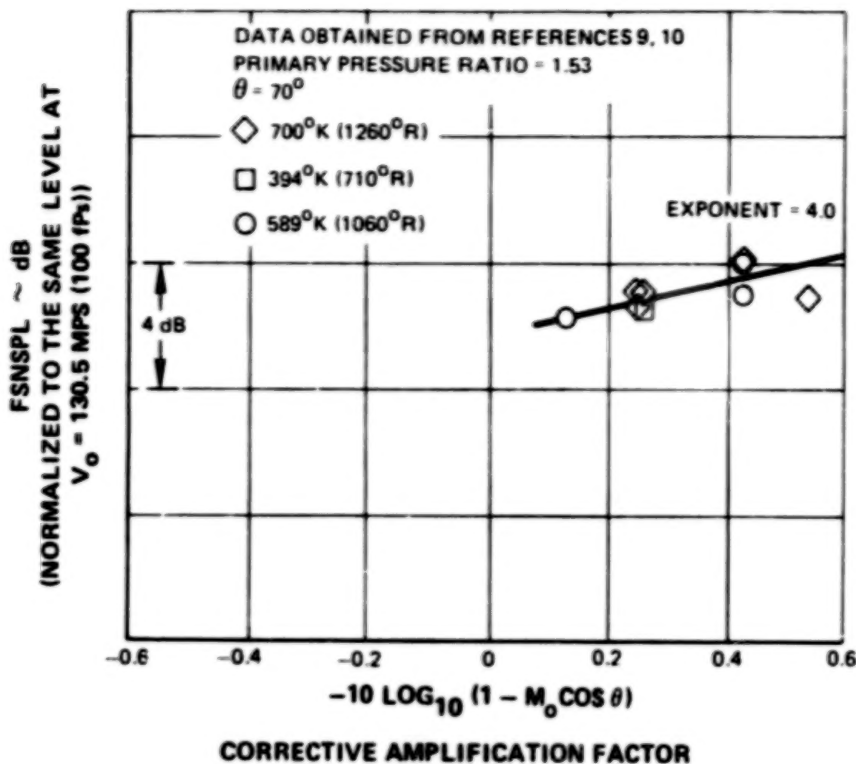


Figure 5.3-8 Definition of Shock Noise Convective Amplification Factor

5.4 SUMMARY OF ACOUSTIC PREDICTION PROCEDURE

The equations and figures required to predict the SPL spectra produced by an inverted velocity profile coannular jet are summarized in this section. The following topics are discussed: the general approach to the prediction procedure, summary of the static prediction procedure, and summary of the flight prediction procedure.

5.4.1 General Approach

Figure 5.4-1 summarizes the use of the prediction procedure. The input variables required for use of the prediction procedure are A_f , R_f , R_p , H , a , A_t , r , θ , V_f , V_p , T_{tf} , T_{tp} , $PNPR$, γ , $FNPR$, T_a , c_a , and V_o . All quantities are defined in the nomenclature section in this report. From these inputs, the high frequency mixing noise, low frequency mixing noise, fan stream shock noise, and primary stream shock noise components are then calculated at the position defined by the coordinates (r, θ) . The total noise spectrum at (r, θ) is the logarithmic sum of the four independent noise components.

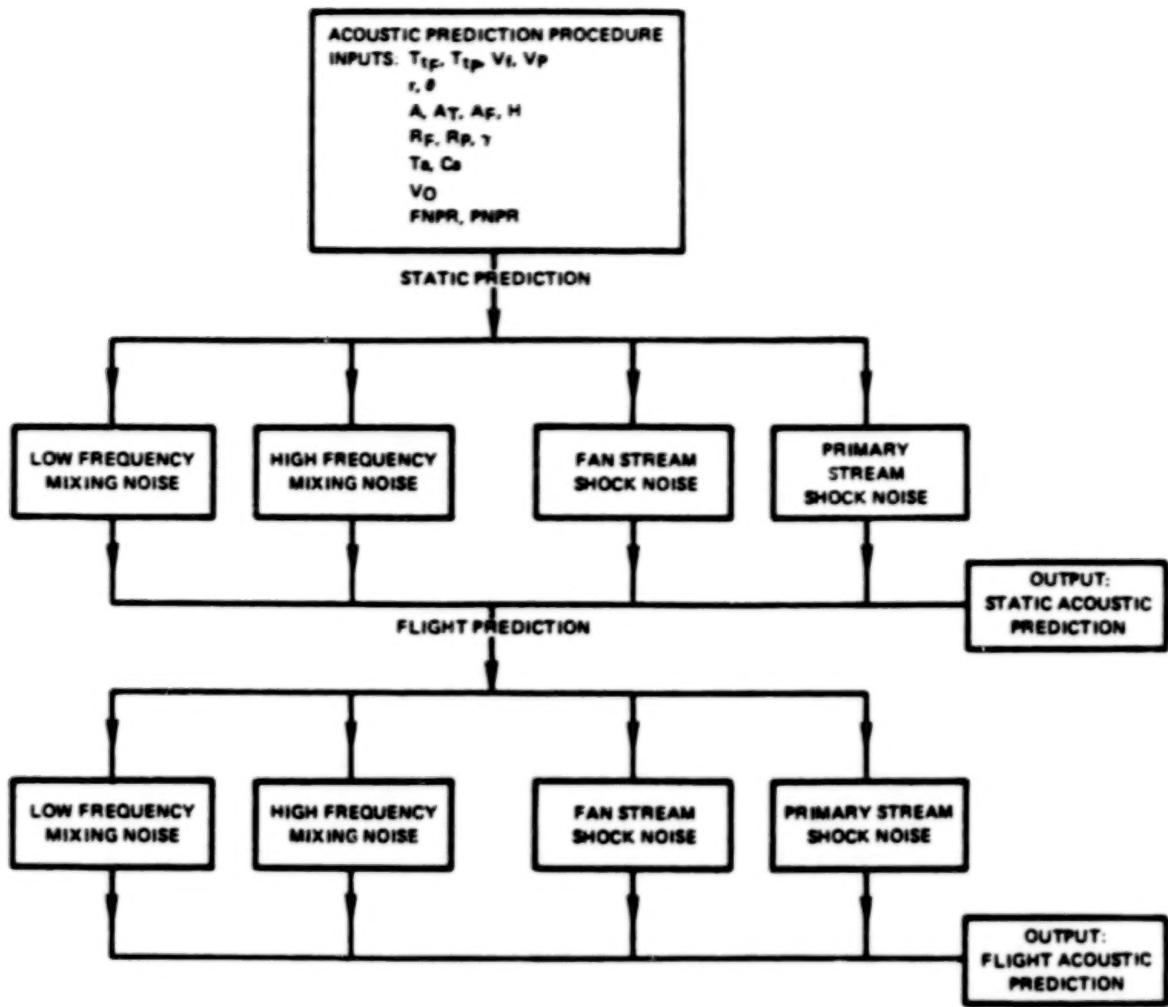


Figure 5.4-1 Flow Chart for the Inverted Velocity Profile Empirical Jet Engine Noise Prediction Procedure

5.4.2 Summary of the Static Acoustic Prediction Procedure

5.4.2.1 Low Frequency Mixing Noise Components

The static prediction of the low frequency mixing noise component is summarized in Figure 5.4-2. The coordinates (r_m, θ_m), measured with respect to the merged region source location, are first calculated using Equation (5-4) after calculating D_t from A_t using the expression $D_t = 2 \sqrt{A_t/\pi}$. Next, the merged region characteristic velocity and temperature, V_m and T_{t_m} , are calculated using Equations (5-9), (5-10) and (5-11). Using the ambient speed of sound, c_a , in conjunction with the merged region velocity, V_m , the normalized low frequency noise component, $LFSPL_{nor}$, can be obtained from Figure 5.2-12 at a given angle θ_m . The absolute low frequency noise level, $LFSPL$, is then determined using ω , as determined from Figure 5.2-1, A_t , r_m , T_{t_m} , and T_a in Equations (5-8) and (5-12).



Figure 5.4-2 Flow Chart for Prediction of the Static Low Frequency Mixing Noise Component

The characteristic low frequency, LF, is then calculated from Equation (5-14) using the merged region Strouhal number, S_m , obtained from Figure 5.2-13.

The low frequency mixing noise component is then obtained by defining the peak level of the low frequency mixing noise component spectrum, obtained from Figure 5.2-14, as LFSPL and defining the frequency corresponding to the peak level as LF.

5.4.2.2 High Frequency Mixing Noise Component

The static prediction of the high frequency mixing noise component is summarized in Figure 5.4-3. First, the initial region characteristic velocity and temperature, V_i and T_{t_i} , are calculated using Equations (5-15) and (5-16). Using the ambient speed of sound, c_a , in conjunction with the initial region velocity, V_i , the normalized high frequency noise component, $HFSPL_{nor}$, can be obtained from Figure 5.2-24 at the given angle θ . The absolute high frequency noise level, $HFSPL$, is then determined using ω , as defined in Figure 5.2-1. A_f , r , T_{t_i} , and ΔSPL (R_f , R_p , \log_{10} , V_i/c_a) in Equations (5-17) and (5-18). The function ΔSPL is determined from Table 5.2-1 using the inputs R_f and R_p and the quantity $10 \log V_i/c_a$.

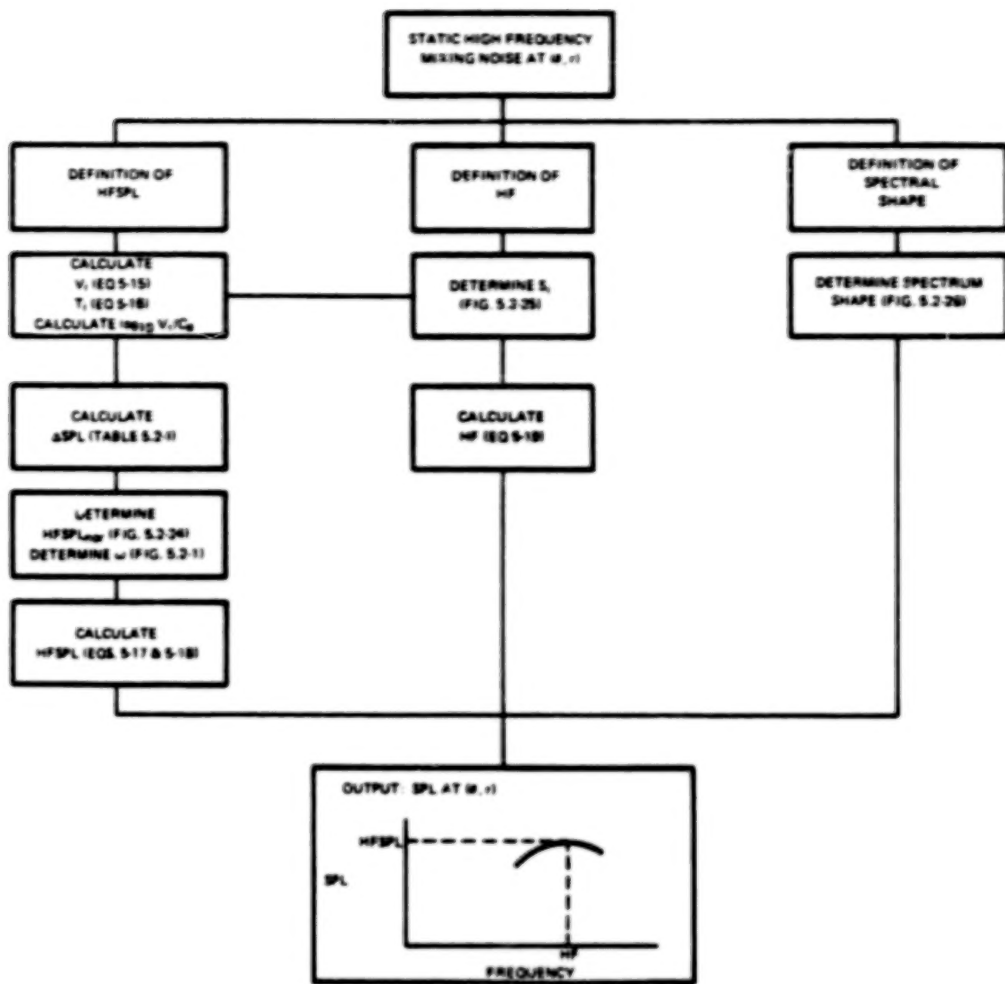


Figure 5.4-3 Flow Chart for Prediction of the Static High Frequency Mixing Noise Component

The characteristic high frequency, HF, is then calculated from Equation (5-19) using the initial region Strouhal number, S_j , obtained from Figure 5.2-25.

The high frequency mixing noise component is then obtained by defining the peak level of the high frequency mixing noise component spectrum, obtained from Figure 5.2-26, as HFSPL and defining the frequency corresponding to the peak level as HF.

5.4.2.3 Fan Stream Shock Noise

If the fan stream is supersonic ($FNPR > 1.89$), the fan stream shock noise component is calculated as indicated in Figure 5.4-4. First, the Mach number, M_i , is calculated from V_i , γ , and T_i ; using compressible adiabatic flow gas tables. Then, the normalized shock noise level, $FSNSPL_{nor}$, at 90 degrees is obtained from Figure 5.2-32. The absolute fan stream shock noise level, $FSNSPL$, is then determined using Equation (5-24). The quantities

ΔSPL ($\frac{PNPR}{1.53}$) and ΔSPL (T_{if}/T_a) are determined from Table 5.2-II. The absolute fan stream

shock noise levels at angles other than 90 degrees are obtained by applying the directivity correction, obtained from Figure 5.2-34, to the absolute level obtained at 90 degrees.

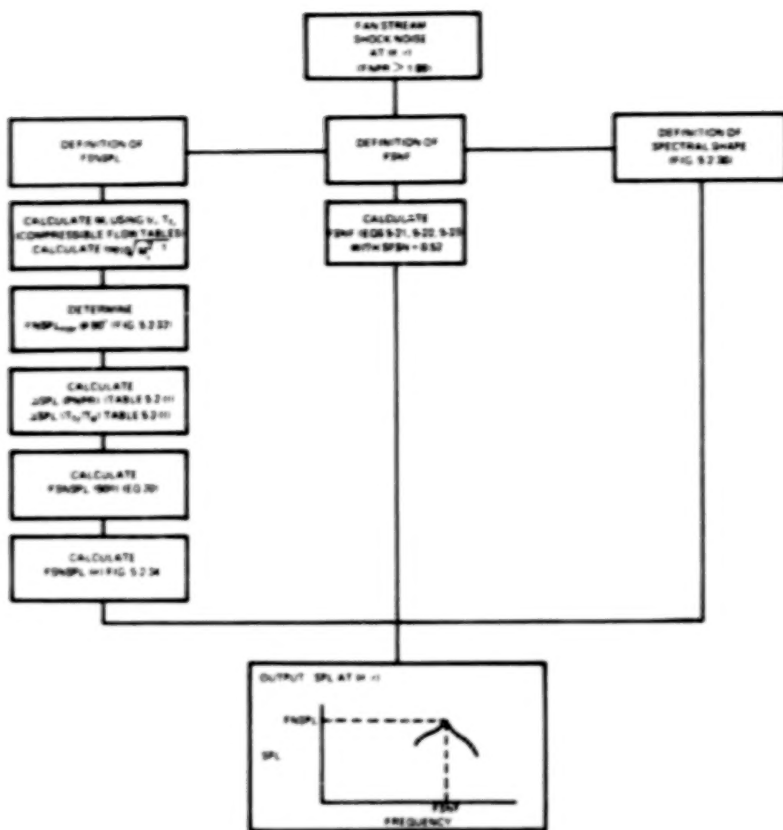


Figure 5.4-4 Flow Chart for Prediction of the Static Fan Stream Shock Noise Component

The characteristic fan stream shock noise frequency, FSNF, is calculated from Equations (5-21), (5-22), and (5-23) using a fan stream shock noise Strouhal number, S_{FSN} , of 0.52.

The fan stream shock noise component is then obtained by defining the peak level of the fan stream shock noise component spectrum, obtained from Figure 5.2-36, as $FSNSPL$ and defining the frequency corresponding to the peak level as FSNF.

5.4.2.4 Primary Stream Shock Noise

If the primary stream is supersonic ($FNPR > 1.89$), the primary stream shock noise component is calculated as indicated in Figure 5.4-5. First, the Mach number M_p is calculated from γ , V_p and T_{tp} using compressible adiabatic flow gas tables. Then, the normalized shock noise level, $PSNSPL_{nor}$, at 90 degrees is obtained from Figure 5.2-38. The absolute primary stream shock noise level, $PSNSPL$, is then determined using Equation (5-24). The absolute primary stream shock noise levels at angles other than 90 degrees are obtained by applying the directivity correction, obtained from Figure 5.2-41, to the absolute level obtained at 90 degrees.

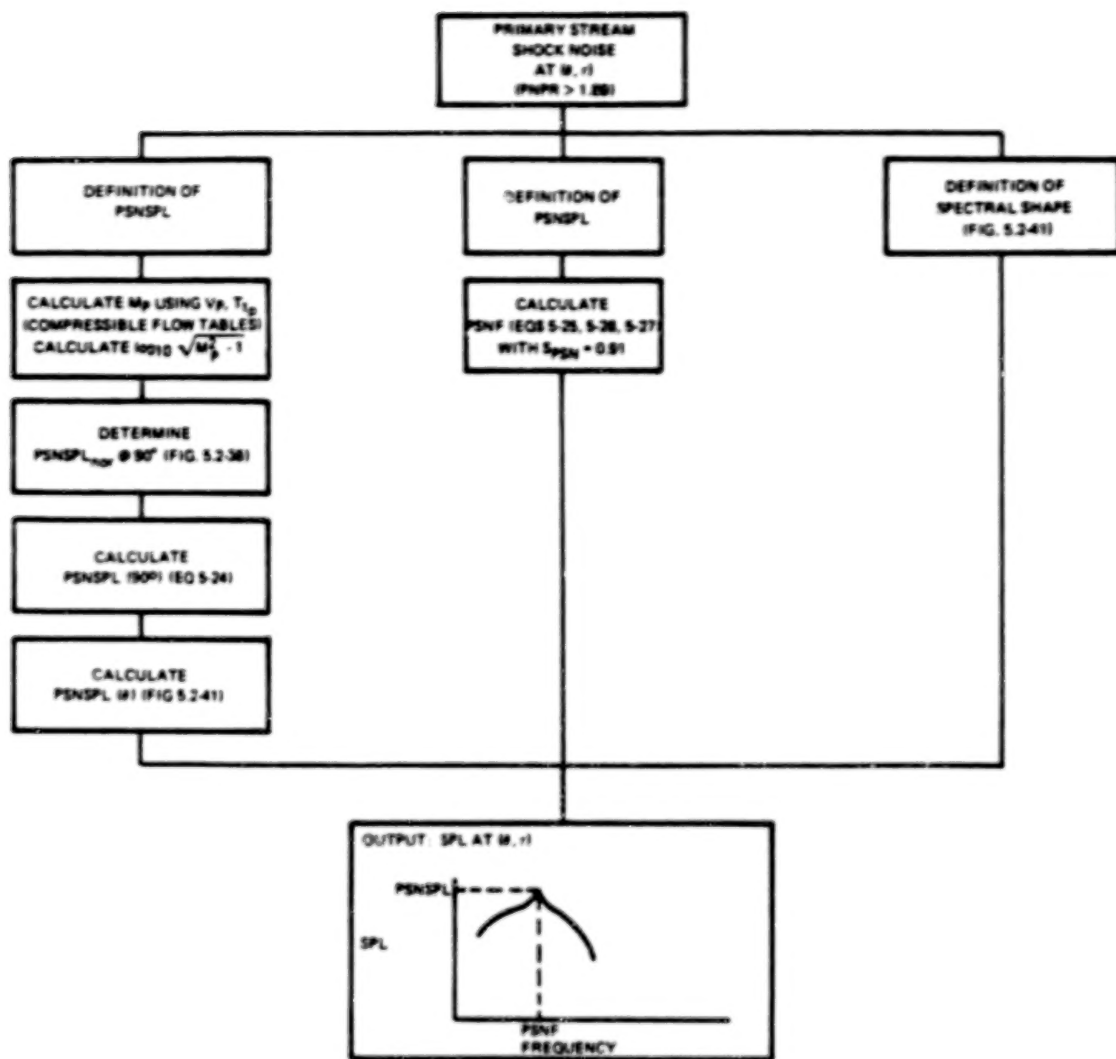


Figure 5.4-5 Flow Chart for Prediction of the Primary Stream Shock Noise Component

The characteristic primary stream shock noise frequency, PSNF, is calculated from Equations (5-25), (5-26), and (5-27) using a primary stream shock noise Strouhal number, S_{pSN} , of 0.91.

The primary stream shock noise component is then obtained by defining the peak level of the primary stream shock noise component spectrum, obtained from Figure 5.2-40, as PSNSPL and defining the frequency corresponding to the peak level as PSNF.

5.4.3 Summary of the Flight Acoustic Prediction Procedure

In the static prediction, the angle θ was measured with respect to the nozzle location. In a flight prediction, this angle corresponds to the noise measured with respect to the position of the aircraft at the retarded source location as discussed in Section 5.3. Consequently, flight predictions are referenced with respect to the retarded aircraft location. Equation (5-28) can be used to convert predictions in this reference frame to coordinates measured with respect to the instantaneous aircraft location.

5.4.3.1 Low Frequency and High Frequency Mixing Noise Components

The flight prediction of the low frequency and high frequency mixing noise components is summarized in Figure 5.4-6. The one-third octave band center frequencies of both noise components are Doppler shifted using Equation (5-32). The low frequency mixing noise spectrum is corrected using Equation (5-35) with the exponent n_m obtained from Figure 5.3-4, and the high frequency mixing noise spectrum is corrected using Equation (5-36) with the exponent n_j obtained from Figure 5.3-7.

5.4.3.2 Fan Stream and Primary Stream Shock Noise Components

The flight prediction of the fan stream and primary stream shock noise components is summarized in Figure 5.4-7. The one-third octave band center frequencies of both noise components are Doppler shifted using Equation (5-32). The spectra are corrected using Equation (5-37).

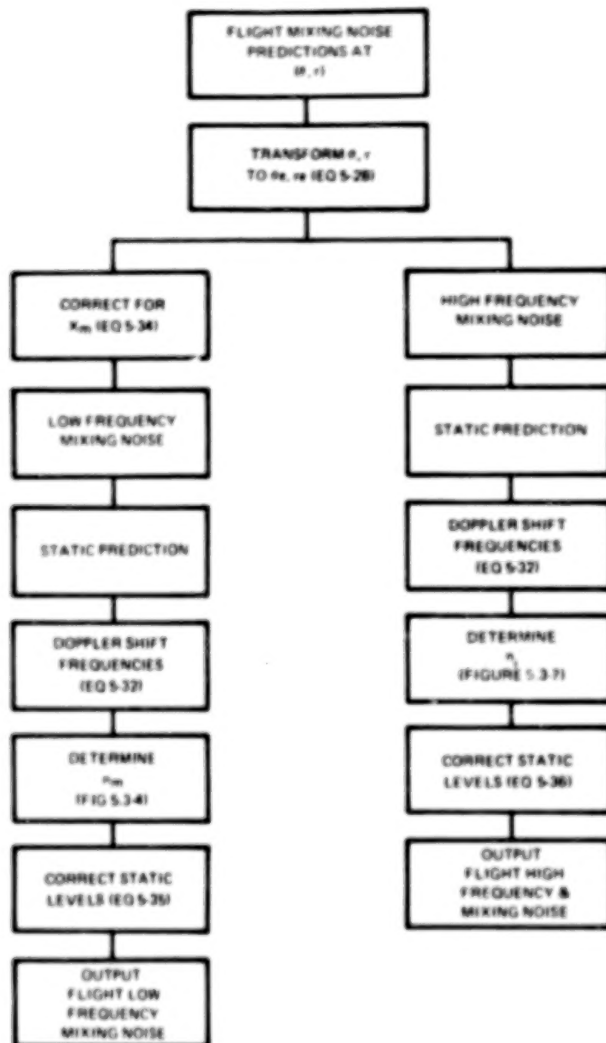


Figure 5.4-6 Flow Chart for Prediction of Flight Effects on the Mixing Noise Components

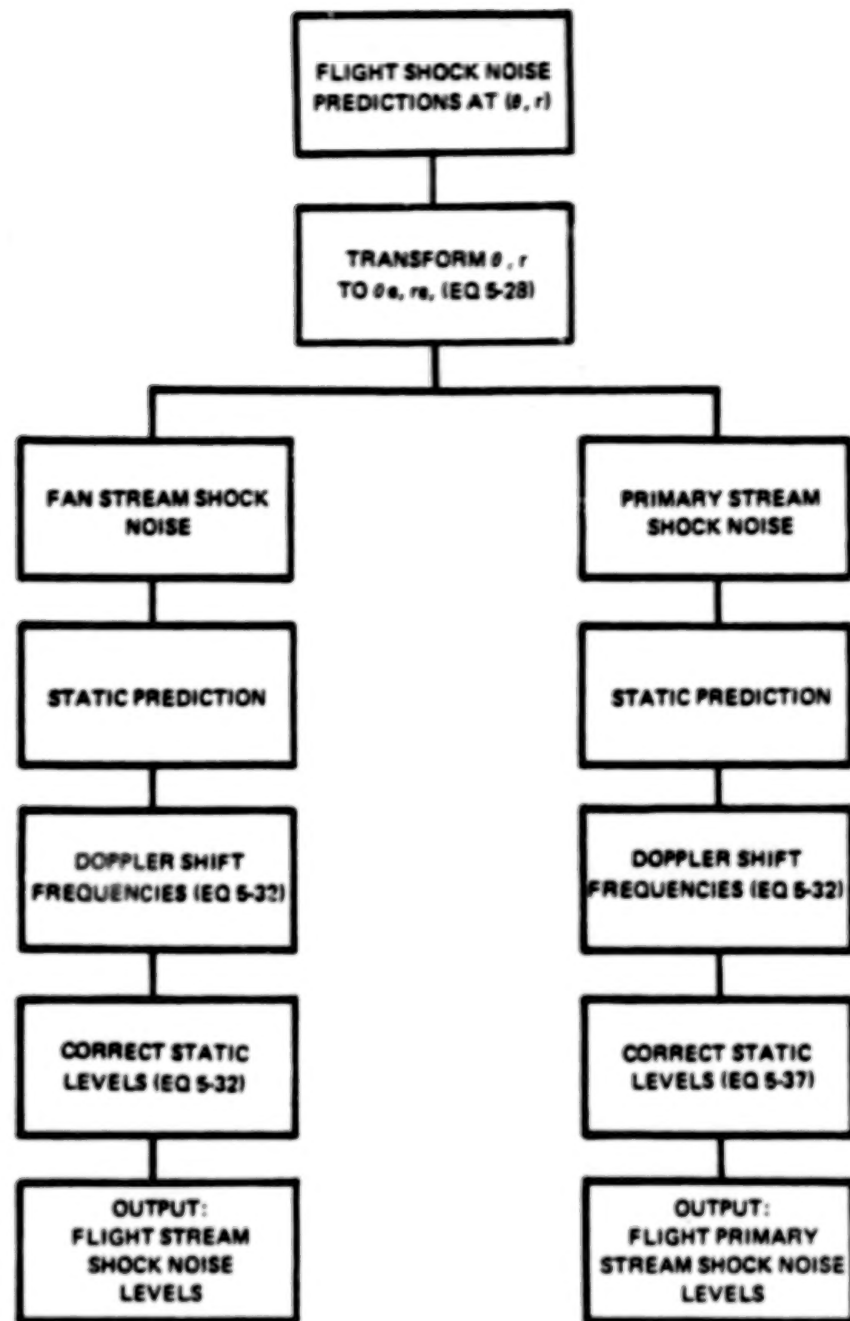


Figure 5.4-7 Flow Chart for Prediction of the Flight Effects on the Shock Noise Components

5.5 SAMPLE CALCULATION

A sample calculation is contained in this section. The following topics are discussed: inputs required for the acoustic prediction, prediction of a static jet exhaust noise spectrum, and prediction of a flight jet exhaust noise spectrum.

5.5.1 Inputs Required for the Acoustic Prediction

For this example, the required inputs to the acoustic prediction procedure, as defined in Section 5.4.1, are:

r	=	4.57 m (15 ft)	
θ	=	90 degrees	
V_f	=	860 m/sec (2820 ft/sec)	$FNPR = 4.1$
V_p	=	616 m/sec (2020 ft/sec)	$PNPR = 2.5$
T_{tf}	=	1089°K (1960°R)	$\gamma = 1.4$
T_{tp}	=	811°K (1460°R)	
a	=	0.75	
A_t	=	0.0126 m ² (0.136 ft ²)	
A_f	=	0.0054 m ² (0.0583 ft ²)	
A_p	=	0.0072 m ² (0.0778 ft ²)	
T_a	=	279°K (502°R)	
c_a	=	335 m/sec (1098 ft/sec)	
H	=	0.0171 m (0.0562 ft)	
R_f	=	0.79	
R_p	=	0	
V_o	=	91.4 m/sec (300 ft/sec)	

5.5.2 Prediction of the Static Jet Exhaust Noise

5.5.2.1 Low Frequency Mixing Noise

From Equation (5-4), using $D_t/r = .028$ ($D_t = 2 \sqrt{A_t/\pi} = 0.127$ m (0.416 ft)),

and $r_m = 1.019r$,
 $\theta_m = 79$ degrees.

From Equation (5-11), at $\theta_m = 79$ degrees, with $v = V_f/V_p = 1.40$

$$\alpha = 0.86.$$

From Equation (5-9) and (5-10) using the information from the input data,

and $V_m = 609$ m/sec (1998 ft/sec),
 $T_{tm} = 788^\circ$ K (1419°R).

Then using $c_a = 335$ m/sec (1098 ft/sec) from the input data,

$$\log_{10} V_m/c_a = 0.260.$$

From Figure 5.2-12,

$$LFSPL_{nor} = 152.7 \text{ dB}.$$

From Figure 5.2-1 (where the limiting value of ω is 2.0),

$$\omega = 2.$$

Then using Equation (5-12), with $A_t = 0.0126 m^2$ (0.136 ft²); $r_m = 1.019 r$; $r = 4.57 m$ (15 ft))

$$\begin{aligned}LFSPL_{corr} &= 152.7 \text{ dB} - 32.2 \text{ dB, or} \\&= 120.5 \text{ dB.}\end{aligned}$$

From Equation (5-8), with $\omega = 2.0$; $T_{t_m} = 788^\circ\text{K}$ (1419°R); $T_a = 279^\circ\text{K}$ (502°R);

$$\begin{aligned}LFSPL &= 120.5 \text{ dB} - 9.0 \text{ dB, or} \\&= 111.5 \text{ dB.}\end{aligned}$$

From Figure 5.2-13, the Strouhal number at $\theta_m = 79$ degrees is

$$S_m = 0.65.$$

From Equation (5-14), with $D_t = 0.127 m$ (0.416 ft) and $V_m = 609 \text{ m/sec}$ (1998 ft/sec),

$$LF = 3117 \text{ Hz.}$$

The spectral shape for the low frequency mixing noise component at $\theta_m = 79$ degrees can be obtained from Figure 5.2-14. Using this spectrum, $LFSPL = 111.5 \text{ dB}$, and $LF = 3120 \text{ Hz}$, the low frequency noise component was plotted in Figure 5.5-1.

5.5.2.2 High Frequency Mixing Noise

From Equations (5-15) and (5-16), using the information from the input data,

$$\begin{aligned}V_i &= 834 \text{ m/sec} (2737 \text{ ft/sec}), \text{ or} \\ \text{and } T_{t_i} &= 1057^\circ\text{K} (1902^\circ\text{R}).\end{aligned}$$

Then using $c_a = 335 \text{ m/sec}$ (1098 ft/sec),

$$\log_{10} V_i/c_a = 0.397.$$

From Figure 5.2-24, at $\theta = 90$ degrees,

$$HFSPL_{nor} = 158.4 \text{ dB.}$$

From Figure 5.2-1,

$$\omega = 2.0.$$

From Table 5.2-1, using $R_f = 0.79$ and $\log V_i/c_a = 0.397$,

$$\Delta SPL = 0.5 \text{ dB.}$$

From Equation (5-18), using $A_f = 0.0054 \text{ m}^2$ (.0583 ft²),

$$\begin{aligned}HFSPL_{corr} &= 158.4 \text{ dB} - 35.9 \text{ dB} - 0.5 \text{ dB, or} \\&= 122.0 \text{ dB.}\end{aligned}$$

From Equation (5-17), using $\omega = 2.0$, $T_{t_i} = 1057^\circ\text{K}$ (1902°R), and $T_a = 279^\circ\text{K}$ (502°R),

$$\begin{aligned}HFSPL &= 122.0 \text{ dB} - 11.6 \text{ dB, or} \\&= 110.4 \text{ dB.}\end{aligned}$$

From Figure 5.2-25, the Strouhal number at $\theta = 90$ degrees is

$$S_j = 0.16.$$

Then from Equation (5-19), using $H = 0.0171 \text{ m}$ (0.0562 ft) and $V_i = 834 \text{ m/sec}$ (2737 ft/sec),

$$HF = 7803 \text{ Hz.}$$

The spectral shape for the high frequency mixing noise component at $\theta = 90$ degrees can be obtained from Figure 5.2-26. Using this spectrum, $HFSPL = 110.4$ dB and $HF = 7803$ Hz, the high frequency noise component was plotted in Figure 5.5-1.

5.5.2.3 Fan Stream Shock Noise

From $V_i = 834$ m/sec (2737 ft/sec), $T_{ti} = 1057^\circ K$ (1902°R) and $\gamma = 1.4$, the Mach number in the initial region can be obtained from compressible flow tables as

$$M_i = 1.555.$$

Then

$$\log \sqrt{M_i^2 - 1} = .0758$$

From Figure 5.2-32,

$$FSNSPL_{nor} = 157.0$$
 dB.

From Table 5.2-II, using $PNPR = 2.5$ and $T_f/T_a = 3.904$

$$\Delta SPL(PNPR) = 12.8$$
 dB, and

$$\Delta SPL(T_f/T_a) = 7.4$$
 dB.

Using Equation (5-20)

$$FSNSPL = 157.0 \text{ dB} - 35.9 \text{ dB} - 12.8 \text{ dB} - 7.4 \text{ dB, or} \\ = 100.9 \text{ dB.}$$

Using Equation (5-23)

$$V_{ci} = 584 \text{ m/sec (1915 ft/sec).}$$

Using Equation (5-22),

$$L_{sf} = 0.0223 \text{ m (.0735 ft).}$$

Also

$$M_{ci} = V_{ci}/c_a, \text{ or} \\ = 1.744.$$

Then from Equation (5-21), using $S_{FSN} = 0.52$,

$$FSNF = 12927 \text{ Hz.}$$

The shock noise spectrum is obtained from Figure 5.2-36. Using this spectrum, $FSNSPL = 100.9$ dB and $FSNF = 12927$ Hz, the fan stream shock noise component was plotted in Figure 5.5-1.

5.5.2.4 Primary Stream Shock Noise

From $V_p = 616$ m/sec (2020 ft/sec) and $T_{tp} = 811^\circ K$ (1460°R), the primary stream Mach numbers can be obtained from compressible flow tables as

$$M_p = 1.241$$

Then

$$\log \sqrt{M_p^2 - 1} = - .134$$

From Figure 5.2-38.

$$PSNSPL_{nor} = 146.0 \text{ dB}$$

Using Equation (5-24), with $A_p = 0.0072 \text{ m}^2$ (0.0778 ft²) and $r = 4.57 \text{ m}$ (15 ft),

$$\begin{aligned} PSNSPL &= 146.0 \text{ dB} - 34.6 \text{ dB, or} \\ &= 111.4 \text{ dB} \end{aligned}$$

From Equation (5-27),

$$V_{cp} = 431 \text{ m/sec (1414 ft/sec)}$$

From Equation (5-26), with $D_p = 2 \sqrt{A_p/\pi} = 0.096 \text{ m}$ (0.315 ft).

$$L_{sp} = 0.077 \text{ m (0.255 ft).}$$

The primary stream shock noise Strouhal number is

$$S_{PSN} = 0.91.$$

From Equation (5-25),

$$PSNF = 4948 \text{ Hz.}$$

The shock noise spectrum is obtained from Figure 5.2-40. Using this spectrum, $PSNSPL = 111.4 \text{ dB}$ and $PSNF = 4948 \text{ Hz}$, the primary stream shock noise component was plotted in Figure 5.5-1.

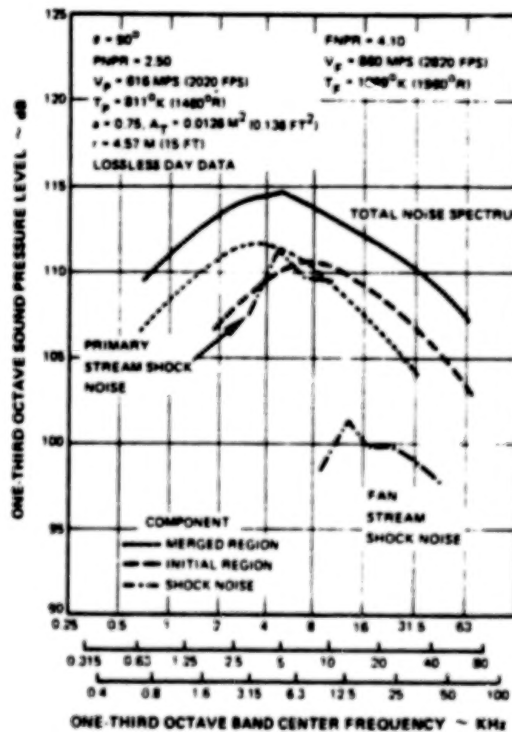


Figure 5.5-1 Prediction of the Static Individual Noise Components and the Total Noise Spectrum

5.5.3 Prediction of the Flight Jet Exhaust Noise

5.5.3.1 Low Frequency and High Frequency Mixing Noise Components

Since the flight velocity is 91.4 m/sec (300 ft/sec), the flight Mach number is

$$\begin{aligned}M_0 &= V_0/c_a \\&= 0.273.\end{aligned}$$

Because $\theta_m = 79$ degrees, the Doppler factor $(1 - M_0 \cos \theta)$ is approximately unity and according to Equation (5-32), the frequency shift is less than one-third octave band.

From Figure 5.3-4 at $\theta_m = 79$ degrees.

$$n_m = 5.0.$$

and using Equation (5-35), with $V_m = 609$ m/sec (1998 ft/sec),

$$LFSPL_{FLIGHT} = LFSPL_s - 3.5 \text{ dB}.$$

Therefore, the static low frequency mixing noise component is reduced 3.5 dB in flight, as illustrated in Figure 5.5-2.

From Figure 5.3-7, at $\theta = 90$ degrees.

$$n_i = 6.1.$$

and using Equation (5-36) with $V_i = 834$ m/sec (2737 ft/sec),

$$HFSPL_{FLIGHT} = HFSPL_s - 3.1 \text{ dB}$$

Therefore, the static high frequency mixing noise component is reduced 3.1 dB in flight, as illustrated in Figure 5.5-2.

5.5.3.2 Fan Stream and Primary Stream Shock Noise Components

At $\theta = 90$ degrees, the Doppler shift in frequency for either shock noise component is insignificant.

Therefore, from Equation (5-36),

$$SNSPL_{FLIGHT} = SNSPL_s,$$

and the shock noise levels are the same in flight for both the fan stream and primary stream shock noise components as illustrated in Figure 5.5-2.

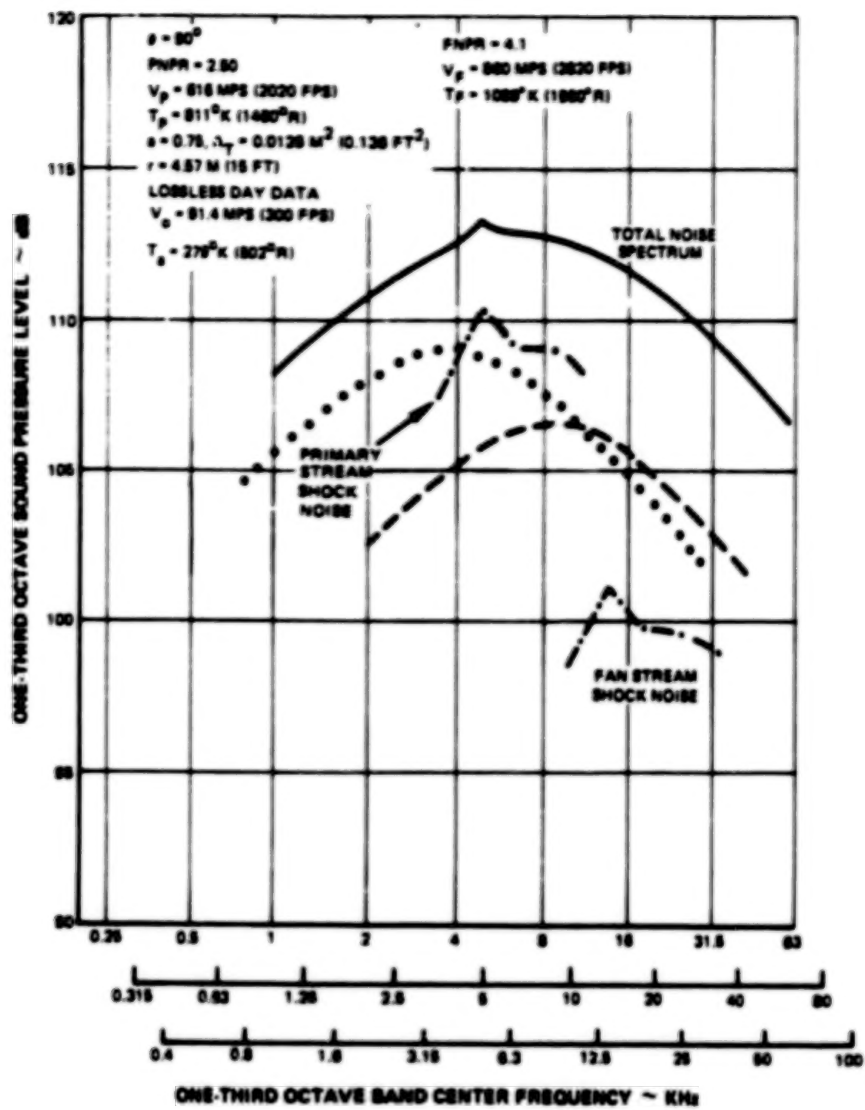


Figure 5.5-2 Prediction of the in Flight Individual Noise Components and the Total Noise Spectrum

5.6 COMPARISON OF DATA WITH PREDICTIONS USING THE ACOUSTIC PREDICTION PROCEDURE

Results of the acoustic empirical prediction system are described in this section. Predictions from the prediction procedure outlined in Section 5.4 are presented in this section and compared with model acoustic data for a wide range of static nozzle operating conditions, including subsonic and supersonic fan and primary flows. Comparisons were also made for different geometric configurations at fixed operating condition. The geometric variations included variations in fan stream and primary stream radius ratios. In addition, comparisons were made for simulated forward flight conditions. The following topics are discussed in Section 5.6: comparison of IVP coannular nozzle noise predictions with measured data and analysis of the accuracy of the prediction procedure.

5.6.1 Comparison of IVP Coannular Nozzle Noise Predictions with Measured Data

Predictions were made both for coannular nozzles in a static environment and for nozzles in simulated forward flight. Sample static acoustic predictions were made for IVP coannular nozzles for fixed geometry but varying nozzle operating conditions and for fixed operating conditions with different nozzle geometries. The predictions for fixed nozzle geometry are contained in Figures 5.6-1 through 5.6-4. In these figures, predictions were made for operating conditions and geometries that are included in the data base obtained from References 7 and 8. For all four cases predicted, the primary stream was subsonic; the primary pressure ratio, velocity, and temperature were 1.53, 402 m/sec (1320 ft/sec) and 700°K (1260°R), respectively. For two of the cases the fan stream conditions were subsonic (fan pressure ratio of 1.8) and for two cases the fan stream conditions were supersonic (fan pressure ratios of 3.2 and 4.1). In Figures 5.6-1 through 5.6-4 the agreement between predictions and experimental data is within the standard deviations established for each individual noise component over the frequency range from 800 Hz to 25,000 Hz.

Figure 5.6-5 contains both predictions and data for an operating condition in which both the fan stream and primary stream were supersonic. The shock noise component visible at 90 degrees in Figure 5.6-5 was due to the supersonic primary stream. The shock noise component from the fan stream was 10 dB below the mixing noise levels and is not visible in the total noise spectrum. The agreement between predictions and experimental data in Figure 5.6-5 was within the standard deviation established for each noise component in Sections 5.2.1.1 and 5.2.1.2 from 800 Hz to 25,000 Hz.

Predictions for fixed operating condition but with different nozzle geometry are contained in Figures 5.6-6 through 5.6-9 for angles of 60, 90, 120 and 150 degrees. Predictions were made for two operating conditions – one with both streams subsonic and one with both streams supersonic. Data and predictions are shown in these figures for Configurations A, C, and E tested in the present program. The model constructions of Configurations A, C, and E are illustrated in Figures 3.3-3, 3.3-5 and 3.3-7. Configurations A and C had the same primary radius ratio but differing fan radius ratio. As the model test data showed, increases in fan radius ratio resulted in reductions of the high frequency noise. This trend was predicted using the prediction procedure and agreed with measured data. Configuration E had the same fan radius ratio as Configuration C but a larger primary radius ratio. Both the data and predictions showed that the high frequency noise was reduced by an increase in primary radius ratio, holding fan radius ratio fixed, and the two agreed within the standard deviations established for each noise component, except for the predictions in Figure 5.6-6, over a range of frequencies from 800 Hz to 25,000 Hz.

Flight predictions were made for one operating condition and flight velocities of 0, 200, and 129 m/sec (425 ft/sec). Predictions were made and compared to data from References 9 and 10 in Figures 5.6-10 through 5.6-13 for angles of 70, 90, 120 and 150 degrees. Data and predictions agreed within the standard deviations established for each noise component over a range of frequencies from 800 Hz to 25,000 Hz.

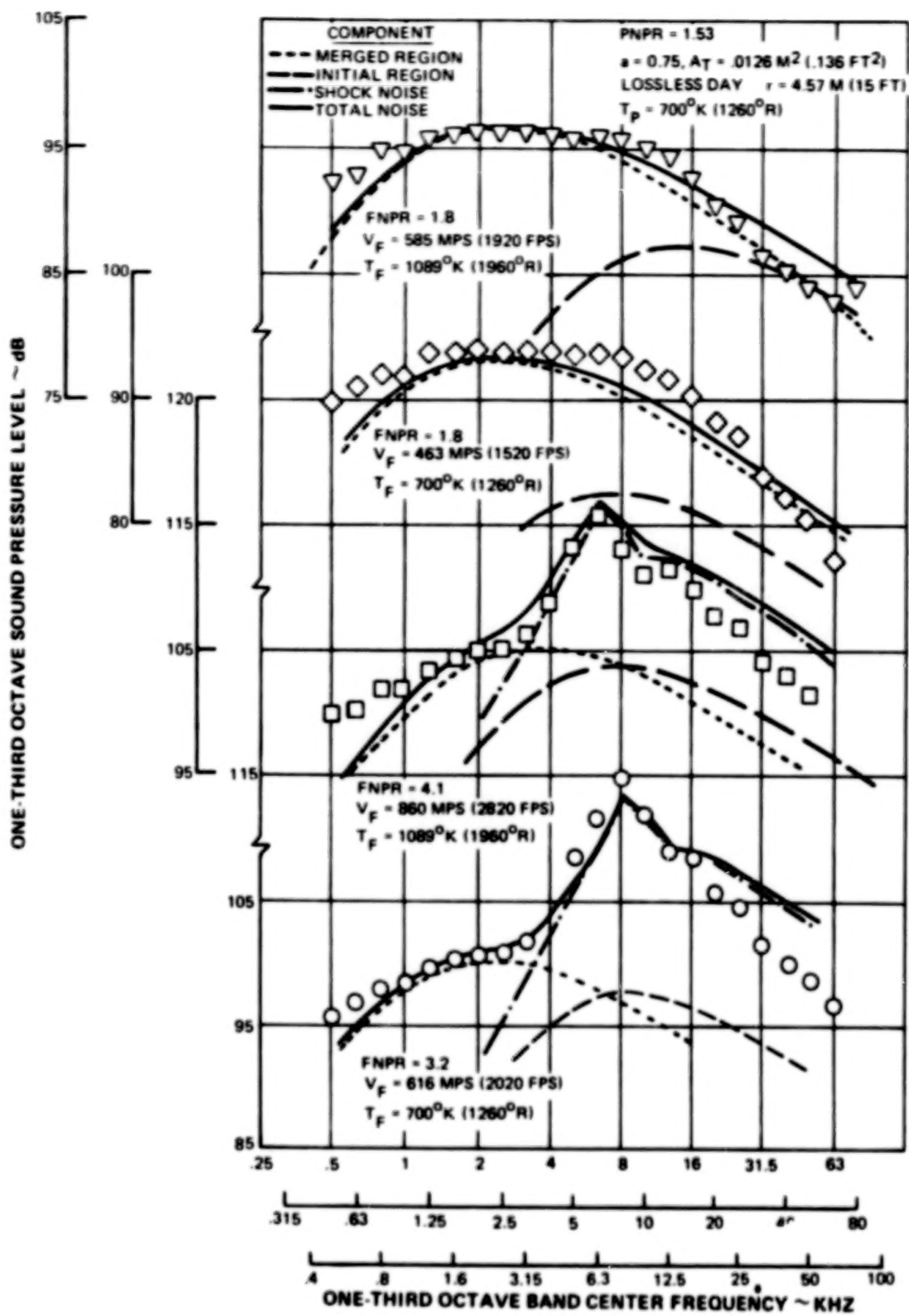


Figure 5.6-1 Comparisons at 60 Degrees of Measured SPL Spectra From References 7 and 8, for a Subsonic PNPR, with Predictions

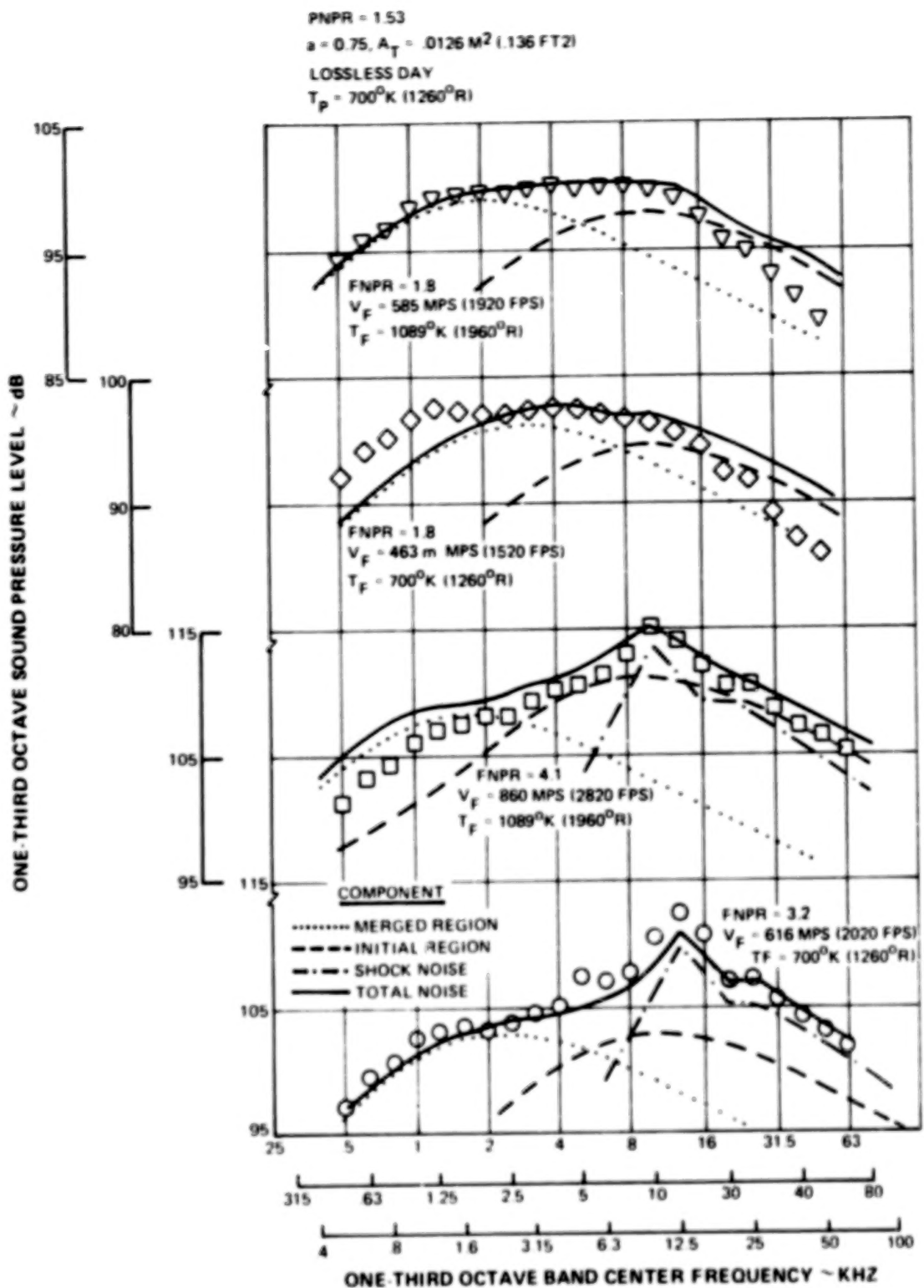


Figure 5.6-2 Comparisons at $\theta = 90$ Degrees of Measured SPL Spectra From References 7 and 8, for a Subsonic PNPR, with Predictions

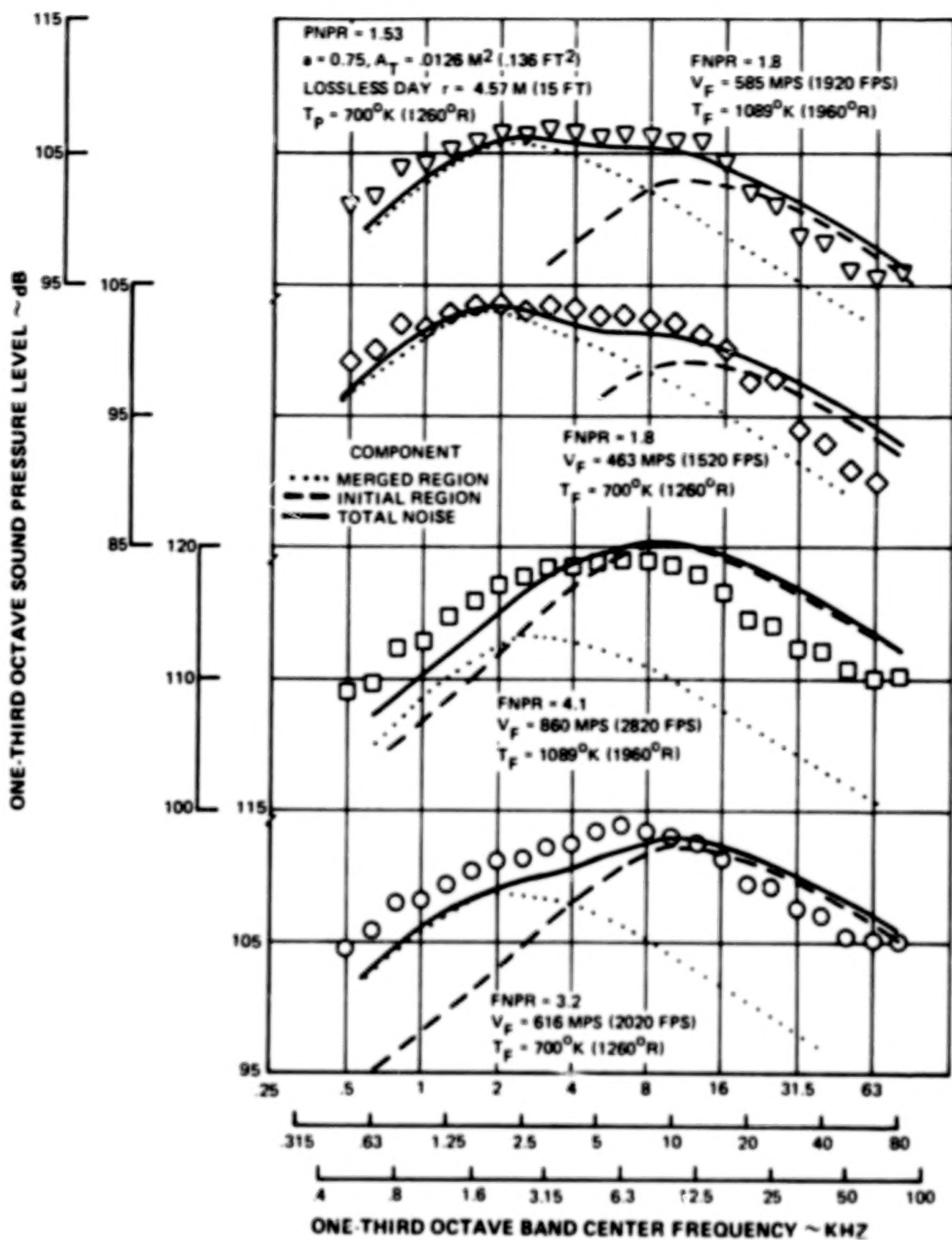


Figure 5.6-3 Comparison at $\theta = 120$ Degrees of Measured SPL Spectra from References 7 and 8, for a Subsonic PNPR, with Prediction

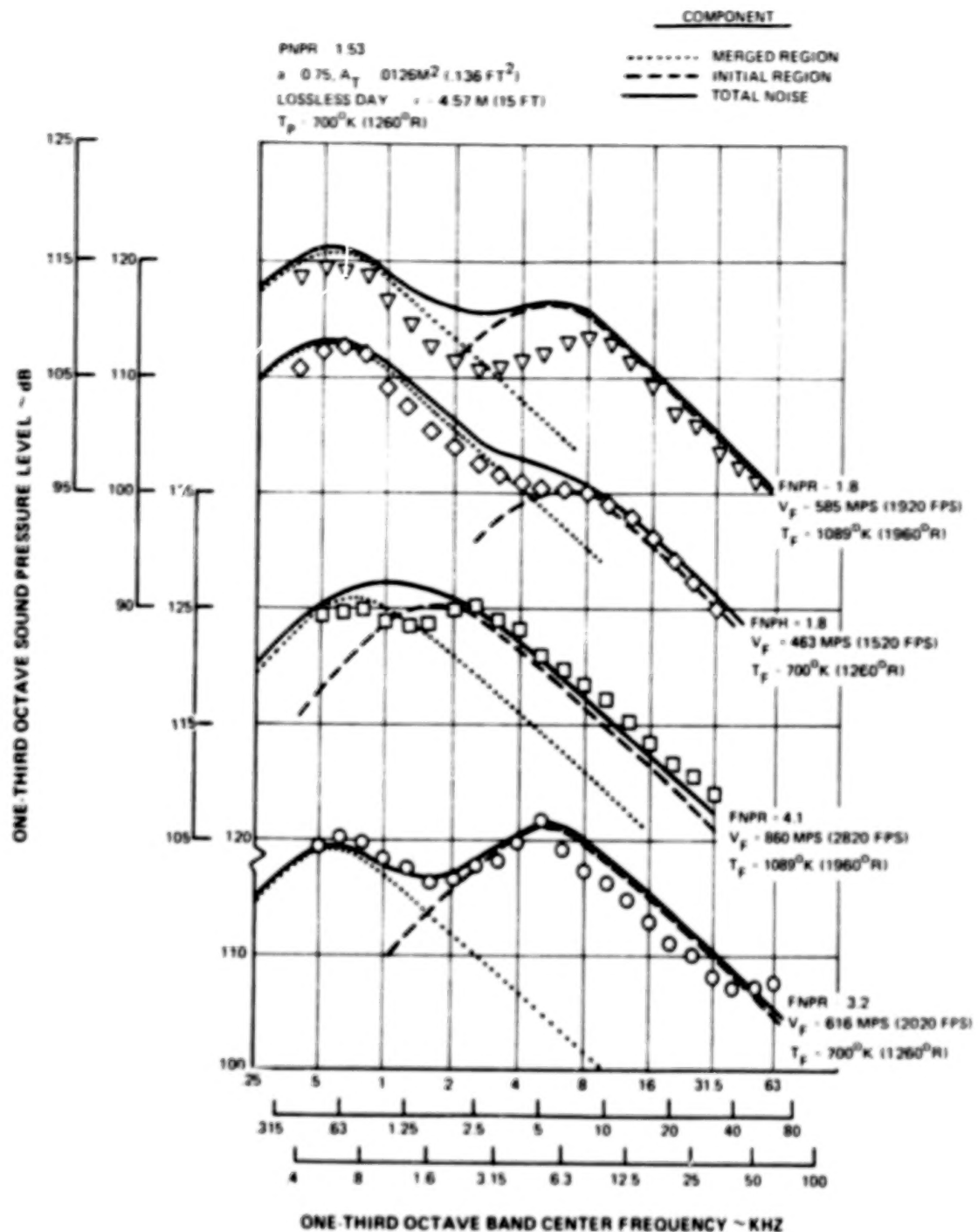


Figure 5.6-4 Comparison at $\theta = 150$ Degrees of Measured SPL Spectra from References 7 and 8, for a Subsonic PNPR, with Predictions

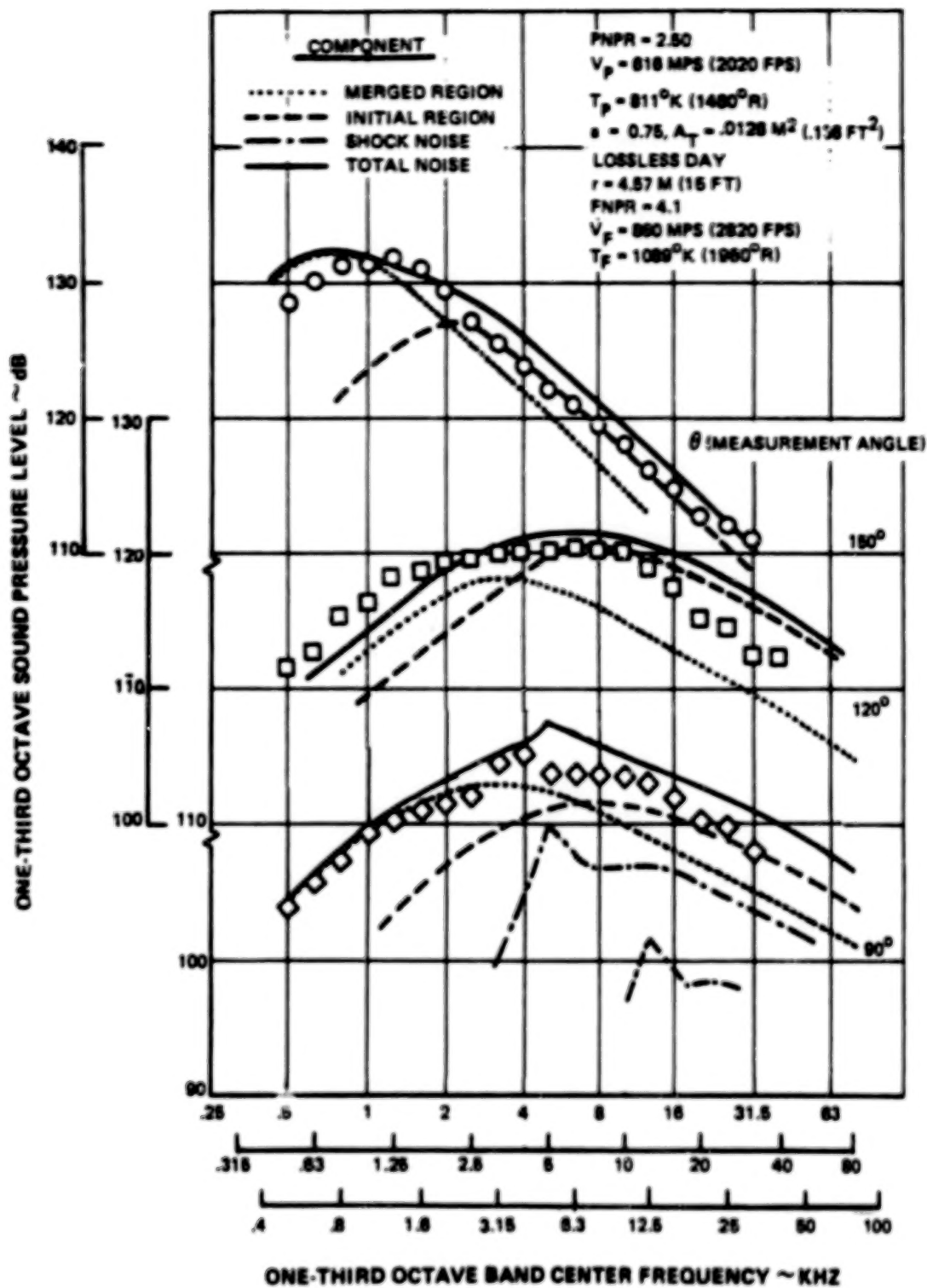


Figure 5.6-5 Comparisons of Measured SPL Spectra From References 7 and 8, for a Supersonic PNPR, with Predictions

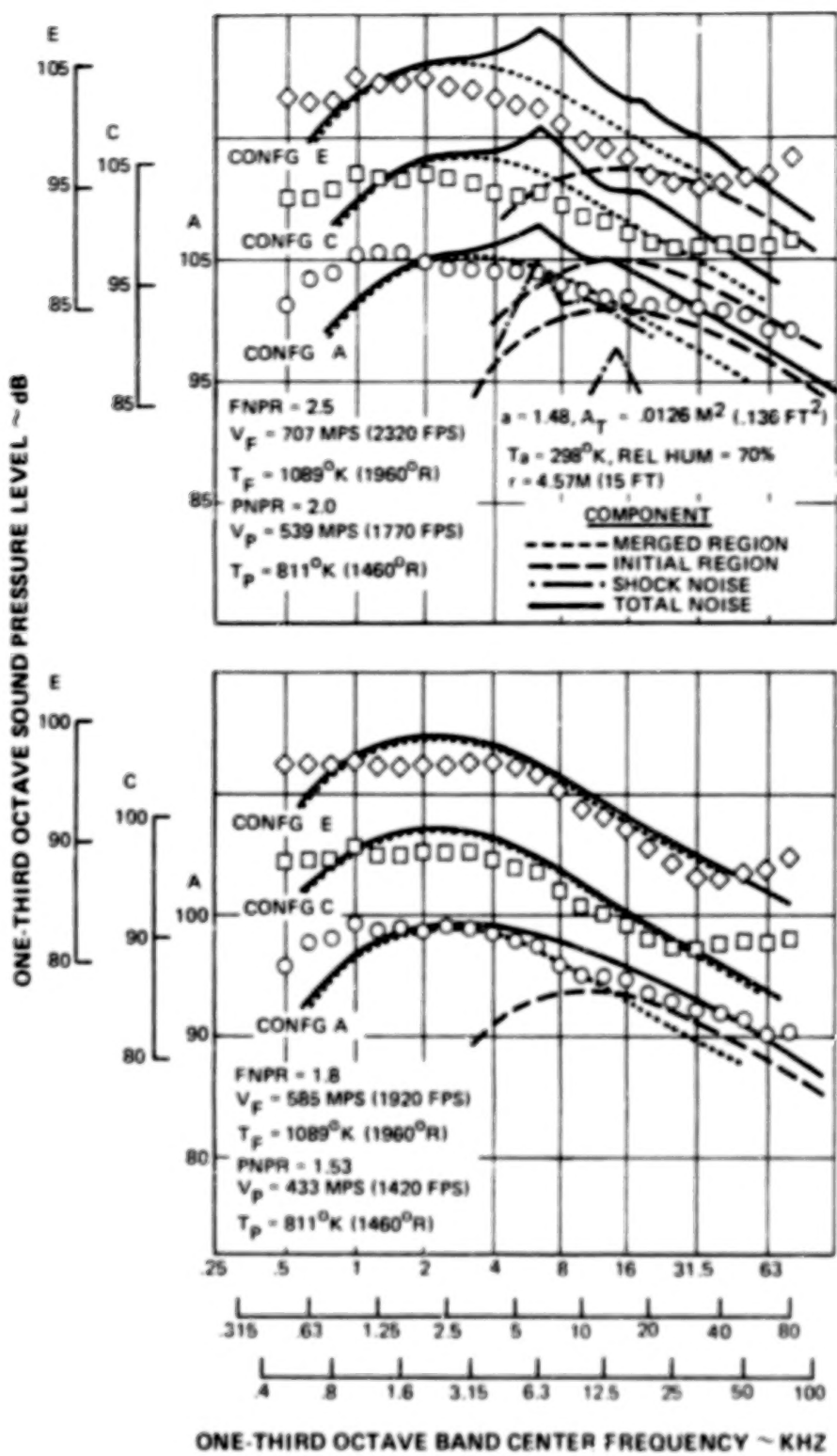


Figure 5.6-6 Comparisons at $\theta = 60$ Degrees of Measured SPL Spectra From the Present Program, for Configuration A, C, and E, with Predictions

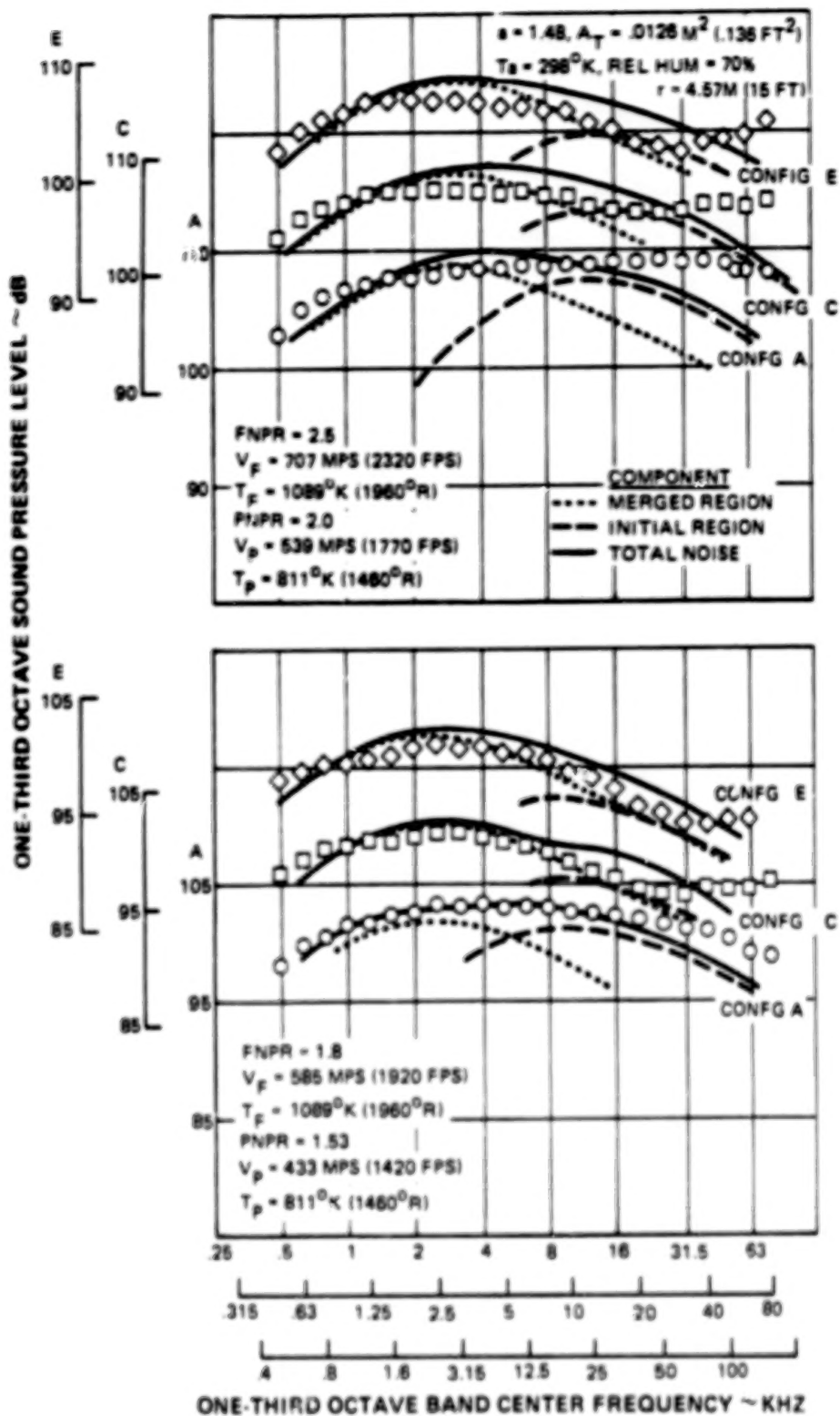


Figure 5.6-7 Comparisons at $\theta = 90$ Degrees of Measured SPL Spectra From the Present Program, for Configuration A, C, and E, with Predictions

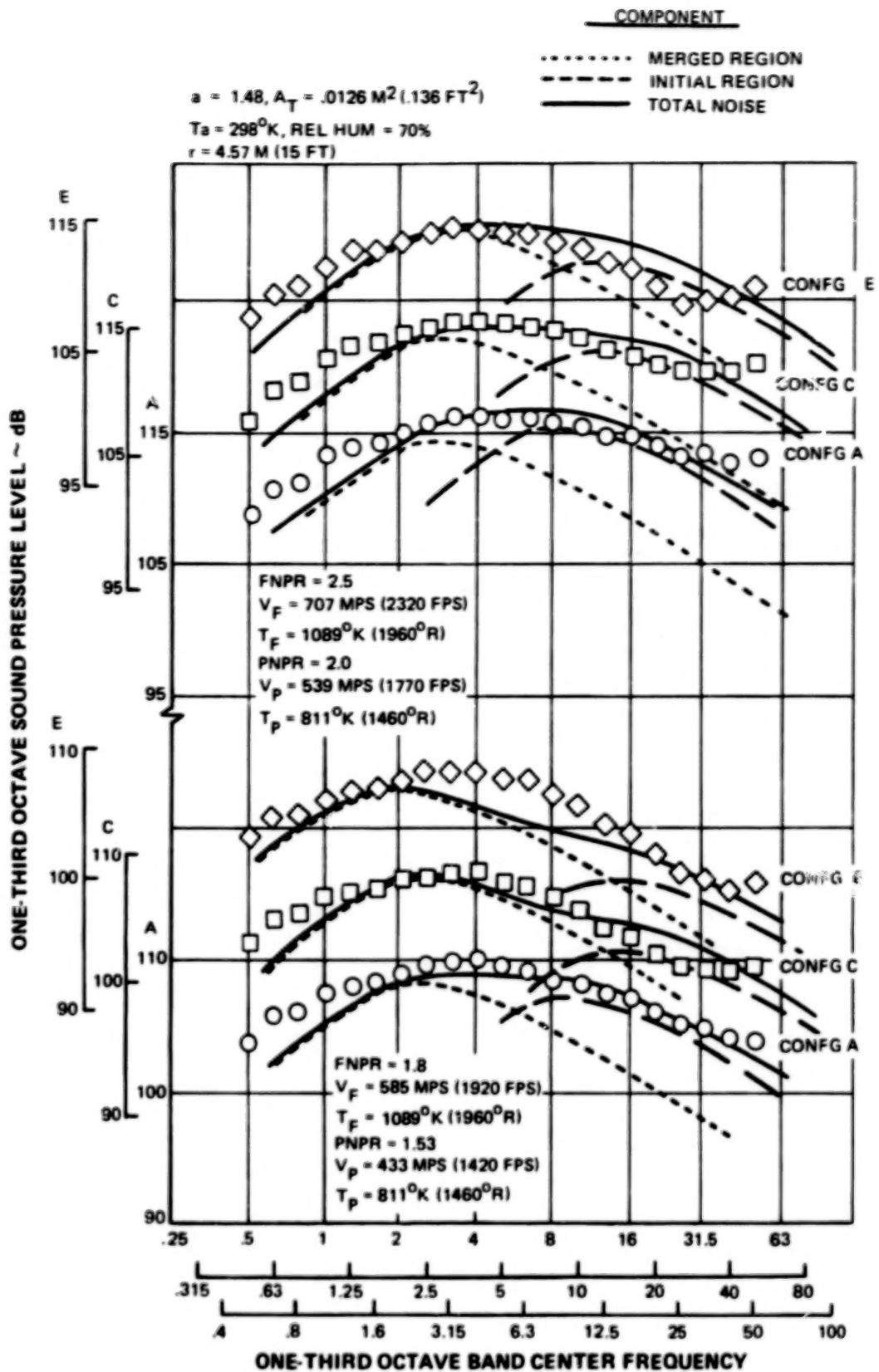


Figure 5.6-8 Comparisons at $\theta = 120$ Degrees of Measured SPL Spectra From the Present Program, for Configurations A, C, and E, with Predictions

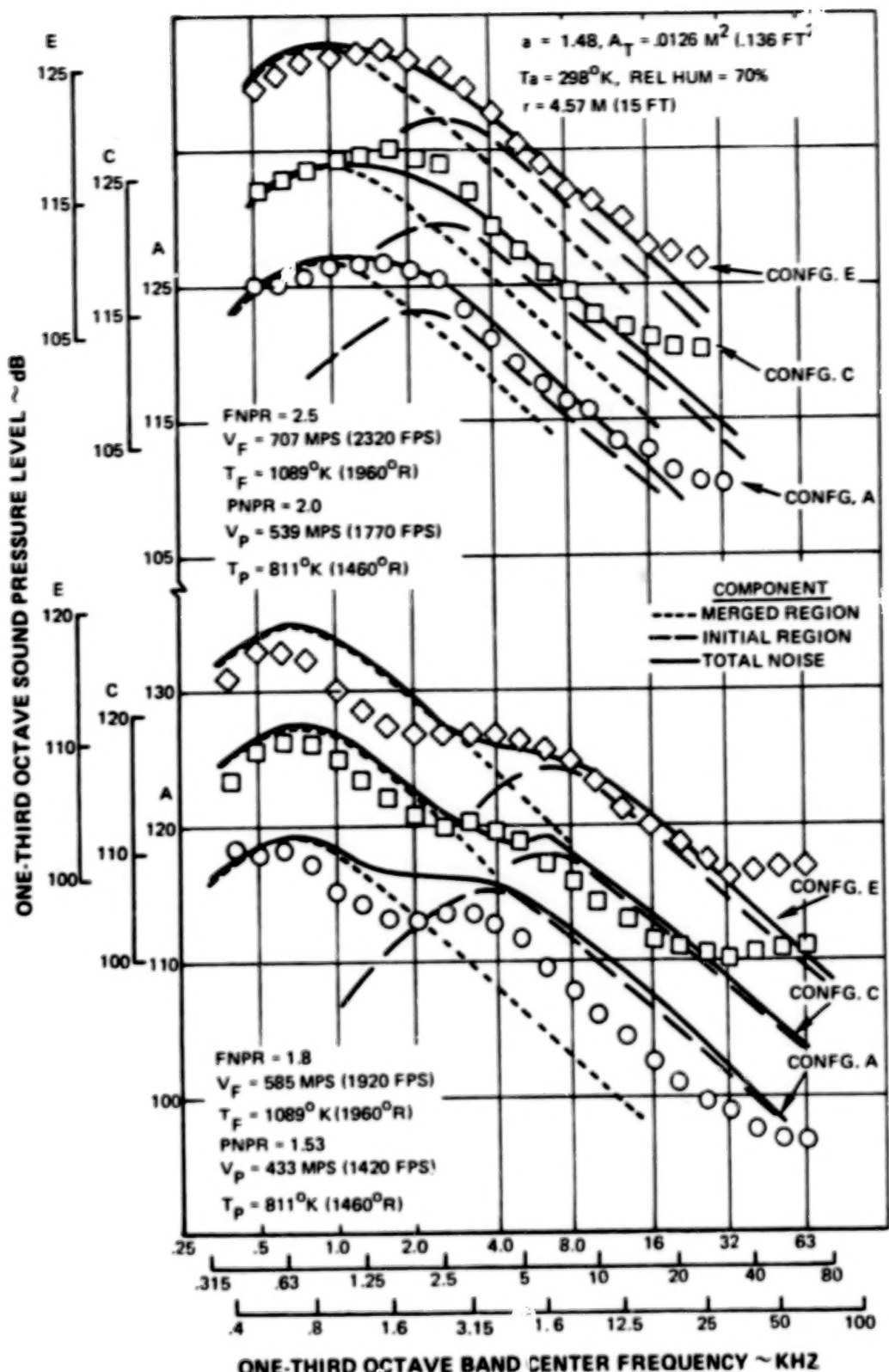


Figure 5.6-9 Comparisons at $\theta = 150$ Degrees of Measured SPL Spectra From the Present Program, for Configurations A, C, and E, with Predictions

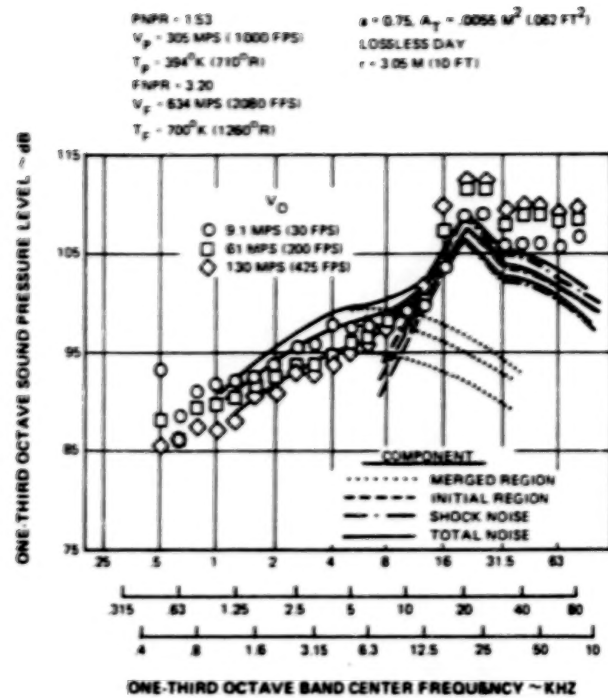


Figure 5.6-10 Comparisons at $\theta = 70$ Degrees of Measured Simulated Forward Flight Data From References 9 and 10 with Predictions

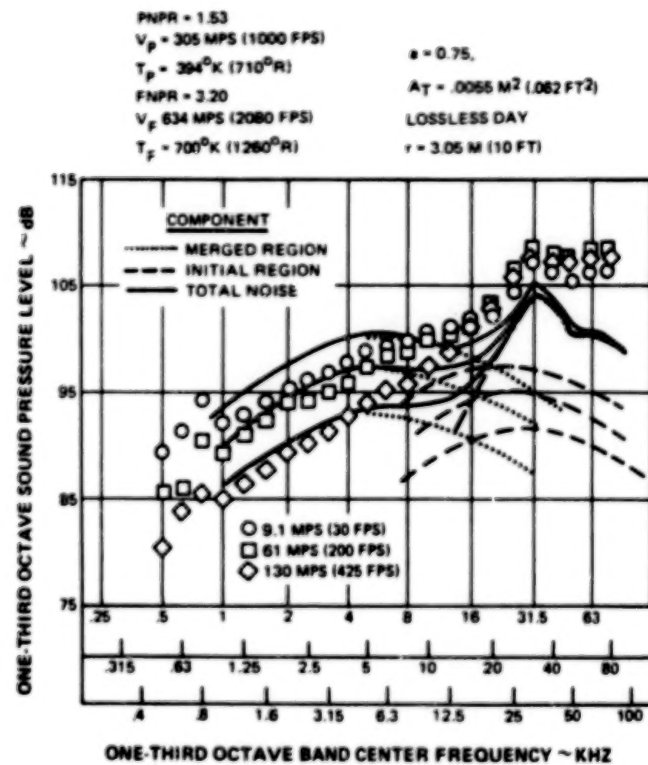


Figure 5.6-11 Comparison at 90 Degrees of Measured Simulated Forward Flight Data From References 9 and 10 with Predictions

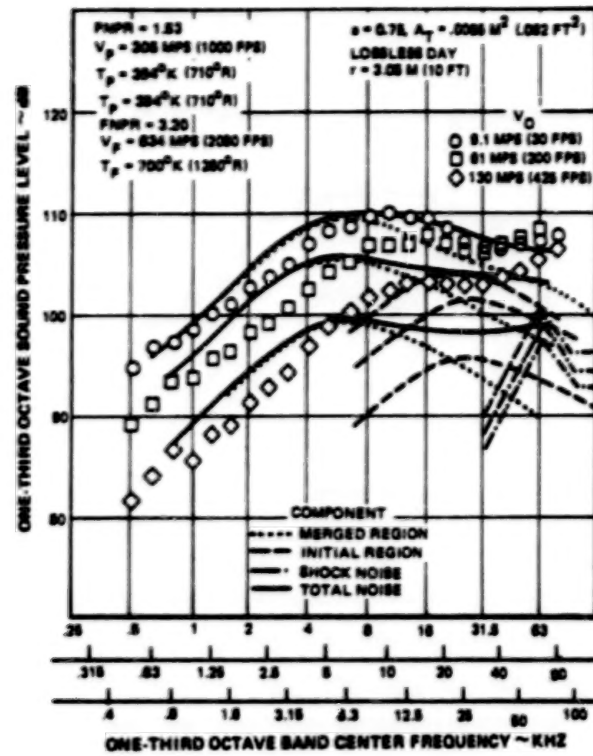


Figure 5.6-12 Comparison at $\theta = 120$ Degrees of Measured Simulated Forward Flight Data From References 9 and 10 with Predictions

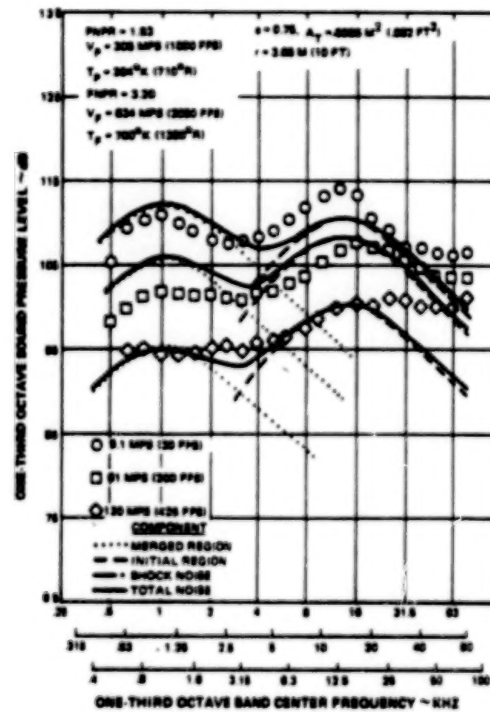


Figure 5.6-13 Comparisons at 150 Degrees of Measured Simulated Forward Flight Data From References 9 and 10 with Predictions

5.6.2 Analysis of the Accuracy of the Prediction Procedure

The accuracy of the acoustic prediction procedure can be stated precisely for nozzle geometries and operating conditions within the parameter extremes of the data base but remains to be established outside the parameter extremes. Within the data base the accuracy limits were as noted in Section 5.3. The standard deviations for the static correlations ranged between ± 1.0 dB and ± 2.4 dB while the standard deviations for the flight correlations ranged between ± 0.8 dB and ± 2.7 dB.

The data prediction comparisons contained in Figures 5.6-1 through 5.6-13 demonstrate that the predicted and measured levels for a variety of cases do agree within the standard deviations obtained for the individual noise components, and these standard deviations therefore are indicative of the accuracy of the total noise prediction over a range of frequencies from 800 Hz to 25,000 Hz.

Relative trends can be predicted more accurately than absolute noise level predictions. For example, in Figure 5.6-9 the reduction in high frequency noise from Configuration A to Configuration E was predicted more accurately than the absolute levels.

The accuracy of predictions made outside of the data base cannot be assessed. Since the mixing noise model used to correlate the high and low frequency noise components is based physically upon the characteristics of the IVP coannular nozzle flow development, it is expected that extrapolations of operating conditions can be made with reasonable accuracy. However, the fan stream shock noise normalizations for primary pressure ratio and fan temperature were developed empirically and may be found to be unreliable when extrapolated to operating conditions outside of the data base. In practice this may be unimportant because shock noise is a decreasing function of primary pressure ratio and fan temperature, and therefore this noise component may be dominated by mixing noise as these two parameters are extrapolated to higher values of velocity than those contained in the data base. Table 5.6-1 contains a summary of the parameter extremes contained in the data base used in developing the acoustic prediction procedure and should be used as an aid in establishing the range of parameters where the noise prediction procedure should provide the most reliable results.

The shock noise prediction procedure could be improved by extending the data base to include higher primary pressure ratios and higher fan temperatures. Alternatively, a theoretical foundation for coannular shock noise could be established by obtaining experimental evidence of the shock structure in the aerodynamic flow from coannular nozzles along with experimental evidence of the noise generation mechanism. As discussed in Section 5.2.2.1, this would include data on the change in shock structure and strength with nozzle operating condition and data on the change in turbulence properties (e.g., turbulence intensity and convection velocity) of eddies convected through the shock structure.

TABLE 5.6-I
SUMMARY OF PARAMETER EXTREMES IN THE
ACOUSTIC DATA BASE

Parameter	Variation in Data Base
Fan to primary velocity ratio	1.03 to 2.80
Fan to primary temperature ratio	0.36 to 2.76
Absolute fan temperature	394°K (710°R) - 1089°K (1960°R)
Fan to primary area ratio	0.65 to 1.48
Fan radius ratio	0.60 to 0.91
Primary radius ratio	0 to 0.81

SECTION 6.0

STATIC AERODYNAMIC PERFORMANCE PREDICTION PROCEDURE

This section describes the static aerodynamic performance prediction procedure developed in this program. The procedure permits estimating nozzle performance by combining an analytical prediction of internal duct loss and external scrubbing loss with an empirically derived reference thrust coefficient in the subsonic operating regime and correlations of shock loss in the supersonic flow regime at supercritical fan nozzle pressure ratios. The empirical shock loss correlation was developed by relating the thrust coefficients of the test models to a reference thrust coefficient established in the sub-critical nozzle pressure range where shocks were not present. The approach to development of the static performance prediction system is discussed in Section 6.1. Viscous losses (internal duct loss, scrubbing loss) and the comparison between prediction and measurement of these losses are discussed in Section 6.2. Off-design shock loss and the relationship of the losses to typical nozzle operating characteristics are discussed in Section 6.3, and a demonstration of the application of the static performance prediction procedure is presented in Section 6.4. In Section 6.5 the static performance prediction procedure is evaluated by comparing predictions made using the procedure with actual nozzle performance measurements.

6.1 APPROACH

6.1.1 Subsonic and Supersonic Nozzle Loss Mechanisms

The static performance prediction procedure divides nozzle operation into two regimes: subsonic (un choked) and supersonic (choked) operation. The loss mechanisms in each regime are depicted in Figure 6.1-1. During subsonic operation, the nozzle losses consist of internal friction (duct) loss, flow angularity losses, and external scrubbing drag loss resulting from the washing of the primary cowl and plug surfaces by jet flow. In the supersonic regime, additional losses are due to flow over or underexpansion resulting in shock cells. Variation in flow angularity loss among the models was minimized because all five models had throat plane and cowl/plug angles of 15 degrees.

6.1.2 Prediction Procedure Concept

The viscous internal duct losses and external scrubbing losses are readily predictable by any of several established analytical methods such as the one described in Reference 32. The shock loss and reference thrust coefficient are not predictable and have been treated empirically by a correlation developed from data acquired in this program. The performance prediction system, then, is a combination of analytical methods and empirical correlations

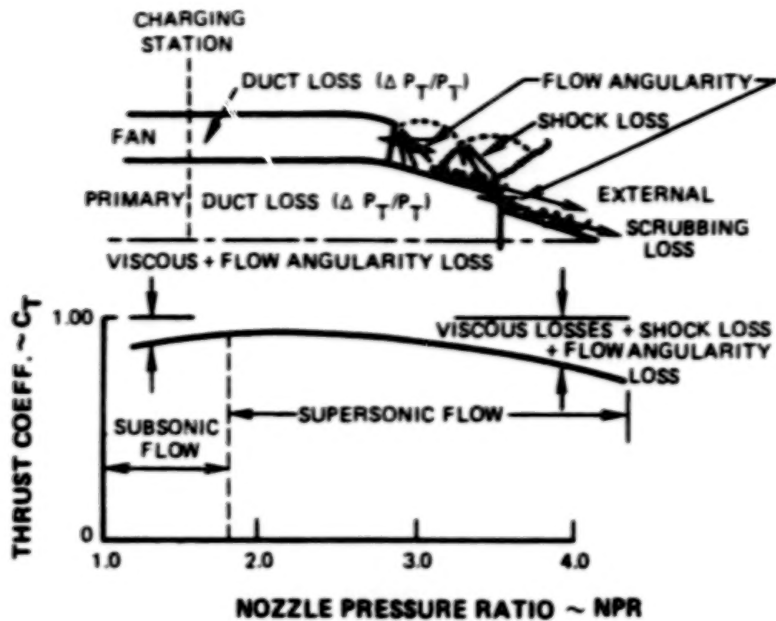


Figure 6.1-1 Nozzle Loss Mechanisms

6.2 VISCOSUS LOSSES

6.2.1 Internal Duct Loss

The internal friction losses are defined as the loss in thrust resulting from the loss in duct total pressure ($\Delta P_t/P_t$) from the pressure measurement station (charging station) to the nozzle throat plane. The duct losses were calculated analytically over the range of nozzle operating conditions using a Reshotko-Tucker one-dimensional compressible flow turbulent boundary layer analysis (Reference 32) modified to provide better agreement with data for adverse pressure gradient flow conditions. Results of the internal duct loss calculation, in terms of thrust coefficient increment at a primary nozzle pressure ratio (PNPR) of 1.53 and 2.0, are shown in Figure 6.2-1 for the five test configurations. The configuration ranking is exactly as expected. The high radius ratio plug Configuration E had the most internal surface area (see Figure 6.2-2 for review of the model configurations) and had the highest duct loss. Configuration A, the lowest fan stream radius ratio model without a plug, had the lowest internal surface area and the lowest internal duct loss.

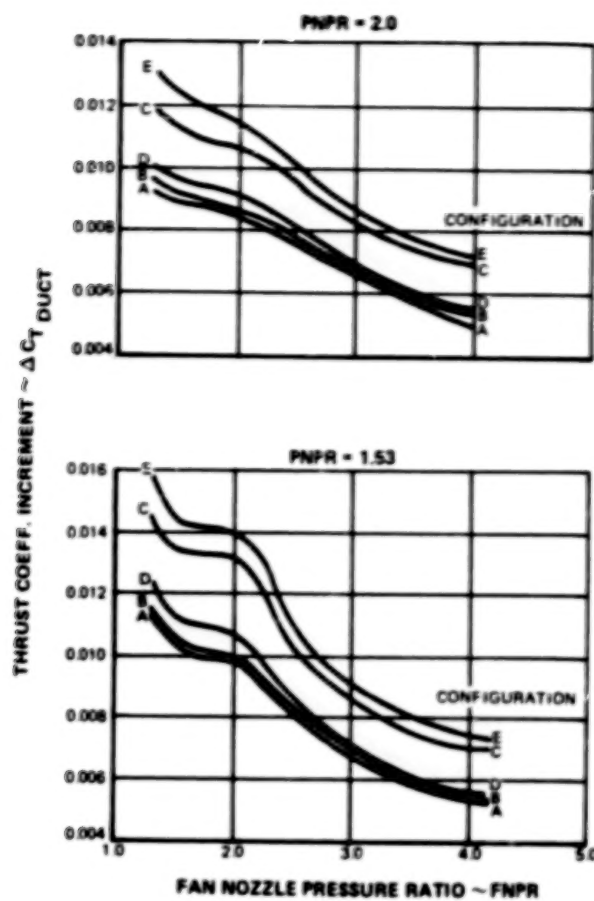


Figure 6.2-1 Test Model Analytical Internal Duct Loss

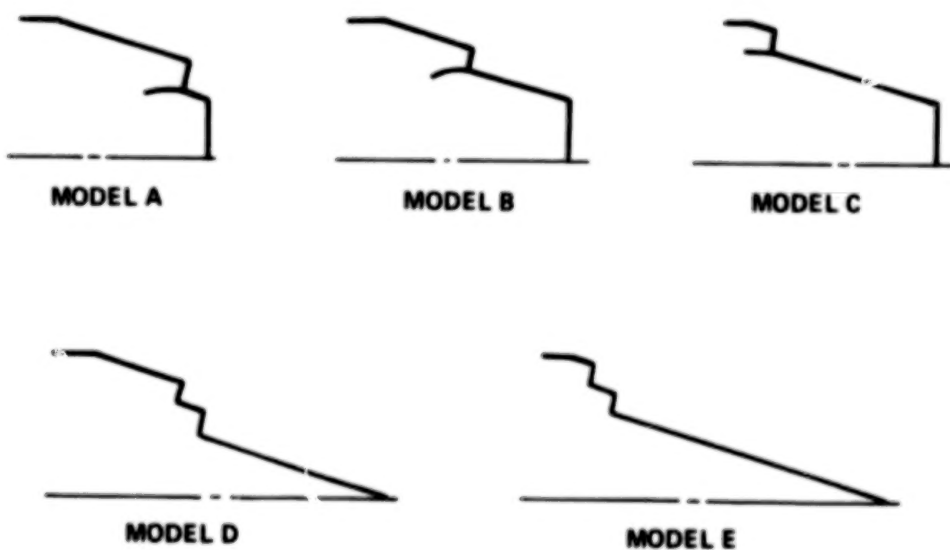


Figure 6.2-2 Review of Model Test Configurations

6.2.2 External Scrubbing Loss

The scrubbing loss is defined as the loss in thrust due to the viscous drag on the primary cowl and plug (if present) surfaces washed by the jet flow.

The scrubbing losses were calculated by assuming that the flow has expanded to jet velocities where the jet static pressure equals ambient pressure and applying the Reshotko-Tucker boundary layer analysis (Reference 32) to define a viscous drag which was converted to a thrust loss.

Examples of the scrubbing losses for the test configurations in terms of thrust coefficient increment at PNPR of 2.0 and 1.53 are shown in Figure 6.2-3. In comparing zero primary radius ratio models, ranking is also as expected with Configuration A exhibiting the lowest scrubbing loss. Plug Configurations D and E are also consistent, with Configuration E exhibiting a larger loss than Configuration D.

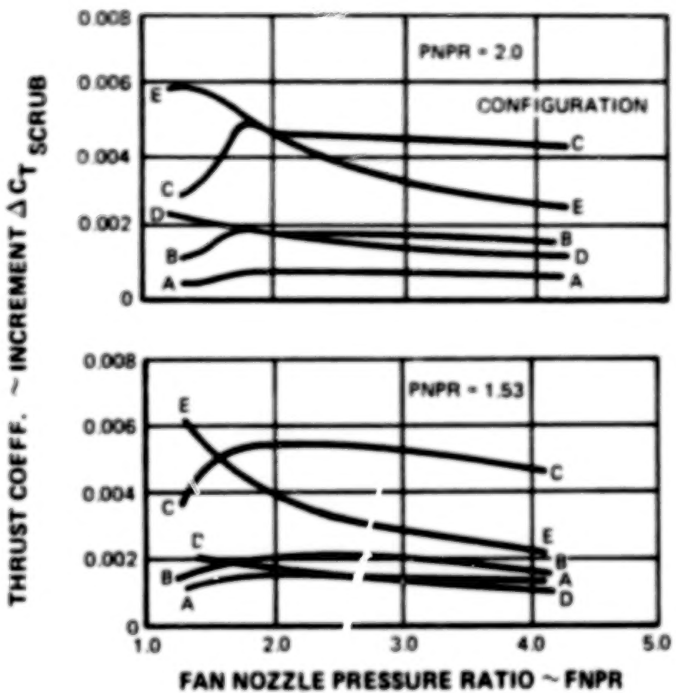


Figure 6.2-3 Thrust Loss From Predicted External Scrubbing Loss (From Reference 32)

Configurations A, B, and C exhibited an increasing scrubbing loss as fan nozzle pressure ratio (FNPR) increased subsonically from 1.2 to 2.0 followed by a slight fall-off in the supersonic region. In the subsonic region, the scrubbing loss increased because the increased primary cowl drag (caused by increased Mach number) increased at a more rapid rate than total nozzle thrust. This drag is proportional to FNPR while total thrust is comprised of constant primary thrust and a moderately increasing fan thrust. Configurations D and E showed decreasing scrubbing drag with increasing FNPR throughout the FNPR range variation. This trend is explained by the fact that for these models, scrubbing drag consists, predominantly, of primary plug drag which remains constant (at the constant test PNPR) while total thrust increases proportionally with FNPR.

6.2.3 Correlation of Subsonic Model Performance

In order to evaluate the validity of the preceding viscous loss assumptions, the thrust coefficients for Configurations A, B, and C were corrected for viscous effects. It should be pointed out that the correlated subsonic performance for Configurations A, B, and C include the flow angularity effects associated with these model designs. The measured thrust coefficients corrected for viscous effects for Configurations A, B and C are compared in Figure 6.2-4 for PNPR of 1.53 and 2.0. At a FNPR of 2.0 the data collapsed within ± 0.002 for a PNPR of 1.53 and within ± 0.0015 for a PNPR of 2.0. The data collapse below a FNPR 2.0 indicates that, in the subsonic flow regime, the major variations in nozzle performance can be attributed to the viscous loss mechanisms.

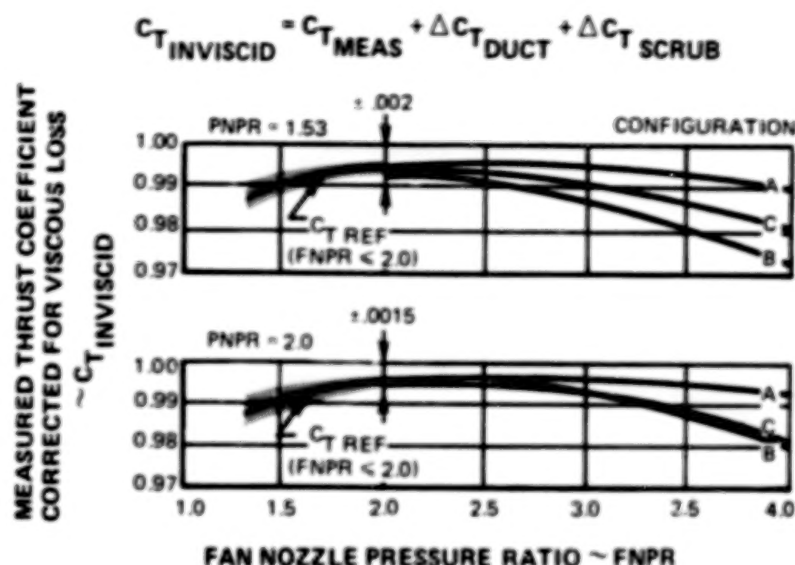


Figure 6.2-4 Viscous Loss Correlation of Measured Thrust Coefficient for Configurations A, B, and C

An empirical reference level of nozzle thrust coefficient, CT_{ref} , can be established as a function of FNPR by fairing a curve through the collapsed data for each PNPR as shown in Figure 6.2-5. A slight difference does exist between CT_{ref} curves established for the two PNPR test conditions. This difference is attributed to the interaction of the fan and primary flow fields as indicated by the primary nozzle flow restriction effects discussed previously in Section 4.2.2.

At FNPR greater than 2.0, Figure 6.2-4, it is observed that the thrust coefficients fall off at varying rates. The variation of the data in the supersonic flow regime indicates that the previously included viscous effects are insufficient to cause data collapse. An additional loss mechanism, shock loss, must be considered for FNPR greater than 2.0. Therefore, the task remaining to complete formulation of the prediction system was to correlate this shock loss as a function of the pertinent geometric parameters.

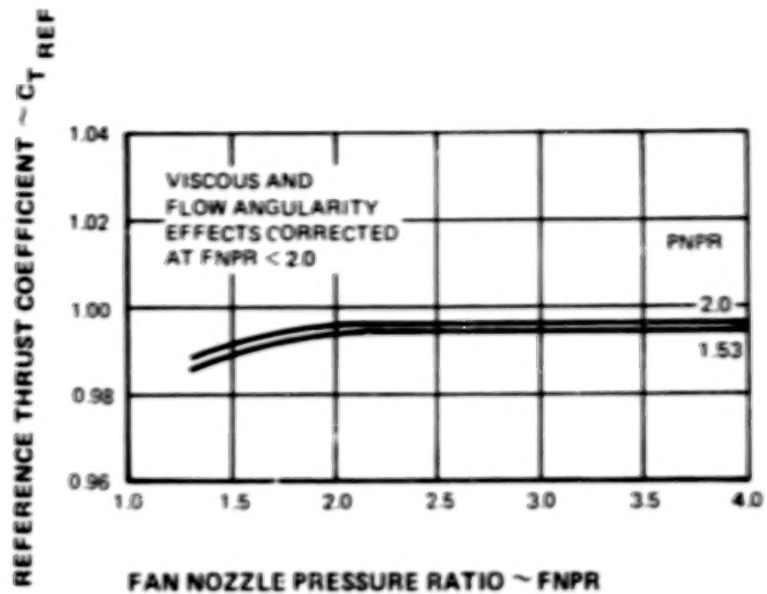


Figure 6.2-5 Reference Thrust Coefficient Established From Viscous Loss Correlations of Configurations A, B & C at $\text{FNPR} < 2.0$

6.3 SHOCK LOSS

6.3.1 Plug Nozzle Operating Characteristics

Plug nozzles aerodynamically adjust to changes in ambient pressure, hence producing acceptable performance levels below the nozzle pressure ratio (NPR) for choked flow. Performance falls off rapidly, however, as NPR is increased above critical pressure ratios into the over-expanded region, as shown in Reference 33 data of Figure 6.3-1. The poor performance in this region is caused by a series of shocks, over-expansion and compressions, emanating from the primary cowl. The resulting flow field breaks down into complex transonic and subsonic flows that are not accurately predicted by analytical techniques. As FNPR is further increased to the design value, performance improves but then falls off in the under-expanded regime as the exhaust plume goes beyond cylindrical, as shown in Figure 6.3-1. The test data from the present program were limited to the unchoked and over-expanded regimes. As shown in the preceding section, viscous losses collapsed the data in the unchoked regimes. The development of the static performance prediction system is then dependent upon the establishment of an empirical shock loss correlation to be used in the over-expansion region.

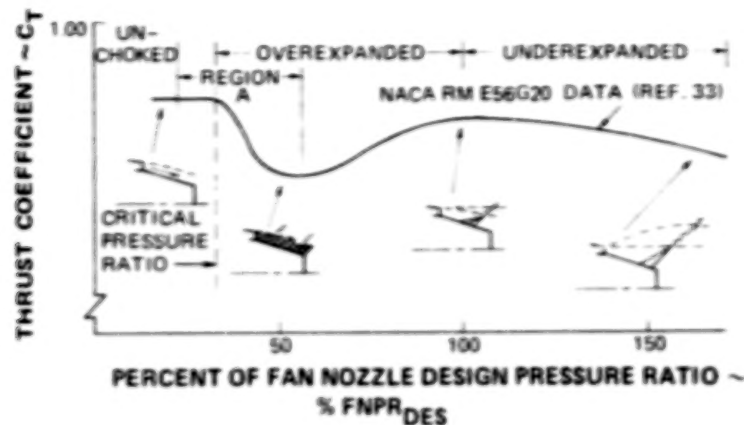


Figure 6.3-1 Typical Nozzle Operating Characteristics

6.3.2 Off-Design Shock Loss

The approach used to develop the shock loss correlation relates the off-design loss to nozzle area ratio (A_{ex}/A_f^*) and the ratio of fan nozzle operating and design pressure ratios (percent design FNPR). Area ratio, A_{ex}/A_f^* , for an annular nozzle is defined in Figure 6.2-2. diagram.

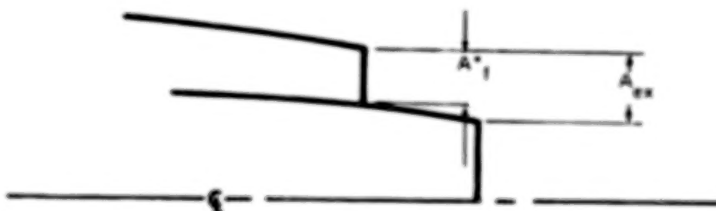


Figure 6.3-2 Definition of Annular Nozzle Area Ratio $\sim A_{ex}/A_f^*$

The shock loss thrust coefficient decrement, ΔCT_{SHOCK} , was determined as the difference between the thrust coefficient adjusted for viscous losses and CT_{ref} for fan nozzle pressure ratios at and above 2.0, as shown conceptually in Figure 6.3-3. Data for the three zero primary radius ratio Configurations A, B and C were selected for the correlation since the fan nozzle area ratio was readily defined by the cylindrical primary plume associated with zero primary radius ratio. The performance of those configurations, adjusted for viscous losses at a FNPR above 2.0, is compared to the reference thrust coefficient are plotted as a function of percent design FNPR in Figures 6.3-4 and 6.3-5 for PNPR 2.0 and 1.53, respectively. Comparison of the two figures indicates that the shock losses for PNPR 2.0 and 1.53 are not exactly the same. While the difference is relatively small, there are apparently sufficient differences in fan and primary stream interactions at the two PNPR levels to produce slightly different shock loss correlations. Crossplotting the data of Figures 6.3-4 and 6.3-5 provides maps of the shock loss correlation, ΔCT_{SHOCK} , as a function of fan nozzle area ratio and percent fan nozzle design pressure ratio as shown in Figure 6.3-6 (PNPR = 2.0) and Figure 6.3-7 (PNPR = 1.53). Combining these shock loss correlations with the CT_{ref} correlation and the analytical viscous loss predictions constitutes the performance prediction procedure.

$$CT_{pred} = CT_{ref} - [\Delta CT_{DUCT} + \Delta CT_{SCRUB} + \Delta CT_{SHOCK}]. \quad \text{Eq. (6-1)}$$

The differences in level of $C_{T_{ref}}$ and shock losses observed at the two PNPR tested, although small, indicate that coannular nozzle performance is dependent on PNPR as well as FNPR particularly in the supersonic flow regime. As a result of these differences, interpolation is required within the range of PNPR tested, 1.53 to 2.0. Extension of the prediction procedure to other PNPR should be restricted until supporting data are obtained.

$$C_T = C_{T \text{ REF}} - \Delta C_{T \text{ DUCT}} - \Delta C_{T \text{ SCRUB}} - \Delta C_{T \text{ SHOCK}}$$

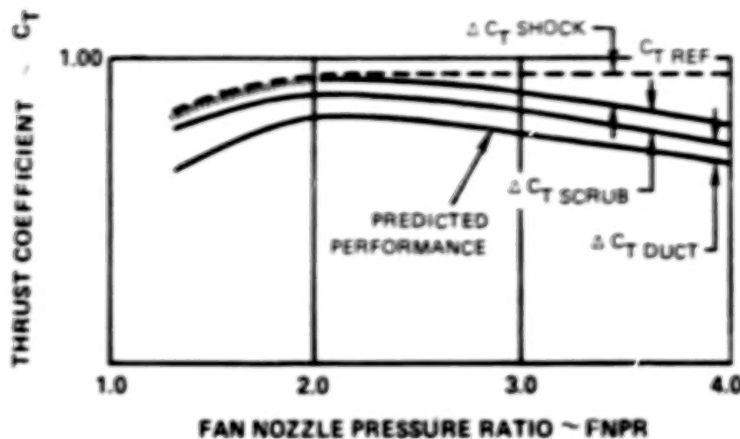


Figure 6.3-3 Thrust Coefficient Elements of the Static Performance Prediction System

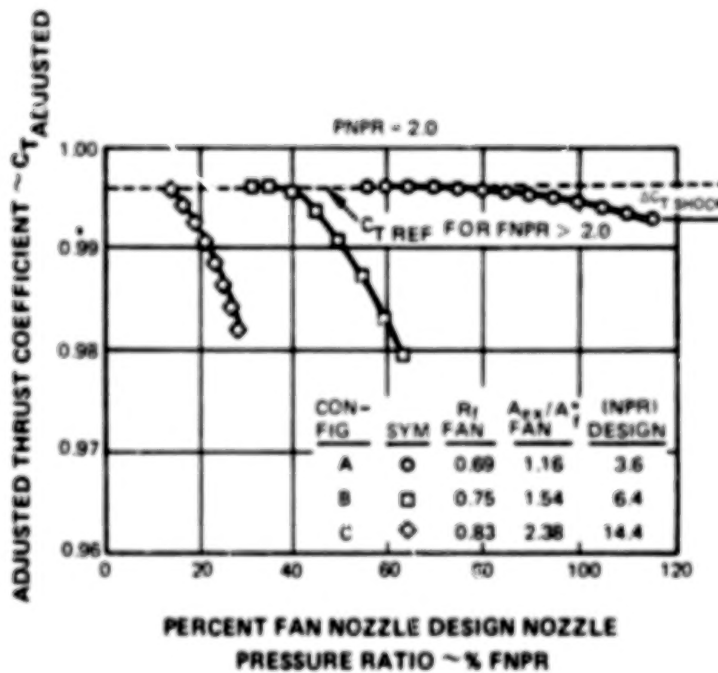


Figure 6.3-4 Off-Design Shock Loss Variations at PNPR = 2.0

TABLE OF CONTENTS

		Page
SECTION 1.0	SUMMARY	1 1/A12
SECTION 2.0	INTRODUCTION	3 1/A14
	2.1 Background	3 1/A14
	2.2 Program Description	4 1/B1
	2.2.1 Test Matrices	5 1/B2
	2.2.2 Test Program Description	5 1/B2
	2.2.3 Aerodynamic and Acoustic Prediction Procedure	6 1/B3
SECTION 3.0	APPARATUS – MODEL TEST AND TEST FACILITIES	7 1/B4
	3.1 Jet Noise Test Facility (X-206 Stand)	7 1/B4
	3.1.1 Test Chamber	7 1/B4
	3.1.2 Acoustic Data Acquisition System	10 1/B7
	3.1.3 Pressure and Temperature Instrumentation	10 1/B7
	3.1.3.1 Nozzle Operating Condition Instrumentation	10 1/B7
	3.1.3.2 Nozzle Exhaust Plume Traverse Instrumentation	12 1/B10
	3.1.3.3 Exhaust Plume Traverse System Description	12 1/B10
	3.1.3.4 Data Acquisition Equipment	15 1/B13
	3.1.4 Acoustic Test Matrix	15 1/B13
	3.1.5 Test Procedure	19 1/C6
	3.2 UTRC Large Nozzle Thrust Facility	19 1/C6
	3.2.1 System Description	19 1/C6
	3.2.2 Instrumentation	20 1/C7
	3.2.3 Facility Thrust Balance Calibration	21 1/C8
	3.2.4 Aerodynamic Performance Test Matrix	23 1/C10
	3.3 Nozzle Models	24 1/C11
	3.3.1 Configuration Selection	24 1/C11
	3.3.2 Model Designs	26 1/C13
SECTION 4.0	TEST DATA	31 1/D4
	4.1 Acoustic Data	31 1/D4
	4.1.1 Acoustic Data Reduction	31 1/D4
	4.1.1.1 Theoretical Day SPL (Model)	32 1/D5
	4.1.1.2 Scaled Engine Data	35 1/D10
	4.1.1.3 Calculation of Acoustic Power Levels	36 1/D11
	4.1.2 Acoustics Results and Discussion	37 1/D12
	4.1.2.1 Comparison of Convergent Nozzle Data With SAE Predictions	38 1/D13
	4.1.2.2 Unsuppressed Coannular Nozzle Results	39 1/D14
	4.1.2.3 Definition of the Acoustic Characteristics of a Single Stream Plug Nozzle	54 1/F1

TABLE OF CONTENTS (Cont'd)

	Page
4.1.2.4 Definition of the Acoustic Characteristics of a Coannular Nozzle with Primary Flow Leakage	57 1/F4
4.2 Aerodynamic Data	61 1/F8
4.2.1 Aerodynamic Data Reduction	61 1/F8
4.2.1.1 Thrust and Discharge Coefficient Data Reduction	61 1/F8
4.2.1.2 Traverse Data Reduction	64 1/F11
4.2.2 Aerodynamic Results and Discussion	64 1/F11
4.2.2.1 Thrust Coefficient	64 1/F11
4.2.2.2 Discharge Coefficient	70 1/G4
4.2.2.3 Nozzle Velocity and Temperature Profiles	76 1/G10
 SECTION 5.0 ACOUSTIC ENGINEERING PREDICTION PROCEDURE	 81 2/A5
5.1 General Approach	81 2/A5
5.1.1 Description of the Acoustic Data Base	81 2/A5
5.1.2 Definition of Spectral Decomposition	84 2/A8
5.1.3 Definition of Acoustic Models Used in Developing the Prediction Procedure	90 2/A14
5.1.4 Definition of Characteristic Velocity, Temperature, and Area for Initial and Merged Regions	91 2/B1
5.2 Static Jet Exhaust Noise Prediction Procedure	93 2/B3
5.2.1 Development of Mixing Noise Data Correlations	93 2/B3
5.2.1.1 Merged Region Mixing Noise	98 2/B8
5.2.1.2 Initial Region Mixing Noise	109 2/C5
5.2.2 Development of Shock Noise Data Correlations	117 2/C13
5.2.2.1 Development of Fan Stream Shock Noise Data Correlations	117 2/C13
5.2.2.2 Development of Primary Stream Shock Noise Data Correlations	125 2/D7
5.3 Flight Jet Exhaust Noise Prediction Procedure	130 2/D12
5.3.1 General Background	130 2/D12
5.3.2 Definition of the Effect of Flight on Mixing Noise	132 2/D14
5.3.2.1 Definition of the Effect of Flight on the Low Frequency Mixing Noise Component	134 2/E2
5.3.2.2 Definition of the Effect of Flight on the High Frequency Mixing Noise Component	136 2/E4
5.3.3 Definition of the Effect of Flight on the Shock Noise Component	138 2/E6

TABLE OF CONTENTS (Cont'd)

	Page	
5.4 Summary of Acoustic Prediction Procedure	139	2/E7
5.4.1 General Approach	139	2/E7
5.4.2 Summary of the Static Acoustic Prediction Procedure	140	2/E8
5.4.2.1 Low Frequency Mixing Noise Component	140	2/E8
5.4.2.2 High Frequency Mixing Noise Component	140	2/E8
5.4.2.3 Fan Stream Shock Noise	141	2/E9
5.4.2.4 Primary Stream Shock Noise	142	2/E10
5.4.3 Summary of the Flight Acoustic Prediction Procedure	143	2/E11
5.4.3.1 Low Frequency and High Frequency Mixing Noise Components	144	2/E12
5.4.3.2 Fan Stream and Primary Stream Shock Noise Components	145	2/E13
5.5 Sample Calculation	145	2/E13
5.5.1 Inputs Required for the Acoustic Prediction	146	2/F1
5.5.2 Prediction of the Static Jet Exhaust Noise	147	2/F1
5.5.2.1 Low Frequency Mixing Noise	147	2/F1
5.5.2.2 High Frequency Mixing Noise	148	2/F2
5.5.2.3 Fan Stream Shock Noise	149	2/F3
5.5.2.4 Primary Stream Shock Noise	149	2/F3
5.5.3 Prediction of the Flight Jet Exhaust Noise	151	2/F5
5.5.3.1 Low Frequency and High Frequency Mixing Noise Components	151	2/F5
5.5.3.2 Fan Stream and Primary Stream Shock Noise Components	151	2/F5
5.6 Comparison of Data with Predictions Using the Acoustic Prediction Procedure	152	2/F6
5.6.1 Comparison of IVP Coannular Nozzle Noise Predictions with Measured Data	153	2/F7
5.6.2 Analysis of the Accuracy of the Prediction Procedure	165	2/G5
SECTION 6.0	STATIC AERODYNAMIC PERFORMANCE PREDICTION PROCEDURE	
6.1 Approach	167	2/G7
6.1.1 Subsonic and Supersonic Nozzle Loss Mechanisms	167	2/G7
6.1.2 Prediction Procedure Concept	167	2/G7
6.2 Viscous Losses	168	2/G8
6.2.1 Internal Duct Loss	168	2/G8
6.2.2 External Scrubbing Loss	170	2/G10
6.2.3 Correlation of Subsonic Model Performance	171	2/G11

TABLE OF CONTENTS (Cont'd)

	Page
6.3 Shock Loss	172 2/G12
6.3.1 Plug Nozzle Operating Characteristics	172 2/G12
6.3.2 Off-Design Shock Loss	173 2/G13
6.4 Application of the Aerodynamic Performance Prediction Procedure	176 3/A6
6.4.1 Procedural Steps and Input Requirements	176 3/A6
6.4.2 Numerical Example of the Procedure Use	179 3/A9
6.5 Evaluation of the Static Aerodynamic Performance Prediction Procedure	182 3/A12
 SECTION 7.0	
SUMMARY OF RESULTS AND CONCLUSIONS	187 3/B3
7.1 Acoustic Results and Conclusions	187 3/B3
7.1.1 Acoustic Prediction Procedure	187 3/B3
7.1.2 Acoustic Test Results	188 3/B4
7.2 Aerodynamic Performance Results and Conclusions	188 3/B4
7.2.1 Static Aerodynamic Performance Prediction Procedure	188 3/B4
7.2.2 Aerodynamic Performance Test Results	189 3/B5
7.3 Prediction System Accuracy	190 3/B6
 APPENDIX A	
 APPENDIX B	
LIST OF SYMBOLS	211 3/D11
REFERENCES	214 3/D14

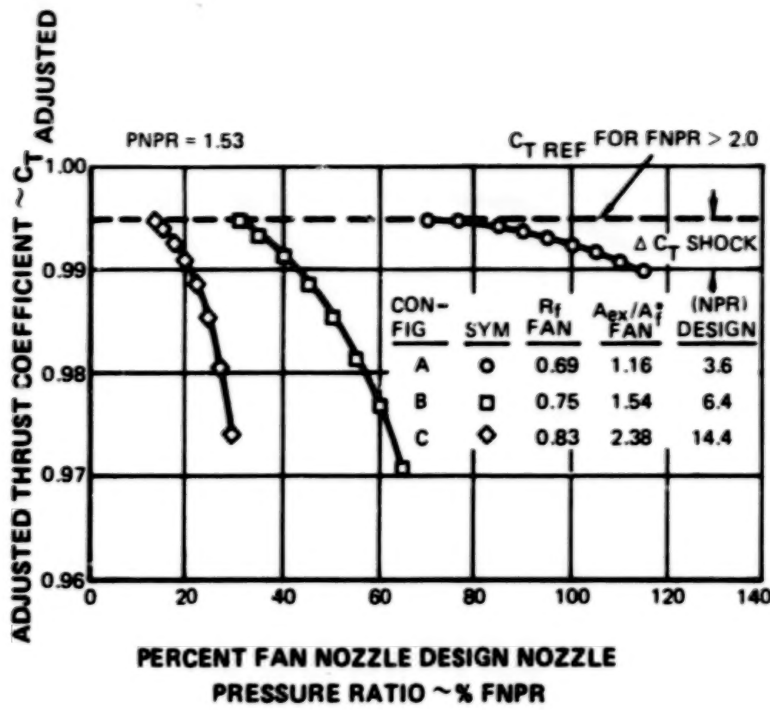


Figure 6.3-5 Off-Design Shock Loss Variations at $\text{PNPR} = 1.53$

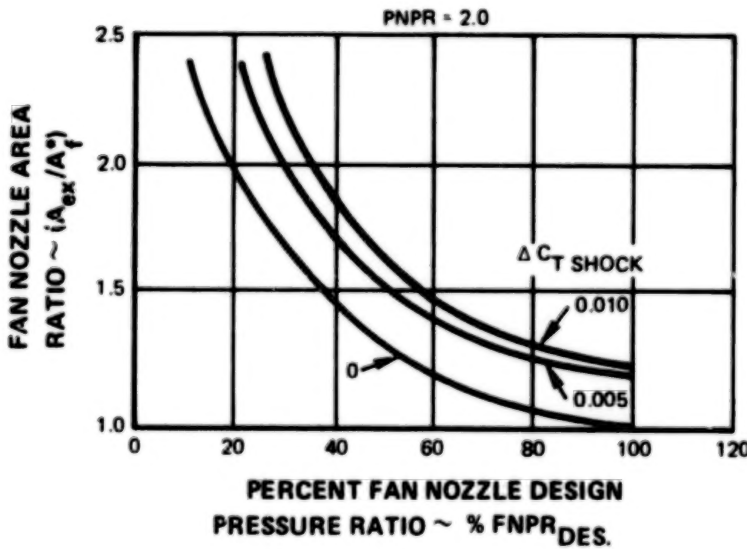


Figure 6.3-6 Empirical Off-Design Shock Loss Correlation

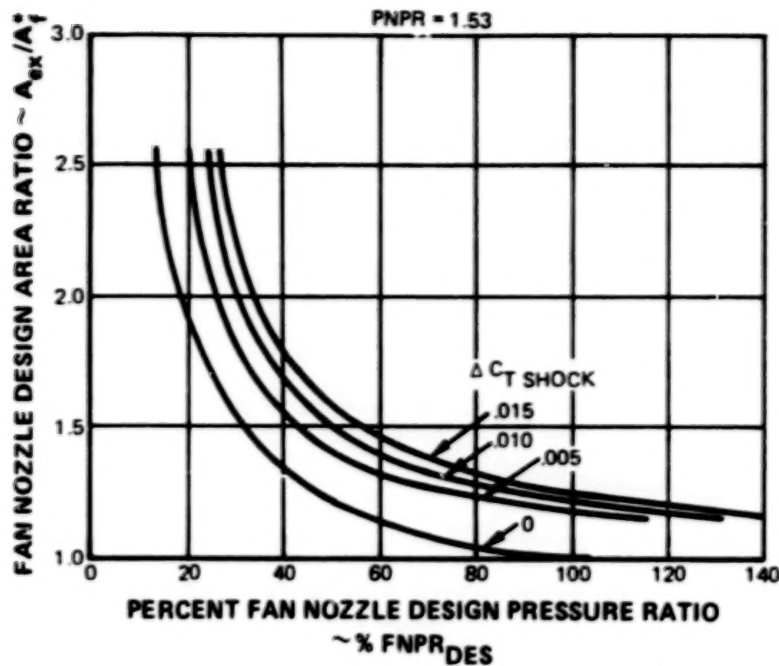


Figure 6.3-7 *Empirical Off-Design Shock Loss Correction*

6.4 APPLICATION OF THE AERODYNAMIC PERFORMANCE PREDICTION PROCEDURE

6.4.1 Procedural Steps and Input Requirements

The input requirements and procedural steps necessary for application of the performance prediction procedure will be discussed in this section. A specific prediction estimate will be discussed in Section 6.4.2 for Configuration E to further clarify use of the procedure. A flow diagram of the required steps is shown in Figure 6.4-1.

1. Determine the nozzle operating conditions for which the performance prediction is desired. These should include fan and primary nozzle pressure ratios and charging station total pressure and temperature.
2. The fan and primary flowpaths must be completely defined including coordinates from the charging station through the exits of fan and primary nozzles (including a center body plug, if present). Some estimate of the nozzle internal surface roughness will be required for the analytically determined viscous loss estimate. The fan nozzle design pressure ratio will be an input to the off-design shock loss correlation.
3. The reference thrust coefficient is read directly from Figure 6.2-5 using the fan and primary operation nozzle pressure ratios, interpolating if necessary between PNPR.

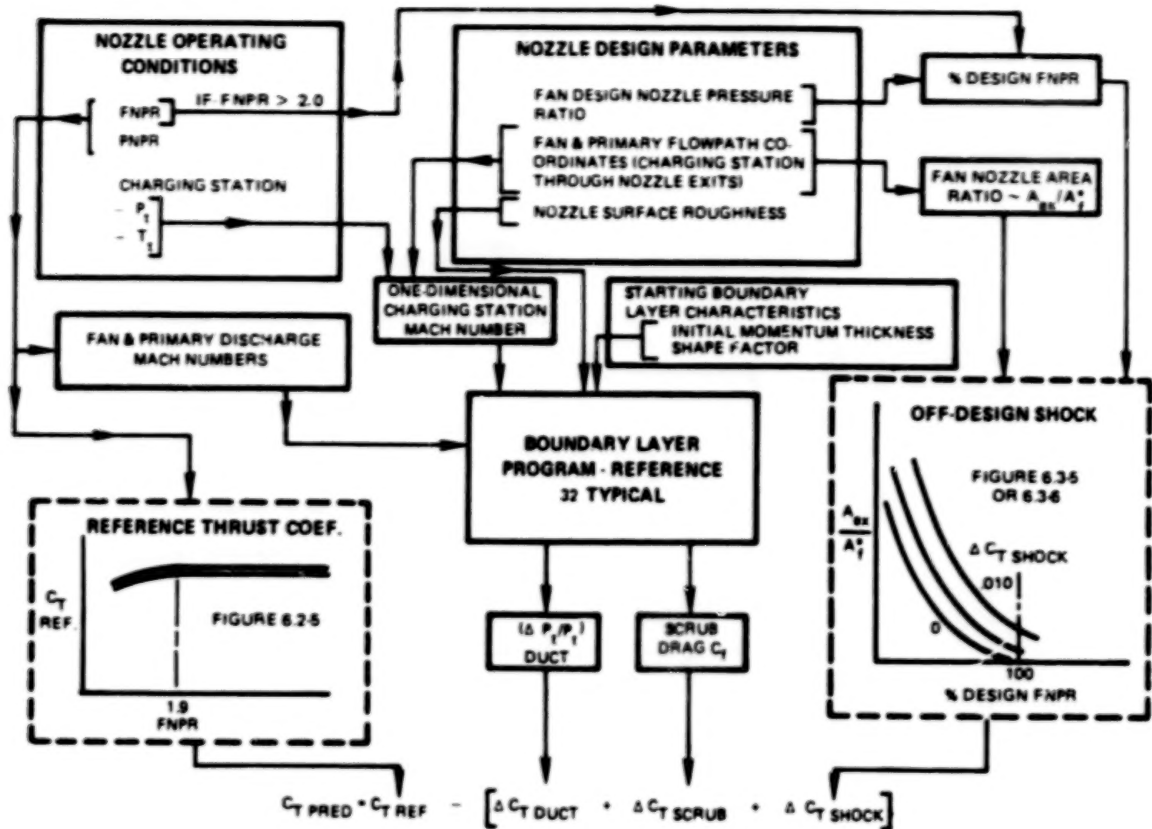


Figure 6.4-1 Aerodynamic Performance Prediction Procedure Flow Diagram

4. The fan and primary discharge Mach numbers needed for the viscous loss estimate of external scrubbing drag can be determined by entering operating FNPR and PNPR into the Mach function equation:

$$M_{ex} = \sqrt{\frac{2}{\gamma - 1}} \left[(NPR) \frac{\gamma - 1}{\gamma} - 1 \right] \quad \text{Eq. (6-2)}$$

where $NPR = P_t/P_a$

5. Analytical prediction of the viscous losses requires use of a boundary layer calculation. The program of Reference 32 (Roshko-Tucker Analysis) is typical. Many such programs may be used for this purpose and may require a different form of input than that needed for the Reference 32 program.

6. Inputs to the Reference 32 boundary layer program include an estimate of the initial momentum thickness at the charging station. This estimate can be based on engineering judgment or preferably the result of an additional boundary layer computation starting from a point of known zero momentum thickness in the ducting upstream of the charging station.

A preliminary (one dimensional) charging station Mach number estimate is required. Nozzle flowpath geometry (see item 2), nozzle exit Mach numbers (see item 4), and nozzle internal surface roughness complete the required inputs to the Reference 32 boundary layer program.

7. Viscous Losses.

The internal duct loss output of the boundary layer analysis is given in terms of duct total pressure loss. This total pressure loss must be converted to an equivalent thrust or CT loss. The procedure is as follows for each stream:

$$\frac{F_{id}}{A^*P_t} = \sqrt{\frac{2\gamma^2}{\gamma-1}} \left(\frac{2}{\gamma+1} \right)^{\frac{\gamma+1}{\gamma-1}} \left[\frac{1-\gamma}{\gamma} \right] \quad . \quad \text{Eq. (6-3)}$$

$$\frac{\Delta F_{id}/F_{id}}{\Delta P_t/P_t} = \frac{\Delta C_{T,DUCT}}{\Delta P_t/P_t} = \frac{d(F_{id}/A^*P_t)/F_{id}/A^*P_t}{d(P_t/P_a)/P_t/P_a} \quad . \quad \text{Eq. (6-4)}$$

Differentiating Equation (6-3), substituting the result into Equation (6-4), and simplifying yields:

$$\frac{\Delta C_{T,DUCT}}{\Delta P_t/P_t} = \frac{\frac{1}{2} \left(\frac{\gamma+1}{\gamma} \right)}{\frac{\gamma-1}{\gamma} \left(\frac{P_t/P_a}{\gamma} - 1 \right)} \quad . \quad \text{Eq. (6-5)}$$

$$\text{and} \quad \Delta C_{T,DUCT} = \frac{\left(\frac{\gamma+1}{\gamma} \right) \Delta P_t/P_t}{2 \left[\left(\frac{P_t/P_a}{\gamma} - 1 \right) \right]} \quad . \quad \text{Eq. (6-6)}$$

For the two stream case, the individual fan and primary thrust coefficient decrements must be thrust weighted to obtain the overall thrust decrement.

$$\Delta CT = \frac{F_{idf} \Delta CT_f + F_{idp} \Delta CT_p}{F_{idf} + F_{idp}} \quad . \quad \text{Eq. (6-7)}$$

The scrubbing drag loss for each stream is computed as the product of skin friction coefficient, C_f (an output of the boundary layer calculation procedure), the external wetted surface area (A_w), and the stream's dynamic head (q):

$$D_{SCRUB} = C_f q A_w \quad . \quad \text{Eq. (6-8)}$$

where

$$q = \frac{1}{2} \rho_a \gamma M_{ex}^2 \quad . \quad \text{Eq. (6-9)}$$

The individual stream scrubbing drags are then converted into an overall thrust coefficient decrement as follows:

$$\Delta CT = \frac{D_{SCRUB_f} + D_{SCRUB_p}}{F_{idf} + F_{idp}} \quad . \quad \text{Eq. (6-10)}$$

8. The off design shock thrust coefficient loss decrement can be determined from Figure 6.3-5 or 6.3-6 by entering the correlation curves with fan nozzle area ratio and percent design fan nozzle pressure ratio, interpolating as required for PNPR.

This completes the static aerodynamic performance prediction procedure sequence.

6.4.2 Numerical Example of the Procedure Use

An example of the use of the static performance prediction procedure will be made for Configuration E.

1. Nozzle Operating Conditions:

	<u>Fan</u>	<u>Primary</u>
Nozzle pressure ratios	3.0	2.0
Charging station		
a) P_t N/m ² (lb/in ²)	3.04×10^6 (44.1)	2.03×10^6 (29.4)
b) T_t °K (°R)	294 (530)	294 (530)
c) γ	1.4	1.4

2. Model Design Parameters and Geometry Definition – Configuration E

- a) Flowpath geometry coordinates of Figure 6.4-2 were input to the Reference 32 Boundary Layer analysis.
- b) The fan and primary nozzle areas are $A_f^* = 0.0075 \text{ m}^2$ (11.72 in²) and $A_p^* = 0.0051 \text{ m}^2$ (7.92 in²).
- c) The fan nozzle area ratio A_{cv}/A_f^* is 1.22.

3. Reference Thrust Coefficient (CT_{ref}):

Inputting FNPR 3.0 and PNPR 2.0 to Figure 6.2-5, Read $CT_{ref} = 0.996$.

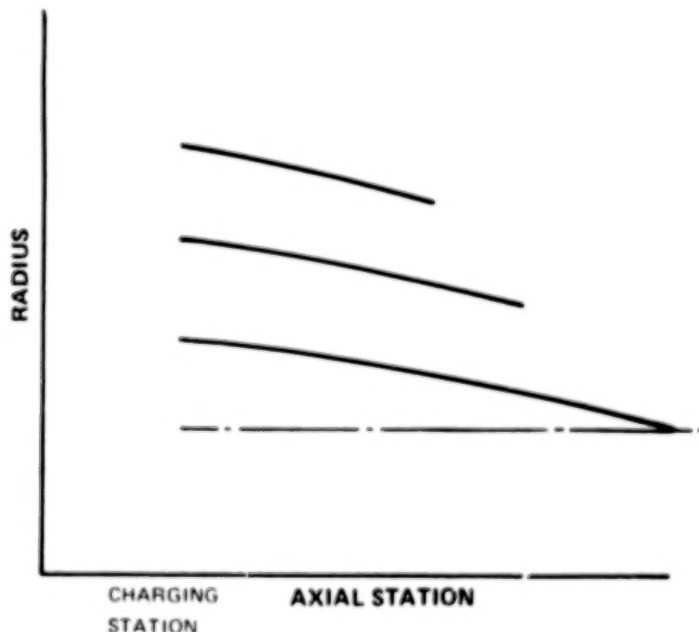


Figure 6.4-2 Configuration E Flow Path Coordinates

4. Internal Duct Loss Analysis:

Inputs:	<u>Fan</u>	<u>Primary</u>
a) Charging station entrance Mach number	.380	.186
b) Surface roughness ~ mm (in.)	.0076(.0003)	.0076(.0003)
c) Momentum thickness ~ mm (in.)	.508 (.02)	.660 (.026)
Outputs: (From Reference 32 analysis)		
a) Duct total pressure loss ($\Delta P_t/P_t$)	.023	.012
b) Throat plane momentum thickness (Input for scrubbing drag Analysis) ~ mm (in.)	.305 (.012)	.076 (.003)
Fan and Primary Thrust Coefficient Decrement (ΔCT) due to duct total pressure loss		
Computed from Equation (6-6)	.009	.0078
Ideal Thrust Fid		
Computed from Equation (6-3) N (lb)	2162 (489)	796 (179)
Overall ΔCT		
Computed from Equation (6-7)	$\Delta CT =$.0086

5. Scrubbing Drag Analysis:

Inputs:	<u>Fan</u>	<u>Primary</u>
a) Fan and primary exit Mach numbers computed from Equation (6-2)	1.358	1.046
b) Surface roughness ~ mm (in.)	.0076(.0003)	.0076(.0003)
c) Momentum thickness (out-put from duct loss analysis) ~ mm (in.)	.305 (.012)	.076 (.003)

	<u>Fan</u>	<u>Primary</u>
Outputs:		
a) Average friction coefficient C _f (from Reference 32 analysis)	.0025	.0028
b) q, computed from Equation (6-9) ~ N/m ² (lb/in ²)	1.308x10 ⁵ (18.971)	0.77x10 ⁵ (11.255)
c) External surface area computed from geometry ~ m ² (in ²)	6.671x10 ⁻³ (10.34)	3.51x10 ⁻² (54.4)
d) Scrubbing drag computed from from Equation (6-8) N (lb)	2.10 (.490)	7.624 (1.714)
Computed from Equation (6-10)	$\Delta CT_{SCRUB} = .00337$	

6. Off design shock loss correlation -

For the fan nozzle area ratio A_{ex}/A_f^* of 1.22, design FNPR = 4.045 and percent design FNPR = $3.0/4.045 = .7417$, from Figure 6.3-5 read $\Delta CT_{SHOCK} = .002$.

7. Configuration E Thrust Coefficient Prediction -

Relating the viscous and shock loss decrement to the CT_{ref} (Equation (6-1)) gives $CT_{pred} = .982$ which compares well with the measured thrust coefficient of .979.

6.5 EVALUATION OF THE STATIC AERODYNAMIC PERFORMANCE PREDICTION PROCEDURE

The performance prediction procedure was first applied to the Configurations D and E by comparing predicted and measured thrust coefficients. These models have fan nozzle design area ratios (A_{ex}/A_f^*) of 1.20 and 1.22, respectively. The results, plotted as predicted minus the measured thrust coefficient vs. FNPR, are shown in Figure 6.5-1 for the PNPR = 2.0. The comparison for the PNPR = 1.53 data is shown in Figure 6.5-2. The PNPR 2.0 data comparison is accurate to within +0.003 for Configuration E and -0.001 for Configuration D at a FNPR of 3.0. The band spread at FNPR 3.0 for the PNPR 1.53 data comparison is greater, from +0.001 to +0.006. This lack of closure indicates that the primary flow is producing an interaction with the fan flow which affects the magnitude of the shock losses on the after-body and on the primary plug.

A second evaluation of the Static Performance Prediction Procedure was made by application of the procedure to a single flow plug nozzle (Configuration E primary flow only). For this example, the PNPR 1.53 shock loss correlation was somewhat better than the PNPR 2.0 data as shown in Figure 6.5-3. The predicted minus measured CT variation was from -0.001 to -0.004 for the PNPR 1.53 data and from 0 to -0.0055 for the latter correlation.

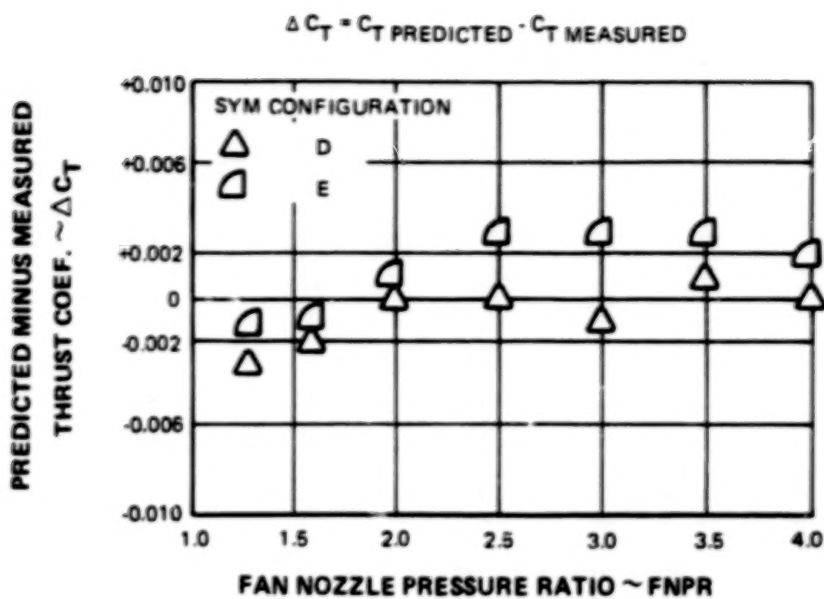


Figure 6.5-1 Predicted - Measured Thrust Coefficient at Primary Nozzle Pressure Ratio = 2.0 for Plug Configuration D&E

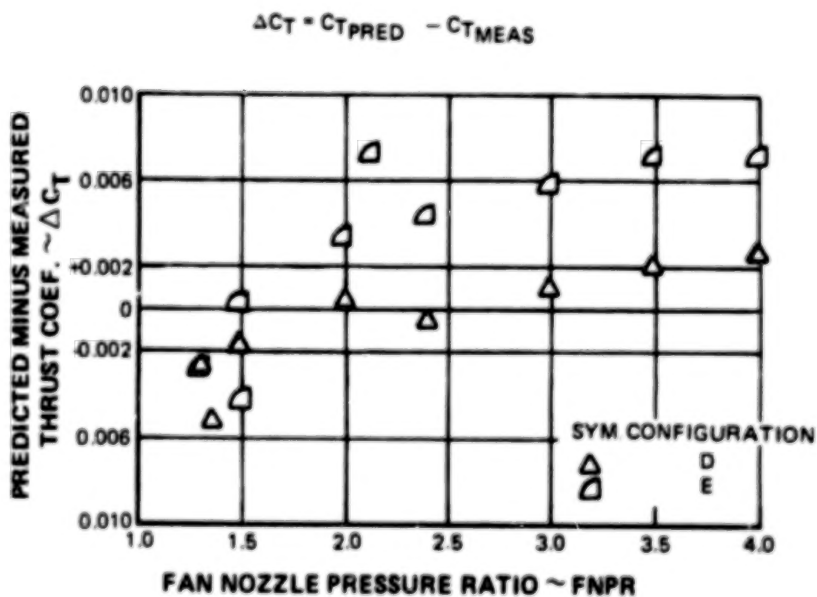


Figure 6.5-2 Predicted - Measured Thrust Coefficient at Primary Nozzle Pressure Ratio = 1.53 for Plug Configurations D&E

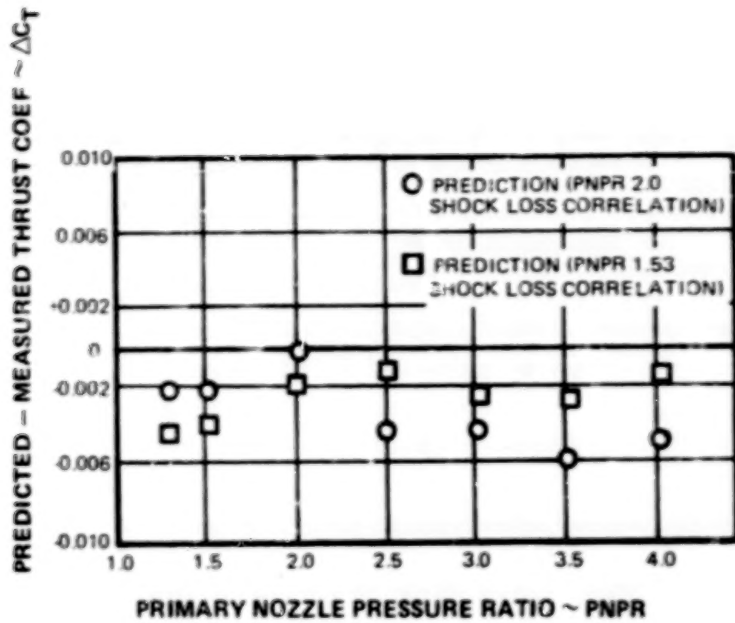


Figure 6.5-3 Predicted - Measured Thrust Coefficient for Configuration E Primary Flow Only

A third evaluation of the procedures was made using the data from the coannular plug models of Reference 34 (NAS-19777). Four of the eight configurations tested in the Reference 34 program (Configurations 2, 3, 5, and 6) were evaluated. These configurations are shown in Figure 6.5-4. The choice of these models is of interest since some of the model geometric parameters fall outside the range of those tested in this program. A comparison of Reference 34 configurations to the prediction system nozzle geometry and pressure ratios tested is given in Table 6.5-1.

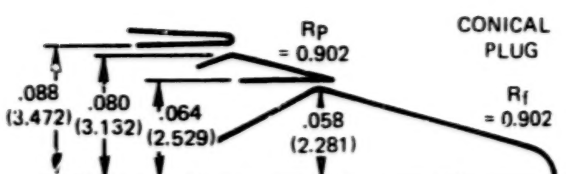
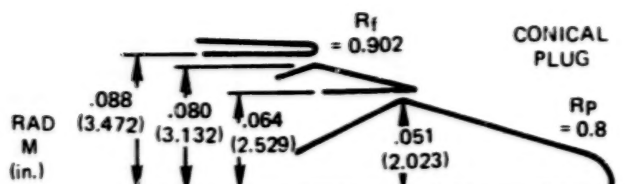
Results of the application of the aerodynamic performance prediction system to the Reference 34 nozzle data are summarized in Figure 6.5-5. Predictions were made for FNPRs of 2.0 and 3.2 at a PNPR of 1.5. The predicted levels of performance were greater than measured for all configurations compared, ranging from 0.3 to 0.6 percent higher for Configurations 2 and 5 and 1.0 to 2.5 percent higher for Configurations 3 and 6. The error in predicted versus measured C_T is much greater than that of the other examples checked. The reason for this disparity is believed to be due to the nozzle throat design of the Reference 34 test configurations. The fan and primary nozzle throats were designed such that the discharge flow exited axially, whereas the prediction system is based on test results of model configurations that were designed to have the nozzle discharge flow aligned with the downstream surface as shown in Figure 6.5-6.

Previous experimental work with single flow plug nozzles, Reference 35, has shown that when the nozzle throat is misaligned with the plug surface, thrust coefficient decreases as shown in Figure 6.5-7.

The conclusion from these comparisons is that the prediction system developed in the current program does not have general applicability to all coannular plug nozzles. The system's use should be restricted to exhaust nozzles similar to those tested, and extrapolating its use to types of configurations other than those tested in this program could result in substantial errors.

CONFIGURATION NO. 2

CONFIGURATION NO. 3



CONFIGURATION NO. 5

CONFIGURATION NO. 6

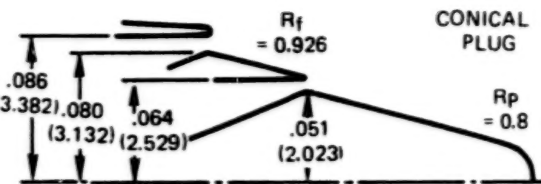
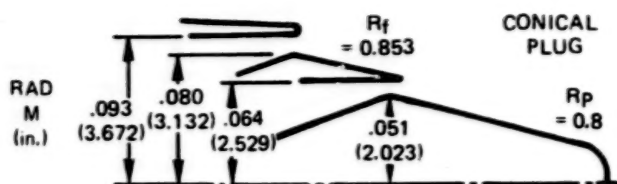


Figure 6.5-4 Nozzle Configurations (Reference 34) Evaluated With Aerodynamic Performance Prediction Procedure

TABLE 6.5-1

COMPARISON OF REFERENCE 34 AND PREDICTION SYSTEM NOZZLE GEOMETRIES AND TEST PRESSURE RATIOS

Prediction System Range	Reference 34 (NAS3-19777 Configurations)				
	Config. 2	3	5	6	
A_f/A_p	1.48	1.0	1.9	1.6	0.7
A_{exp}/A_f^*	1.2 - 2.4	2.5	2.3	1.9	3.1
A_{exp}/A_p^*	1.0 - 2.7	2.8	5.4	2.8	2.8
Cowl Angle	15°	15°	15°	15°	15°
R_f	15°	0°	0°	0°	0°
R_p	0.69 - 0.83	0.9	0.9	0.85	0.93
r_{Dp}/r_{ODp}	0 - 0.81	0.8	0.9	0.8	0.8
FNPR	1.3 - 4.1		1.5 - 3.2		
PNPR	1.53 & 2.0		1.5, 2.5, 3.5		

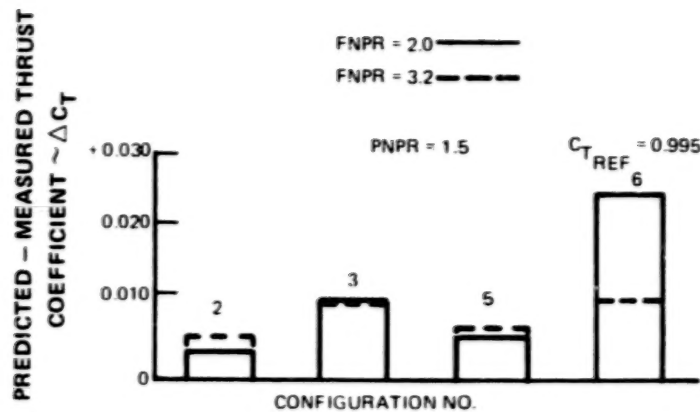


Figure 6.5-5 Predicted Minus Measured Thrust Coefficient (Reference 34 Nozzle Models)

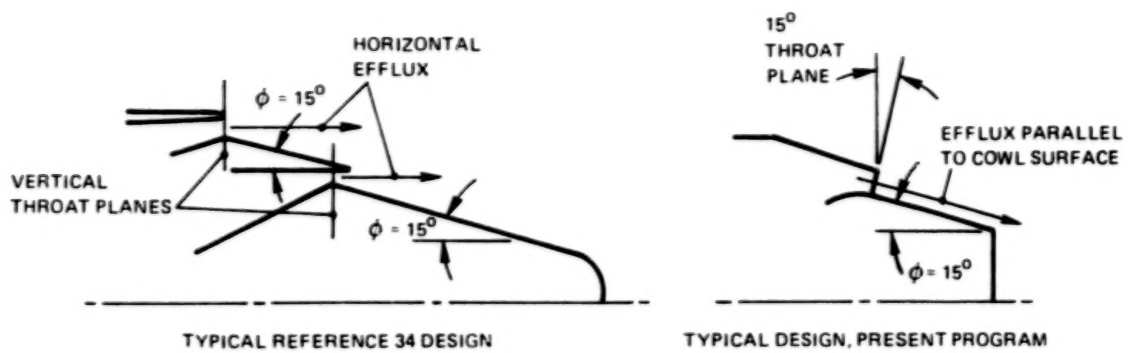


Figure 6.5-6 Nozzle Geometry Differences Between the Reference 34 and Test Configurations

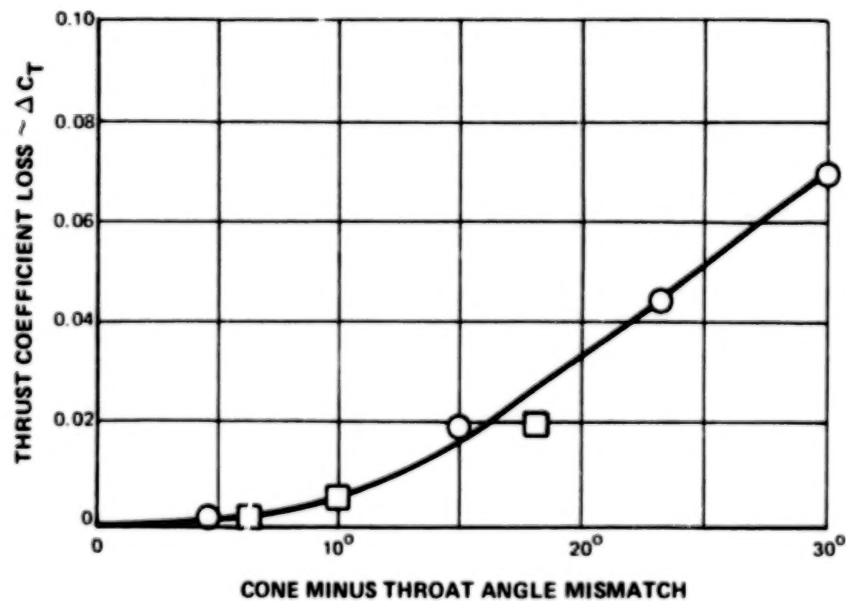


Figure 6.5-7 Effect of Throat Angle Relative to Cone Angle on Plug Nozzle Performance (Reference 35)

SECTION 7.0

SUMMARY OF RESULTS AND CONCLUSIONS

Static acoustic and aerodynamic performance characteristics were determined for five coannular nozzle models. Aerodynamic and acoustic test data were obtained at primary nozzle pressure ratios of 1.53 and 2.0 over a range of fan nozzle pressure ratio from 1.3 to 4.1. Acoustic tests were run over a range of fan stream temperatures of 700°K (1260°R) to 1089°K (1960°R) at a primary stream temperature of 811°K (1460°R).

Each of the five test configurations was designed for a total exhaust jet area of .0126 m² (.136 ft²). Fan to primary area ratio was held constant at 1.48. Fan stream radius ratio for the three zero primary radius ratio configurations varied from 0.69 to 0.83. The two plug configurations had fan radius ratios of 0.75 and 0.83 and primary radius ratios of 0.60 and 0.81.

An aero/acoustic design prediction procedure was developed to provide acoustic and performance capability over a range of nozzle geometries and nozzle operating conditions.

A data bank comprising all of the results of this program has been established and documented in the Comprehensive Data Report (Reference 19).

7.1 ACOUSTIC RESULTS AND CONCLUSIONS

7.1.1 Acoustic Prediction Procedure

An empirical acoustic design procedure for inverted velocity profile coannular nozzles was developed, capable of predicting jet noise sound pressure level spectra as a function of nozzle geometry, operating condition, and flight velocity.

1. Acoustic spectra were decomposed into:
 - a high frequency mixing noise component
 - a low frequency mixing noise component
 - a fan stream shock noise component
 - a primary stream shock noise component
2. The total noise for a full scale engine is obtained by prediction of each of the four noise components at a given angle and summing them logarithmically.
3. Data correlations developed for each noise component collapsed the peak SPL of each noise component with standard deviations varying from ±0.8 dB to ±2.7 dB.

4. The acoustic prediction procedure accuracy is currently limited by the parameter extremes of the existing data base. Consideration should be given to the further extension of the data base parameters to improve applicability of the procedure. In particular, it is recommended that acoustic data be obtained for fan stream temperatures more typical of duct burning propulsion systems (1811°K (3260°R)).

7.1.2 Acoustic Test Results

1. The acoustic characteristics of coannular nozzles were found to be a function of fan and primary stream radius ratios. For a fan stream velocity of 610 m/sec (2000 ft/sec) and a primary stream of 778 m/sec (1400 ft/sec):
 - Increasing fan radius ratio from 0.69 to 0.83 reduced peak PNL 3 dB.
 - Increasing primary radius from 0 to 0.81, at constant fan radius ratio, reduced peak PNL an additional 1 dB.
 - The ratio of passage height to cowl extension (H/L) was not a good noise correlation parameter.
2. The effects of fan and primary radius ratios were also a function of operating condition. As fan stream velocity was increased, the noise reductions with increasing fan and primary stream radius ratio decreased. At a fan stream velocity of 853 m/sec (2800 ft/sec), no additional noise reduction was obtained with increasing fan stream or primary stream radius ratios.

7.2 AERODYNAMIC PERFORMANCE RESULTS AND CONCLUSIONS

7.2.1 Static Aerodynamic Performance Prediction Procedure

A static performance prediction procedure was developed capable of predicting nozzle performance over the range of nozzle geometries and operating conditions tested.

1. The procedure developed makes use of analytical predicted viscous losses (internal duct loss and external scrubbing loss) and empirically derived off-design shock loss to obtain the predicted nozzle thrust coefficient.
2. The procedure collapsed the zero primary radius ratio model thrust coefficient data to within ± 0.0015 at a FNPR of 2.0 and a PNPR of 2.0. It predicted a plug nozzle thrust coefficient to within 0.003 of the test data at a FNPR of 4.1 and a PNPR of 2.0. Application of the prediction procedure to the coannular nozzles of Reference 34 gave inconsistent results with differences between measured and predicted C_T varying from zero to 0.025. The disparity is attributed to the nozzle throat design of the referenced configurations.

7.2.2 Aerodynamic Performance Test Results

1. Nozzle thrust coefficient was found to be adversely effected by increasing fan radius ratio. Increasing fan radius ratio from 0.69 to 0.83 at zero primary radius ratio, reduced thrust coefficient from 1 percent at a fan nozzle pressure ratio of 2.0 to 2 percent at a fan nozzle pressure ratio of 4.1.
2. Nozzle thrust coefficient was not significantly affected by primary radius ratio because the primary stream thrust contribution to total thrust is relatively small for the tested configurations and operating conditions.
 - Increasing primary radius ratio from zero to 0.80 at a constant 0.83 fan radius ratio had a relatively small effect on thrust coefficient over the tested range of FNPR.
3. Fan discharge coefficient CD_f increased slightly with fan radius ratio
 - When fan radius ratio was increased from 0.69 to 0.83 at zero primary radius ratio, CD_f increased 1.5 percent at the higher FNPR.
4. Fan discharge coefficient CD_f was not significantly affected by primary stream radius ratio.
 - Changing primary radius from 0 to 0.81 at a 0.83 fan radius ratio did not change CD_f at a FNPR greater than 2.5.
 - Changing primary radius ratio from 0 to 0.6 at a 0.75 fan radius ratio increased CD_f 0.7 percent above a FNPR of 2.5.
5. The effects of fan and primary stream radius ratio on primary discharge coefficient were masked by flow restriction of the primary stream by the fan stream.
 - The zero primary radius ratio configurations showed significantly greater primary flow restriction than did the plug models.
 - The primary flow restriction for all configurations was substantially reduced at increased primary nozzle pressure ratio.
 - Improvement in primary discharge coefficient for these models could be made by:
 - a) Use of convergent-divergent primary nozzle.
 - b) Use of an isentropic splitter contour to reduce fan to primary stream impingement angle.
 - c) Reduction in fan cowl angle to reduce fan to primary impingement angle.
 - d) Use of a primary plug.

7.3 PREDICTION SYSTEM ACCURACY

Definition of the accuracy of the aero/acoustic prediction procedure was limited to nozzles whose geometries and design concepts are within the prediction procedure data base. Application of the acoustic prediction procedure has been limited to examples which fall within the acoustic data base. Under these conditions, prediction accuracy has been good. The accuracy of the prediction procedure for configurations outside the parameter extremes of the data base cannot be assessed. Application of the aerodynamic performance prediction system to configurations outside of the parameter extremes of the performance data base indicated that the performance prediction procedure should be restricted to configurations similar to those tested in the present program.

Application of the aero/acoustic procedure could be extended to include other types of nozzles by further extension of the data base and by including experimental and/or analytical corrections to account for different types of designs.

APPENDIX A

**Acoustic Power and Perceived Noise
Level Directivity Data
Scaled 12 x to 1.52 M (5 ft.) Equivalent
Diameter Size
Representative of Full-Scale AST Powerplant
and
Overall Sound Pressure Level Directivity Data
Scaled 12 x to 1.52 M (5 Ft.) Equivalent
Diameter Size
Representation of Full-Scale AST Powerplant**

TABLE A-1
ACOUSTIC TEST MATRIX

Point No.	FAN				PRIMARY				Run Numbers				
	T ₁ °K	T ₁ °R	Pressure Ratio	Velocity m/sec (ft/sec)	T ₁ °K	T ₁ °R	Pressure Ratio	Velocity m/sec (ft/sec)	A	B	C	D	E
1	700	(1260)	1.3	314 (1030)	811	(1460)	1.53	427 (1400)	8301	8201	8401	8501	8601
2	700	(1260)	1.8	457 (1500)	811	(1460)	1.53	427 (1400)	8302	8202	8402	8502	8602
3	700	(1260)	2.5	564 (1850)	811	(1460)	1.53	427 (1400)	8303	8203	8403	8503	8603
4	700	(1260)	3.2	625 (2050)	811	(1460)	1.53	427 (1400)	8304	8204	8404	8504	8604
5	1089	(1960)	1.8	573 (1880)	811	(1460)	1.53	427 (1400)	8305	8205	8405	8505	8605
6	1089	(1960)	2.5	707 (2320)	811	(1460)	1.53	427 (1400)	8306	8206	8406	8506	8606
7	1089	(1960)	4.1	853 (2800)	811	(1460)	1.53	427 (1400)	8307	8207	8407	8507	8607
8	700	(1260)	1.3	314 (1030)	811	(1460)	2.0	540 (1770)	8308	8208	8408	8508	8608
9	700	(1260)	1.8	457 (1500)	811	(1460)	2.0	540 (1770)	8309	8209	8409	8509	8609
10	700	(1260)	2.5	564 (1850)	811	(1460)	2.0	540 (1770)	8310	8210	8410	8510	8610
11	700	(1260)	3.2	625 (2050)	811	(1460)	2.0	540 (1770)	8311	8211	8411	8511	8611
12	1089	(1960)	1.8	573 (1880)	811	(1460)	2.0	540 (1770)	8312	8212	8412	8512	8612
13	1089	(1960)	2.5	707 (2320)	811	(1460)	2.0	540 (1770)	8313	8213	8413	8513	8613
14	1089	(1960)	4.1	853 (2800)	811	(1460)	2.0	540 (1770)	8314	8214	8414	8514	8614
15 ^{1,2}	No Fan Flow				700	(1260)	1.3	314 (1030)					8215
16	No Fan Flow				700	(1260)	1.8	457 (1500)					8216
17	No Fan Flow				700	(1260)	2.5	564 (1850)					8217
18	No Fan Flow				700	(1260)	3.2	625 (2050)					8218
19	700	(1260)	1.3	314 (1030)	No Primary Flow				8219				8519
20	700	(1260)	1.8	457 (1500)	No Primary Flow				8220				8520
21	700	(1260)	2.5	564 (1850)	No Primary Flow				8221				8521
22	700	(1260)	3.2	625 (2050)	No Primary Flow				8222				8522
23	1089	(1960)	1.8	573 (1880)	No Primary Flow				8223				8523
24	1089	(1960)	2.5	707 (2320)	No Primary Flow				8224				8524
25	1089	(1960)	4.1	853 (2800)	No Primary Flow				8225				8525
26	Fan				700	(1260)	1.3	314 (1030)					8626
27	Fan				700	(1260)	1.8	457 (1500)					8627
28	Fan				700	(1260)	2.5	564 (1850)					8628
29	Fan				700	(1260)	3.2	625 (2050)					8629
30	Fan				1089	(1960)	1.8	573 (1880)					8630
31	Fan				1089	(1960)	2.5	707 (2320)					8631
32	Fan				1089	(1960)	4.1	853 (2800)					8632

1 Convergent nozzle reference points

2 The fan cowl was removed when testing with primary flow alone

CONFIGURATION A
ACOUSTIC DATA

PNL @ 648.6 M (2128 FT) SIDELINE
T_a = 298°K (537°R), Rei. Hum. = 70%

Run No.	OAPWL	60°	70°	80°	90°	100°	110°	120°	130°	140°	150°	160°
8301	158.0	78.9	81.2	83.2	85.4	86.7	88.0	89.5	89.5	89.5	87.5	80.7
8302	163.2	86.6	88.3	90.6	92.9	94.4	96.2	97.1	97.1	95.7	94.0	89.0
8303	169.3	96.6	97.3	98.9	100.4	101.0	102.6	103.1	103.7	104.1	103.1	97.3
8304	173.1	103.0	103.9	105.1	106.1	106.0	106.8	107.2	108.1	108.7	106.4	99.2
8305	166.2	89.9	92.6	95.1	97.6	99.2	100.8	100.5	100.1	100.3	99.6	93.1
8306	172.5	95.9	98.2	101.0	103.1	104.9	106.6	107.7	108.1	108.6	105.8	97.9
8307	178.8	105.0	106.6	108.5	110.4	111.0	112.2	114.7	115.3	114.3	109.8	100.8
8308	166.0	84.9	87.2	89.1	91.6	95.0	94.9	96.7	98.3	100.4	97.5	89.6
8309	168.6	89.0	91.2	93.4	95.8	97.2	98.9	100.4	101.3	102.8	100.9	93.3
8310	172.6	93.6	95.7	98.0	100.5	101.4	103.2	105.0	106.0	108.1	106.5	98.1
8311	175.4	98.9	101.1	103.7	105.3	105.8	106.7	108.3	109.8	111.6	108.7	100.2
8312	170.0	91.8	94.0	96.2	98.6	100.1	101.6	102.6	103.7	105.1	103.3	94.7
8313	174.6	96.9	99.1	101.6	104.3	105.5	107.4	108.5	109.7	111.1	107.1	97.8
8314	179.2	103.3	105.4	107.9	110.1	111.0	112.6	114.6	115.6	115.2	109.7	100.3

CONFIGURATION B
ACOUSTIC DATA
PNL @ 648.6 M (2128 FT) SIDELINE
T_a = 298°K (537°R), Rel. Hum. = 70%

Run No.	OAPWL	60°	70°	80°	90°	100°	110°	120°	130°	140°	150°	160°
8201	158.2	78.4	80.5	82.5	84.4	86.0	87.8	89.4	90.6	89.8	87.3	80.7
8202	162.8	85.6	87.7	90.0	92.1	93.8	95.5	96.6	96.7	95.0	93.6	88.8
8203	169.0	94.1	95.8	97.0	98.1	99.6	101.3	102.8	102.9	103.5	103.0	97.6
8204	173.3	101.4	103.3	103.9	104.3	104.5	105.3	106.2	107.3	108.9	107.4	100.1
8205	165.1	88.4	91.0	93.1	95.2	97.1	99.2	100.1	99.6	98.3	97.2	92.2
8206	171.7	92.5	96.0	98.0	100.1	102.3	104.8	106.5	107.1	107.7	104.9	93.7
8207	178.2	103.1	105.1	107.0	108.7	109.4	110.2	112.5	115.0	114.8	108.7	99.9
8208	166.1	84.4	86.6	88.8	90.8	92.4	94.7	97.0	98.8	100.5	97.1	81.3
8209	168.3	88.0	90.0	92.5	94.5	95.8	97.9	99.6	101.0	102.3	100.1	93.8
8210	172.2	93.4	95.3	97.6	99.1	100.3	102.3	104.1	104.8	107.2	106.4	98.9
8211	174.4	97.3	99.5	101.7	102.7	103.3	105.1	106.6	107.5	110.5	108.4	99.9
8212	170.0	90.1	92.0	94.6	97.2	99.1	100.8	102.2	103.1	105.3	103.1	95.1
8213	171.4	94.2	96.8	98.9	101.0	103.3	105.6	107.2	110.6	110.5	107.1	100.0
8214	178.8	102.6	104.7	106.7	108.4	109.3	110.5	112.9	115.8	115.6	109.1	99.9
8219	145.7	70.9	73.1	75.4	76.8	77.6	78.8	79.4	78.6	76.0	71.2	63.5
8220	161.3	83.6	85.8	88.1	89.8	91.1	93.2	94.5	94.8	94.0	92.5	87.9
8221	170.4	95.1	96.2	97.8	98.8	99.3	101.0	102.7	103.7	105.6	104.4	97.4
8222	175.0	102.3	104.3	106.0	106.6	106.3	106.7	107.3	108.6	111.7	107.9	99.8
8223	167.2	88.0	90.4	92.8	94.8	96.4	98.4	100.2	100.9	101.8	99.8	93.6
8224	173.8	93.5	95.9	98.5	100.6	102.3	104.7	107.2	110.1	111.2	105.3	96.8
8225	179.2	101.7	104.2	106.7	108.0	108.7	110.6	113.2	117.6	114.6	107.9	98.7

CONFIGURATION C
ACOUSTIC DATA
PNL @ 648.6 M (2128 FT) SIDELINE
T_a = 298° K (537° R), Rel. Hum. = 70%

Run No.	OAPWL	60°	70°	80°	90°	100°	110°	120°	130°	140°	150°	160°
8401	157.5	77.2	79.5	81.4	83.5	85.2	86.5	87.8	88.9	88.7	87.0	80.2
8402	162.4	84.4	86.8	88.9	91.0	92.7	94.4	95.5	95.3	94.4	93.3	87.9
8403	168.6	93.5	95.1	96.3	98.1	99.3	100.9	102.1	102.3	102.4	102.3	96.8
8404	173.5	101.7	103.4	104.2	104.7	104.9	105.3	106.2	107.2	108.5	107.6	100.5
8405	164.7	87.6	90.3	92.7	94.6	96.6	98.7	99.6	98.9	97.7	96.6	91.7
8406	171.9	94.0	96.4	98.7	100.7	102.6	104.6	106.8	107.4	107.7	105.5	98.8
8407	178.7	102.5	105.3	107.5	108.8	109.9	110.7	113.1	114.7	115.3	110.7	101.4
8408	164.9	83.5	85.7	87.7	89.8	91.6	93.3	95.3	96.9	98.6	96.4	88.3
8409	167.6	87.3	89.4	91.4	93.7	95.4	97.0	98.3	99.8	100.8	99.5	92.5
8410	172.1	93.9	95.5	97.2	99.0	100.4	102.1	103.7	104.5	106.1	106.4	99.1
8411	175.2	98.6	100.7	102.2	103.6	104.3	105.6	107.0	108.1	110.7	109.7	101.1
8412	169.5	90.0	92.3	94.6	96.7	98.5	100.1	101.6	101.9	103.3	102.9	95.8
8413	174.1	94.8	97.4	99.6	101.6	103.6	105.5	107.4	108.5	110.3	108.0	99.1
8414	179.2	102.9	105.4	107.8	109.0	110.1	111.1	113.1	114.9	115.9	110.9	101.6

CONFIGURATION D
ACOUSTIC DATA

PNL @ 648.6 M (2128 FT) SIDELINE

T_a = 298°K (537°R), Rel. Hum. = 70%

Run No.	OAPWL	60°	70°	80°	90°	100°	110°	120°	130°	140°	150°	160°
8501	156.8	77.6	79.7	82.1	83.7	85.3	86.5	87.8	88.5	88.0	85.3	78.6
8502	162.4	85.3	87.6	89.9	91.7	93.6	95.2	96.4	96.4	94.1	92.8	87.8
8503	168.8	96.3	97.5	99.1	99.4	100.6	101.8	103.0	103.0	103.4	103.2	97.4
8504	173.7	102.5	103.6	105.3	105.8	105.7	106.3	107.3	107.7	109.8	107.9	100.1
8505	164.9	88.7	91.0	93.2	95.5	97.1	99.2	100.2	99.6	98.3	97.4	91.4
8506	172.1	94.5	97.0	98.8	101.2	103.0	105.6	107.4	108.3	108.6	105.6	97.9
8507	179.0	104.0	106.8	108.1	109.5	110.2	111.7	114.5	116.3	114.8	110.2	100.6
8508	164.7	84.0	86.1	88.3	89.9	91.6	93.4	95.1	96.7	97.9	95.8	88.7
8509	167.3	87.5	89.7	91.9	93.7	95.5	97.1	98.5	99.5	100.5	98.8	92.0
8510	176.1	93.6	95.4	97.6	99.2	100.8	102.5	104.0	104.6	106.5	106.6	99.2
8511	175.3	98.6	100.3	102.4	103.7	104.8	106.0	107.6	108.4	111.4	109.7	101.2
8512	169.5	90.5	93.0	94.8	97.1	98.7	100.8	101.9	102.4	103.6	103.1	95.1
8513	174.3	95.0	97.7	99.7	102.0	103.9	106.2	108.0	109.6	111.0	107.7	98.4
8514	179.5	101.9	104.5	106.6	108.6	109.9	112.0	114.4	116.6	116.0	110.7	101.8
8519	147.5	72.4	74.5	76.7	78.1	79.4	80.1	80.6	80.0	77.6	72.7	63.7
8520	162.3	84.9	87.0	89.3	90.9	92.6	94.2	95.5	95.9	95.1	92.9	86.6
8521	171.3	95.5	96.4	97.7	98.9	100.0	101.5	102.9	104.5	105.6	105.0	97.8
8522	175.8	101.4	102.7	103.8	104.6	104.9	105.9	107.2	109.5	111.9	109.2	100.7
8523	167.9	89.2	92.2	93.5	95.8	97.4	99.2	100.9	101.8	101.7	100.1	92.9
8524	175.7	96.0	97.6	99.8	102.1	103.9	106.1	108.4	111.7	112.3	107.5	98.4
8525	182.0	105.5	107.1	109.3	110.5	111.6	113.0	115.6	119.9	118.3	111.7	100.8

CONFIGURATION E
ACOUSTIC DATA
PNL @ 648.6 M (2128 FT) SIDELINE
T_a = 298°K (537°R), Rel. Hum. = 70%

Run No.	OAPWL	60°	70°	80°	90°	100°	110°	120°	130°	140°	150°	160°
8601	155.8	76.5	79.2	81.0	82.6	85.2	85.7	87.3	87.7	87.4	83.9	77.3
8602	161.6	84.3	87.0	88.9	90.5	93.2	94.0	95.7	95.3	94.3	91.2	86.4
8603	167.8	95.8	97.7	98.3	99.0	100.8	100.6	102.4	101.8	101.9	100.9	96.8
8604	173.1	103.1	104.4	105.3	105.3	106.1	105.6	106.6	106.6	108.4	106.9	100.7
8605	163.8	87.3	90.0	92.0	93.8	96.9	97.7	99.3	98.2	97.2	95.3	90.2
8606	170.8	93.5	96.0	98.0	99.9	102.7	103.8	106.0	106.1	107.3	104.2	97.8
8607	178.2	103.4	105.6	107.7	108.2	108.7	110.1	112.6	114.0	114.6	110.3	101.2
8608	163.8	83.2	85.8	87.3	88.9	91.5	92.4	94.6	95.6	96.8	94.7	88.7
8609	166.9	87.2	89.6	91.3	93.1	95.6	96.4	98.1	98.9	99.9	98.5	92.6
8610	171.2	92.9	95.0	96.6	98.3	100.5	101.2	103.3	103.6	105.2	105.5	99.8
8611	174.6	97.8	100.0	101.5	102.5	104.3	104.7	106.9	107.4	110.4	109.1	101.4
8612	168.4	89.2	91.5	93.9	95.6	96.9	98.9	100.2	100.7	101.5	101.6	95.1
8613	173.2	93.8	96.2	98.7	100.5	102.1	104.3	106.3	107.1	109.3	107.4	99.9
8614	178.6	100.3	102.8	105.5	106.9	108.0	110.0	112.5	114.6	115.2	110.6	101.2
8626	143.9	68.8	70.9	73.4	74.8	75.6	76.9	77.6	77.0	75.4	70.8	63.3
8627	158.4	80.7	82.8	85.2	86.7	88.0	89.7	91.6	92.4	92.0	90.2	85.2
8628	167.5	91.8	92.9	94.5	95.7	96.0	97.7	99.8	101.0	102.7	102.3	95.7
8629	172.3	98.5	99.9	101.4	101.7	101.6	102.5	104.5	105.9	109.7	106.1	97.5
8630	164.7	85.5	87.6	90.0	91.8	93.3	95.5	97.8	98.8	99.9	98.4	91.6
8631	171.9	91.7	93.8	96.4	98.2	99.9	102.5	105.3	108.4	109.8	103.9	94.8
8632	178.1	101.2	103.3	106.0	107.1	108.2	109.9	112.7	117.1	114.1	107.4	97.9

198

REFERENCE CONVERGENT NOZZLE
ACOUSTIC DATA
PNL @ 648.6 M (2128 FT) SIDELINE
 $T_a = 298^\circ\text{K}$ (537°R), Rel. Hum. = 70%

Run No.	OAPWL	60°	70°	80°	90°	100°	110°	120°	130°	140°	150°	160°
8215	146.1	71.8	73.8	75.6	77.3	79.1	79.6	80.3	79.5	77.1	72.7	65.6
8216	161.1	84.0	86.0	87.6	89.5	91.8	92.7	94.6	94.9	94.5	93.9	89.2
8217	170.1	98.9	100.2	100.6	101.1	101.5	101.5	102.8	103.8	107.0	104.4	96.1
8218	174.6	104.7	106.6	107.6	108.0	108.1	107.3	107.7	108.7	111.7	106.5	98.3

CONFIGURATION A
ACOUSTIC DATA
OASPL @ 45.7 M (150 FT) RADIUS
T_a = 298°K (537°R), Rel. Hum. = 70%

Run	60°	70°	80°	90°	100°	110°	120°	130°	140°	150°	160°
8301	102.7	103.7	104.6	106.4	107.7	109.6	112.2	114.3	118.9	121.4	120.0
8302	108.8	109.2	110.7	112.6	114.1	116.4	118.5	121.1	123.5	125.7	125.2
8303	117.2	116.8	118.0	119.0	119.9	122.2	124.0	126.7	129.4	132.2	131.4
8304	122.9	123.1	123.8	124.6	124.8	126.2	128.0	130.7	133.5	135.2	133.9
8305	111.7	113.0	114.7	116.7	118.4	120.6	122.5	123.0	126.0	128.8	127.6
8306	117.2	118.3	120.0	121.8	123.7	126.1	128.4	130.3	133.3	134.9	132.7
8307	125.7	126.2	127.3	128.9	129.9	131.9	135.3	137.3	140.0	140.6	136.3
8308	108.3	109.2	110.0	112.0	113.3	115.6	118.7	122.4	128.3	129.6	126.8
8309	111.6	112.4	113.5	115.6	117.0	119.2	121.9	125.0	130.6	132.2	129.4
8310	115.6	116.3	117.6	119.6	120.8	123.2	125.9	129.4	134.3	136.1	133.4
8311	120.0	120.9	122.5	123.7	124.6	126.4	129.1	132.5	137.1	138.5	135.5
8312	114.0	114.7	115.9	117.9	119.4	121.6	123.8	126.0	131.9	133.5	130.1
8313	118.2	119.2	120.6	122.9	124.4	127.0	129.3	132.0	136.6	137.2	133.4
8314	124.1	124.9	126.6	128.5	129.8	132.2	135.2	137.7	141.0	140.5	136.7

CONFIGURATION B
ACOUSTIC DATA
OASPL @ 45.7 M (150 FT) RADIUS
T_a = 298°K (537°R), Rel. Hum. = 70%

Run	60°	70°	80°	90°	100°	110°	120°	130°	140°	150°	160°
8201	102.7	103.5	104.4	105.7	107.4	109.6	112.3	116.0	119.2	121.2	120.1
8202	108.2	109.1	110.4	112.0	113.7	116.0	118.2	120.9	123.0	125.3	125.0
8203	115.5	116.1	116.7	117.7	119.0	121.2	123.8	126.1	129.0	132.2	131.8
8204	121.7	122.3	122.7	122.9	123.4	125.0	127.0	130.0	133.8	136.5	135.0
8205	110.4	111.8	113.1	114.8	116.7	119.2	121.3	123.1	124.7	127.2	126.8
8206	115.1	116.5	117.6	119.3	121.6	124.5	127.3	129.9	132.5	134.3	132.5
8207	124.0	124.7	125.7	127.1	128.1	129.9	133.2	137.4	140.4	139.3	135.7
8208	108.2	109.0	110.0	111.5	113.0	115.7	119.0	123.4	128.4	129.2	126.8
8209	111.1	111.8	113.3	114.7	116.1	118.5	121.4	125.5	130.3	131.6	129.2
8210	115.5	116.2	117.6	118.7	119.9	122.4	125.2	128.4	133.7	136.0	133.6
8211	118.6	119.6	121.0	121.6	122.6	124.9	127.5	130.5	136.1	138.1	135.3
8212	112.5	113.2	114.7	116.8	118.7	120.8	123.4	126.9	132.0	133.2	130.2
8213	115.9	117.3	118.5	120.2	122.6	125.4	128.0	133.4	136.0	136.9	135.7
8214	123.5	124.3	125.5	126.8	128.2	130.2	133.5	138.1	141.3	140.0	136.3
8219	93.8	94.9	96.6	97.8	98.7	100.6	102.4	104.0	105.4	106.4	105.4
8220	106.1	107.2	108.6	109.9	111.2	113.6	116.1	118.8	121.8	124.2	124.1
8221	115.7	116.0	117.1	117.9	118.8	120.9	123.7	127.0	131.9	134.0	132.1
8222	123.0	123.7	124.8	124.9	124.9	126.3	128.2	131.5	137.3	137.4	134.4
8223	110.3	111.5	113.0	114.5	116.1	118.6	121.6	125.1	128.8	130.0	127.9
8224	114.9	116.2	118.1	119.8	121.6	124.4	128.1	133.2	136.7	135.0	131.4
8225	122.3	123.8	125.7	126.6	127.7	130.2	134.0	140.5	141.1	138.8	134.9

CONFIGURATION C
ACOUSTIC DATA

OASPL @ 45.7 M (150 FT) RADIUS

T_a = 298°K (537°R), Rel. Hum. = 70%

Run	60°	70°	80°	90°	100°	110°	120°	130°	140°	150°	160°
8401	101.5	102.5	103.4	105.1	106.8	108.6	110.8	114.4	118.2	121.2	119.9
8402	107.1	108.3	109.4	111.2	112.9	115.1	117.3	119.6	122.6	125.5	124.7
8403	114.8	115.4	116.2	117.6	118.9	120.9	123.1	125.4	128.5	131.9	131.3
8404	121.9	122.4	122.9	123.4	124.0	125.2	127.1	129.8	133.7	136.9	135.4
8405	109.7	111.1	112.6	114.1	116.1	118.2	120.8	122.4	124.4	127.0	127.0
8406	115.6	116.8	118.3	120.0	121.9	124.4	127.6	129.9	132.5	134.6	133.2
8407	123.6	125.0	126.4	127.4	128.8	130.4	133.9	137.1	140.6	140.9	137.4
8408	107.2	107.9	108.9	110.5	112.4	114.4	117.4	121.4	126.8	128.8	126.3
8409	110.4	111.2	112.2	114.1	115.8	117.8	120.2	124.2	129.1	131.5	129.2
8410	115.6	116.3	117.1	118.7	120.1	122.3	124.9	128.0	132.9	136.3	134.0
8411	119.7	120.6	121.5	122.6	123.7	125.6	128.0	131.1	136.4	139.3	136.4
8412	111.2	113.3	114.8	116.4	118.2	120.3	123.0	125.8	130.6	133.4	131.2
8413	116.5	117.8	119.3	120.9	122.9	125.3	128.3	131.1	135.8	137.6	134.7
8414	123.9	125.3	126.7	127.7	129.1	130.9	133.9	137.2	141.3	141.3	137.8

CONFIGURATION D
ACOUSTIC DATA
OASPL @ 45.7 M (150 FT) RADIUS
T_a = 298°K (537°R), Rel. Hum. = 70%

Run	60°	70°	80°	90°	100°	110°	120°	130°	140°	150°	160°
8501	101.6	102.6	103.9	105.2	106.8	108.6	111.0	114.1	117.7	119.9	118.9
8502	107.6	108.6	110.1	111.6	113.6	115.7	118.0	120.1	122.6	124.8	124.5
8503	116.7	117.0	118.0	118.6	119.8	121.6	123.8	125.8	128.7	131.8	131.4
8504	122.3	122.7	123.7	124.3	124.8	126.1	128.2	130.3	134.3	136.5	135.2
8505	110.5	111.6	113.0	114.9	116.5	119.1	121.2	123.0	124.6	127.1	126.3
8506	115.9	117.2	118.3	120.3	122.2	125.3	128.1	130.8	133.1	134.3	132.3
8507	124.7	126.3	127.0	128.3	129.3	131.5	135.2	138.4	140.2	140.5	136.6
8508	107.8	108.5	109.6	110.8	112.6	114.7	117.4	121.5	126.4	128.4	126.4
8509	110.5	111.4	112.7	114.1	115.9	117.9	120.5	124.1	120.8	130.9	128.8
8510	115.4	116.1	117.5	118.8	120.5	122.6	125.1	128.1	133.0	136.2	134.0
8511	119.7	120.3	121.7	122.6	124.1	126.0	128.5	131.2	136.6	139.2	136.4
8512	112.9	114.1	115.0	116.8	118.4	120.9	123.2	126.3	130.6	133.4	130.5
8513	116.7	118.1	119.3	121.2	123.1	126.0	128.7	132.1	136.1	137.3	133.8
8514	122.9	124.5	125.8	127.4	129.1	131.7	135.1	138.7	141.4	141.2	137.2
8519	95.6	96.7	98.3	99.5	100.9	102.3	104.0	105.8	107.5	108.2	106.2
8520	107.2	108.2	109.7	111.0	112.8	114.9	117.4	120.3	123.2	125.0	123.5
8521	116.5	116.5	117.3	118.5	119.7	121.7	124.2	128.3	132.5	135.1	132.6
8522	122.0	122.1	122.8	123.6	124.4	126.0	128.4	132.8	137.9	139.0	135.8
8523	111.5	112.3	113.8	115.7	117.3	119.6	122.6	126.3	129.2	130.7	128.1
8524	117.5	118.1	119.5	121.4	123.3	126.0	129.5	135.1	138.3	137.5	133.5
8525	126.7	127.0	128.2	129.4	130.5	132.8	136.6	143.0	144.2	141.8	136.7

CONFIGURATION E
ACOUSTIC DATA
OASPL @ 45.7 M (150 FT) RADIUS
T_a = 298°K (537°R), Rel. Hum. = 70%

Run	60°	70°	80°	90°	100°	110°	120°	130°	140°	150°	160°
8601	100.6	102.0	102.9	104.1	106.6	107.6	110.4	113.2	117.0	118.5	117.9
8602	106.8	108.2	109.3	110.7	113.2	114.6	117.5	119.4	122.2	123.6	123.5
8603	116.4	117.0	117.3	117.8	119.7	120.5	123.3	124.9	127.9	130.1	130.4
8604	122.8	123.5	123.9	123.9	125.2	125.3	127.5	129.3	133.4	135.6	135.1
8605	109.3	110.8	111.9	113.4	116.4	117.7	120.5	121.8	123.9	125.3	125.3
8606	115.1	116.4	117.6	119.1	121.9	123.6	126.8	128.7	132.0	132.9	131.9
8607	124.1	125.1	126.7	127.1	128.0	130.1	133.3	136.4	139.8	140.5	137.3
8608	107.3	108.3	108.9	110.0	112.4	113.8	116.9	120.3	125.3	127.3	126.2
8609	110.5	111.5	112.3	113.7	116.0	117.3	120.2	123.4	128.2	130.5	129.2
8610	115.1	116.0	116.8	118.1	120.3	121.4	124.5	127.2	131.9	139.3	134.1
8611	119.1	120.1	120.8	121.6	123.8	124.4	127.8	130.4	135.8	138.5	136.6
8612	111.8	112.8	114.4	115.6	116.9	119.3	121.7	124.8	129.1	132.4	130.7
8613	115.8	116.9	118.6	119.9	121.6	124.2	127.2	130.0	134.6	136.8	134.3
8614	121.6	122.9	124.8	125.9	127.4	129.9	133.3	136.9	140.6	141.1	137.5
8626	91.4	92.6	94.3	95.3	96.4	98.2	100.0	101.9	103.9	105.1	104.5
8627	103.1	104.0	105.5	106.6	107.9	110.1	113.0	115.9	119.1	121.3	121.1
8628	112.6	112.8	113.9	114.7	115.6	117.8	120.6	124.0	128.7	131.3	129.6
8629	118.8	119.2	120.3	120.5	120.8	122.5	125.3	128.7	134.9	135.1	132.1
8630	107.5	108.4	110.1	111.3	112.9	115.5	119.0	122.6	126.4	127.7	125.6
8631	112.9	113.9	115.8	117.4	119.2	122.3	126.1	131.3	134.9	133.0	129.4
8632	121.9	122.9	124.9	125.7	127.2	129.7	133.4	139.6	139.8	137.5	133.6

REFERENCE CONVERGENT NOZZLE
ACOUSTIC DATA

OASPL @ 45.7 M (150 FT) RADIUS

T_a = 298°K (537°R), Rel. Hum. = 70%

Run	60°	70°	80°	90°	100°	110°	120°	130°	140°	150°	160°
8215	94.1	95.3	96.2	97.6	99.4	100.6	102.6	104.3	105.9	107.2	106.6
8216	106.0	106.8	107.6	109.1	111.4	112.9	115.7	118.4	121.5	124.2	123.7
8217	119.1	119.1	119.1	119.5	120.4	121.2	123.7	126.7	132.0	132.8	130.0
8218	125.4	125.9	126.1	126.1	126.6	126.8	128.7	131.5	136.7	135.7	132.8

APPENDIX B

VERIFICATION OF DATA ACQUISITION PROCEDURE

As discussed in Section 4.1.2.1, model data did not have a constant rolloff at high frequencies as predicted by the SAE prediction procedure. This phenomenon appeared most prominent in model data transformed to a theoretical day. In order to preclude the possibility that the measurement system of environmental conditions in the test facility was adversely affecting the measurements, the following tests were conducted.

1. System Electrical Noise

Purpose - To define the system noise floor over the range of recording gain settings and determine the contribution of electrical noise to the measured signal.

Test - Each microphone system was calibrated by applying a B&K pistonphone. This 250 Hz reference sine wave signal was recorded on all data channels at normal gain settings. A record was then made of all data channels at a range of gain settings used during model testing with the microphones capped.

Reduction - Based on the reference sine wave signal, the recorded data were reduced to 1/3 octave band values and plots of each channel output made at all gain settings. Values so obtained were corrected for gain settings and the 1/3 octave band values referenced to the 250 Hz signal value of 124 dB.

Results - Figures B-1 and B-2 show typical plots of recorded acoustic data compared to the system electrical noise spectra, both referred to the same acoustic level. The spectra for data recorded at the 150 degree angle (Figure B-2) show that the noise is 12 dB below the signal level. This indicated that the contribution of the noise to the signal was less than 0.3 dB. The system electrical noise spectra were compared to all data points measured during the test. In those cases where the signal to noise differences were less than 8 dB, correction was made to the measured signal by subtracting the noise level. Of all the measurements taken, approximately 1.0 percent required correction and in no case did the correction exceed 3.0 dB. That is, the measured signal level was never less than 3 dB above the system electrical noise. In no cases were corrections required in other than the last three 1/3 octave bands (50, 63 and 80K Hz).

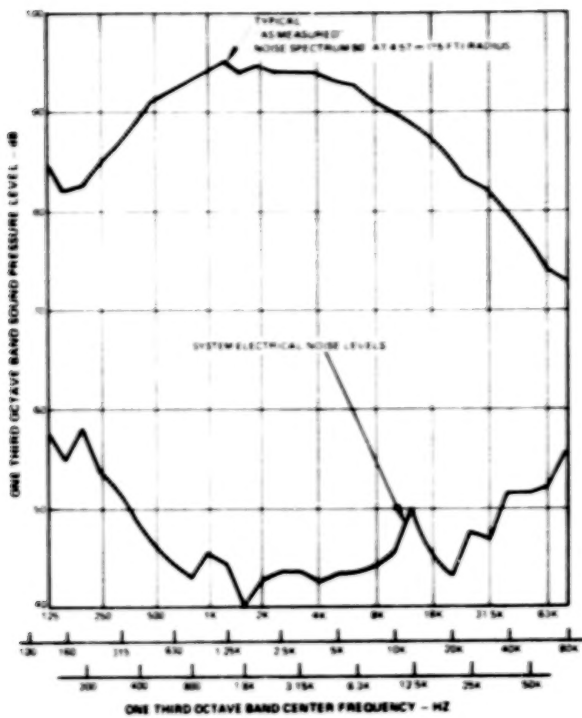


Figure B-1 System Electrical Noise Test, $\theta = 90$ Degrees at 4.57m (15 ft) Radius

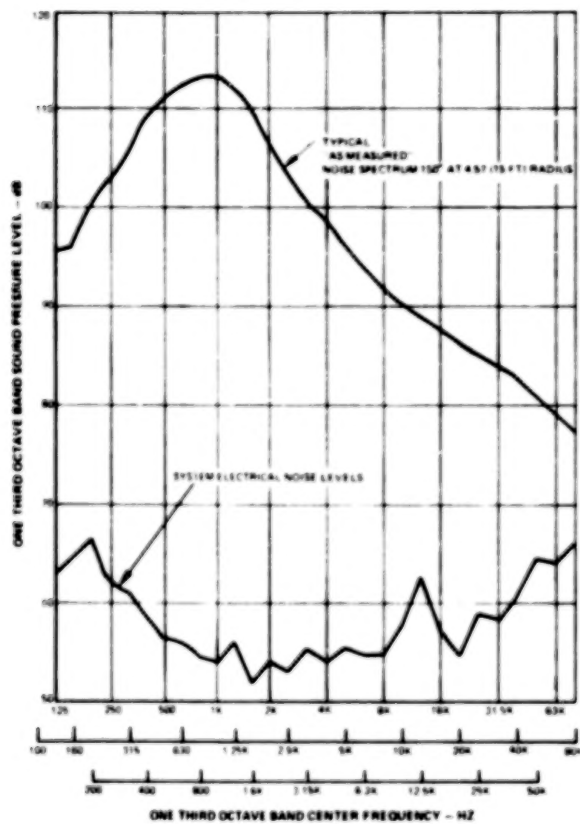


Figure B-2 System Electrical Noise Test, $\theta = 150$ Degrees at 4.57m (15 ft) Radius

2. Microphone Complement Noise

Purpose - To determine the minimum levels of acoustic signals that may be received and conditioned by the microphone complement system without distortion by electrical noise.

Test - Two microphone systems (90 and 150 degrees) were calibrated with a B&K pistonphone and the 250 Hz sine wave signal recorded as an acoustic reference level of 124 dB. The microphones were then removed and a pink noise signal applied. Records of the pink noise output were made at zero gain (cal.) setting and at -10, -20, -30, -40 and -50 dB attenuation steps. For each recording adjustment the signal conditioning amplifiers provided optimum signal level input to the tape recorder.

Reduction - Based on the reference sine wave signal, reduction of the recorded data to 1/3 octave band values was made. Plots of the results for each channel, with all data referred in acoustic level to the reference sine wave signal of 124 dB, were made.

Results - The signal conditioning amplifiers were adjusted to provide optimum signal level to the tape recorder with each reduction of the input. This would result in constant system electrical noise with the exception of the microphone, preamplifier, cable and power supply which made up the microphone complement or front end of the system.

Figure B-3 shows the results of a pink noise signal inserted into the microphone preamplifier. Deviations from the desired 10 dB input interval were within the input noise generation system specifications down to 50 dB, except at low frequencies where line frequency harmonics exist, indicating that there was no system front-end noise affecting SPL measurements down to an equivalent acoustic level of at least 66 dB (within the frequency range of interest). This indicates that the system front-end was capable of delivering noise free signals as low or lower than the recording system can faithfully record.

3. System Dynamic Range

Purpose - To define the system dynamic range at a typical recording gain setting for each 1/3 octave band.

Test - A typical microphone system was calibrated by recording the 250 Hz sine wave signal as an acoustic reference level of 124 dB. Then the microphone was removed and a pink noise signal inserted to the pre-amplifier. Recording of the pink noise output at zero gain (cal.) setting with the signal conditioning system gain adjusted for optimum signal level was made. The input signal was reduced in approximately 5 dB steps (to -45 dB) and recordings made at each level at this same gain setting.

Reduction - One third octave band values were obtained for all records and the resultant spectra plotted.

Results - As shown in Figure B-4 the system dynamic range on a 1/3 octave band basis for a pink noise signal (flat spectrum) was approximately 35 dB.

4. Temperature and Humidity Measurement

Purpose - To determine whether the atmospheric measurements from the temperature and humidity sensor are representative of the acoustic path to assure accurate corrections to the recording data.

Test - Temperature and humidity readings were taken at 11 positions within the sound measurement field between the nozzle and microphones. The measurements were obtained during the various settings of secondary airflow through the chamber walls which were representative of those used during the nozzle model tests.

Reduction - Comparisons were made of the readings taken at 11 measurement positions with the installed monitor system at each secondary airflow configuration. The maximum error attributable to these variances was calculated.

Results - For all airflow configurations tested, the measured relative humidity did not vary greater than $\pm .5\%$ and the measured temperature was within $\pm 1^{\circ}\text{K}$ (2°R) of these parameters measured by the installed monitor system. The results of a typical survey is shown in Figure B-5. The most significant adjustments to the data due to the effects of temperature and relative humidity occurred at the higher frequencies. Adjustments applied to the acoustic data at the 80 KHz one-third octave band center frequency could be in error by $\pm .3$ dB if the extremes of the temperature and humidity variations represent the difference in the conditions of the noise path to that which was measured by the monitor system.

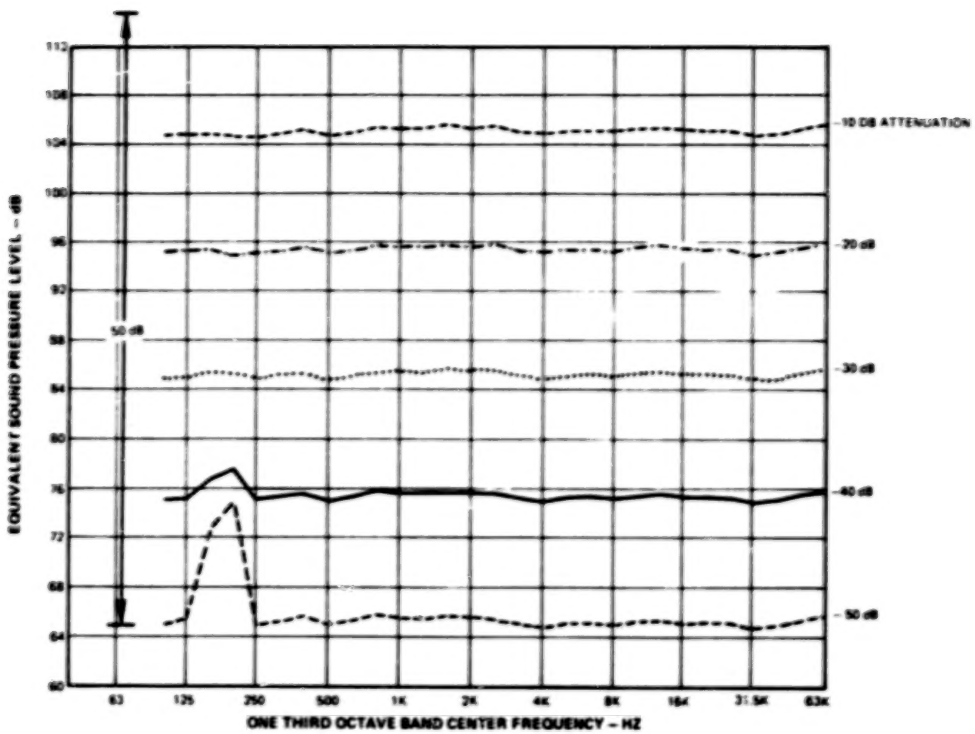


Figure B-3 Microphone Complement Noise Test

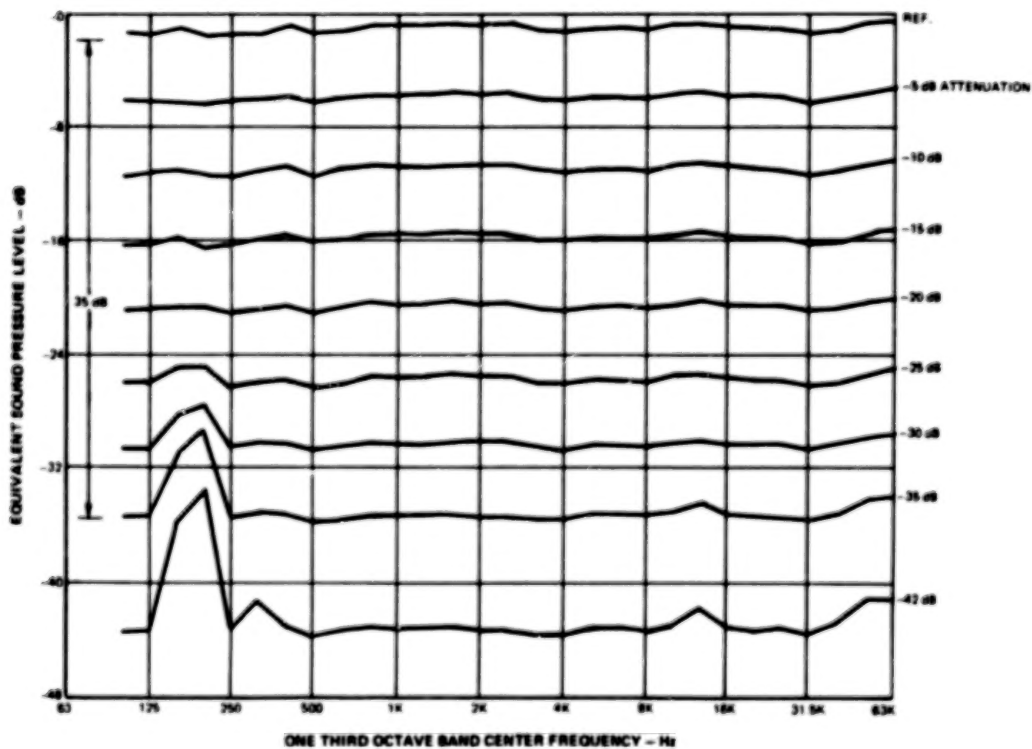


Figure B-4 System Dynamic Range Test

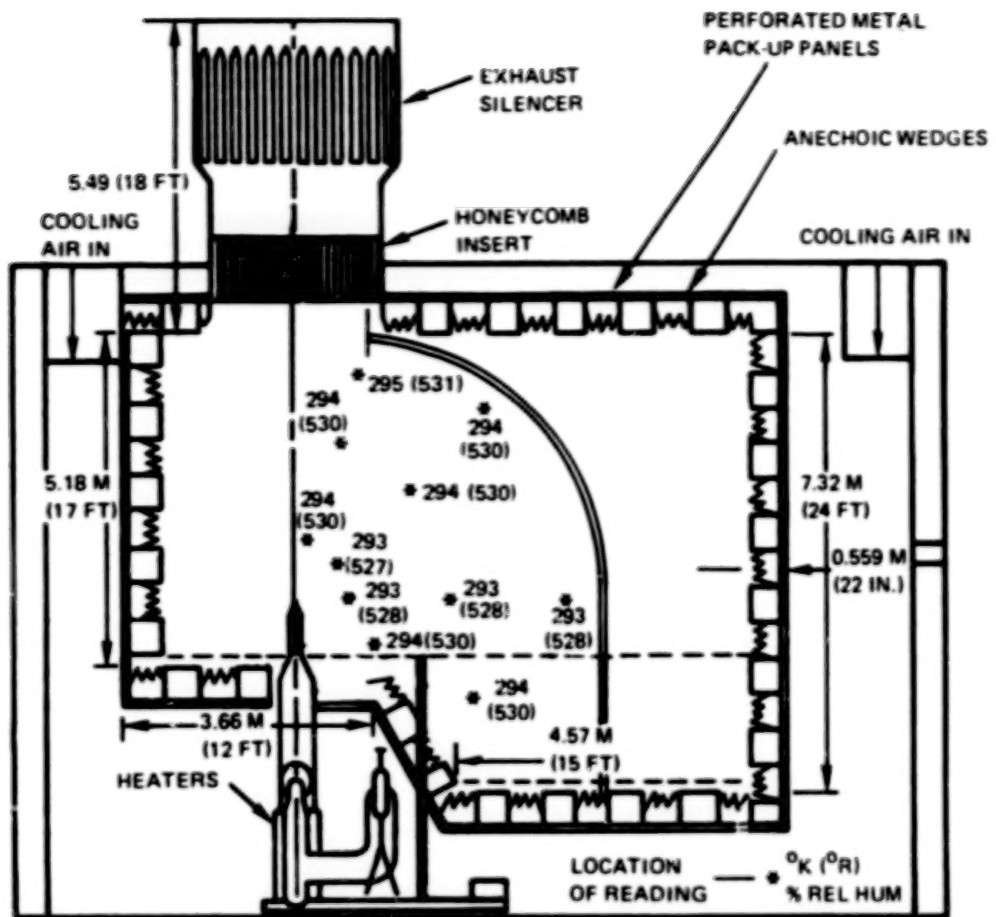


Figure B-5 Results of Temperature and Relative Humidity Survey of the X-206 Stand

LIST OF SYMBOLS

a	Area ratio
A	Area
b	Mixing layer width
c	Acoustic velocity
C_D	Discharge coefficient - actual weight flow/ideal weight flow
C_T	Thrust coefficient - actual thrust/ideal thrust
D	Diameter, Drag
f	Frequency
F	Thrust
$FNPR$	Fan nozzle pressure ratio
$FSNF$	Fan stream shock noise frequency
$FSNSPL$	Fan stream shock noise SPL
g_c	Gravitational constant
H	Annulus height
HF	High frequency generated by initial region
$HFSPL$	High frequency SPL generated by initial region
IVP	Inverted velocity profile
L	Length of cowl extension
L_s	Shock cell spacing
LF	Fan frequency generated by merged region
$LF SPL$	Low frequency SPL generated by merged region
m_i	Ratio external flow velocity to initial region velocity
m_m	Ratio external flow velocity to merged region velocity
M	Mach number
M_c	Convective Mach number of turbulent eddy with respect to the ambient acoustic velocity
M_o	Flight velocity divided by ambient acoustic velocity
n_i	Initial region relative velocity exponent
NPR	Nozzle pressure ratio
n_m	Merged region relative velocity exponent
n_s	Shock noise convective amplification exponent
$OASPL$	Overall Sound Pressure Level (Also OSPL in Section 4.1)
P	Pressure
$PN^{\circ}R$	Primary nozzle pressure ratio
PNL	Perceived noise level
PWL	Power level - dB re 10^{-12} watts
$PSNF$	Primary stream shock noise frequency
$PSNSPL$	Primary stream shock noise SPL
q	Dynamic pressure

LIST OF SYMBOLS (Cont'd.)

r	Radius
R	Radius ratio or
	Universal gas constant
Ref	Reference
S	Strouhal number
SL	Side line
SNF	Shock noise frequency
SNSPL	Shock noise SPL
SPL	Sound pressure level re .0002 degrees/Cm ²
ΔSPL	SPL correction for radius ratio
ΔSPL(PNPR)	Shock noise SPL correction for primary nozzle pressure ratio
ΔSPL(T _{t₁} /T _a)	Shock noise SPL correction for fan nozzle pressure ratio
T	Temperature (Static with no subscript, total with "t" subscript)
T(x)	Peak mean temperature at axial position
V	Velocity
v	Ratio - fan to primary velocity
V(X)	Peak mean velocity at position X
V _e	Eddy convection velocity
V _o	Free jet wind tunnel velocity
W	Weight flow
X _c	Axial distance from nozzle exit plane

Greek Letters

α	Empirical parameter used in definition of V _m
θ	Angle measured from upstream jet axis
ϕ	Cowl angle
ω	SAE density exponent
γ	Ratio of specific heats
ρ	Mass density
Δ	Difference in noise or aerodynamic performance levels

LIST OF SYMBOLS (Cont'd.)

Subscripts

a	ambient
ex	exit
f	fan
i	initial region
ID	Inner Diameter
OD	Outer Diameter
id	ideal
j	jet
m	merged
o	initial conditions
p	primary
s	static
t	total

REFERENCES

1. Williams, T.J., M.R.M. Ali, and J.S. Anderson: Noise and Flow Characteristics of Coaxial Jets, *Journal of Mech. Engr. Sc.*, Vol. 11, No. 2, pp. 133-142, April, 1969.
2. Eldred, K.: Far Field Noise Generation by Coaxial Flow Jet Exhausts, Vol. I: Detailed Discussion, FAA-RD-71-101, Vol. 1, Wyle Laboratories, Inc., El Segundo, Calif., 1971.
3. Olsen, W., and R. Friedman: Jet Noise from Coaxial Nozzles Over a Wide Range of Geometric and Flow Parameters, NASA TM X-71503, 1972, or AIAA Paper No. 74-43, 1974.
4. Bielak, G.W.: Coaxial Flow Jet Noise, D6E-10041-1, Boeing/Aeritalia Co., Seattle, Wash., 1972.
5. Stone, J.R.: Interim Prediction Method for Jet Noise, NASA TMX-71618, 1975.
6. Dosanjh, Darshan S., Yu, James C., and Abdelhamid, Amr N.: Reduction of Noise from Supersonic Jet Flows, *AIAA Journal*, Vol. 9, No. 12, pp. 2346-2453, Dec., 1971.
7. Kozlowski, H., and Packman, A.B., "Aero/Acoustic Tests of Duct Burning Turbofan Nozzles," NASA CR-2628, 1976.
8. Kozlowski, H., and Packman, A.B., "Aero/Acoustic Tests of Duct Burning Turbofan Nozzles - Comprehensive Data Report," NASA CR-134910, 1976.
9. Kozlowski, H., and Packman, A.B., "Flight Effects on the Aero/Acoustic Characteristics of Inverted Velocity Profile Coannular Nozzle," NASA CR-3018, 1978.
10. Kozlowski, H., and Packman, A.B., "Flight Effects on the Aero/Acoustic Characteristics of Inverted Velocity Profile Coannular Nozzle - Comprehensive Data Report," NASA CR-135189, 1978.
11. Knott, P.R., et.al., "Acoustic Tests of Duct-Burning Turbofan Jet Noise Simulation," NASA CR-2966, 1978.
12. Knott, P.R., et. al., "Acoustic Tests of Duct-Burning Turbofan Jet Noise Simulation - Comprehensive Data Report," NASA CR-135236, 1977.
13. Lilly, G.M., et. al., "On the Theory of Jet Noise and its Application," AIAA Paper No. 73-987, 1973.
14. Giesebe, P.R., and Balsa, T.F., "Aero/Acoustics of Axisymmetric Single and Dual Flow Exhaust Nozzles," AIAA Paper No. 77-924, 1977.

15. Larson, R.S., "Theoretical Jet Exhaust Model for the Duct Burning Turbofan," AIAA Paper No. 77-1264, 1977.
16. Stone, J.R., "An Empirical Model for Inverted Velocity Profile Jet Noise Prediction," NASA TM-73838, 1978.
17. Noise Control Engineering, pp. 60-67, Vol. 9, No. 2, October, 1977.
18. Howlett, R.A., et. al., "Advanced Supersonic Propulsion Study Phase III Final Report," NASA CR-13548.
19. Comprehensive Data Report for "Aerodynamic and Acoustic Investigation of Inverted Velocity Profile Coannular Exhaust Nozzle Models and Development of Aerodynamics and Acoustic Prediction Procedures", Vol. I CR-15915 and Vol. II CR-159516.
20. Society of Automotive Engineers: Aerospace Recommended Practice, ARP 866A, March 15, 1975.
21. Shields, F.D., and Bass, H.E., "Atmospheric Absorption of High Frequency Noise and Application to Fractional-Octave Bands," NASA CR-2760, June, 1977.
22. Society of Automotive Engineers: Aerospace Recommended Practice, ARP 865.
23. Society of Automotive Engineers: Proposed Aerospace Recommended Practice 876, Gas Turbine Jet Exhaust Noise Prediction, April 1, 1975.
24. Harper-Bourne, and Fisher, M. J., "The Noise from Shock Waves in Supersonic Jets," Agaard Conference Proceedings No. 131 on Noise Mechanisms, Section 12, September, 1973.
25. Abramovich, G.N., *The Theory of Turbulent Jets*, M.I.T. Press, 1963.
26. Larson, R.S., McColgan, C.J., and Packman, A.B., "Jet Noise Source Modification Due to Forward Flight," *AIAA Journal*, Vol. 16, No. 3, pp. 225-232, March, 1978.
27. Harsha, P.T., "A General Analysis of Free Turbulent Mixing," Report No. AEDC-TR-73-177, Air Force Office of Scientific Research, Arlington, Va., May, 1974.
28. Shapiro, A.H., *The Dynamics and Thermodynamics of Compressible Fluid Flow* - Vol. 1, Ronald Press Co., Table B.2, 1953.
29. Paterson, R.W., Vogt, P.G., and Foley, W.M., "Design and Development of the United Aircraft Research Laboratories Acoustic Research Tunnel," *Journal of Aircraft*, Vol. IV, p. 417, July, 1973.
30. Packman, A.B., Ng, K.W., and Paterson, R.W., "Effect of Simulated Forward Flight on Subsonic Jet Noise," *Journal of Aircraft*, Vol. 13, pp. 1007-1013, December, 1976.

31. Morse, P.M., and Ingard, K. U., *Theoretical Acoustics*, McGraw Hill, Section 11.2, 1968.
32. Reshotko, E., and Tucher, M., "Approximate Calculation of the Compressible Turbulent Boundary Layer with Heat Transfer and Arbitrary Pressure Gradient," NACA TN-4154, 1957.
33. Crull, H.G., Beale, U.T., and Schmedlin, R.F., "Effect of Several Design Variables on Internal Performance of Convergent-Plug Exhaust Nozzles," NACA E56G20, 1956.
34. Staid, P.S., "Wind Tunnel Performance Tests of Coannular Plug Nozzles," NASA CR-2990, 1978.
35. Wynosky, T.A., and Spurrell, R.M., "Final Progress Report Exhaust System Interaction Program," PWA Report 4745, dated June, 1973. Air Force Contract F33615-70-C-1450.
36. Obermeier, F., "Sound Generation by Heated Subsonic Jets," Journal of Sound and Vibration, Vol. 41, No. 4, pp. 463 – 472, 1975.
37. Mani, R., "The Influence of Jet Flow or Jet Noise, Part 2, The Noise of Heated Jets," Journal of Fluid Mechanics, Vol. 73, Part 4, pp. 779 – 793, 1976.

1. Report No. NASA CR-3168	2. Government Accession No.	3. Recipient's Catalog No.
4. Title and Subtitle AERODYNAMIC AND ACOUSTIC INVESTIGATION OF INVERTED VELOCITY PROFILE COANNULAR EXHAUST NOZZLE MODELS AND DEVELOPMENT OF AERODYNAMIC AND ACOUSTIC PREDICTION PROCEDURES		5. Report Date August 1979
7. Author(s) Richard S. Larson, Douglas P. Nelson, and Bradley S. Stevens		6. Performing Organization Code
9. Performing Organization Name and Address Pratt & Whitney Aircraft Group United Technologies Corporation East Hartford, Connecticut 06108		8. Performing Organization Report No. PWA 5550-8
12. Sponsoring Agency Name and Address National Aeronautics and Space Administration Washington, D.C. 20546		10. Work Unit No.
15. Supplementary Notes Final report. Project Manager, Albert G. Powers, V/STOL and Noise Division, NASA Lewis Research Center, Cleveland, Ohio 44135.		11. Contract or Grant No. NAS3-20061
16. Abstract <p>This program provided the experimental data necessary to establish aerodynamic and acoustic prediction systems for coannular exhaust nozzles with inverted velocity profiles (IVP). Five coannular nozzle models, covering a systematic variation of nozzle geometry, were tested statistically over a range of exhaust conditions including IVP (fan to primary stream velocity ratio >1) and non IVP profiles. Fan nozzle pressure ratio (FNPR) was varied from 1.3 to 4.1 at primary nozzle pressure ratios (PNPR) of 1.53 and 2.0. Fan stream temperatures of 700 K (1260° R) and 1089 K (1960° R) were tested with primary stream temperatures of 700 K (1260° R), 811 K (1460° R), and 1089 K (1960° R). At fan and primary stream velocities of 610 and 427 m/sec (2000 and 1400 ft/sec), respectively, increasing fan radius ratio from 0.69 to 0.83 reduced peak perceived noise level (PNL) 3 dB, and an increase in primary radius ratio from 0 to 0.81 (fan radius ratio constant at 0.83) reduced peak PNL an additional 1.0 dB. There were no noise reductions at a fan stream velocity of 853 m/sec (2800 ft/sec). Increasing fan radius ratio from 0.69 to 0.83 reduced nozzle thrust coefficient 1.2 to 1.5% at a PNPR of 1.53, and 1.7 to 2.0% at a PNPR of 2.0. The developed acoustic prediction procedure collapsed the existing data with standard deviation varying from ± 0.8 dB to ± 2.7 dB. The aerodynamic performance prediction procedure collapsed thrust coefficient measurements to within ± 0.004 at a FNPR of 4.0 and a PNPR of 2.0.</p>		
17. Key Words (Suggested by Author(s)) Coannular exhaust nozzle; Inverted velocity profile; Advanced supersonic technology; Aerodynamic and acoustic nozzle prediction; Procedure		18. Distribution Statement Unclassified - unlimited STAR Category 07
19. Security Classif. (of this report) Unclassified	20. Security Classif. (of this page) Unclassified	21. No. of Pages 222
		22. Price* A10

* For sale by the National Technical Information Service, Springfield, Virginia 22161

NASA-Langley, 1979

END

April 16, 1981